THE KINETICS OF REDUCTION OF IRON FROM SILICATE MELTS BY CARBON MONOXIDE - CARBON DIOXIDE GAS MIXTURES AT 1300°C

by

Timothy Van Johnson

B. S. Mineral Eng., University of Minnesota
(1978)

M. S. Mineral Eng., University of Minnesota
(1979)

Submitted to the Department of Materials Science and Engineering
in Partial Fulfillment
of the Requirements for the Degree of

DOCTOR OF SCIENCE

at the

MASSACHUSETTS INSTITUTE OF TECHNOLOGY

May 1987

Signature of Author Signature redacted
Department of Materials Science and Engineering
May 1987

Certified by Signature redacted
Professor John F. Elliott
Thesis Supervisor

Accepted by Signature redacted
Professor Samuel M. Allen
Chairman, Departmental Committee on Graduate Students

p. 40

ABSTRACT

THE KINETICS OF REDUCTION OF IRON FROM SILICATE MELTS BY CARBON MONOXIDE - CARBON DIOXIDE GAS MIXTURES AT 1300°C

by Timothy V. Johnson

Submitted to the Department of Materials Science and Engineering on May 1, 1987 in partial fulfillment of the requirements for the degree of Doctor of Science

The gaseous reduction of iron oxides in the presence of silicate melts is an integral part of most high-temperature iron-ore reduction processes. Because the liquid silicate wets the solid iron-oxide grains, much of the iron is produced from reaction of the gas with the slag. The purpose of this investigation is to study the kinetics of reduction of iron oxides from slags using CO_2/CO gas mixtures.

Slag samples contained in magnesia crucibles or iron cups are reduced at 1300°C in a vertical tube furnace equipped with a Cahn 1000 microbalance and a data acquisition computer. Microscopic examinations contribute to the thermogravimetric study and provide information on the morphology of the product iron.

By comparing the observed reduction rates of the melts, containing from 12 to 30 percent silica, to derived kinetic models of the reaction, the rate controlling step of the reduction of iron-silicate melts was determined to be the chemisorption reaction:

$$O\ (ads) + CO\ (g) = CO_2\ (ads)\ . \qquad (1)$$

By comparing the derived models to data in the literature on the isotopic exchange reaction on equimolar $CaO\text{-}FeO\text{-}SiO_2$(l) and FeO(l), the rate controlling step for reduction of these melts by gas containing CO is

$$O\ (ads) + CO\ (ads) = CO_2\ (ads) + g \qquad (2)$$

The rate expression for step (1) is

$$-dO/dt = \beta_1\ \theta_v\ (\ P_{CO}\ a_O - P_{CO_2}\ )$$

and for step (2) is

$$-dO/dt = \beta_2\ \theta_v^2\ (\ P_{CO}\ a_O - P_{CO_2}\ )\ ,$$

where β is the reaction rate constant, θ_v is the fraction of vacant reaction sites available on the melt surface, and a_O is the oxygen activity of the melt expressed as the ratio CO_2/CO in the gas in equilibrium with the melt. The reaction rate constant β_1 has a value of 1.00 ± 0.07 and 2.2 ± 0.05 mole O /(m^2.sec.atm) at 1300 and 1400°C, respectively, the later being determined from published results. The value of β_2 for $CaO\text{-}FeO\text{-}SiO_2$(l) and FeO(l) at 1420°C are 27 ± 5 and 2.4 ± 0.15 mole O /(m2.sec.atm), respectively. The fraction of vacant reaction sites on the melt surface is calculated using

$$\theta_v = 1\ /\ (1 + K_{SiO_2} a_{SiO_2}) \qquad (3)$$

for the iron silicates, and

$$\theta_v = 1 / (1 + K_O a_O + K_{SiO_2} a_{SiO_2}) \quad (4)$$

for the CaO-FeO-SiO_2(1) and FeO(1). The Gibbs-Langmuir adsorption isotherm equation is used to determine the adsorption coefficients K in equations (3) and (4) from surface energy- and activity-composition relationships. The values determined for the adsorption coefficients of oxygen and silica are 4 ($\pm$ 2.4) and 93 ($\pm$ 9), respectively at 1300°C, and 3.7 and 64, respectively, at 1400°C.

The carbon monoxide adsorbs on the surfaces of FeO(1) and CaO-FeO-SiO_2(1), but not on FeO-SiO_2(1). The FeO(1) has a high fraction of vacant reaction sites, so adsorption of CO is not inhibited by oxygen or silica. Adsorbed CO probably gains stability on the surface of the CaO-FeO-SiO2(1) from the formation of carbonate-type bonds, which Ca^{2+} is expected to promote. Reaction kinetics are greatly enhanced if the CO reacts as an adsorbed species instead of as a gaseous species.

The oxygen in the adlayer was determined to be atomic instead of ionic because of the different and distinguishable reaction kinetics. Phosphorous additions to 25 percent SiO_2 melts at the 1 mole percent P_2O_5 level decreased the reduction rate by 25 percent.

The liquidus region of the FeO-SiO_2-Fe_2O_3 system at 1300°C was reevaluated and modified to account for recent data on the enthalpy of mixing SiO_2(s) with FeO(1).

Thesis supervisor: John F. Elliott
Professor of Metallurgy

TABLE OF CONTENTS

TABLE OF CONTENTS (continued)

LIST OF FIGURES

75 figures

LIST OF FIGURES (continued)

LIST OF FIGURES (continued)

LIST OF FIGURES (continued)

LIST OF FIGURES (continued)

LIST OF FIGURES (continued)

LIST OF TABLES

13 tables

ACKNOWLEDGMENTS

Sincere appreciation is given to the United States Steel division of the USX Corporation for the generous financial support of this research and of my graduate education at M.I.T. Thanks are also given to the American Iron and Steel Institute, for financial support provided through Professor Elliott's distinguished professor award, and to the United States Bureau of Mines, for financial support provided through the Mineral Resources Research Institute at M.I.T. Additional thanks are given to the Corning Glass Works for allowing me to use the office facilities, supplies, and library and computer resources to complete the writing of this manuscript.

Much gratification is given to Professor Elliott for is guidance, support, and suggestions provided throughout my tenure at M.I.T. Professor Elliott skillfully used my thesis research as an invaluable teaching tool by allowing me to independently plan, execute, and evaluate the experiments, and by providing his assistance only when needed. His relationship with me made my research experience and education at M.I.T. truly rewarding and memorable.

Thanks are extended to my peers in Professor Elliott's group, and in Professor Yurek's group, with whom I shared the laboratory. Special recognition is given to: Bob Frank, who offered many valuable suggestions in discussions, and provide much needed help with the computer system; Dr. Charles Finn, who provided much technical advise; Mike Maloney, Dr. Daniel Eppelsheimer, Dr. Kazimierz Pryzbylski, Ken Sandhage, and Raymond Lam, all of whom offered support through valuable friendships.

Very special recognition is given to my loving wife, Rebecca, who gave unending love, support, patience, and encouragement for me throughout the experience. Her professional drafting of the figures, and all the time spent in helping me put this manuscript together is truly appreciated.

Chapter 1

INTRODUCTION

Most of the processes used or being developed to produce iron from ore involve the high-temperature gaseous reduction of iron oxide in the presence of silicate impurities. When the iron oxide is reduced to wustite, it fluxes the silicate gangue creating a liquid phase. In the case of the pure oxides, FeO and SiO_2, the fluxing action will occur at about 1140°C, but with other common components of the gangue present, such as CaO and Al_2O_3, a liquid can be formed at temperatures less than 1100°C. The liquid phase develops and increases in volume as the temperature increases and reduction proceeds, and very effectively wets the solid iron-oxide particles. The wetting action changes the reduction from a gas-solid to a gas-liquid reaction. Studies have shown that if the liquid comes in contact with coke or other forms of solid carbon, the rate of the overall direct reduction reaction

$$FeO\ (slag) + C = Fe + CO\ (g) \qquad (1\text{-}1)$$

is controlled by the step

$$FeO\ (slag) + CO\ (g) = Fe + CO_2\ (g)\ . \qquad (1\text{-}2)$$

So in effect, almost all of the iron produced by carbon-based reduction of iron ores at temperatures greater than about 1200°C is produced by reaction (1-2).

Although reaction (1-2) is commercially important, it has not been studied directly in much detail. The kinetics of reaction (1-2) have been studied indirectly in investigations on the

kinetics of the direct reduction reaction (1-1), and by studies on the isotopic exchange reaction

$$^{14}CO_2\ (g) + CO\ (g) = {}^{14}CO\ (g) + CO_2\ (g) \qquad (1\text{-}3)$$

on the surface of ferruginous melts. But reaction (1-1) is very difficult to analyze because it involves the complicated interaction of four phases. The isotopic exchange reaction was studied at liquid-gas equilibrium in relatively oxidizing conditions ($CO_2/CO = 1$ in the gas), and may not be applicable to reducing and non-equilibrium conditions.

1.1 Statement of Objective and Experimental Plan

The objective of this investigation is to study the reduction of iron oxide from silicate melts by carbon monoxide, and determine the rate controlling step.

Iron-silicate melts are reduced in iron crucibles in a thermogravimetric apparatus at 1300°C under CO_2-CO gas mixtures. The experimental reduction rates are compared to derived rate expressions for proposed reaction steps to determine which step controls the reaction. The results and the derived rate expressions are compared to the results of other investigations on the same and different systems to determine the applicability of the models proposed.

Chapter 2

LITERATURE SURVEY

2.1 Studies on the Reduction of Iron from Slags by Carbon Dissolved in Iron

Studies using X-ray fluoroscopy techniques (1, 2) to observe the reaction between droplets of iron in slag provide strong visual evidence that the reduction of slags by carbon dissolved in iron

$$FeO\ (slag) + \underline{C} = Fe\ (l) + CO\ (g) \qquad (2\text{-}1)$$

proceeds through the two reaction steps

$$\underline{C} + CO_2\ (g) = 2\ CO\ (g) \qquad (2\text{-}2)$$

and

$$FeO\ (slag) + CO\ (g) = Fe + CO_2\ (g)\ . \qquad (2\text{-}3)$$

Although the reaction was shown to be rather complex, with several different reaction stages involving the nucleation of carbon monoxide bubbles in the metal, and a fast reaction period followed by a slower reaction period, the overall reaction (2-1) is thought to be controlled by the reaction at the slag-gas interface (3, 4, 5), reaction (2-3), over most of the reduction period.

Grieveson (3) presented a review of the literature on the reduction of iron oxide from slags by graphite or carbon dissolved in iron, and showed that the forward rate constants of reactions (1-1) and (2-1) were similar. Uphadya and Sommerville (4) measured the volume of gas evolved from iron droplets in slag and found that the rate of reaction (2-1) was independent of

carbon levels in iron melts containing more than 2 percent carbon. Belton (5) compared the rates of CO_2 dissociation on molten iron determined using the isotopic exchange technique, to reported rates for reaction (2-1), and determined that the rate controlling step for the overall reaction shifts to reaction (2-2) at the gas-metal interface if the metal contains more than about 0.010 percent sulfur. However, results on the rate of gaseous reduction of iron-oxide slags are needed to support the hypothesis (5).

2.2. Reduction of Iron from Melts by Gas Mixtures

Table 1 is a summary of the more pertinent studies on the reduction of iron from melts. The top portion of the table summarizes the results on gaseous reduction of ferruginous melts. The other studies summarized in the table are representative of the studies in which carbon was used as the reductant. Figure (2-1) is an Arrhenius plot of reduction rates obtained using CO (dashed lines) and solid carbon (solid lines) as the reductants. Included in the figure are results on the rate of dissociation of CO_2 using the isotopic exchange reaction technique on several melts.

Nagasaka, Iguchi, and Ban-ya (6) used a thermogravimetric technique to study the reduction of iron-saturated liquid iron oxide with additions of silica, calcia, titania, and alumina by $CO-CO_2$, $CO-CO_2-Ar$, and CO-Ar gas mixtures from 1270 to 1450°C. Very high gas flowrates (4 l/min) were used to shift the reaction

Table 2-1 Summary of Some Investigations on the Reduction of Ferruginous Melts by Gaseous Reductant or Carbon

Reference	System	Test Method	Results
Nagasaka, Iguchi, Banya; 1986; (7)	FeO (pure), FeO + SiO_2, + Al_2O_3, + TiO_2, + CaO; 1270-1400°C; Fe. cruc.;	thermogravimetric; 10%CO, bal. Ar; init. rates;	red. of FeO(l) gas diff. controlled; Al_2O_3 had no effect; CaO incr. rates; TiO_2, SiO_2 decr. rates; chemisorp. contr.; E_a=205 kJ/mole
Fine, Meyer, Janke Engell; 1985; (6)	68%FeO,14.2%CaO,5.7%MgO 12.4% SiO_2;MgO sat.1600C	CO at 1 atm; infrared gas analysis of CO_2;	rate 0th order w.r.t. FeO to 48% FeO; chemisorption control for FeO < 48%
Katayama, Taguchi, Tsuchiya; 1982; (8)	5-15%FeO, 39-42%CaO, 33-36%SiO_2, 15-17%Al_2O_3; 1450°C; MgO crucibles;	thermogravimetric; H_2-H_2O;	init. rate controlled by chemisorption rxn: H(ad)+O(ad)=OH(ad); later rxn is liquid phase diffusion controlled; D=3X10^{-8} m^2/sec
Tsukihashi, Kato Otsuka, Soma; 1982; (9)	FeO(l); 1450 and 1600°C	1 atm CO;gas transport of 25 μm particles; % red. by chem. anal.	mixed control; gas diffusion, chemisorption; rates=0.13 to 0.18 mole O/(m^2.sec) (1450,1600°C) E_a = 260 kJ/mole for chemisorption component
Shalimov, Boronenkov, Lyamkin;1980;(11)	60-100% FeO, balance SiO_2; 1300-1450°C P = 0.125-2 atm	C contact w/ or sep. from slag (Al_2O_3 cruc.) thermogravimetric;	1.2 order w.r.t. FeO act.; E_a=190 kJ/mole; controlled by chemisorption reaction; rate = 1.25-3.96 X 10^{-2} mole O /(m^2.sec)
C. Borgianni; 1978; (10)	80%FeO, 3-20%CaO, 0-17% SiO_2; 1250-1450°C vitreous C crucibles	coke particles in slag; thermogravimetric;	for %red.<75%, Fe nucl. control; % red > 75%, diff. control in slag; E_a(rx)=230 kJ/mol; E_a(nucl.) = -75 kJ/mol; E_a(diff.)=318 kJ/mol
Davies, Hazeldean, Smith; 1973; (1)	60-95%FeO, 5-40%SiO_2; and 5-95%FeO with bal. CaO/SiO_2=0.11 to 0.59; 1400-1500°C	C cruc.; periodic sampling;	FeO-SiO_2 : 0th or 1st order w.r.t. %FeO for slags w/ FeO>60%; 0th order E_a=280 kJ/mol; slags w/ CaO: 1st order in mid conc. range; inconclusive; not gas diff. cont.; 1400°C: rate = 0.111-0.195 mole O/(m^2.sec)
Fun; 1970; (12)	20-50% FeO, balance CaO/SiO_2=1.2; 1650°C	C rod reductant; MgO cruc. grab samples	1.77 order w.r.t. %Fe_tO; not C gasification controlled; rate = 0.83 mole O/(m^2.sec);
Krainer, Beer, Brandl; 1966; (13)	70%FeO-SiO_2; 70%FeO, bal. CaO, SiO_2, Al_2O_3; 1200-1500°C	graphite or coke cruc. thermogravimetric;	1st order w.r.t. %FeO; E_a = 80-170 kJ/mole; at 1300-1450°C: rate=1.8-19X10^{-2} mole O/(m^2.sec)

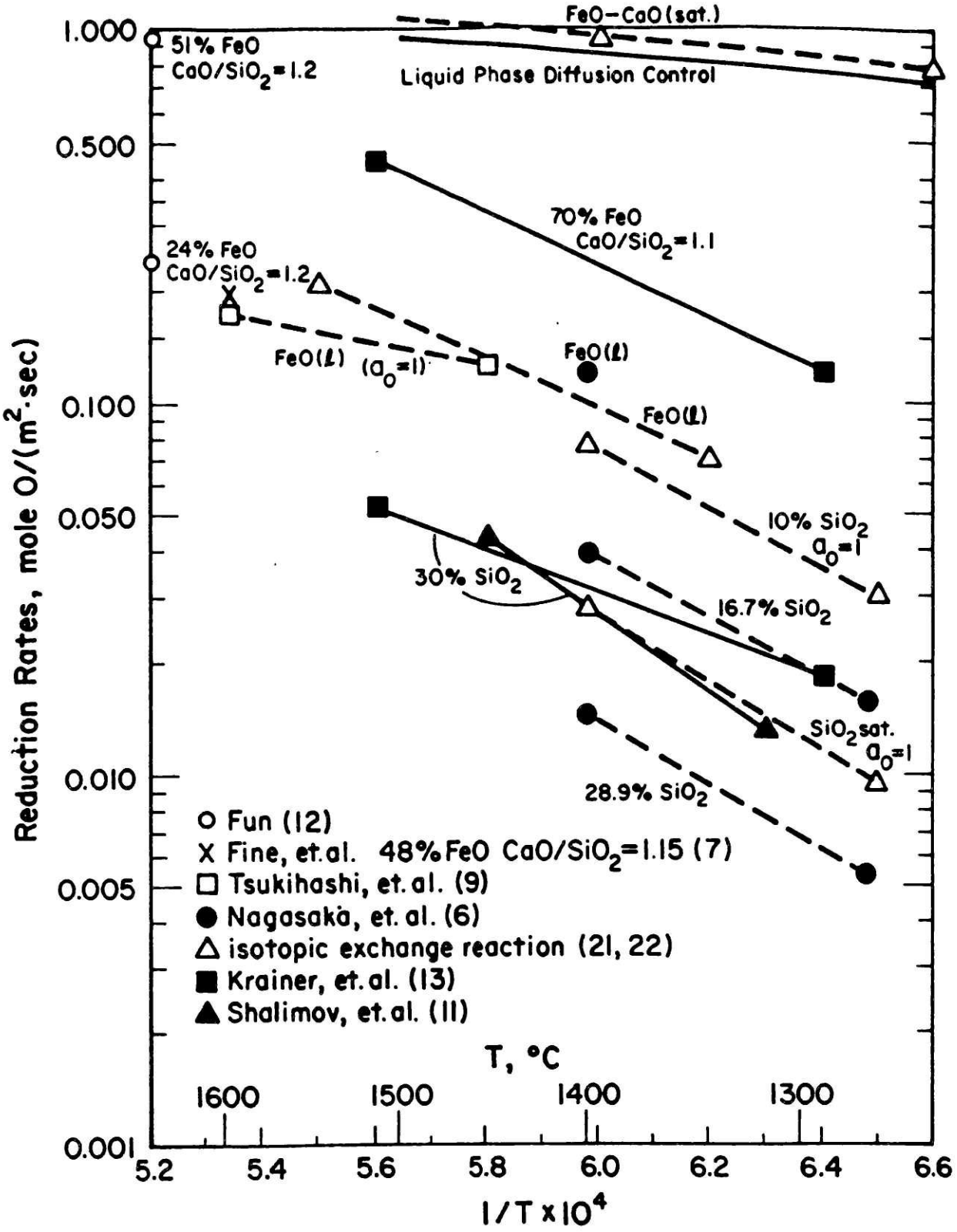

Figure 2-1. Arrhenius plot of reduction rates of various ferruginous melts. $P_{CO} = 1$.

from gas phase diffusion control, and low partial pressures of CO (down to P_{CO} = 0.003 in some tests) were used to shift the rate controlling step from liquid-phase diffusion control to chemisorption control, which is dependent on pressure. The results were analyzed using the general chemisorption rate expression

$$R = k_a (P_{CO}\, a_O - P_{CO_2}) , \qquad (2\text{-}4)$$

where R is the reduction rate, k_a is the rate constant, and a_O is the oxygen activity of the melt (a_O = 1 for CO_2/CO = 1). Only data on the reduction of the pure liquid and of the silicate melts were presented, but alumina additions were stated to have no effect on the rates, titania and silica additions retarded the reduction, and calcia additions increased the rates. The reaction rate constant for the pure oxide is 0.46 mole O/(m^2.sec.atm) at 1400°C , and decreased to 0.076 mole O / (m^2.sec.atm) with silica additions to the 31.8 weight percent silica level. The rate constants of the various melts were empirically correlated to the $(Fe^{3+})^{2/3}/Fe^{2+}$ ratios of the melts. The activation energy of the rate constant k_a for the reduction of the silicate melts is calculated to be 205 kJ/mole.

Fine, Meyer, Janke, and Engell (7) held slags containing up to 68 percent FeO, and 12.4 percent SiO_2, 14.2 percent CaO, and 5.7 percent MgO in magnesia crucibles and reduced them at 1600°C under pure CO. They monitored the reaction by analyzing the product gas for CO_2 using an infrared analyzer. The reaction rate

was independent of FeO content down to the 48 percent level. Fine, et.al. deduced that the activity of FeO in the melt at the higher FeO levels changed very little on reduction. At the lower FeO contents, it was proposed that the reaction was controlled by a chemisorption reaction.

Katayama, Taguchi, and Tsuchiya (8) studied the reduction of iron oxide from blast-furnace type slags by H_2O-H_2-Ar gas mixtures at 1450°C using a thermogravimetric technique. The slag was held in magnesia crucibles and contained SiO_2, CaO, Al_2O_3, and less than 15 percent FeO. They deduced that the initial reduction rate was controlled by the reaction:

$$H(ad)+O(ad)=OH(ad) \ . \qquad (2\text{-}5)$$

After about 15 minutes the reaction shifted to diffusion control in the slag phase. The interdiffusivity of FeO in the slag was determined to be $3X10^{-8}$ m^2/sec.

Tsukihashi, Kato, Otsuka, and Soma (9) reduced wustite particles by conveying them through a furnace at 1450 and 1600°C with CO carrier gas. The reduction rate was determined by chemical analyses of the reduced particles. Iron was found to form in the middle of the iron-oxide particles, which were spherical after reduction and about 25 μm in diameter. The reaction was controlled by gas-phase diffusion and a chemisorption reaction. The Marshall-Ranz equation was used to estimate the the mass transfer coefficient, which was compared to the overall reduction

rate coefficient to determine the chemisorption reaction rate coefficient. Calculations of the reaction rate constant k_a from the data yields values of 0.55 and 1.0 mole O / (m^2.sec.atm) at 1450 and 1600°C, respectively. Extrapolation to 1400°C gives 0.33 mole O / (m^2.sec.atm) for the rate constant, which compares with 0.46 mole O / (m^2.sec.atm) determined by Nagasaka, et. al. at the same temperature.

2.3 Reduction of Iron from Ferruginous Melts by Solid Carbon

The results of studies on the reduction of slags by carbon are difficult to interpret and are often contradictory. The reaction involves the interplay between four phases in which mass transport and carbon surface properties are important and therefore is dependent on the experimental conditions. Davies, Hazeldean, and Smith (1) give a good review of early work in the area and present results on some experimental work. Emphasis was placed on the significance of the carbon surface and how it effects the nucleation of CO bubbles. The wide range of reaction rates and activation energies reported in earlier studies was attributed to varying conditions at the carbon-slag interface.

Borgianni (10) stressed the importance of interfacial properties at the slag-gas interface on the reduction kinetics. An iron nucleation model was used to fit the kinetics up to a reduction degree of about 70 percent, after which the reaction became diffusion controlled. The reaction rates of solid and liquid

slags were on the same Arrhenius line, indicating that the step controlling the rate of nuclei growth was the same in both states.

Shalimov, et.al. (11) used three separate experimental arrangements to conclude that the reaction was controlled at the slag-gas interface. A thermogravimetric technique was used to follow the reduction of high FeO silicate slags by graphite in contact with or separated from the slags at 1300-1450°C and pressures from 0.125 to 2 atm. The reduction behavior was the same in all configurations, and the rates generally increased with increasing pressure. Further, the reduction rate was independent of the slag to graphite distance in those tests using alumina crucibles with graphite lids, indicating that the reaction was not gaseous diffusion controlled. The only rate controlling step that is consistent with the above observations is that at the slag-gas interface.

Fun (12) reduced slags containing 20 to 50% FeO in the $CaO-SiO_2-MgO$ system by graphite rods using MgO crucibles at 1650°C. The MgO + FeO content of the slags remained almost constant. The observed reduction rates were lower than those if carbon gasification was limiting, except for pure FeO(l).

Krainer, et.al. (13) reduced high FeO content silicate, calcium silicate, and calcium-alumina-silicate slags by graphite and coke

at 1200-1600°C. Based on the apparent activation energies of 80-170 kJ/mole, they concluded that the reaction was controlled at the slag-gas interface. Slags containing lime reacted about an order of magnitude faster than iron-silicate slags, but had the same apparent activation energy. This indicates that the reaction was not diffusion controlled in the slag because lime adversely affects the diffusivity of iron ions in these types of slags (14).

Philbrook and Kirkbride (15), and Tarby and Philbrook (16), concluded that the reduction of low FeO slags is liquid-state diffusion controlled. Plyshevskii, et.al. (17) obtained an apparent activation energy for the reduction of similar slags by graphite at 1500-1700°C of 200 kJ/mole, which agrees with those obtained by Tarby and Philbrook of 160 to 230 kJ/mole. Turkdogan (18) estimates that the apparent activation energy for diffusion in iron-silicate slags is about 140-180 kJ/mole at 30 weight percent FeO and about 45-85 kJ/mole at 65 weight percent FeO. From the results of Agrawal and Gaskell (19) and Mori and Suzuki (20) on the interdiffusivity of iron and oxygen in melts containing 70 percent FeO, the activation energy for diffusion is about 45 kJ / mole. The rates of reduction expected under liquid-phase diffusion control using the results of Agrawal and Gaskell are shown in Figure 2-1.

The reduction rates for the different melts in Figure 2-1 vary by more than an order of magnitude at constant temperatures. But the

activation energies of reaction are similar to those expected for chemisorption controlled reactions. In general, the reduction rates of melts containing calcia are much greater than the rates of the other melts, and silica is shown to adversely affect the reduction rates.

2.4 Results on the Isotopic Exchange Reactions on Oxide Melts

Belton and co-investigators have conducted several studies on the isotopic exchange reaction on a variety of metal and oxide melts. The overall exchange reaction

$$^{14}CO_2\ (g) + CO\ (g) = {}^{14}CO\ (g) + CO_2 \qquad (2\text{-}6)$$

occurs by a series of reaction steps that include reactions of the form

$$^{14}CO_2\ (g) = {}^{14}CO\ (g) + O\ (ads) \qquad (2\text{-}7a)$$

and

$$CO\ (g) + O\ (ads) = CO_2\ (g)\ , \qquad (2\text{-}7b)$$

where O (ads) is adsorbed oxygen on the surface of the melt. The CO and CO_2 in reactions (2-7a and b) may also be adsorbed on the surface of the melt. The rate of the overall exchange reaction (2-6) is equal to the rate of the slowest reaction step in any of several chemisorption reaction mechanisms that may be proposed. For example, the exchange reaction may be controlled by the adsorption/desorption of CO and CO_2, the charge transfer between the adsorbed species and the melt, or reaction steps of the form in (2-7a and b) that may include O^{2-}(ads) or CO_2^{2-}(ads).

The studies are conducted with the gas in equilibrium with melts held in silica, calcia, or Pt/Rh crucibles. A gas with tagged CO_2 and CO is delivered to the melt surface through a small-diameter ceramic tube, which is placed coaxially inside a larger ceramic tube. The larger tube is submerged in the melt, so the gas is in contact with only the melt and tube surfaces at temperature. The CO_2 in the reacted gas is removed, and the remaining CO is oxidized over CuO at 300°C, and analyzed by using the internal Geiger-Muller tube method or a scintillation spectrometer.

Two papers have been published on the rate of the exchange reaction on molten oxides. The first, by Sasaki, Hara, Gaskell, and Belton (21), was conducted on liquid iron oxides and calcia saturated ferrites at temperatures up to 1550°C. The second study, by El-Rahaiby, Sasaki, Gaskell, and Belton (22), was conducted on several melts -- silica-saturated iron and manganese silicates, unsaturated iron silicates with unit oxygen activities, equimolar $CaO-FeO-SiO_2$, and $CaO-FeO-SiO_2$ with 5 to 80 mole percent FeO and $CaO/SiO_2 = 1$ (mole basis). The rates of the exchange reaction on some of these melts are shown in Figure (2-1).

The results of the studies were analyzed using the chemisorption rate expression, equation (2-4)

$$R = k_a \left(P_{CO}\, a_O - P_{CO_2}\right) . \qquad (2\text{-}4)$$

Except for the $CaO-FeO-SiO_2$ melts, the reaction rate constants k_a were found to be inversely proportional to the oxygen activities of the melt

$$k_a = k_a^\circ / a_O \quad , \tag{2-8}$$

where k_a° was defined as the apparent rate constant. Sasaki, et. al. determined that the dependency of the rate constant on oxygen activities was related to a charge transfer reaction of the form

$$CO_2 \text{ (ads)} + 2\,[Fe^{2+}] = CO_2^{2-} \text{ (ads)} + 2\,[Fe^{3+}] \quad , \tag{2-9}$$

where the brackets indicate species in the melt. For reaction (2-9) at equilibrium,

$$\Gamma_{CO_2^{2-}} \propto P_{CO_2} \, (Fe^{2+}/Fe^{3+})^2 \quad , \tag{2-10}$$

where the variable on the left side represents the concentration of the weakly adsorbed CO_2^{2-} species on the melt surface. If the rate controlling step in the overall exchange reaction is

$$CO_2^{2-} \text{ (ads)} = CO \text{ (ads)} + O^{2-} \quad , \tag{2-11}$$

where the oxygen is adsorbed, or directly incorporated into the melt, then the forward rate law for the overall exchange reaction is

$$R = k \, P_{CO_2} (Fe^{2+}/Fe^{3+})^2 \quad . \tag{2-12}$$

For the iron oxide and calcium ferrite melts,

$$(Fe^{3+}/Fe^{2+})^2 \propto a_O \quad , \tag{2-13}$$

thus the empirical relationship in equation (2-8) fits the model.

It was also shown that equation (2-8) may fit a model in which the adsorption of CO_2 is slow because of a limitation in

available reaction sites, wherein

$$\Gamma_v \propto (a_O)^{-1} \quad . \qquad (2\text{-}14)$$

Although this relationship holds true for the iron-oxide melts, it is not true for the ferrite melts. Therefore, it was deduced that reaction (2-11) was controlling the isotopic exchange reaction. As Figure 2-1 shows, there is reasonable agreement with the results obtained in reduction tests on liquid iron oxide.

In the second study, El-Rahaiby, et.al. found that the rate constants k_a were also indirectly proportional to the oxygen activities of the melts, equation (2-8), for silica saturated iron- and manganese-silicate melts, and equimolar $CaO-FeO-SiO_2$ melts. However, melts with CaO/SiO_2 (mole basis) and FeO levels of 1.0 and 5.0 mole percent did not fit equation (2-8). El-Rahaiby, et.al. performed similar analyses as Sasaki, et.al. on the relationships between the reaction rate constants, the oxygen activities of the melts, and the Fe^{2+}/Fe^{3+} ratios in the melts, and claimed that all of the melts fit the model in which reaction (2-11) controls the exchange rates, and equation (2-12) describes the rate of the overall reaction. (Information on the Mn^{2+}/Mn^{3+} ratios in the manganese-silicate melts is not available.)

Closer analysis shows that although the reaction rate constants k_a for the liquids containing calcia are directly proportional to the $(Fe^{2+}/Fe^{3+})^2$ in the melts, the relationship does not hold for

the iron-silicate melts at silica saturation, shown in Figure 2-2, indicating that other effects may be influencing the rates, such as the concentration of vacant reaction sites on the surface of the melts.

El-Rahaiby compared the reduced rate constant $k_a°$ to the mole fraction of silica in iron silicates and calcia-iron-silicates, and found that the rate constant decreased with increasing silica contents. The trend was qualitatively related to the excess surface concentration of silica on the melt. Also, it was shown that the rate constants for a wide variety of melts at unit oxygen activity, when compared together, increase with the Fe^{3+}/Fe^{2+} ratios in the melts, in apparent contradiction with the observations within each melt type in which the rate constants increase with the Fe^{2+}/Fe^{3+} ratios. El-Rahaiby, et.al. explained that the Fe^{3+}/Fe^{2+} ratio is a measure of the propensity of the melt to accommodate charge transfer to adsorbed species, and that the generally increasing rates with this ratio indicate that the surface constitution of the melts may not be important. However, the relationship between the rate constants and the ferrous:ferric ratios in melts should be consistent whether comparisons are made within specific melts types or between melt types, if the same rate expressions apply to all melts. The recommendation was made that further studies be conducted with small levels of strongly adsorbed species, such as P_2O_5, added to the melt to determine if vacant reaction site concentration is important.

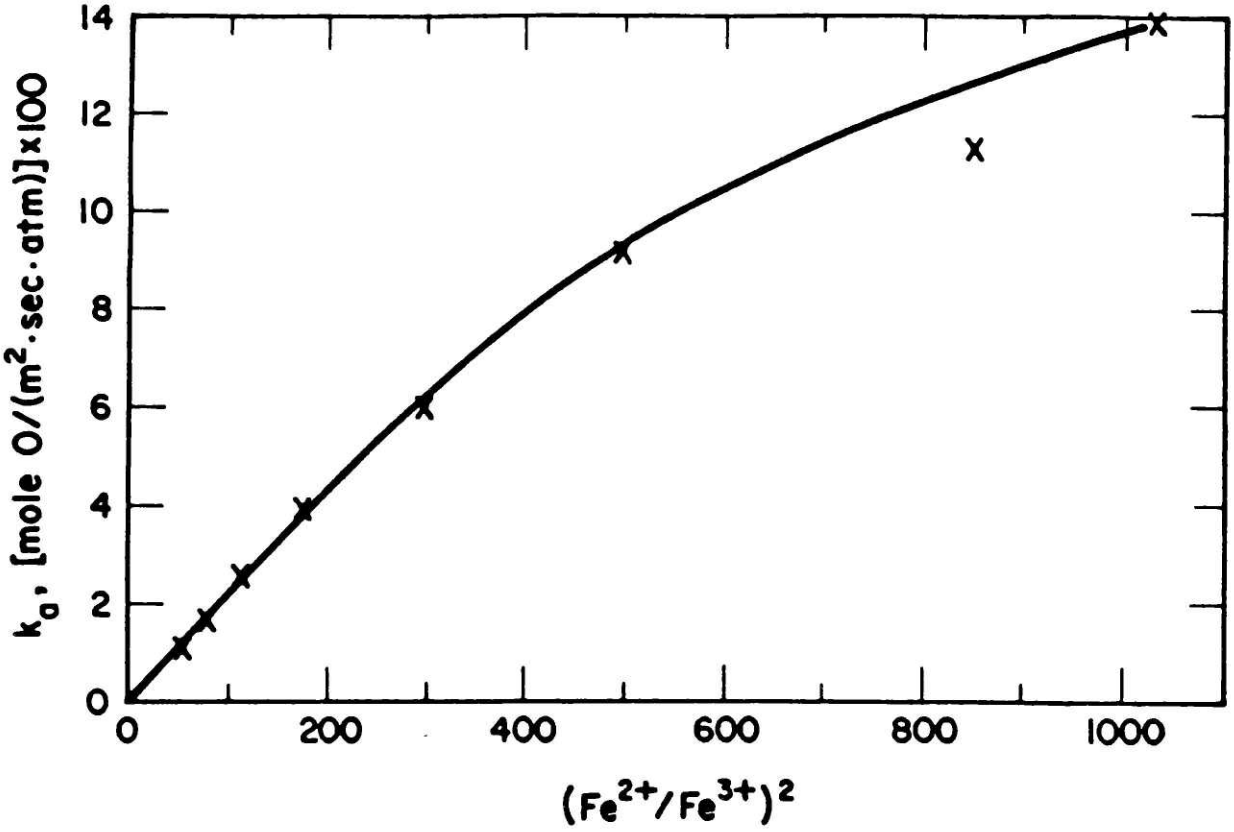

Figure 2-2. Relationship between rate constant k_a and $(Fe^{2+}/Fe^{3+})^2$ for the isotopic exchange reaction on SiO_2 sat. melt. 1400°C. (22)

The results on the isotopic exchange reaction provide valuable information on the chemisorption rates on several oxide melts. But the studies were carried out on melts in which little is known about the surface energies, thus correlation of the rate results with surface constitution is difficult and speculative.

2.5 Studies on the Surface Structure of Metals and Metal Oxides

Direct evaluation of surface structures involves the use of instruments that that require precise alignment of well-defined surfaces under ultra-high vacuums. Some of the more common methods used include low-energy electron diffraction (LEED), Auger electron spectroscopy (AES), and X-ray photoelectron spectroscopy (XPS). While each has limitations, combinations of techniques are used with theoretical analyses to develop models of the structure of surfaces. The nature of adsorption, dissociation, and desorption is quite well understood on metal surfaces at temperatures up to about 1000°C, much less is understood about oxide surfaces, and because of the limitations of the instruments, no direct determinations have been done on melts.

Adsorbed species on metals form covalent bonds with the metal atoms. Carbon monoxide forms carbonyl-type bonds on metals, with the axis of the CO molecule perpendicular to the surface, and the carbon atom bonded to two metal atoms (23). Carbon monoxide is very strongly adsorbed on metal surfaces and may inhibit the adsorption of oxygen, dramatically decreasing catalytically

enhanced oxidation reactions. But CO is only very weakly adsorbed on most oxides, but can interact strongly on oxides that tend to form carbonates (24).

The adsorption-dissociation of molecular oxygen on metals is very well understood. On iron, the adsorption of oxygen molecules results in dissociation followed by immediate formation of independent quasimolecules of wustite (25, 26) that show very little interaction, even at oxygen potentials close to saturation at 800°C (27). The Fe-O bond length is close to that in wustite (28), but the effective hard-sphere radius of the adsorbed oxygen is about 0.83 Angstroms, which is much less than the ionic radius of oxygen in wustite of about 1.24 Angstroms. Oxygen adatoms have been shown to be very mobile on iron surfaces at 800°C, but cluster into two-dimensional networks on cooling (27). Little is known about the adsorption of oxygen on metal oxides. The heat of adsorption of oxygen on oxides is about 1/2 of the heat of formation of the oxide (29). It is difficult to distinguish between adsorbed oxygen and bulk oxygen with current techniques.

Carbon dioxide has been observed on metal surfaces only at low temperatures (about 200 K) (23), but shows stronger adsorption tendencies on oxides (24).

Chapter 3

KINETIC MODEL

The overall reaction

$$FeO\ (slag) + CO\ (g) = Fe\ (\gamma) + CO_2\ (g) \qquad (3\text{-}1)$$

can be thought of as occurring through a sequence of intermediate steps that make up a coherent overall reaction mechanism. Although proposed reaction mechanisms can get rather complex, all mechanisms for the above overall reaction can be subdivided into four general steps which can be analyzed separately:

1) gaseous diffusion of reactants or products to or from the reaction interface
2) liquid phase diffusion of reactants or products to or from the reaction interface
3) adsorption and reaction of species at the interface
4) nucleation and growth of a new product phase.

The kinetics of the reduction reaction is analyzed using a concept introduced by Wagner (30, 31), in which the "virtual maximum rate" of each individual step in a reaction mechanism is determined. Each step in a proposed reaction mechanism is assigned a rate expression that would be observed if all previous and subsequent steps in the mechanism are fast and virtually at equilibrium relative to the step being analyzed. The observed rate for the overall reaction is then compared to the derived rate expression for each individual step in the proposed mechanism to determine the rate controlling step.

Each of the four general reaction steps will be analyzed in this chapter with the objective of providing a method of determining which of the steps may be controlling the overall reaction rate.

3.1 Gas Phase Diffusion Control

Gas-phase diffusion control would be expected in a system in which the chemical reaction is very fast, or the concentration of reducing gas is low, or the flowrate of gas to the reaction site is slow or dependent on natural convection. The gaseous reduction of pure liquid iron oxide is similar to the reaction under study here, and is controlled by gas diffusion except under conditions where a high flowrate of gas is impinging on the melt surface (6). It is not unreasonable to expect that gas diffusion may be controlling the reaction rate in this study.

Gas phase diffusion is not limiting the reaction rate if the observed reaction rates are dependent on melt composition under constant reduction driving forces. However, gas diffusion control could affect the reaction rate of the melt for which the highest overall rate of reaction is observed. The influence of gas diffusion on the rate of this melt is tested by simply changing the gas flow rate and observing if the resulting reduction rate changes. Also, modeling of the fluid flow may be used to determine if gas diffusion control is likely.

The crucible assembly is shown to scale in Figure 3-1. There are no fluid-flow models readily available in the literature that fit

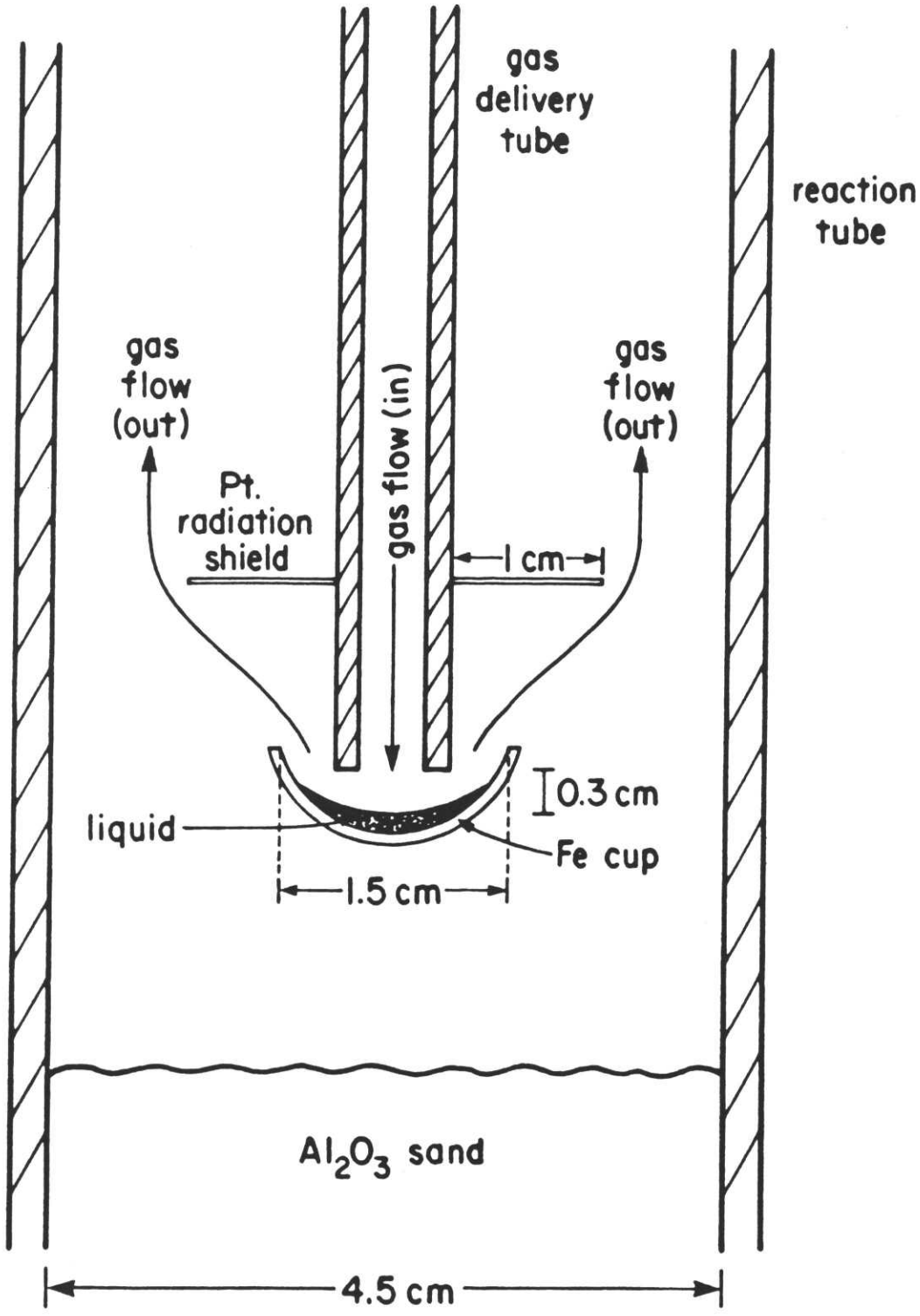

Figure 3-1. Scale model drawing of crucible assembly.

precisely this configuration. However there are two simple systems for which models have been developed that provide a narrow range of mass transfer coefficients from which it is possible to estimate the coefficient for the current arrangement: One is a gas stream impinging on a flat plate, and the other is a horizontal flat plate that is enclosed by a vertical cylindrical wall (such as with a flat sample contained in a deep crucible). Table 3-1 defines the variables and contains the values chosen for applying the models. The values are determined for a gas with $CO_2/CO = 0.143$ at 1300°C.

The flat plate model was developed by Rao and Trass (32), who dissolved a plate of transcinnamic acid by a submerged jet of water. Sain and Belton (33) included a factor containing the Schmidt number to the original correlation to account for the much different results they observed in studying the decarburization of molten iron by carbon dioxide. The resulting equation is:

$$Sh = B\ Re^{1.06}\ Sc^{0.33}\ (a/d)^{-0.09} \qquad (3\text{-}2)$$

for

$$(a/d) \leq 6.5 \text{ and } (x/d) \leq 4.5 \ .$$

The calculated values for the Sherwood number and the mass transfer coefficient are 0.865 and 0.58 m/sec, respectively. The expected reaction rate under gas diffusion control is estimated from the calculated mass transfer coefficient using the equation

Table 3-1. Variable Definitions and Chosen Values used in Applying the Fluid-Flow Models

Definition	Variable	Value	Units
constant	B	0.026-0.046	-
Sherwood number	Sh	md/D	-
mass transfer coefficient	m	determined	m / sec
interdiffusivity of the reactants and products in the gas phase	D	2.96×10^{4}	m^2 / sec
inside diameter of nozzle	d	4.3	mm
Reynolds number at tube outlet	Re	$dv\rho/\eta = 27.8$	-
gas velocity at tube outlet	v	1.52	m / sec
gas density	ρ	0.233	kg / m^3
gas viscosity	η	5.74×10^{-5}	kg / m sec
Schmidt number	Sc	$\eta/\rho D = 0.793$	-
nozzle to surface distance	a	3	mm
radial distance from nozzle centerline	x	6	mm
outside diameter of nozzle	d_o	7.1	mm
inside diameter of crucible	d_i	15	mm
molecular weight of oxygen	M	0.016	kg / mole
activity of FeO in melt with the highest rate	$a_{FeO(l)}$	0.909	-
activity of FeO in the gas	$a_{FeO(g)}$	0.431	-
equilibrium constant for reaction (3-1) at 1300°C	K_e	0.3314	

$$R = (m\rho K_e/M)[a_{FeO(l)} - a_{FeO(g)}] , \qquad (3\text{-}3)$$

and is 0.134 mole O / (m^2.sec).

The cylindrical wall model was developed by Taniguchi, Kikuchi, and Maeda (34), who studied the sublimation of naphthalene and the evaporation of pure liquids into a nitrogen stream using several different crucible configurations. Their relationship is

$$Sh = 0.40(\pm 0.13)\ (d/x)\ (Re)^{0.66}\ Sc^{0.5} \qquad (3\text{-}4)$$

for

$$a/d \leq 0.0046(Re)^{0.68}(x/d)^{1.5}[\exp(3.96d_o/d_i)](\exp Sc)/Sc .$$

The calculated values for the Sherwood number and the mass transfer coefficient using equation 3-4 are 1.55 and 0.107 m/sec, respectively. Using this value for the mass transfer coefficient, m, in equation (3-3) gives an estimated reduction rate of 0.246 mole O / (m^2.sec) using the cylindrical wall model.

Under gas diffusion control, the observed reaction rate would be similar to the two rates calculated above. The fastest reaction rates observed in this study and reported in the literature are almost two orders of magnitude slower. Gas diffusion control is not expected in the current study.

3.2 Diffusion Control in the Liquid Phase

Katayama, Taguchi, and Tsuchiya (8) reduced blast-furnace type slags (40% CaO, 40% SiO_2, 15% Al_2O_3) containing 5 to 15 percent FeO under H_2/H_2O atmospheres at 1450°C in a similar experimental configuration used in this study, and concluded that the reaction

was liquid phase diffusion controlled. Others have studied the reduction of slags of low FeO activity reduced by carbon in somewhat turbulent conditions (15, 16) and concluded that diffusion in the liquid is limiting the reaction.

Diffusion control in the liquid can be tested experimentally. Under liquid phase diffusion control, the observed reaction rate is dependent only on the difference between the activity of iron-oxide at the surface of the melt, where it is assumed to be in equilibrium with the gas phase, and that of the bulk liquid. For a gas containing CO_2, CO, and Ar, the oxygen activity is dependent only on the CO_2/CO ratio of the gas. If the reaction rate is independent of the argon content of the gas at constant CO_2/CO ratios, liquid phase diffusion is controlling the reaction.

Diffusion control in the liquid can also be tested in this system by varying the oxygen activity of the reducing gas to activities lower than that at the iron-silica-liquid equilibrium. Any gas with a CO_2/CO ratio of less than 0.120 at 1300°C will ultimately reduce the melt to only silica and metallic iron. For liquid-phase diffusion control, the activity of oxygen at the surface of the melt, with iron and silica present, is determined by the invariant equilibrium and is independent of the oxygen activity of the gas, at CO_2/CO ratios in the gas of less than 0.120 at 1300°C. If liquid phase diffusion is controlling the reaction, the reduction rate should be independent of the CO_2/CO ratio of the gas for ratios less than the value at the iron-silica-liquid equilibrium.

p. 40

$$R = [\, k_f P_{CO}\, a_{O(ads)} \,] - [\, k_b P_{CO_2} a_v \,] \qquad (3\text{-}6)$$

where R is the observed reaction rate per unit gas-melt interfacial area, k_f and k_b are the rate constants for the forward and reverse reactions respectively, and a_i are the activities of species i. The thermodynamic activity of the adsorbed oxygen is not directly measurable. But, assuming that step (a) is virtually at equilibrium, the activity of adsorbed oxygen can be expressed by known activities using the equilibrium constant, K_a, for the step a in the proposed reaction mechanism:

$$a_{O(ads.)} = K_a\, a_{[O^{2-}]}\, a_v\, a_{[Fe^{3+}]}^2 \,/\, a_{[Fe^{2+}]}^2 \qquad (3\text{-}7)$$

Also, the rate constants k_f and k_b are related to the equilibrium constant for reaction step (b) by

$$k_b = \frac{k_f}{K_b} \,. \qquad (3\text{-}8)$$

The overall equilibrium constant, K_o can be expressed as the product of all the equilibrium constants of the reaction steps,

$$K_o = K_a K_b K_c \,. \qquad (3\text{-}9)$$

Substitution of equations (3-7) through (3-9) into equation (3-6) gives

$$R = k_f\, K_a\, a_v \left(\frac{P_{CO}\, a_{[O^{2-}]}\, a_{[Fe^{3+}]}^2}{a_{[Fe^{2+}]}^2} - \frac{K_c\, P_{CO_2}}{K_o} \right) \qquad (3\text{-}10)$$

Further simplification can be done by inserting into equation (3-10), the equilibrium expression for reaction step (c) expressed as

$$K_c \, a_{[Fe^{2+}]} = a_{[Fe^{3+}]}^2 \, / \, a_{[Fe^{2+}]}^2$$

giving

$$R = k_f \, K_a \, K_c \, a_v \left(P_{CO} \, a_{[Fe^{2+}]} \, a_{[O^{2-}]} - \frac{P_{CO_2}}{K_o} \right) . \quad (3\text{-}11)$$

The equilibrium expression for the overall reaction (3-5) is

$$a_{[Fe^{2+}]} \, a_{[O^{2-}]} = \frac{a_{O,t}}{K_o} , \quad (3\text{-}12)$$

where $a_{O,t}$ is the CO_2/CO ratio in the gas in equilibrium with the melt at time t . Substituting equation (3-12) into equation (3-11) and simplifying gives the final rate expression

$$R = \beta \, \theta_v \, [\, PCO \, a_{O,t} - PCO_2 \,] , \quad (3\text{-}13)$$

Where β is a constant incorporating the forward reaction rate constant, the equilibrium constants, and the activity coefficient of the vacant reaction sites on the melt, and θ_v is the fraction of total reaction sites that are vacant. All of the variables in equation (3-13) can be determined, and if reaction step (b) is controlling the overall reaction, equation (3-13) should describe the observed reaction rate.

Similar derivations were done for all of the steps in the above proposed mechanism, and for steps in other reaction mechanisms. A summary of the results is shown in Table 3-2. A specific reaction step which may occur in several reaction mechanisms will have only one rate expression, allowing the categorization in Table 3-2. Although a specific reaction step may be identified as

Table 3-2

Summary of Chemisorption Reaction Rate Expressions

$$R = k_a(P_{CO}\, a_{O,t} - P_{CO_2})$$

Reaction Step and Controlling Reaction	k_a / β *
I. Adsorption Reactions	
a. $CO(g) + v = CO\ (ads)$	$\theta_v / a_{O,t}$
b. $[O^{2-}] + v = O^{2-}(ads)$	$\theta_v / C_{[Fe^{2+}]}\, P_{CO}$
c. $\left[\begin{array}{l}[O^{2-}] + v = O\ (ads) + 2e^- \\ 2[Fe^{3+}] + 2e^- = 2[Fe^{2+}]\end{array}\right]$ $2[Fe^{3+}] + [O^{2-}] + v = 2[Fe^{2+}] + O\ (ads)$	$\theta_v\, (C_{[Fe^{2+}]})^2 / P_{CO}$
d. $\left[\begin{array}{l}[O^{2-}] + v = O\ (ads) + 2e^- \\ [Fe^{2+}] + 2e^- = Fe\ (\gamma)\end{array}\right]$ $[Fe^{2+}] + [O^{2-}] + v = Fe\ (\gamma) + O\ (ads)$	θ_v / P_{CO}
II. Intermediate Reactions	
a. $CO\ (g) + O^{2-}(ads) = CO_2^{2-}(ads)$	$\theta_{v_2} / C_{[Fe^{+2}]}$
b. $CO\ (ads.) + O^{2-}(ads) = CO_2^{2-}(ads) + v$	$(\theta_v)^2 / C_{[Fe^{+2}]}$
c. $CO\ (ads.) + O\ (ads) = CO_2\ (ads) + v$	$(\theta_v)^2$
d. $CO\ (g) + O\ (ads) = CO_2\ (g) + v$	θ_v
e. $CO_2^{2-}(ads) + [Fe^{2+}] = CO_2(ads) + Fe(\gamma)$	θ_v
f. $CO_2^{2-}(ads) + [Fe^{2+}] = CO_2(g) + Fe(\gamma) + v$	θ_v
g. $CO_2^{2-}(ads) + 2[Fe^{3+}] = CO_2(ads) + 2[Fe^{2+}]$	$\theta_{v_3}(C_{[Fe^{2+}]})^2$
h. $3[Fe^{2+}] = 2[Fe^{3+}] + Fe(\gamma)$	$(C_{[Fe^{2+}]})^3 / P_{CO} a_{O,t}$
III. Desorption Reaction	
$CO_2\ (ads) = CO_2\ (g) + v$	θ_v

* Constant β incorporates the applicable rate and equilibrium constants and activity coefficients, and has a different value for each step.

controlling the overall reaction, it may not be possible to deduce the exact reaction mechanism. Also, if several reaction steps have the same rate expressions, the specific reaction step may not be determined when the experimental results fit such a rate expression.

Appendix A contains the derivation of step II.b. in Table 3-2. The derivation illustrates that in some cases the activity of an ion, in this case Fe^{2+}, cannot be eliminated. Henrian behavior of the ions is assumed, and the activity coefficient is combined with the other constants.

3.4 Nucleation and Growth Control

The nucleation and growth of a new phase may control a reaction if the interfacial surface energies associated with the product phase are much higher than the surface energy of the interface the product displaces. Gamma-iron has a surface energy of about 1950 mJ/m^2 (35) and the interfacial surface energy between the slag and iron is estimated to be about 1200 mJ/m^2 (36). The liquid silicate has a surface energy from 415 to 480 mJ/m^2 for melts with silica contents from 35 to 15 weight percent , respectively (37) . Nucleation and growth control of the early reaction is probable because the surface energies of the iron phase are much larger than the surface energy of the liquid silicate. Calculations shown in Appendix B using the interfacial surface energies given above, indicate that growth of

hemispherical grains of iron on the surface are favored over cylindrical grains growing into the melt from the surface.

For the overall reaction (3-1) to proceed, iron has to form and grow. If the liquid is electronically conductive, the iron will grow at sites giving the lowest Gibb's free energy (at the iron crucible) by the reaction

$$[Fe^{2+}] + 2e^- = Fe\ (\gamma) \quad . \qquad (3\text{-}14)$$

If the conductivity of the melt is too low to accommodate the transfer of electrons produced by the reactions

$$CO_2^{2-}(ads) = CO_2\ (ads) + 2e^- \qquad (3\text{-}15)$$

or

$$[O^{2-}] + v = O\ (ads) + 2e^- \quad , \qquad (3\text{-}16)$$

then iron has to nucleate and grow.

The nucleation and growth of the product iron may be modeled applying the principles of the Johnson-Mehl model of nucleation and growth. If the iron nucleates at a constant rate, I, and grows hemispherically at a constant growth rate, U, and the reduction rate is proportional to the surface area of the iron that is available:

$$R \propto [\text{number of nuclei}]\ X\ [\text{surface area of each nucleus}]$$

$$R \propto [\ I\ t\ ]\ X\ [\ 4\ \pi\ (\ U\ t\ )^2\ ]/2 \qquad (3\text{-}17)$$

and $R \propto t^3$. If the nuclei are formed very rapidly at a fixed number of nucleation sites, N, and only the growth of the nuclei is rate limiting, then

$$R \propto N\ X\ [\ 4\ \pi\ (\ U\ t\ )^2\ ]/2 \qquad (3\text{-}18)$$

and $R \propto t^2$.

The above analysis assumes that the slag has sufficient conductivity to allow significant electron transfer from the gas-liquid interface to the iron-liquid surface. If electrons are produced at the iron-melt-gas interfacial line by oxidation reactions such as reactions (3-15) or (3-16), and are conducted through the iron and consumed by the reduction of ferrous iron at the melt-iron interface by reaction (3-14), the reduction rate could be dependent on the length of the gas-liquid-iron line of contact available or the perimeter of the hemispherical grain exposed to the gas. In this case, if nucleation and growth is controlling

$$R \propto [\, I\, t\,]\, X\, [\, 2\, \pi\, (\, U\, t\,)\,] \qquad (3\text{-}19)$$

and $R \propto t^2$. For the case of fast nucleation at a fixed number of sites

$$R \propto N\, X\, [\, 2\, \pi\, (\, U\, t\,) \qquad (3\text{-}20)$$

and $R \propto t$.

(31)

In summary, the reduction rate increases as the area or perimeter of the product increases, until another process starts to control the reaction.

CHAPTER 4

THERMODYNAMIC ANALYSIS

4.1 Introduction

An accurate thermodynamic analysis of the $FeO-Fe_2O_3-SiO_2$ system is needed to evaluate reduction kinetics of the melts. For chemisorption control, derived rate expressions for each step in the overall reaction

$$FeO\ (slag) + CO\ (g) = Fe(\gamma) + CO_2\ (g) \qquad (4\text{-}1)$$

take the general form

$$R = k_a\ (\ P_{CO}\ a_O - P_{CO_2}\ )\ , \qquad (4\text{-}2)$$

in which R is the observed rate of the overall reaction, k_a is an observed rate constant and a_O is the oxygen activity of the melt expressed as the ratio of CO_2/CO in the gas in equilibrium with the melt. The chemical or thermodynamic driving force is dependent on the activity of FeO in the melt by the equilibrium constant, K_1, for reaction (4-1)

$$K_1 = (\ a_{Fe}\ P_{CO_2}\ )\ /\ (a_{FeO}\ P_{CO})\ ,$$

or

$$a_O = P_{CO_2}/\ P_{CO} = K_1\ a_{FeO}\ /\ a_{Fe}\ . \qquad (4\text{-}3)$$

Evaluation of the activity of FeO in the melt requires that the standard free energy of formation of the iron oxide in the pure state be known, and that equilibrium of reaction (4-1) or the counterpart involving H_2O/H_2 be known as a function of composition and temperature.

Moreover, the reaction rate constant, k_a in equation (4-2), is dependent on the activity of vacant reaction sites on the surface of the melt, a_v:

$$k_a = k\ (a_v)^n$$

or, assuming ideal behavior of reaction sites on the surface

$$k_a = k'\ (\theta_v)^n\ , \qquad (4\text{-}4)$$

in which θ_v is the fraction of vacant reaction sites and n is the order of the reaction with respect to the fraction of open sites. The reaction rate constant is composition dependent and evaluation of θ_v requires use of the Gibbs adsorption isotherm

$$\Gamma_b = -\partial\ \sigma\ /\ [\ RT\ \partial\ \ln(a_b)]\ , \qquad (4\text{-}5)$$

in which Γ_b is the excess concentration of species b on the surface of the melt relative to the bulk, σ is the surface energy of the melt at the absolute temperature, T, and activity of species b, a_b, and R is the universal gas constant.

This chapter is divided into three sections

1) evaluation of the wustite field in the Fe-O system
2) evaluation of the equilibrium of reaction (4-1) at the temperatures and compositions of interest
3) evaluation of θ_v using available surface energy data.

4.2 The Wustite Field in the Fe-O System

The iron-oxygen system has been studied extensively, and there have been more than 40 investigations conducted on the solid wustite ($Fe_{1-y}O$) field alone. The phase diagram is reproduced in

Figure 4-1 is from a review paper by Spencer and Kubaschewski (38), who conducted an extensive thermodynamic assessment of the whole system using the well-studied solid wustite phase as the starting point.

The foundation for the wustite region of the iron-oxygen system was put forth in 1945 and 1946 with the classic experimental work and thermodynamic analyses by Darken and Gurry (39, 40). In the first work, the equilibrium for the reaction

$$Fe_{0.947}O\ (s) + CO_2\ (g) = 0.947\ Fe\ (\gamma) + CO_2\ (g) \qquad (4\text{-}6)$$

was determined by suspending an iron strip through a well defined temperature gradient in a vertical tube furnace. A gas stream with a known CO_2/CO ratio was passed through the furnace for about an hour, after which the strip was removed and examined carefully. At a fixed gas composition the reduction potential of the gas phase decreases with increasing temperature, so a sharp interface developed between the wustite surface layer in the middle of the furnace, and iron in the cooler regions. The magnetite (Fe_3O_4) - wustite equilibrium was determined similarly using either CO_2/CO or CO_2/H_2 atmospheres. The equilibrium determinations resulted in the wustite field of the Fe-O phase diagram shown in Figure 4-2 (38). The standard free energy of formation of iron-saturated wustite from gamma-iron calculated from Darken and Gurry's data is given by

$$\Delta G_f^\circ(Fe_{0.947}O) = -52{,}4622 + 128.4\ T\ \ J\ /\ mole. \qquad (4\text{-}7)$$

The reported equilibrium CO_2/CO values for reaction (4-6) and the free energies of formation of $CO(g)$ and $CO_2(g)$ from the JANAF Tables (41) were used to determine the above equation.

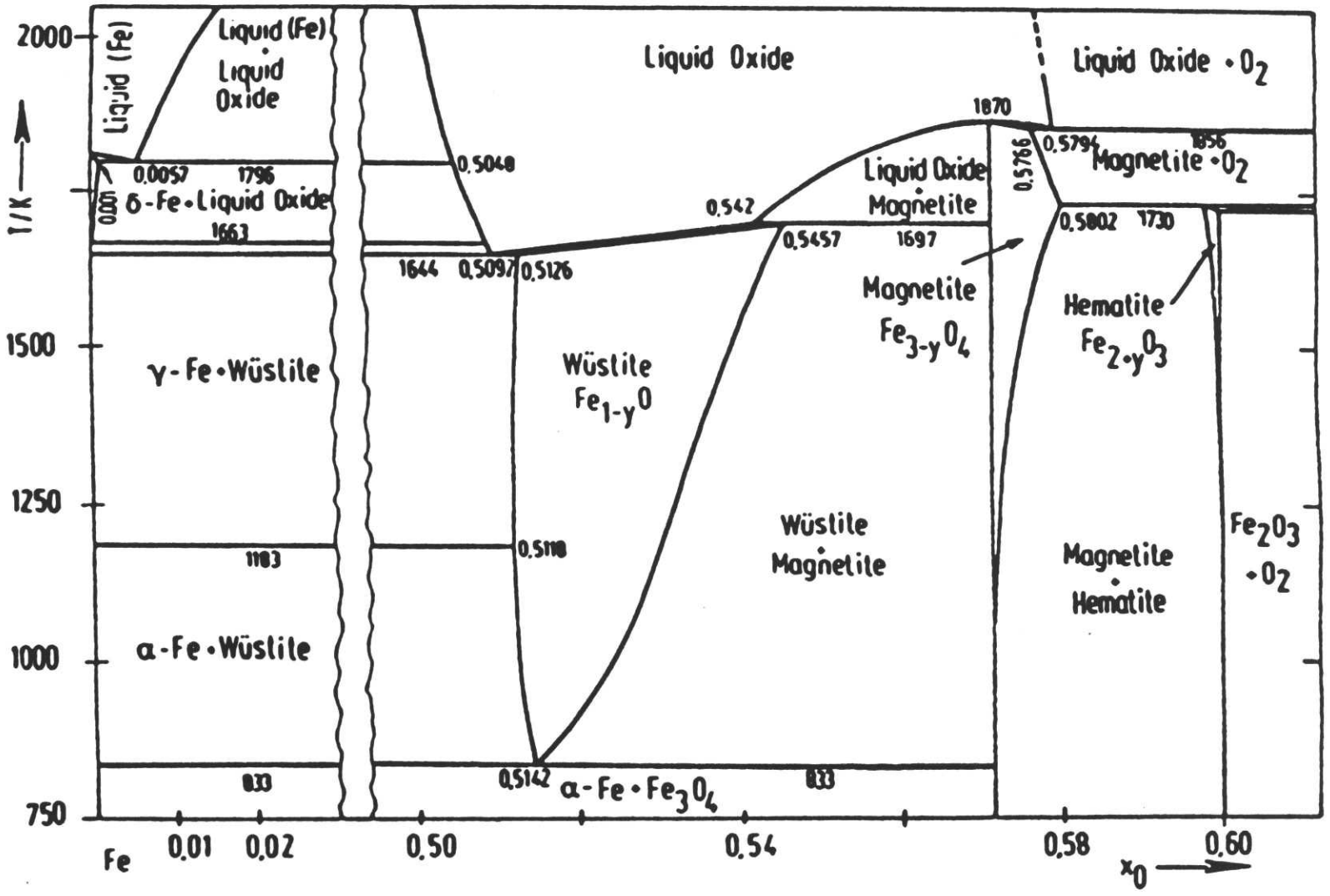

Figure 4-1. Fe-O phase diagram. Spencer and Kubaschewski (38)

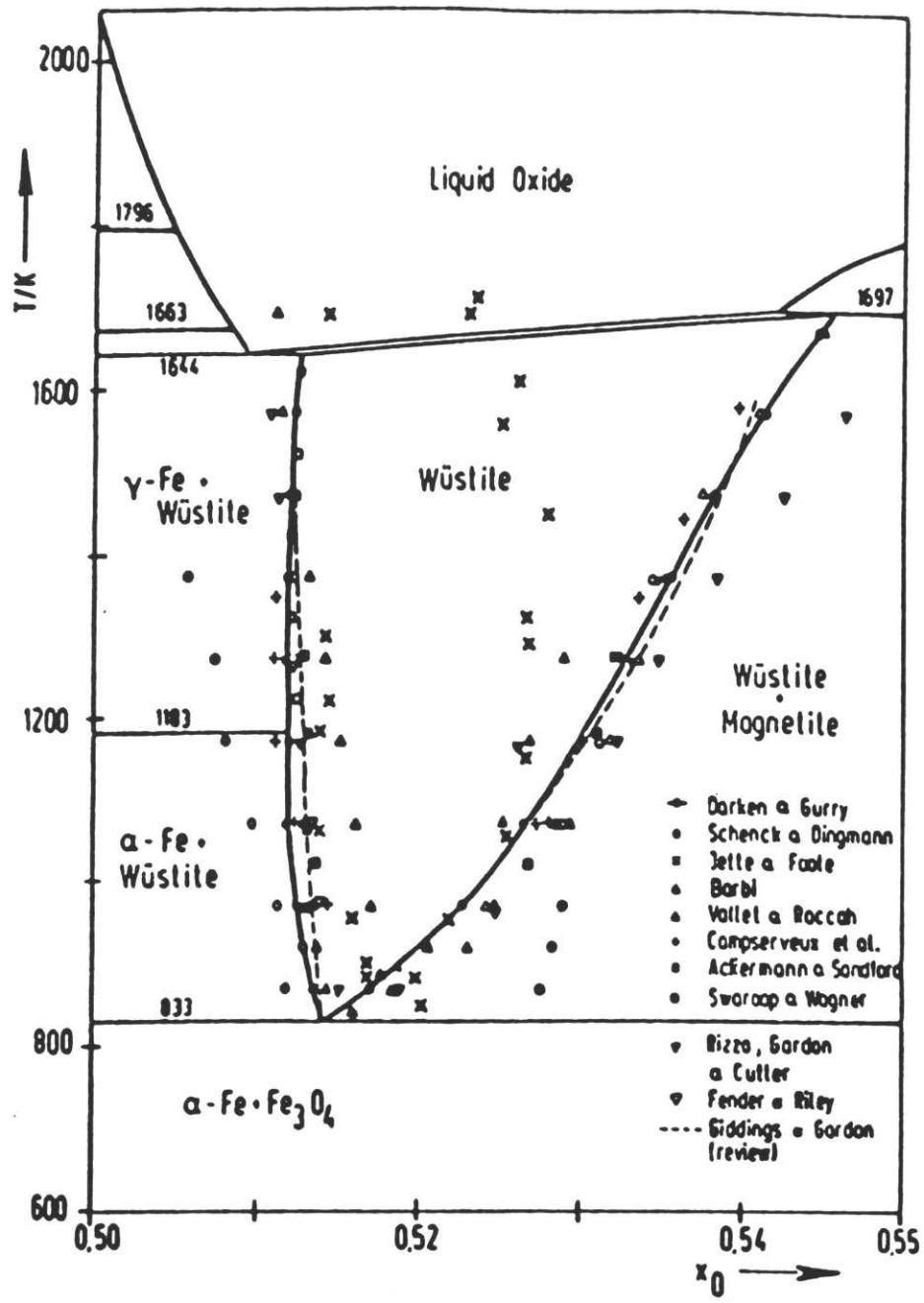

Figure 4-2. Wustite field of the Fe-O phase diagram. Spencer and Kubaschewski (38)

Darken and Gurry (40) followed this investigation with a study of the liquid-oxide phase field from iron saturation to a pressure of oxygen of one atmosphere in the temperature range from 1370 to 1640°C. Melts of the oxide were contained in iron or platinum crucibles and equilibrated with gas phase of known oxygen partial pressure. This study resulted in the iron-oxygen phase diagram which is essentially the same as that in Figure 4-1, except for equilibria related to the hematite solid-solution at the right side of the diagram. The calculated standard free energy of formation of FeO(l) from delta-iron using Darken and Gurry's data is given by

$$\Delta G_f^\circ(FeO(l)) = -459839 + 89.00\ T \quad J / mole. \qquad (4\text{-}8)$$

The equation was calculated in the same manner as the equation for wustite except that the two points reported for equilibrium with liquid iron were corrected to equilibrium with delta-iron using the recommended values of Darken and Gurry (42).

Spencer and Kubaschewski (38) combined the data from many papers on the Fe-O system to produce a package of thermodynamic values that are internally consistent for equilibria among the various phases of the system. Of relevance here, they combined the standard free energy change of reaction (4-6) or for the H_2/H_2O counterpart to obtain the temperature independent values of the relative partial molar enthalpies and entropies of mixing of oxygen over most of the composition range of wustite. Although their calculated values were different from cited (43) calorimetric values (about 5 and 18 percent lower for the partial

molar enthalpy and entropy of mixing of oxygen respectively), consistency was obtained when extrapolating within the wustite field with most of the standard free energy data. Oxygen isobars were calculated across the wustite field, and the standard free energy of formation of iron-saturated wustite was given as

$\Delta G_f^\circ(Fe_{0.953}O) = -518993 + 125.04T$ J / mole (1050-1550 K). (4-9)

When extrapolated to 1573 K, the standard free energy of formation of wustite is only 407 J / mole (+0.13%) greater than that given be equation (4-7). Spencer and Kubaschewski accepted Darken and Gurry's (40) standard free energy of formation for the iron-rich liquid oxide phase given in equation (4-8).

Figure 4-3 compares graphically the standard free energy change of reaction (4-6) calculated using the values of Darken and Gurry (39), Spencer and Kubaschewski (38), and the JANAF Tables (41). Also shown in Figure 4-3 is the standard free energy change for the reaction

$$FeO\ (l) + CO\ (g) = Fe\ (\gamma) + CO_2\ (g) \qquad (4\text{-}10)$$

calculated using the experimental data of Darken and Gurry (40) and the values from the JANAF Tables (4). The liquid oxide values were corrected for equilibrium with gamma iron instead of delta iron using the small values recommended by Darken and Gurry (42) and the similar values available in the JANAF Tables (44). The values employed for making the corrections are shown graphically in Figure 4-4.

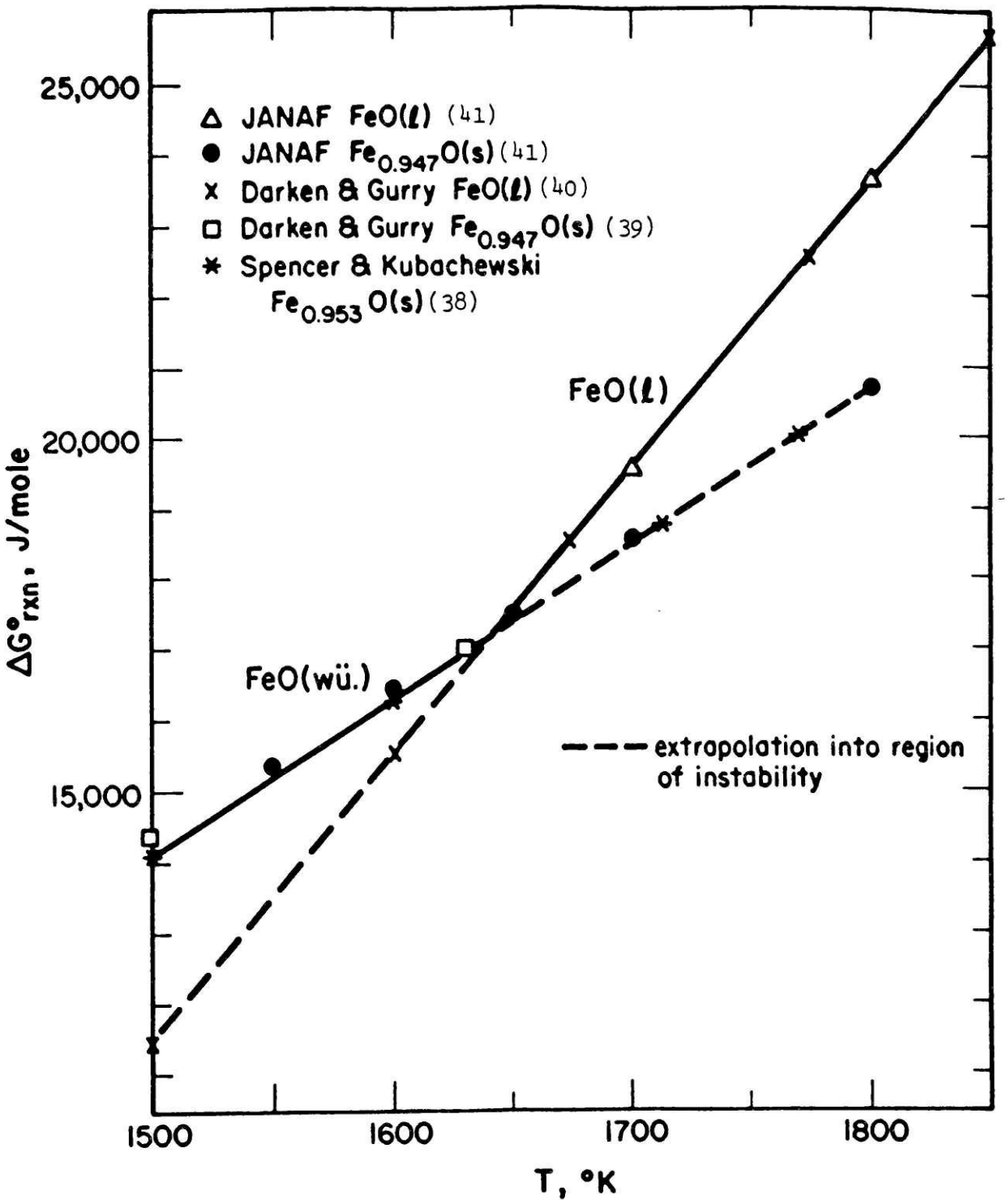

Figure 4-3. Standard free energy change for reactions (4-6) and (4-10). Iron saturation

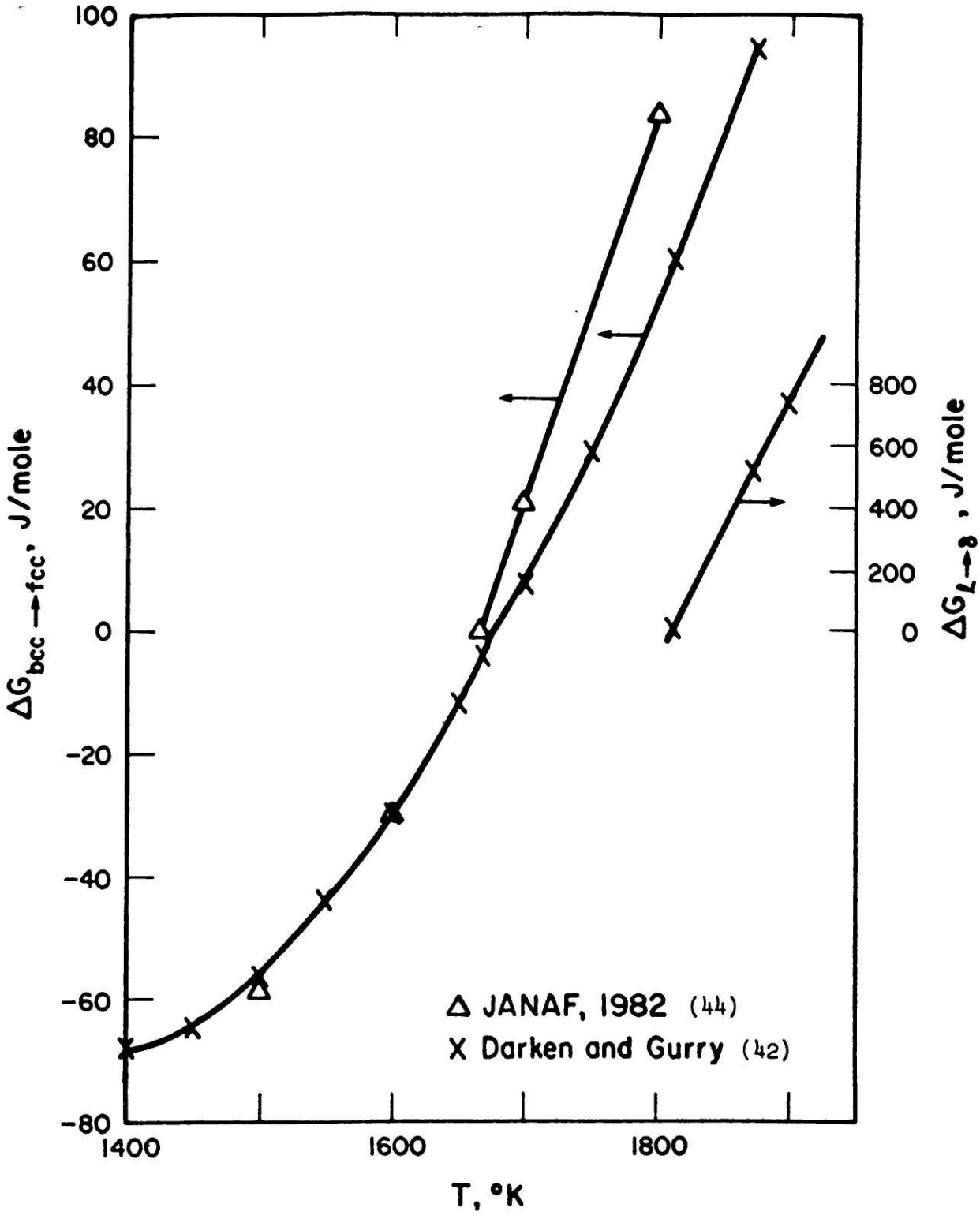

Figure 4-4. Standard free energy change for iron phase transformations.

The values for the reaction that were determined by Spencer and Kubaschewski for the solid phase and Darken and Gurry for the liquid phase will be used in this study because the values are consistent with the phase diagram of the Fe-O system provided by those investigators. As shown in Figure 4-3, the differences are very small (about 299.3 J/ mole or 1% at 1573 K) and the choice has a negligible effect on the evaluation of the activity of iron oxide in the liquid silicate. The thermodynamic values for the Fe-O system used in this study are summarized in Table 4-1.

Table 4-1

Standard Gibbs Free Energy Values used in This Study

Reaction	Standard Gibbs Free Energy (J)	Ref.
$FeO\ (l) + CO\ (g) = Fe\ (\gamma) + CO_2\ (g)$	-98729 + 81.01 T	40
$FeO(l) + H_2\ (g) = Fe\ (\gamma) + H_2O\ (g)$	-39225 + 25.77 T	40,41
$Fe_{0.953}O\ (s) + CO\ (g) = Fe\ (\gamma) + CO_2\ (g)$	-37371 + 43.61 T	38
FeO (wustite) = FeO (l)	61357 - 37.40 T	38,40
$CO\ (g) + 1/2\ O_2\ (g) = CO_2\ (g)$	-556772 + 168.94 T	41
$H_2\ (g) + CO_2\ (g) = H_2O\ (g) + CO\ (g)$	59503 - 55.24 T	41
$Fe(\delta) = Fe(\gamma)$	-1484 + 0.89 T	42
$Fe\ (l) = Fe\ (\delta)$	30220 + 16.68 T	42

4.3 Thermodynamics of Iron-silicate melts

The $FeO-Fe_2O_3-SiO_2$ phase diagram that was reported by Muan (45) and the isothermal section (46) at 1300°C are shown in Figure 4-5. The liquid region at 1300°C is saturated with gamma iron on

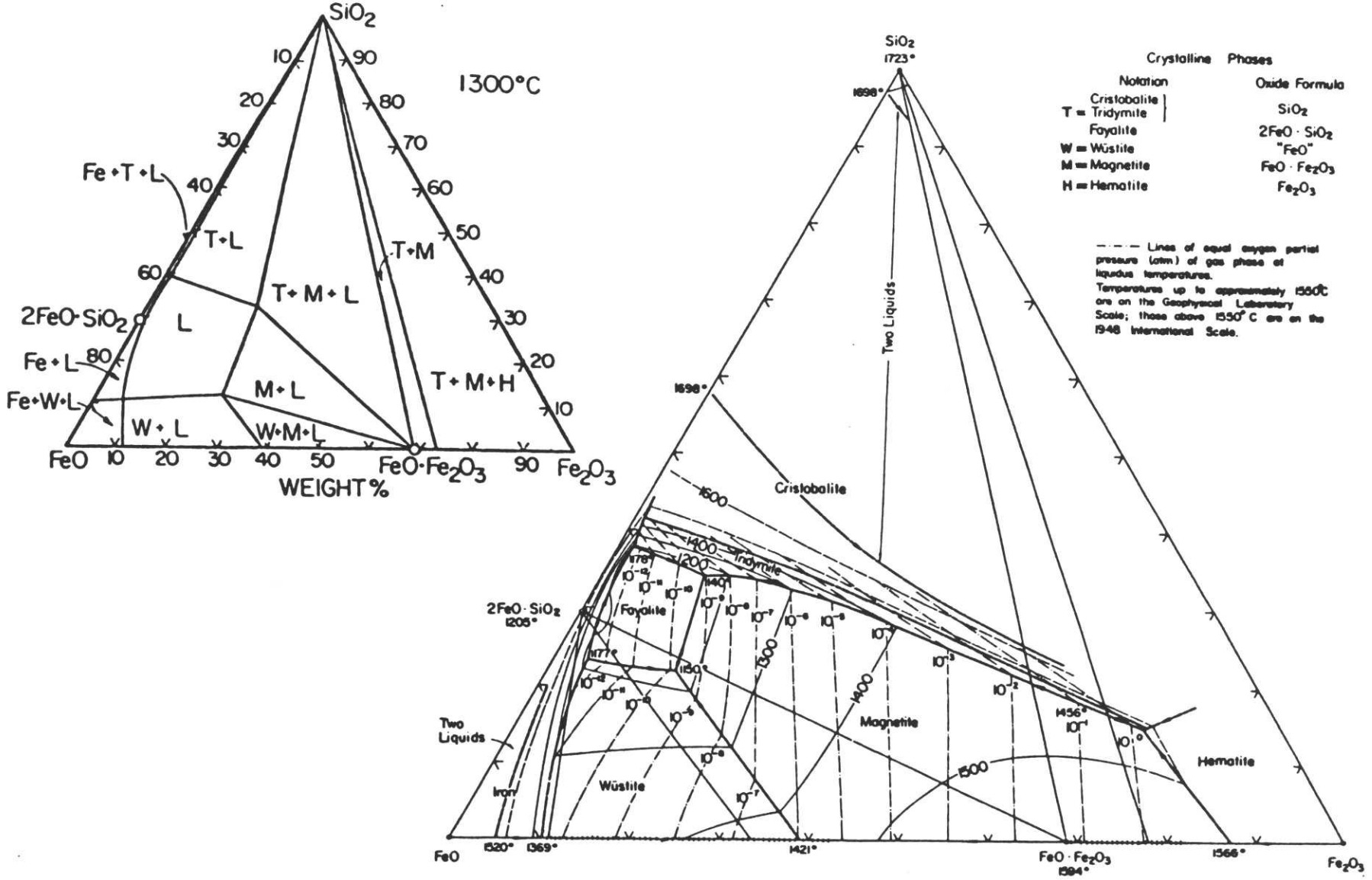

Figure 4-5. $FeO-Fe_2O_3-SiO_2$ phase diagram (45), and isothermal section at 1300°C (46).

the left, silica on the top, magnetite on the right, and wustite of variable composition on the bottom. Equilibria at iron and silica saturation can readily be determined using iron or silica crucibles. Equilibria can be investigated over the liquid region of stability, particularly at higher oxygen potentials, using platinum-based alloy crucibles.

Schuhmann and Ensio (47) were the first to investigate extensively the thermodynamic properties of silicate slags when saturated with gamma iron at temperatures from about 1260 to 1360°C. They held approximately 150 grams of the melt in a high-purity iron crucible and bubbled CO_2/CO gas mixtures through the melts. The gas composition was changed until equilibrium was achieved with the melt. During the adjustment periods, the composition of the gas was determined using a thermal-conductivity unit. The final determinations were done using ascarite to absorb the CO_2.

Bodsworth (48) determined the equilibrium of H_2O/H_2 gas mixtures with iron-silicate melts under near identical conditions to those of Schuhmann and Ensio. Equilibrium was determined using slag analyses and a rapid-acting katharometer (thermal conductivity) to determine the composition of the outlet gas. Excellent agreement with the results of Schuhmann and Ensio was obtained. Ban-ya, Chiba, and Hikosaka (49) equilibrated iron-silicate melts contained in iron crucibles with an atmosphere in which the ratio H_2O/H_2 was fixed for up to 9 hours at 1400°C. The slag was

analyzed periodically to determine equilibrium. Their results correlated well with those of Schuhmann and Ensio, and Bodsworth.

The published experimental results of the three studies were evaluated using the equilibria defined by the first two equations of Table 4-1. The chosen standard state of iron oxide is the pure iron-oxide liquid in equilibrium with gamma-iron:

$$a_{FeO(l)} = 1 \quad \text{at Fe}(\gamma) \text{ saturation.} \qquad (4\text{-}11)$$

The calculated data points for the activity of FeO(l) as a function of silica content for the melts at 1260, 1310, 1360, and 1400°C in Figures 4-6 through 4-9. Also included in the figures are values determined at iron- and silica-saturation by Michal and Schuhmann (50). Although the results of the three studies are in close agreement and show that within experimental error the activity of FeO(l) is independent of temperature, reliable calorimetric results indicate otherwise and refinement of the activity results is possible.

Ban-ya, Iguchi, Honda, and Ishizuka (51) recently determined the molar enthalpy of mixing of binary silicate melts at 1420°C by measuring the heat released when solid silica was incrementally added to liquid oxide held in iron crucibles. Figure 4-10 shows their measurements; a second order regression curve has been fitted to the data. The partial molar enthalpy of mixing of FeO(l), $H^M_{FeO(l)}$, is defined as the change in enthalpy of the solution when an infinitesimal amount of FeO(l) is added to the

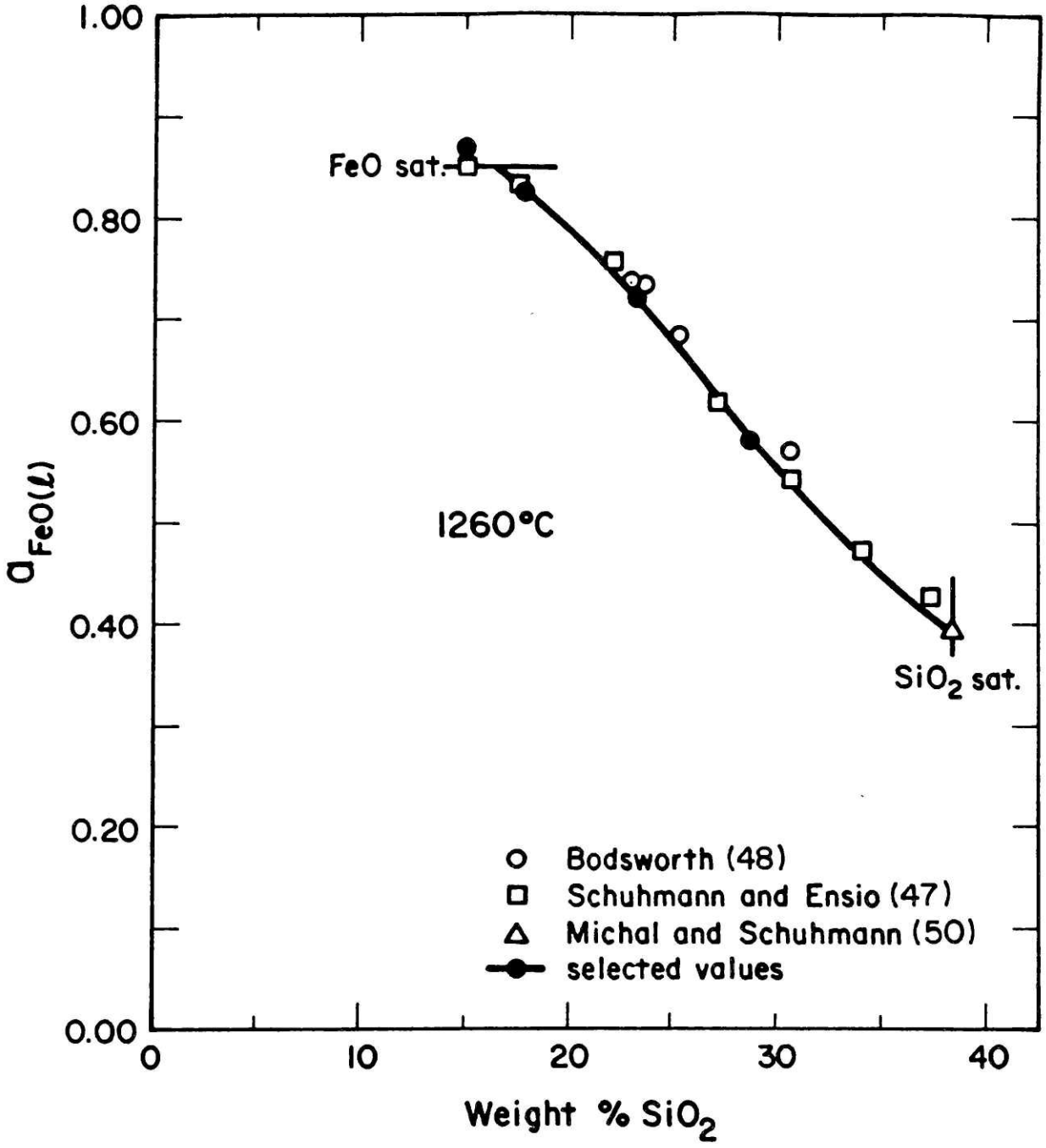

Figure 4-6. Activity-composition relation for FeO(l) at 1260°C in the system $FeO-Fe_2O_3-SiO_2$ at iron saturation.

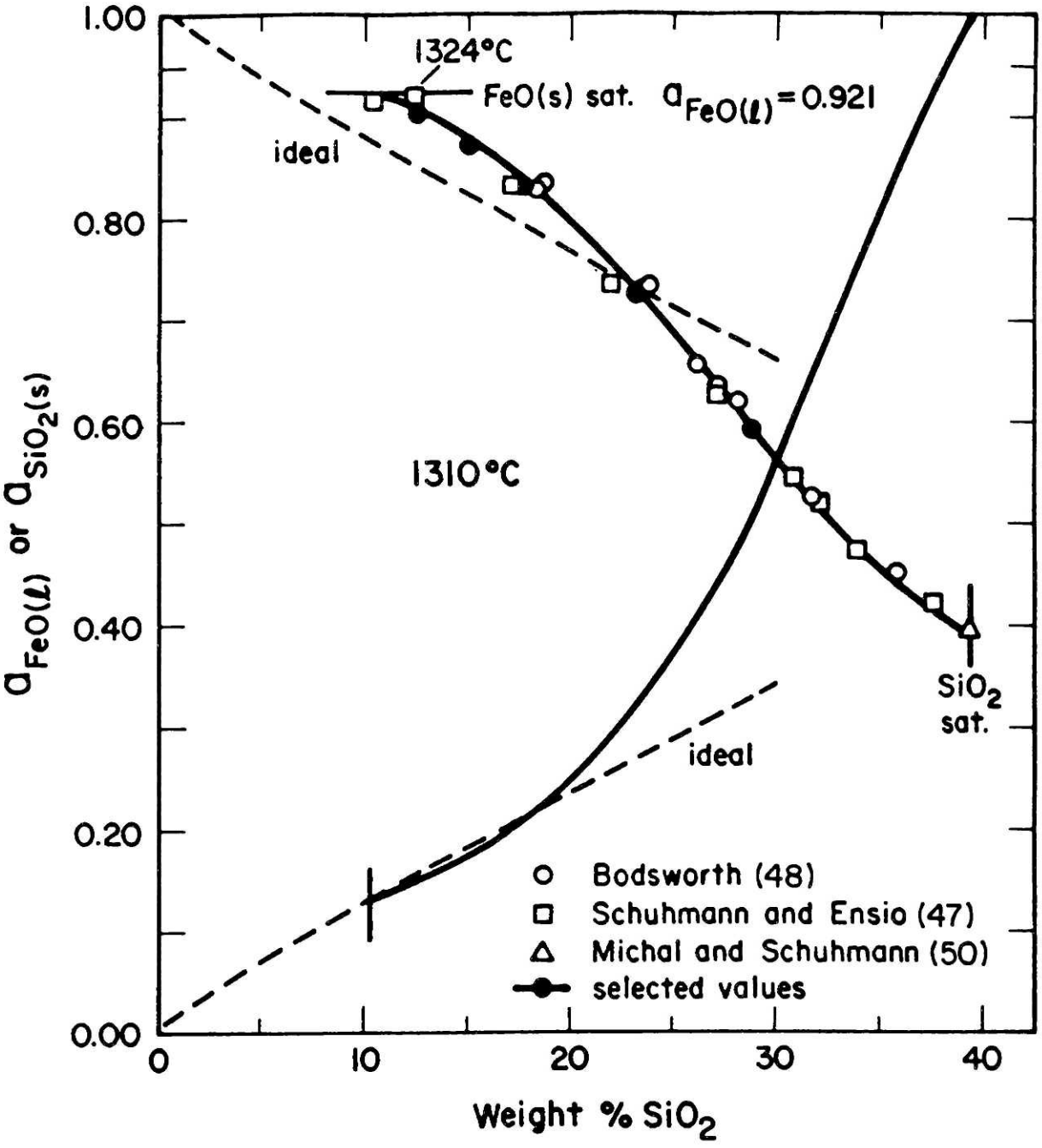

Figure 4-7. Activity-composition relation for FeO(1) and SiO_2(s) at 1310°C in the system FeO-Fe_2O_3-SiO_2 at iron saturation.

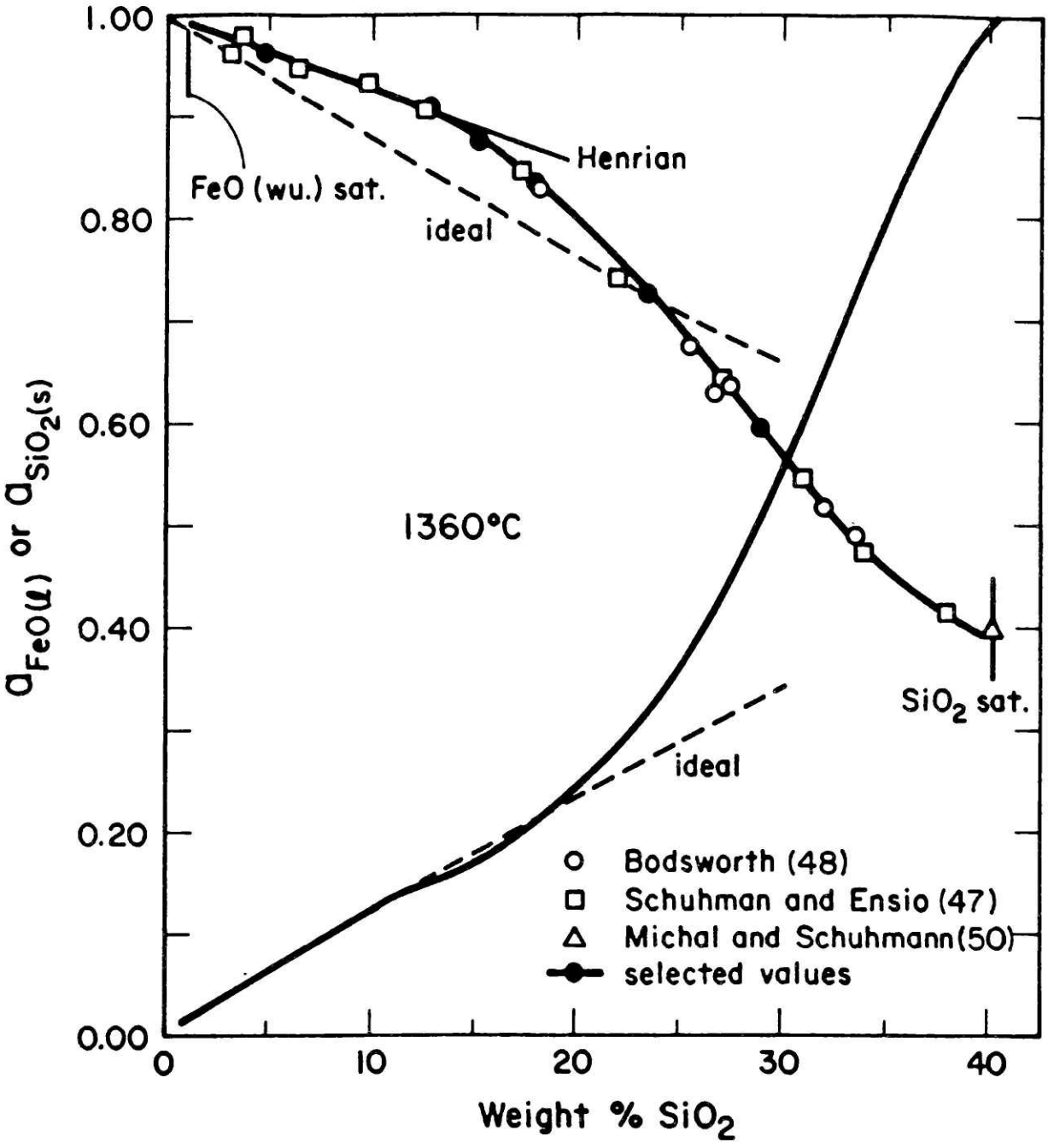

Figure 4-8. Activity-composition relation for FeO(l) and SiO_2(s) at 1360°C in the system FeO-Fe_2O_3-SiO_2 at iron saturation.

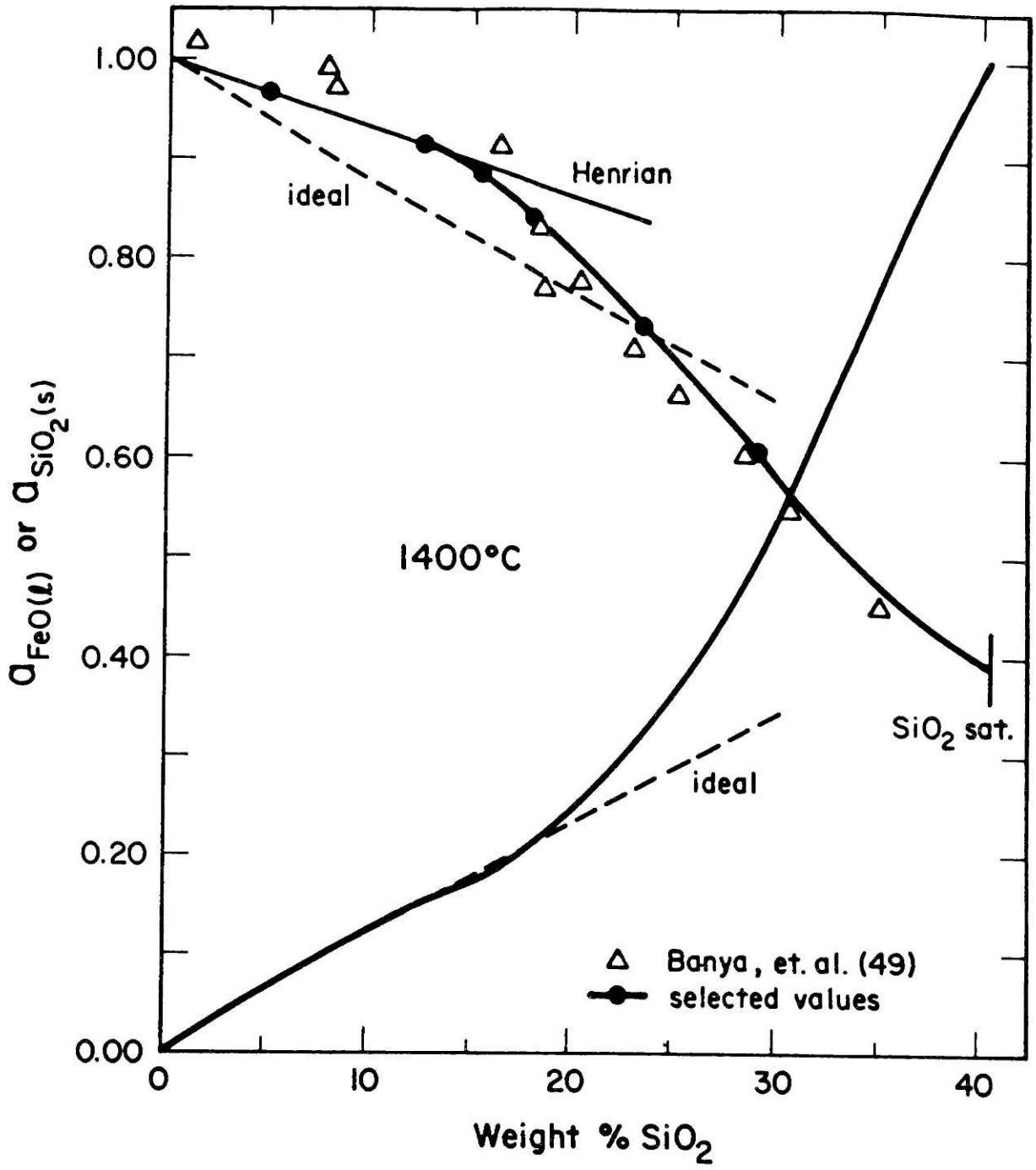

Figure 4-9. Activity-composition relation for FeO(l) and SiO_2(s) at 1400°C in the system FeO-Fe_2O_3-SiO_2 at iron saturation.

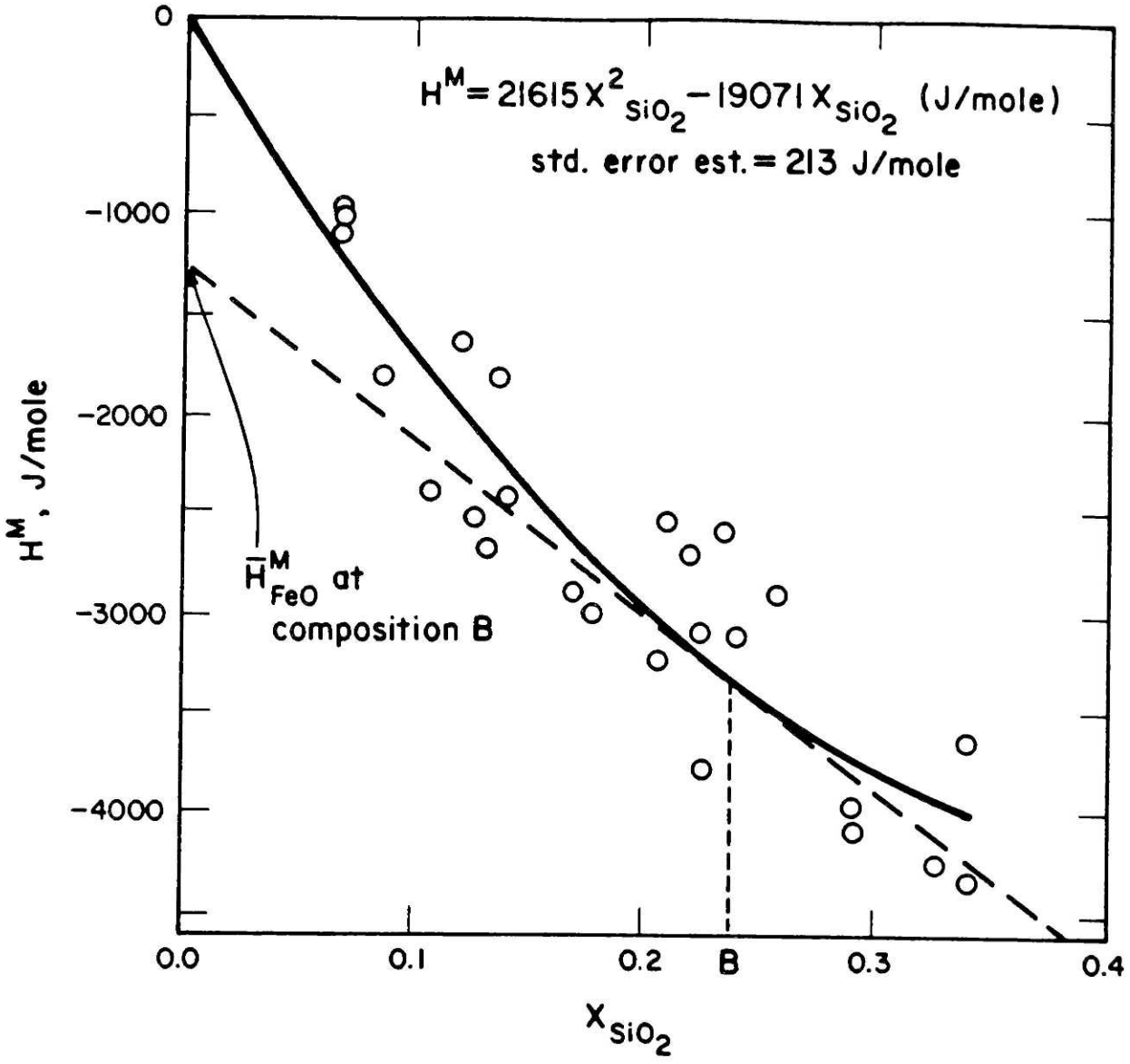

Figure 4-10. Experimental determinations of the molar enthalpy of mixing SiO_2(s) to FeO(l) at 1420°C. Fe saturation. (51)

solution under constant temperature, pressure, and composition. Figure 4-10 shows how $H^M_{FeO(l)}$ is determined graphically from the molar enthalpy of mixing. Employing the regression equation shown in Figure 4-10 and simplifying, the partial molar enthalpy of mixing of FeO(l) is

$$H^M_{FeO(l)} = -21615\ (X_{SiO_2})^2 \ . \qquad (4\text{-}12)$$

The reaction is only weakly exothermic, and by the relationship

$$H^M_{FeO(l)} = R \left[\frac{\partial \left[\ln a_{FeO(l)} \right]}{\partial\ (1/T)} \right]_{X_{SiO_2},\ X_O/X_{Fe}} \qquad (4\text{-}13)$$

the activity of FeO(l) should increase slightly with increasing temperature. In equations (4-12) and (4-13) X_i is the mole fraction of species i in the melt. Equation (4-13) can not be used directly to compare the activity of FeO(l) at the various temperatures for iron-saturation because the composition of the melt changes slightly with temperature. For example, X_O/X_{Fe} decreases from 1.025 to 1.018 upon increasing the temperature from 1260 to 1400°C at 17 weight percent silica. The partial derivative can be manipulated to the following form

$$\left(\frac{\partial \ln a_{FeO(l)}}{\partial\ (1/T)} \right)_{X_{SiO_2},\ X_O/X_{Fe}} = \left(\frac{\partial \ln a_{FeO(l)}}{\delta\ (1/T)} \right)_{a_{Fe}=1,\ X_{SiO_2}} + \alpha \qquad (4\text{-}14)$$

where

$$\alpha = \left(\frac{\partial (X_O/X_{Fe})}{\partial (1/T)} \right)_{X_{SiO_2}, a_{Fe}=1} \left(\frac{\partial\ X_{SiO_2}}{\partial (X_O/X_{Fe})} \right)_{a_{FeO}, T} \left(\frac{\partial \ln a_{FeO}}{\partial\ X_{SiO_2}} \right)_{T,\ X_O/X_{Fe}} . \qquad (4\text{-}15)$$

The last two partial derivatives in equation (4-15) have to be measured from the iso-activity FeO(l) curves across the liquidus region at temperature. For this purpose, the iso-activity curves determined by Schuhmann (52) at 1360°C and those calculated by Korakas (53) at 1270 and 1300°C were used for the first approximation. Figure 4-11 shows the general behavior of the iso-activity curves in the system at 1300°C.

Equations (4-13), (4-14), and (4-15) can be rearranged to

$$\left(\frac{\partial \ln a_{FeO}}{\partial (1/T)}\right)_{a_{Fe}=1,\ X_{SiO_2}} = \frac{H^M_{FeO(l)}}{R} - \alpha \quad . \qquad (4\text{-}16)$$

Plots of $\ln a_{FeO(l)}$ at iron saturation and constant silica contents versus inverse temperature will have slopes equal to the right-hand side of equation (4-16).

Figure 4-12 shows how α varies with composition and temperature. At $X_{SiO_2} = 0.15$, α is nearly equal to $H^M_{FeO(l)}$ at 4988 J/mole, but at $X_{SiO_2} = 0.33$, α is 10 percent of $H^M_{FeO(l)}$ at 400 J / mole. Also evident from the figure is that α is temperature dependent, making the slopes described by equation (4-16) increase with increasing temperature. The magnitude of the change in slope, however, is at most about 15 percent of the total slope. Assuming an average constant slope introduces an error in the activity of FeO(l) of only about 0.001 over the temperature range 1260 to 1400°C.

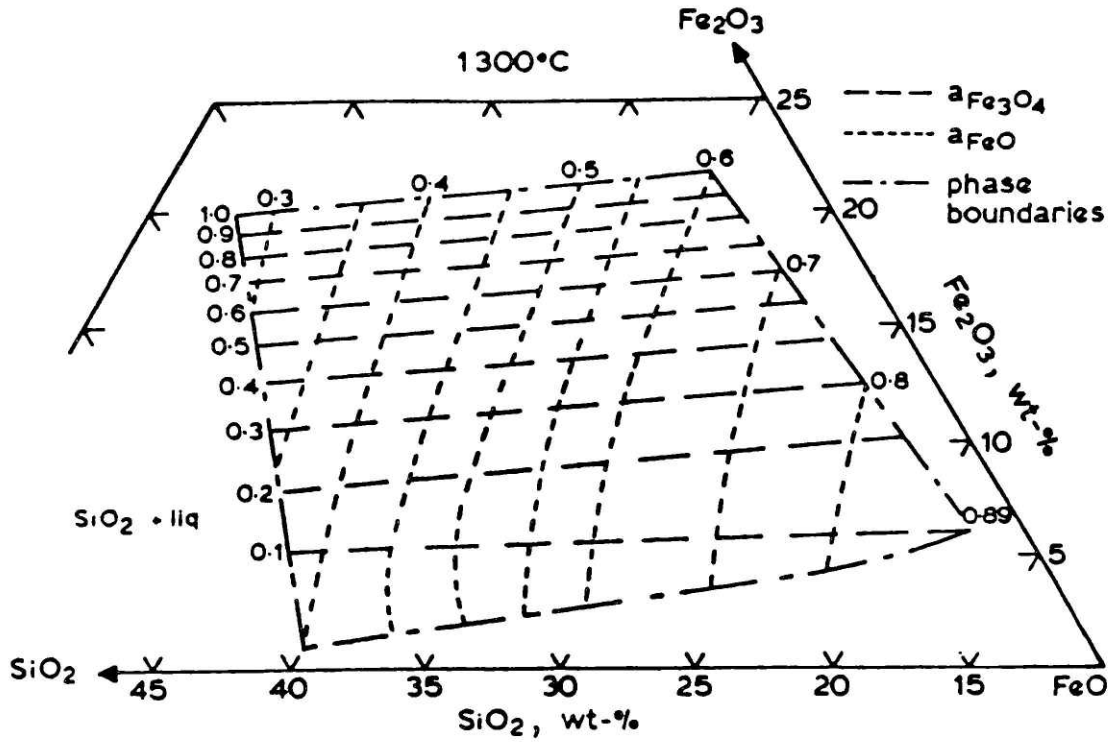

Figure 4-11. Iso-activity curves in the liquid region of the $FeO-Fe_2O_3-SiO_2$ system at 1300°C. (53)

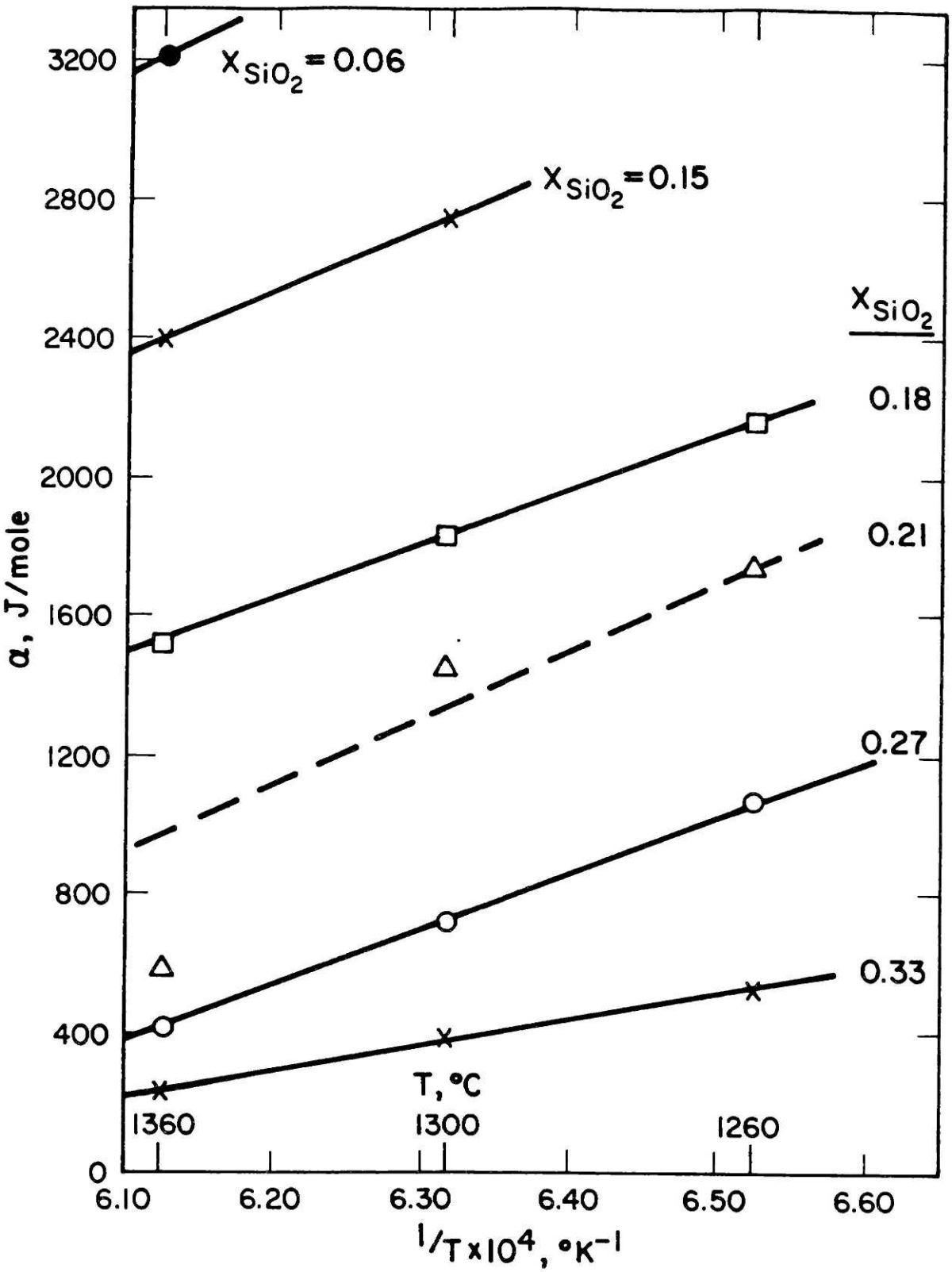

Figure 4-12. Effect of temperature and silica content on α (equation 4-15).

Plots of ln $a_{FeO(l)}$ versus inverse temperature for several silica contents are shown in Figure 4-13. The points represent values taken from a curve drawn through the experimental data in Figures 4-6 through 4-9, and the error bars about these points indicate the estimated range of values the point could reasonably have, considering the variability in the data. The lines drawn in the figure have temperature independent slopes calculated from equations (4-14) and (4-15). These lines were drawn to best fit the activity data provided. The adjusted activities determined in this figure are plotted in Figures 4-6 through 4-9 and a smooth lines were drawn through them. The adjusted activity curves are best matched to the experimental data at 1360°C by choice because the agreement between Bodsworth, and Schuhmann and Ensio is the closest. The match is also good at 1310°C and satisfactory at 1260°C. The agreement with the data of Ban-ya, et al. at 1400°C is not very good. This disparity cannot be readily explained. But, as shown in Figure 4-14, their ferric iron analyses are much higher than would be expected when compared with the values obtained by Bodsworth, and Schuhmann and Ensio at lower temperatures, and those used by Muan (45) at 1400°C for the phase diagram in Figure 4-5.

Gibbs-Duhem integrations were applied to the adjusted iron oxide activities to obtain the activities of silica (a_{SiO_2} = 1 for tridymite) as a function of composition, shown in Figures 4-7 through 4-9.

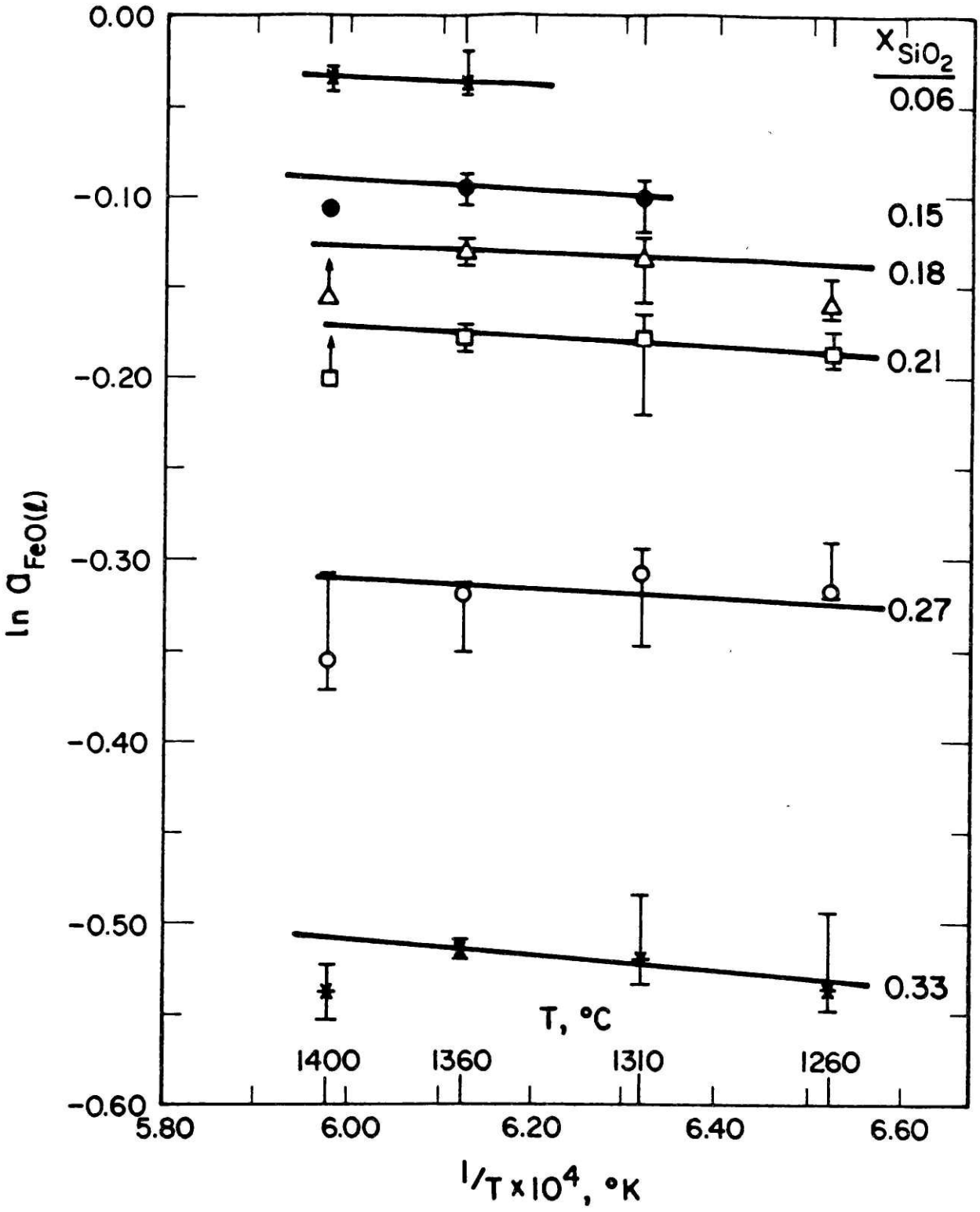

Figure 4-13. Activity of FeO(l) as a function of temperature and SiO_2 content. Points are from Figures (4-6) to (4-9), slopes calculated from Equation (4-16). Fe saturation.

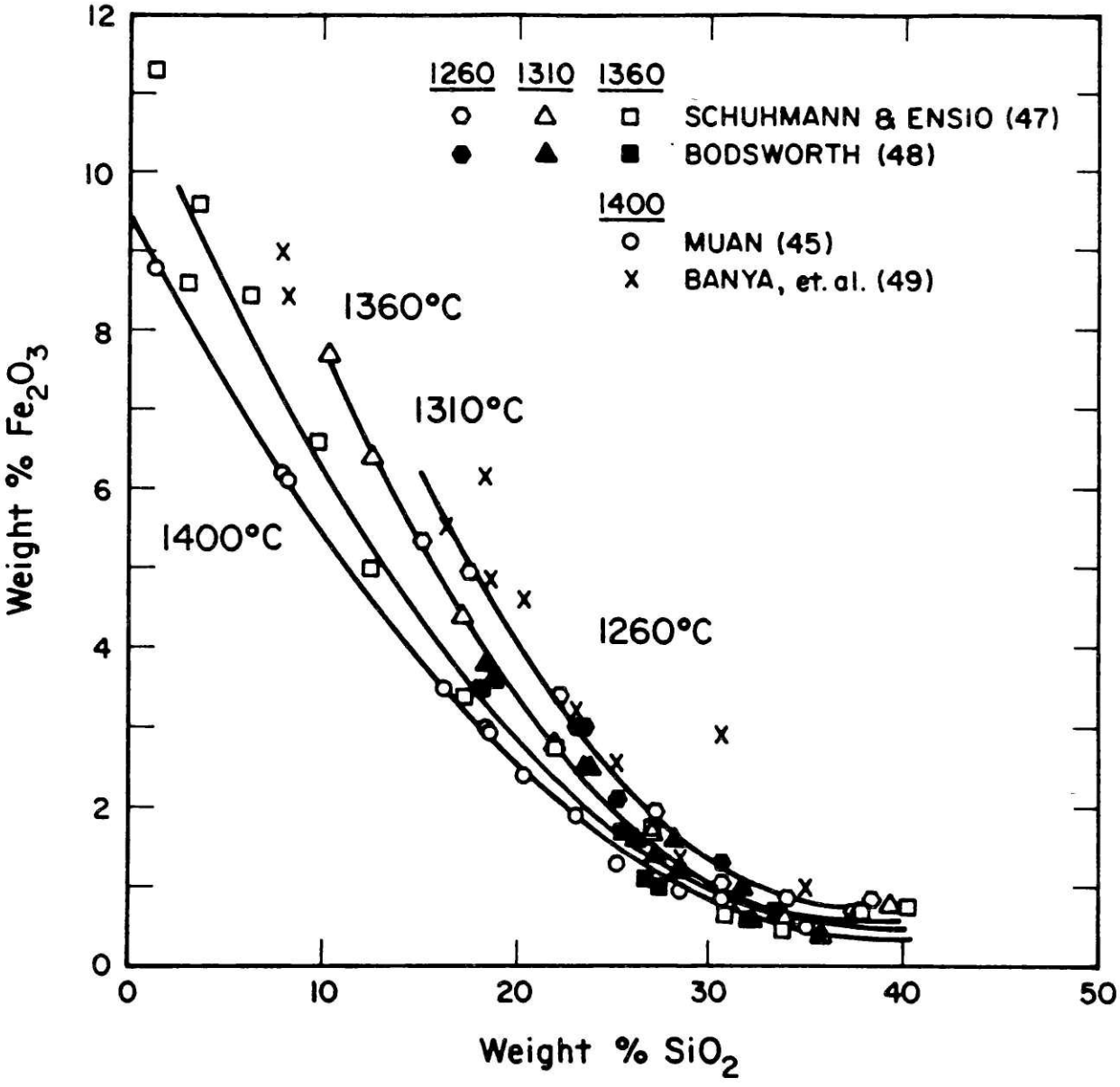

Figure 4-14. Fe_2O_3 contents of Fe saturated melts as a function of SiO_2 content and temperature.

With accurate activity values available for the melt at the iron-saturation boundary, reliable equilibrium data available at silica saturation provided Michal and Schuhmann (50), and much other data across the melt region from Muan (45), Gibbs-Duhem integrations were performed to determine new iso-activity curves across the melt region. The method recommended by Schuhmann (52) was used, and the results at 1310°C are shown in Figure 4-15.

The location of the two liquidus boundaries at magnetite and wustite saturation determined by Schuhmann, Powell, and Michal (54) varies substantially from those of Muan (45). Also, Muan positioned the silica boundary at higher silica concentrations than those established by Michal and Schuhmann. There is agreement, however, when the oxygen isobars for nonsaturated melts determine by Muan are extrapolated to the silica boundary recommended by Michal and Schuhmann. Thus, the oxygen isobars drawn in Figure 4-15 through Muan's experimental points, also shown, provide the starting points for determining the iso-activity FeO(l) curves. The resultant lines are used to determine the iso-activity SiO_2 curves, calculated from the silica activities at iron saturation. The iso-activity SiO_2 curves correlate well with the silica saturation boundary determined by Michal and Schuhmann. The magnetite/wustite corner of the melt region is adjusted outwardly to better correlate the iso-activity FeO(l) curves with Darken and Gurry's recommended equilibrium values (39).

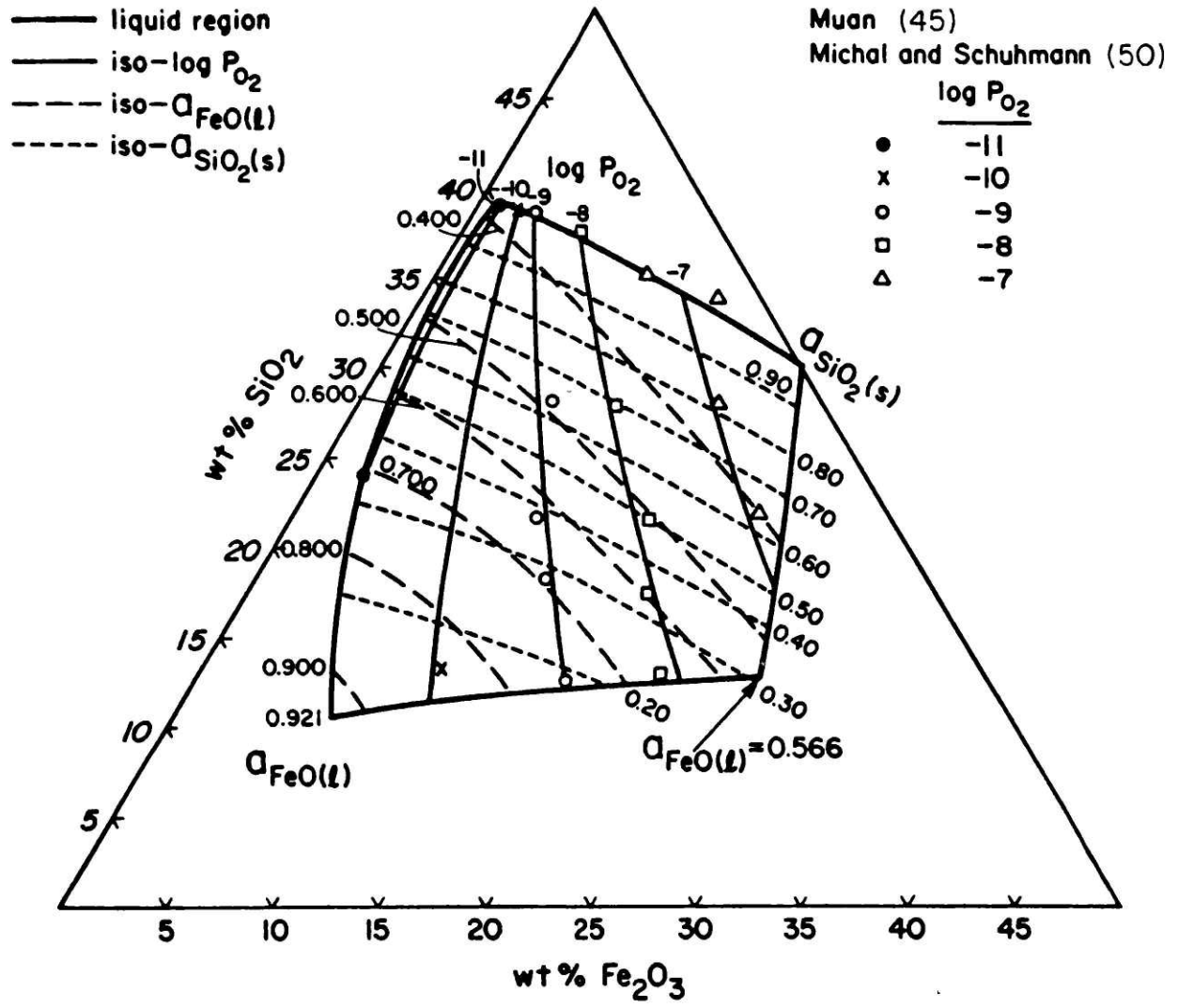

Figure 4-15. Redetermined iso-activity curves in the melt region of the $FeO-Fe_2O_3-SiO_2$ system at 1300°C.

The extent of the melt region and the locations of the iso-activity lines are somewhat different from those determinated by Korakas (53) in Figure 4-10, which is used to determine α. Changes in the value of α using Figure 4-15 are too minor to warrant another iteration of the above adjustments to the activity values at iron saturation.

4.4 Determination of Fraction of Open Reaction Sites

For the ternary system of interest here, Fe-O-SiO_2, the Gibbs adsorption isotherm may be written

$$-d\sigma = \Gamma_O \, d\mu_O + \Gamma_{SiO_2} d\mu_{SiO_2} + \Gamma_{Fe} \, d\mu_{Fe} \, , \qquad (4\text{-}17)$$

where σ is the surface energy, and Γ_i and μ_i are the surface excess concentrations (or adsorption) and the chemical potential of component i in the melt. The Gibbs-Duhem equation for the system is

$$X_O d\mu_O + X_{SiO_2} d\mu_{SiO_2} + X_{Fe} d\mu_{Fe} = 0 \, . \qquad (4\text{-}18)$$

Combination of equations (4-17) and (4-18) and assuming iron saturation ($d\mu_{Fe} = 0$) yields

$$\frac{-d\sigma}{d\mu_{SiO_2}} = \Gamma_{SiO_2} - \left(\frac{X_{SiO_2}}{X_O} \right) \Gamma_O \, . \qquad (4\text{-}19)$$

The assumption is made here, and will be substantiated later, that the adsorption of oxygen is small relative to the adsorption

of silica. Equation (4-19) then reduces to the binary Gibbs adsorption equation (4-5), which can be used to calculate the surface excess concentration of silica in the melts.

In the Langmuir adsorption model, the surface of the melt contains a fixed number of total reaction sites, such that

$$\theta_{SiO_2} + \theta_v = 1 \ , \qquad (4\text{-}20)$$

where θ_{SiO_2} and θ_v represent the fraction of the total sites that are occupied by silica or are vacant, respectively. For the adsorption reaction

$$SiO_2 + v = SiO_2 \ (ads) \ , \qquad (4\text{-}21)$$

the equilibrium constant K_{SiO_2} can be written

$$K_{SiO_2} = \frac{\theta_{SiO_2}}{a_{SiO_2}\theta_v} \ , \qquad (4\text{-}22)$$

assuming ideal site behavior. Combination of equations (4-20) and (4-22) yields

$$\theta_v = \frac{1}{1 + K_{SiO_2} a_{SiO_2}} \ . \qquad (4\text{-}23)$$

Belton (55) combined the Langmuir adsorption isotherm model with the Gibbs adsorption equation to derive the Gibbs-Langmuir adsorption isotherm:

$$\sigma^\circ - \sigma = R\ T\ \Gamma^\circ \ln (1 + K_b\ a_b) \ , \qquad (4\text{-}24)$$

where σ° is the surface energy of the pure melt, Γ° is the surface saturation coverage of species b, and K_b is the equili-

brium constant (or adsorption coefficient) for the adsorption reaction of solute b. Belton used equation (4-24) to determine the adsorption coefficients of some solutes in iron and copper melts, and Sain and Belton (33) used equation (4-24) to analyze the interfacial kinetics of the decarburization of liquid iron by carbon dioxide. Equation (4-24) is used in this study to calculate the adsorption coefficient for silica in the melts.

Kidd and Gaskell (37) recently measured the surface energy of liquid iron oxides over a wide range of oxygen activities at 1460°C, and iron-saturated binary silicates and calcium ferrites at 1410°C using the Padday cone technique. In the method, the maximum forces exerted on a cone immersed in or withdrawn from the melt are measured and used to calculate surface energy values. The stated advantage of this technique of measurement over other methods is that the meniscus between the solid and the liquid is not broken (by gas as in the maximum bubble pressure technique, or by withdrawal of a hollow cylinder in that method), making it an equilibrium measurement. This allows precise measurements to be made that are free of the various corrections and the possible hysteresis effects of the other two techniques.

Kidd and Gaskell's surface energy measurements for silicate melts are plotted for application of the Gibbs adsorption isotherm in Figure 4-16. Also shown in the figure are the results of Kozakevitch (56) and King (57), who both used the hollow cylinder technique, and Kawai and Mori, et.al. (58) who used the maximum

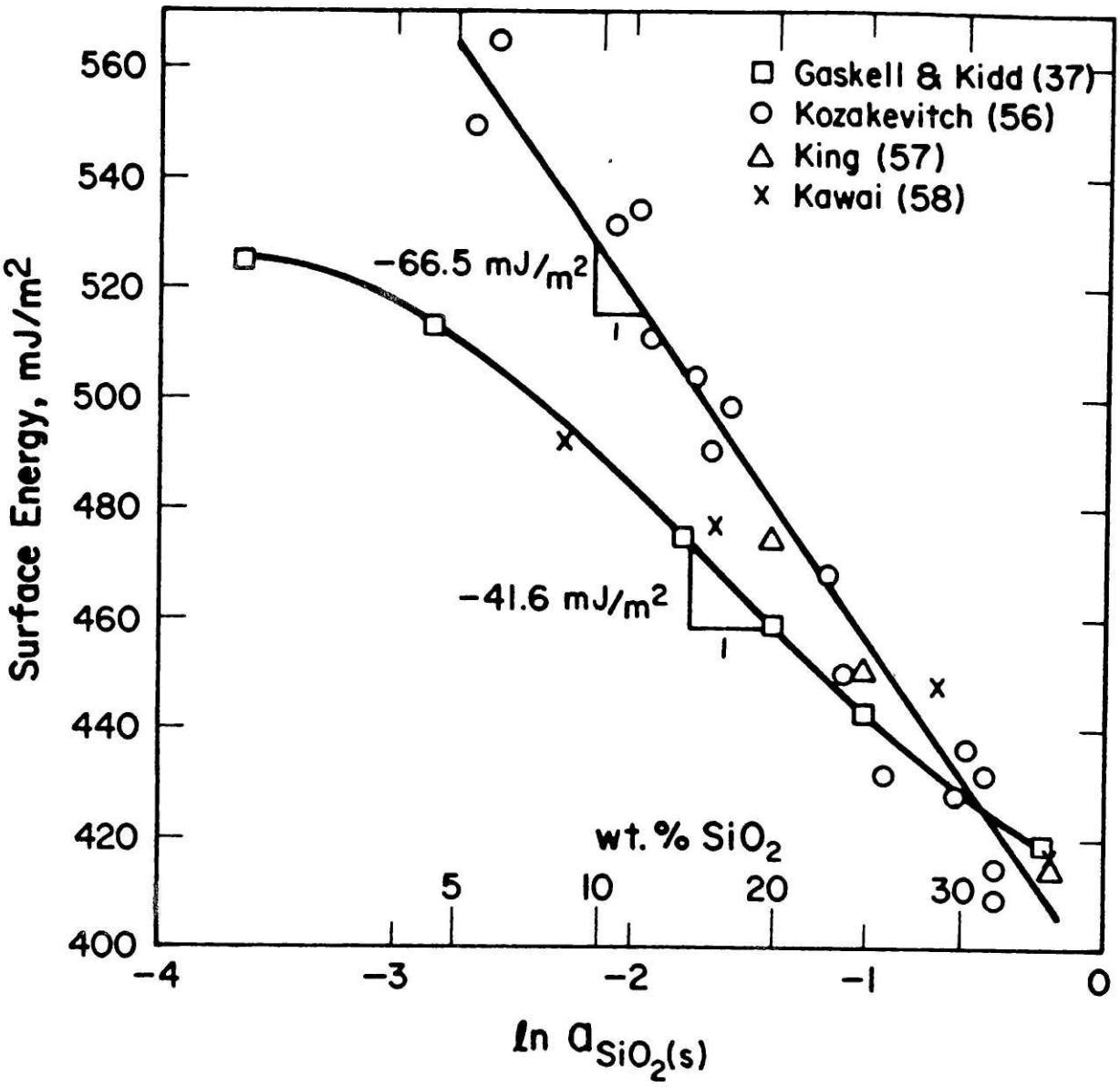

Figure 4-16. Surface energy of FeO(l) as a function of SiO_2 level. 1400°C; Fe saturation;

bubble pressure method. The silica activities from Figure 4-9 are used, and all of the results are slightly adjusted to 1400°C using the temperature coefficients ($d\sigma/dT$) determined by King (59) and verified by Kidd and Gaskell.

The values of Kidd and Gaskell are fit to a third order polynomial regression equation, which is plotted through the data in Figure 4-16. The regression equation is used to determine the surface excess concentration of silica on the surface of the melt as a function of silica content, shown on Figure 4-17.

The limiting slopes are used to determine saturation of the surface with silica, Γ°. Using Kidd and Gaskell's data, surface saturation coverage by silica is about 3×10^{-6} moles/m^2 (or 1.8×10^{18} sites/m^2) and occurs at about 17.5 weight percent silica. Using this value for Γ° and Kidd and Gaskell's value of 577 mJ/m^2 for the surface energy of pure iron-saturated liquid oxide at 1400°C,

$$K_{SiO_2} = 64 \qquad (1400°C)$$

as calculated from the Gibbs-Langmuir adsorption isotherm in equation (4-24). There are few data on the surface energy available for iron-silicate melts at 1300°C, but King (57) measured the surface energies of three melts of intermediate silica concentrations. Extrapolations of Kidd and Gaskell's data from 1400°C to melts at 1300°C using King's (59) temperature coefficients show excellent agreement with the measured values.

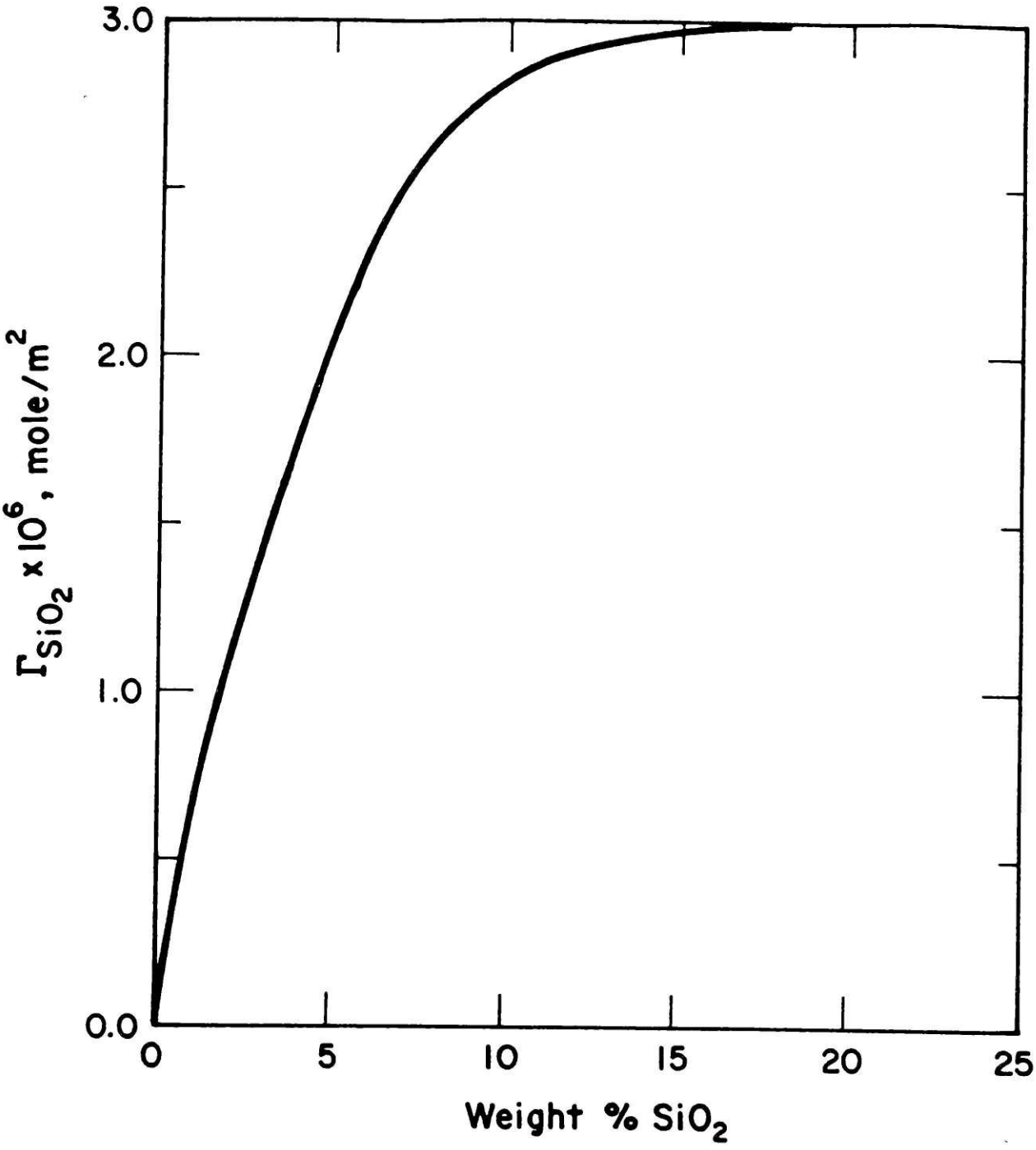

Figure 4-17. Relationship between surface excess concentration of SiO_2 and composition. 1400°C; Fe sat.

Calculation of the adsorption coefficient of silica using the extrapolated surface energy values gives

$$K_{SiO_2} = 93 \qquad (1300°C) \ .$$

This estimated value for the adsorption coefficient of silica is used in equation (4-23) to calculate the fraction of vacant reaction sites on the melt surfaces.

There is little surface energy data available that can be used to evaluate the adsorption behavior of oxygen in silicates. Kidd and Gaskell measured the surface energy of pure liquid iron oxide over a wide range of oxygen activities. However, because there are significant discrepancies in the literature on the densities of these melts, Kidd and Gaskell could not unambiguously determine the surface energies of the liquid oxides. Using the density data of Mori and Suzuki (20), they showed that oxygen or ferrite ions have weak adsorption behavior. Using the density data of Irie, Hara, et.al. (60), oxygen appears not to be surface active. Figure 4-18 shows how the surface energy of liquid iron oxide varies with the oxygen activity at 1460°C using the density data of Mori and Suzuki. Using this surface energy data, the adsorption coefficient for oxygen is

$$K_O = 4 \qquad \text{(liquid Fe-oxide at 1460°C)} \ .$$

If the adsorption behavior of oxygen is similar in silicate melts as it is in the pure oxide, the previous assumption that the

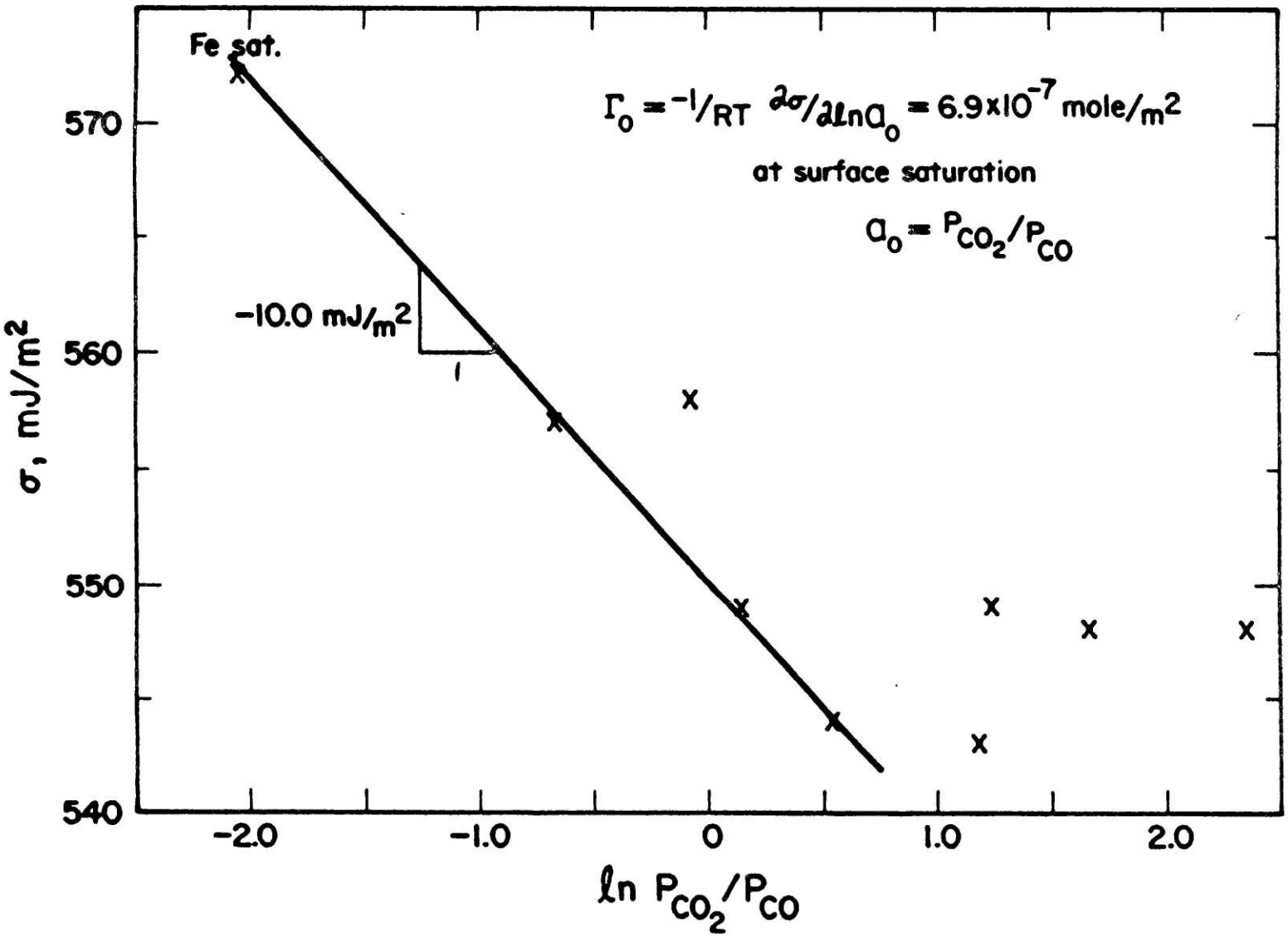

Figure 4-18. Surface energy of pure FeO(l) as a function of oxygen activity. 1460°C ; (37, 40)

adsorption of oxygen is small compared to the adsorption of silica is valid. Referring to equation (4-19), provided again here

$$\frac{-\,d\sigma}{d\mu_{SiO_2}} = \Gamma_{SiO_2} - \left(\frac{x_{SiO_2}}{x_O} \right) \Gamma_O \quad , \qquad (4\text{-}19)$$

$$\frac{x_{SiO_2}}{x_O}\,\Gamma_O = 0.020\,\Gamma_{SiO_2} \quad \text{at 12 percent } SiO_2 \ ,$$

and

$$\frac{x_{SiO_2}}{x_O}\,\Gamma_O = 0.0071\,\Gamma_{SiO_2} \quad \text{at 30 percent } SiO_2 \ .$$

Thus, the use of the Gibbs adsorption isotherm to determine the saturation coverage of silica on the melt surface is valid. Equation (4-23) can be rewritten to include the adsorption oxygen

$$\theta_v = \frac{1}{1 + K_O a_O + K_{SiO_2} a_{SiO_2}} \quad . \qquad (4\text{-}25)$$

Depending on the adsorbed species involved in rate controlling step, either equation (4-23) or (4-25) will be used to determine the fraction of vacant reaction sites. If oxygen is the only adsorbed species in the controlling step, equation (4-23) is used because only silica occupies sites needed for oxygen adsorption. If other adsorbed species take part in the rate controlling step, such as CO, these species have to compete for sites with both oxygen and silica. In this case, equation (4-25) is used.

Appendix C is a summary of the procedure used to determine the fraction of vacant reaction sites on the surface of the melts.

Chapter 5

EXPERIMENTAL APPARATUS AND PROCEDURES

5.1 Apparatus

Figure 5-1 is a schematic diagram of the experimental apparatus, showing the general relationships of the main components: the gas delivery system, the furnace and the microbalance unit, and the data acquisition system.

The gas delivery system is constructed of glass, copper, and stainless steel. All three gases, carbon monoxide, carbon dioxide, and argon, are of ultra-high purity grade (about 99.99 percent pure), and pass through standard gas getter furnaces (copper mesh for CO and Ar, and CuO granules for CO_2) and drying columns to remove impurity water vapor and carbon dioxide. The flowrates of the gases are regulated and measured using typical vented capillary-manometer arrangements. The manometers were calibrated using a bubble type volumetric flowmeter. The flow rates of the individual gases can be adjusted to within 0.5 normal milliliters per minute (Nml/min) or about 0.3% of the total flow rate.

A diagram of the reaction furnace is presented in Figure 5-2. The furnace is kanthal wound and will sustain temperatures of about 1320°C for extended periods of time, and up to 1350°C for several hours. The furnace is mounted on vertical runners, so it and the reaction tube can be lifted into position after the sample is in

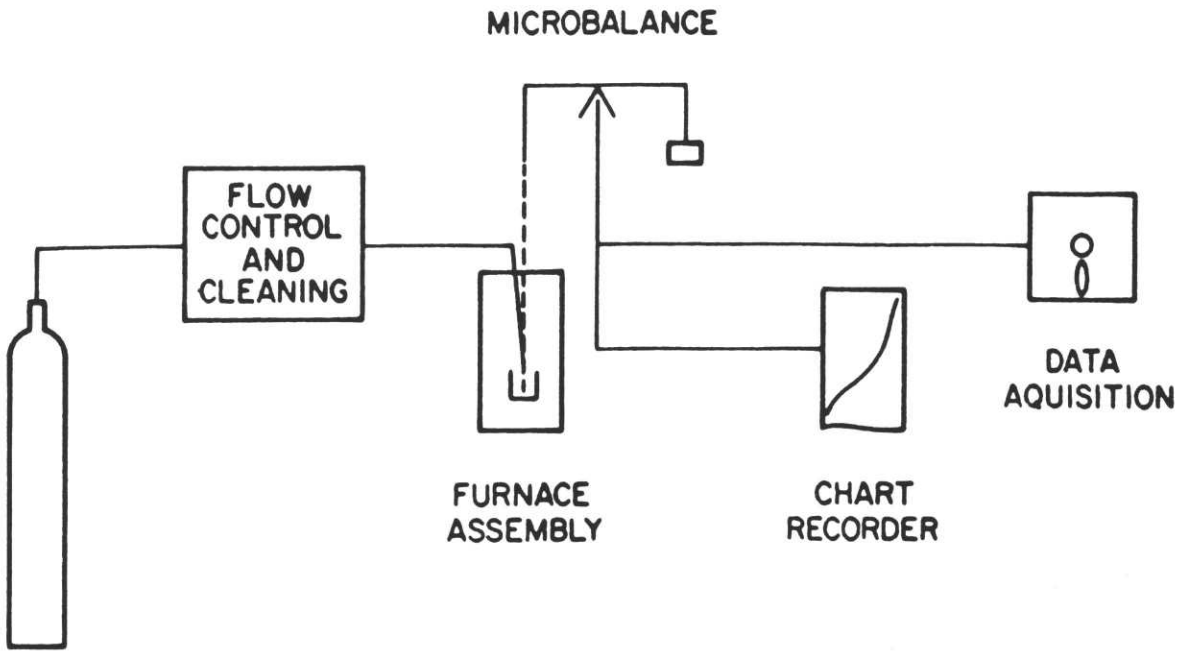

Figure 5-1. Schematic layout of the experimental apparatus.

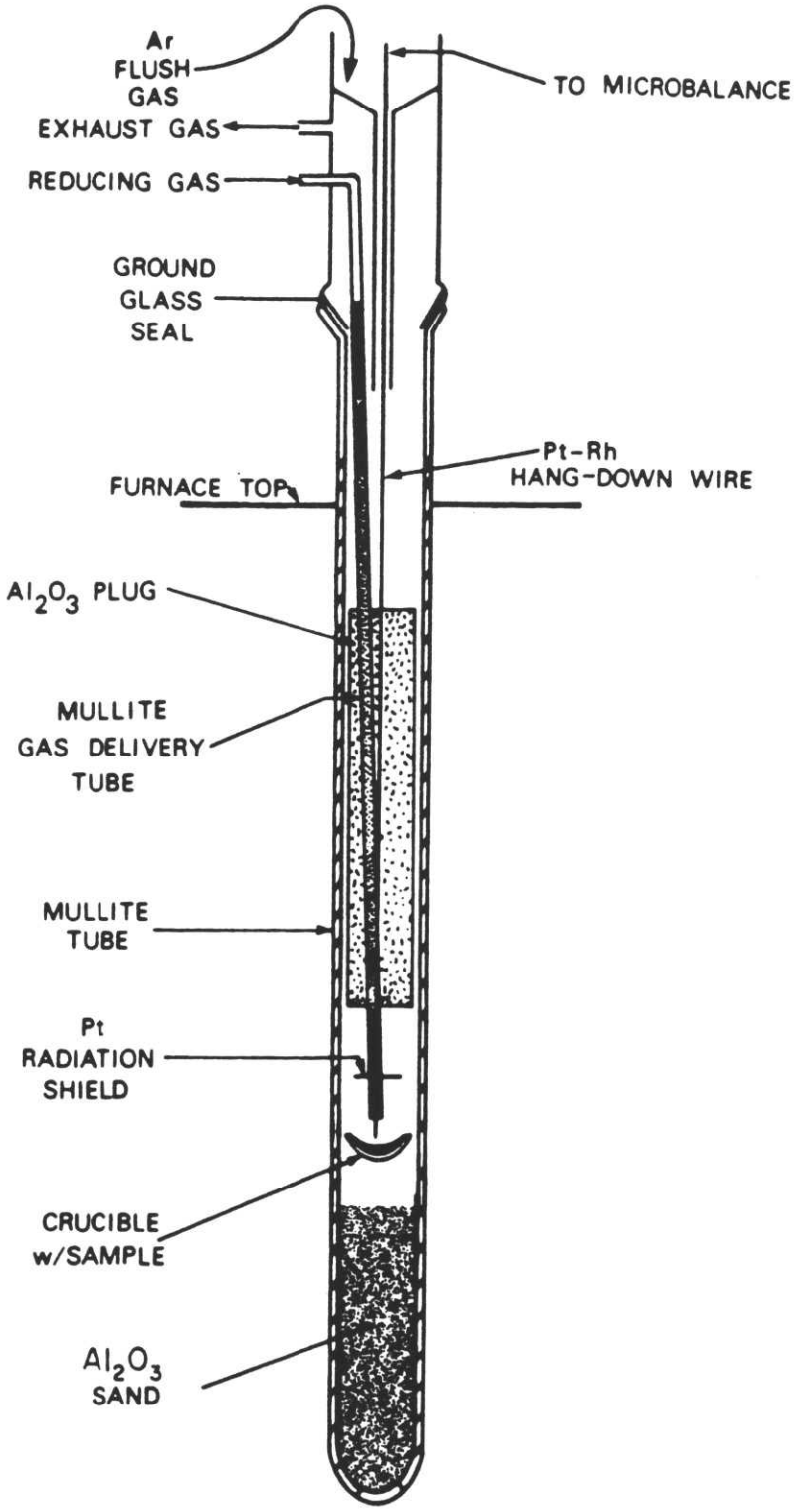

Figure 5-2. Diagram of reaction furnace.

place. Alumina plugs are attached to the outside of the gas delivery tube, and positioned where the greatest furnace temperature gradients occur (200 to about 1200°C) to inhibit the natural convection currents. The mullite furnace tube is joined to a ground glass joint, which seals the glass housing of the balance to the furnace tube. Figure 5-3 is a photograph showing the gas delivery tube assembly with a crucible in position, and the ground glass seals of the furnace tube and balance housing. There is a constant temperature (± 3°C) zone of about 4 centimeters in which the crucible hangs. At 1300°C with gas flowing, the temperature in the vicinity of the crucible was measured by a calibrated Pt-10%Rh thermocouple, and a correlation with the furnace control thermocouple was determined. The crucible and sample are suspended by a Pt-Rh wire from a Cahn 1000 microbalance. The balance output was recorded on a strip chart recorder, and stored in the data acquisition computer. The resolution of the balance and data acquisition computer is estimated at ± 0.1 mg.

5.2 Experimental Procedure

5.2.1 Experimental Materials

A master slag batch was made by melting a mixture of reagent grade ferric oxide, calcined silicic acid, and powdered (-0.250 mm) electrolytic iron in a 6.0 X 10^{-5} m^3 (60 ml) covered Ferrovac E iron crucible. The melting was done under an argon atmosphere in an induction furnace at 1200°C. After about 2 hours at temperature, the melt was quickly poured onto a water-cooled brass plate. The quenched melt was ground in a steel laboratory

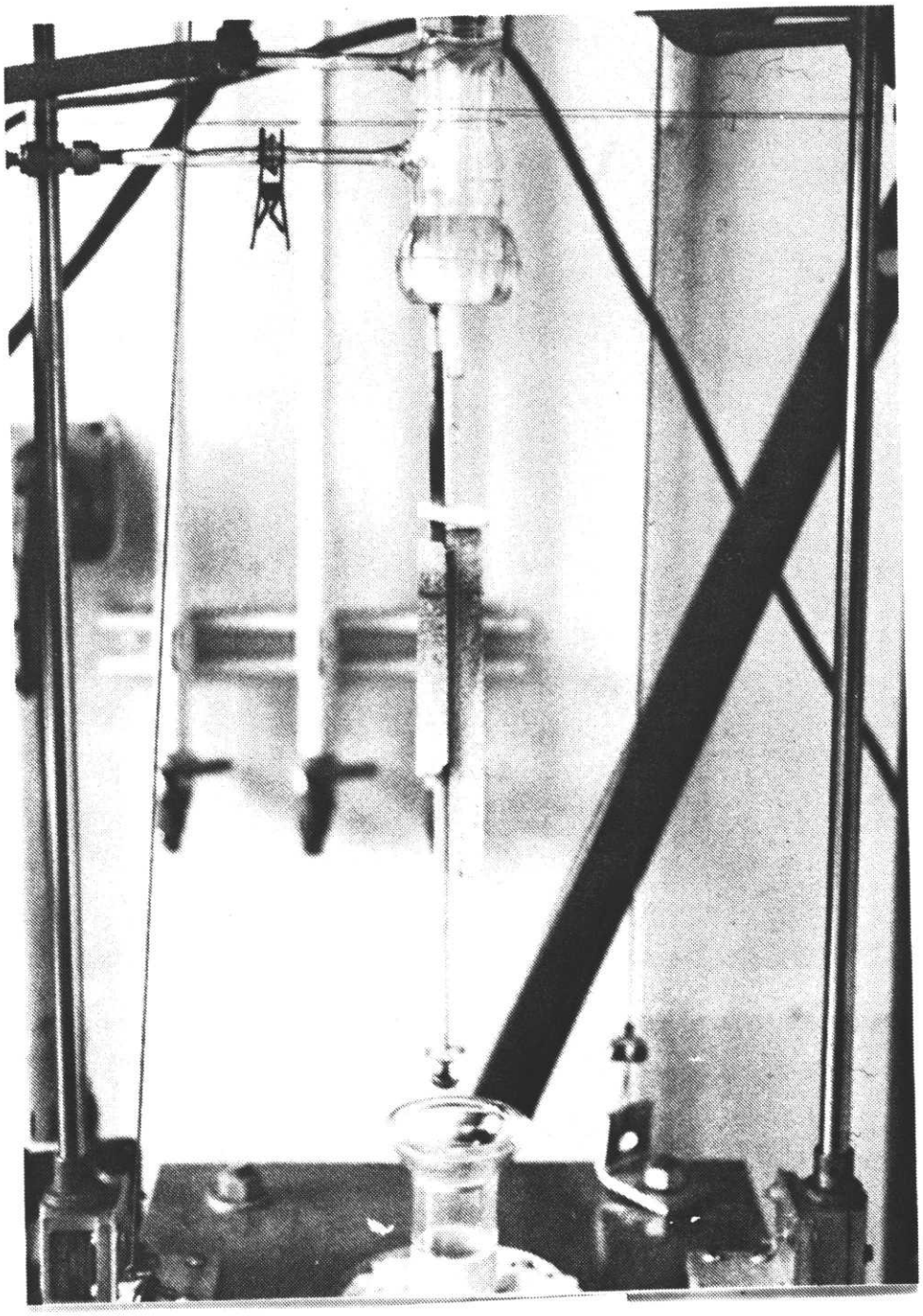

Figure 5-3. Photograph of gas delivery tube assembly.

ball mill to -0.053 mm, and analyzed in two different analytical laboratories for total, metallic, and ferrous iron, and silica. A sample of the pulverized slag was also analyzed qualitatively for the presence of trace elements in a plasma emission spectrometer. The the analyses are presented in Table 5-1.

Table 5-1. Chemical Analyses of the Master Slag (averages of 4 determinations for each component)

Analysis	avg. wt. %	σ
Fe°	0.25	±0.01
"FeO"	67.80	0.24
Fe_2O_3	10.12	0.17
SiO_2	21.48	0.92
total	99.65	

Ferric iron determined by difference;

Trace elements (less than 2 mg/kg): Cr, Al, Na, Mg, Mn, Ni

The slag is much more oxidizing than expected. At iron saturation and 1200°C, the melt should contain approximately 4 weight percent Fe_2O_3 at this silica level. Much of the electrolytic iron in the mixture sank to the bottom of the crucible when the liquid was formed, and sintered to a relatively dense mass. Apparently the melt period was not sufficient to equilibrate the melt with the crucible. A microscopic analysis showed a very fine dendritic structure (arm spacing of 7μm) of wustite with fayalite needles in the interdentritic regions.

The master slag was then mixed with reagent grade ferric oxide, calcined silicic acid, and electrolytic iron to make batches of powdered samples for the experimental work. The master slag comprised from about 55 to 95 percent of the final mixtures. Although there was a tendency for the iron particles to settle on the bottom of the crucibles when the master slag batch was made, the problem was not encountered in the slag mixtures for the reduction tests. The calculated melt compositions of the main test batches are shown in Table 5-2.

Table 5-2 . Calculated Melt Compositions of the Experimental Slag Batches

Batch Name (wt. % SiO_2)	"FeO"	Fe_2O_3
12.00	81.30	6.70
12.80	80.89	6.31
18.00	77.91	4.09
25.00	73.04	1.96
30.00	68.96	1.04

5.2.2 Experimental Procedure

Before each run, a compact of the slag mixture was made by pressing the powder to about 7 X 10^7 N/m^2. The compact was weighed and set into the crucible without touching the sides of the crucible. The placement of the compact allowed the melt to form a natural meniscus with the crucible, making the surface area easier to measure.

The crucible was suspended from the microbalance and aligned with the gas delivery tube, and the furnace with the furnace tube was lifted around the crucible assembly and the assembly was sealed.

The microbalance was then calibrated against a 10 mg standard weight. Argon gas was passed through the balance and furnace assembly in tests 1 through 50 for about 2 hours prior to heatup. In the other tests, the system was evacuated and back-filled with argon. The data acquisition computer was calibrated before each test using the thumbwheel electronic tare on the microbalance to provide the calibration weights.

The sample was heated to temperature (1300°C in most experiments) under argon in about 3 hours. A CO_2-CO gas mixture close to that in equilibrium with the melt was passed over the sample, and adjusted until the sample weight remained constant. This equilibration procedure normally lasted approximately one hour. The equilibration gas was then diverted to vent, and argon was blown over the sample while the reduction gas composition was being adjusted. When the reduction gas composition was set, the argon flow rate was increased to a value such that the momentum of the argon gas stream was equal to the momentum of the reducing gas stream. This step helped minimize crucible disturbance when the reducing gas was introduced.

The data collection program was started, and the argon flow was turned off, while simultaneously the reducing gas was diverted from the vent to the gas delivery tube. The minor disturbance to the crucible that resulted was recorded by the microbalance, allowing the starting time of the experiment to be determined to within about 5 seconds. After the reduction test was completed,

the furnace was lowered and the crucible was cooled by ambient forced air.

The sample was mounted in clear epoxy and sectioned axially through the center of the slag by grinding away the mount. An enlarged (about 6X) photograph of the section was used to measure the dimensions required to calculate the surface area. Because of the crucible shape, the slag surface normally formed a near perfect spherical sector, making the surface energy measurement straightforward. Figure 5-4 shows the measurements needed to calculate the surface area of the slag (61). These same measurements are used to calculate the slag volume. The measured volume of the slag was compared to the volume based on the original weight of the slag as a confirmation of the surface area measurements.

5.3 Data Analysis

The data acquisition computer and software were used for all the tests except tests 1 through 9. The data acquisition program was written to collect and store as many points as possible in the first 6 minutes of the reduction run, and then to collect points, calculate, and store average values every second after the initial 6 minute period. The computer was capable of collecting and storing 5 data points per second, and calculating and storing the average of about 100 readings each second. The raw experimental data was analyzed to determine the starting and ending times and then fed into a computer program that calculated the reduction curves and reduction rates.

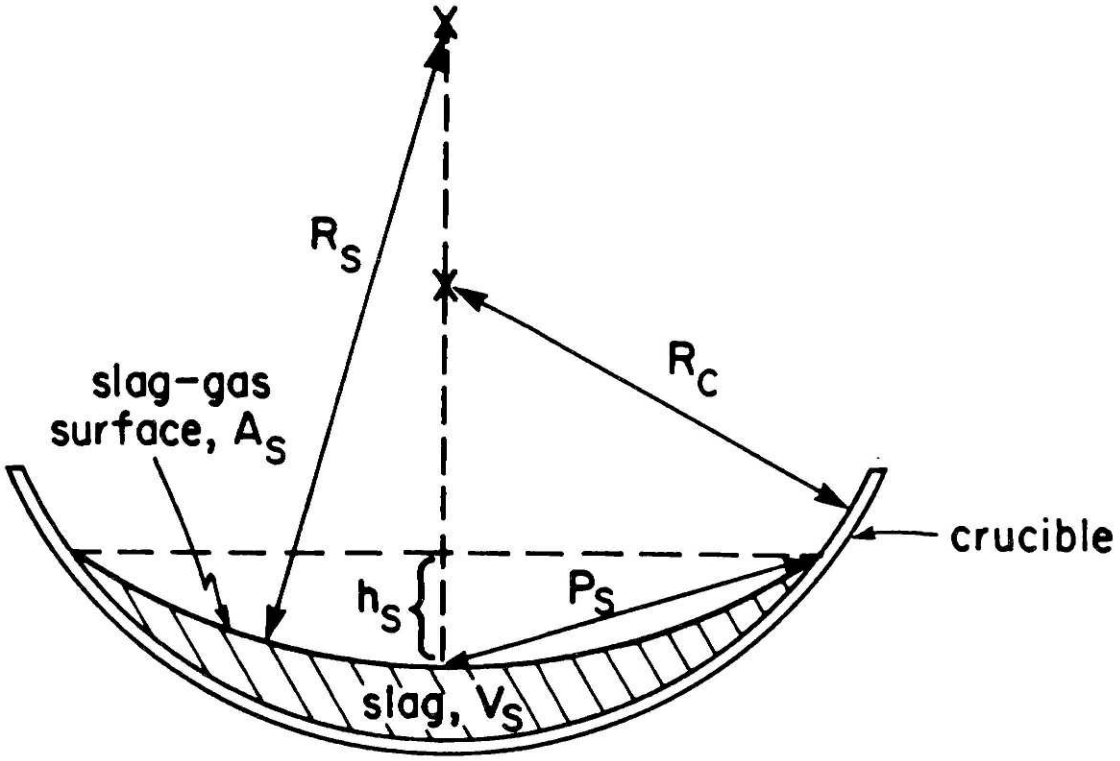

$$A_s = 2 \pi R_s h_s = \pi p_s^2 \qquad (61)$$

$$V_s = \pi / 3 \{[R_c - (R_c^2 - p_s^2 + h_s^2)^{1/2}]^2 [2R_c + (R_c^2 - p_s^2 + h_s^2)^{1/2}] - 3R_s h_s^2 + h_s^3 \}$$

Figure 5-4. Dimensions and formulas used to calculate surface area, A_s, and volume, V_s, of the melt.

The curves and rates were calculated manually for tests 1 through 9. The reduction rates for the subsequent tests were calculated using a "parabolic moving regression curve". The program calculates the best-fit second-order regression curve for the data points in the initial time period of specified length (normally 120 seconds). The first derivative of the resulting regression curve is calculated at five second intervals up to the midpoint of the regression curve. The regression curve is advanced 5 seconds by deleting the data in the first five seconds of the regression and adding on the data from the next five seconds. The first derivative is then calculated at the new midpoint of the regression curve. The procedure is repeated until the regression curve includes the last data point.

CHAPTER 6

RESULTS AND DISCUSSION

6.1 Introduction

The experimental program was carried out in three distinct stages. In the first stage, tests 1 through 15, slags saturated with respect to iron and near wustite saturation (12.8 percent silica) were held in dense magnesia crucibles. The magnesia crucibles could not be used for slags of higher silica contents at iron saturation because the melt crept up the crucible wall.

In the second experimental stage, tests 16 through 40, a suitable iron crucible was developed. The main problems were related to the wetting of the iron crucible and support structure by creep of the melt. In the third stage, tests 41 through 92, the necessary data was generated to develop a kinetic model. Many tests were aborted because the hang-down wire caught on the ceramic structures in the furnace.

This chapter contains the results of tests conducted using magnesia crucibles, followed by a brief description of the development of a suitable iron crucible. The results obtained using iron-silicate melts in iron crucibles are then presented, followed by error analyses of all the determinations. The experimental results, along with the results of Nagasaka, et.al. (6) and El-Rahaiby, et.al. (22), are compared to the chemisorption models presented in Table 3-2. The chapter is closed with a discussion of the rate-controlling steps and reaction mechanisms.

6.2 Tests Using Magnesia Crucibles

6.2.1 Microprobe Analyses and Phases Assemblages

The initial test work was done using magnesia crucibles because the solubility of magnesia in iron-silicate slags (62) at 1300°C ranges from less than 1 percent magnesia at 11 percent silica to about 8 percent magnesia at silica saturation (45% silica). All tests with magnesia crucibles were conducted using the 12.8 percent silica mixture.

Figure 6-1 is a photomicrograph showing a portion of the slag and crucible from test 6. The sample was equilibrated at 1300°C for 13 hours and reduced for 35 minutes under a gas of relatively high reduction potential (CO_2/CO=0.170). The sample lost approximately 38 milligrams (2.5 weight percent). The microstructure of the crucible and melt is very similar in all of the tests using magnesia crucibles. The phases present in the micrograph in sequence from the crucible to the slag-gas interface are the:

a) magnesia crucible
b) magnesiowustite reaction zone in the crucible
c) magnesiowustite blocky grains formed from the liquid
d) solid-solution olivine
e) melt region with a dendritic solidification structure
f) product iron.

The numbers shown in the figure refer to phases identified in Figure 6-2. The average electron microprobe analyses of the phases are shown on the FeO-MgO-SiO_2 phase diagram (62) in Figure 6-2.

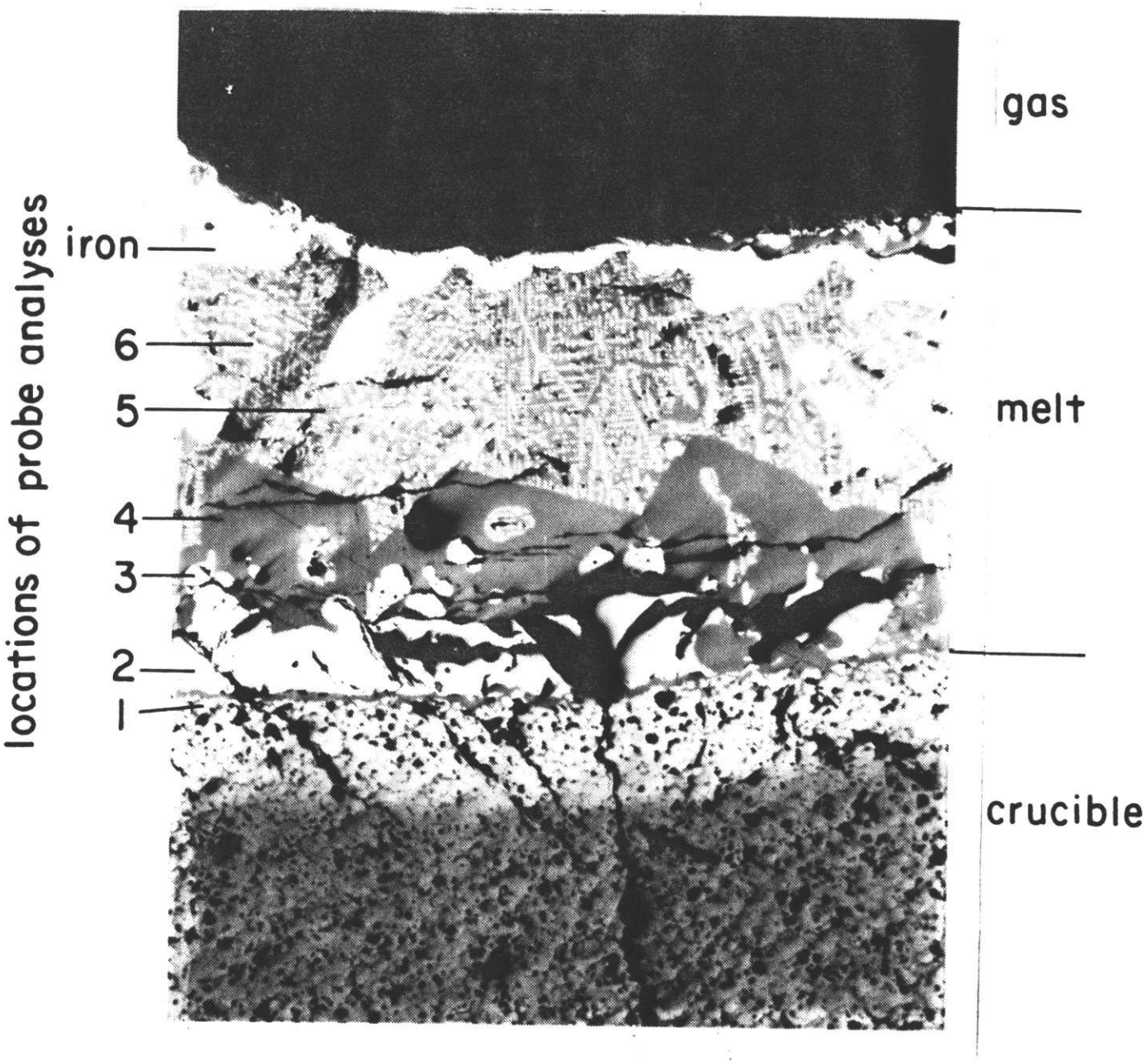

Figure 6-1. Phases present in reduction tests using MgO crucibles. Numbers refer to compositions identified in Figure 6-2. Test 6; 71X;

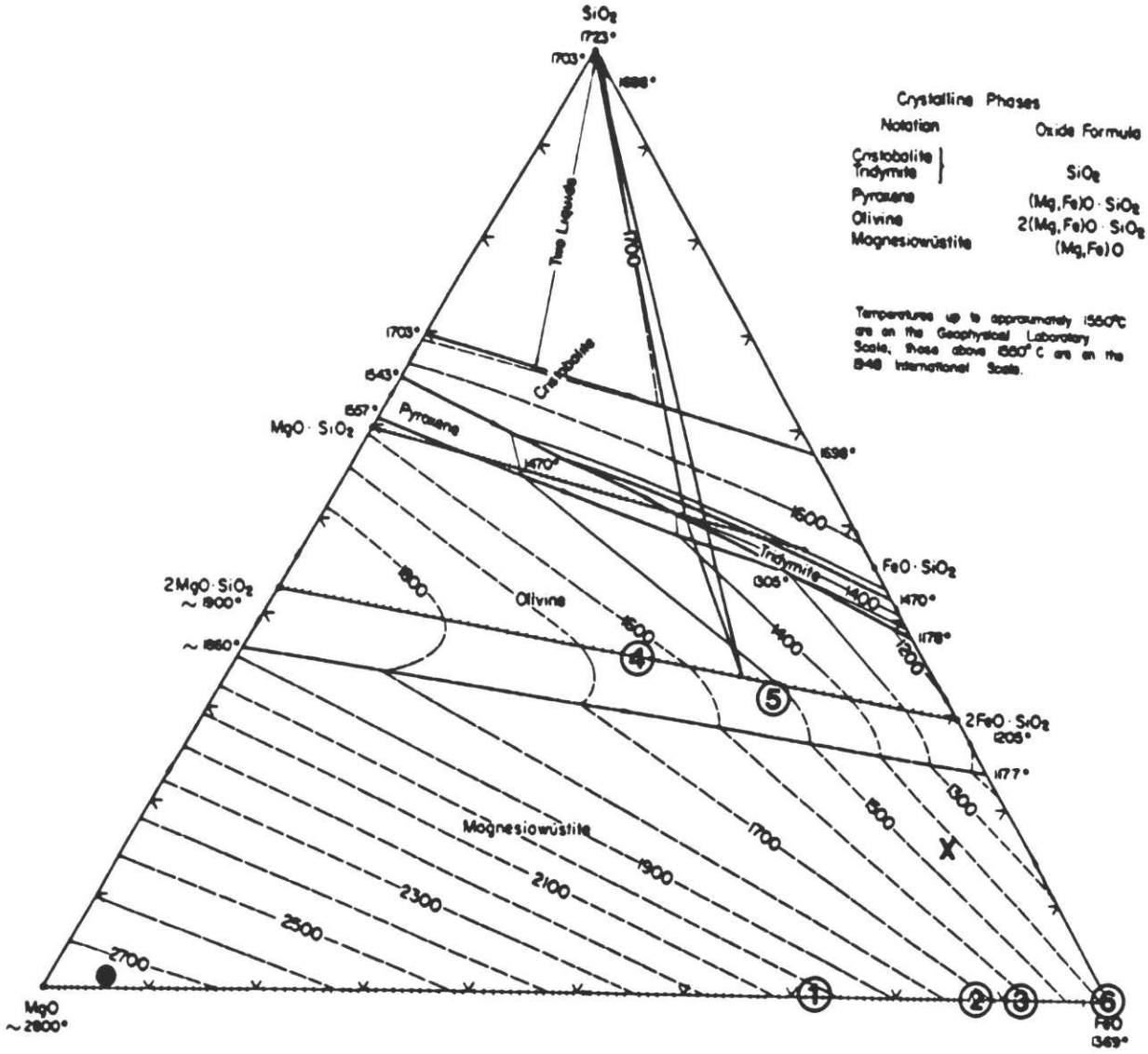

1) crucible near blocky magnesiowustite
2) blocky (Mg, Fe)O near crucible
3) blocky (Mg, Fe)O near olivine
4) olivine
5) interdendritic region of the melt
6) dendrites in the melt

X estimated liquid composition
● bulk composition

Figure 6-2. Microprobe analyses of the phases present in the melt in tests using MgO crucibles.

The apparent reaction zone of the slag with the crucible extends about 250 μm into the crucible. The extent of the reaction zone changes little with the time held at temperature (15 minutes to 30 hours). Magnesia and wustite form an ideal solid solution of magnesiowustite, and the visible extent of the reaction zone probably depends on the level of FeO dissolved in the magnesiowustite. The crucible grains closest to the melt contain about 27 weight percent MgO, balance FeO. No silica was detected in the magnesiowustite or the dendritic wustite. The large blocky magnesiowustite grains, adjacent to the crucible, formed from the melt by the reaction

$$FeO\ (slag) + MgO\ (s) = MgO\text{-}FeO\ (s.s.)\ . \qquad (6\text{-}1)$$

The phase contains about 12 weight percent MgO near the crucible interface and about 9 percent MgO near the top of the phase.

The magnesiowustite is covered by olivine, a solid solution between the magnesium and iron orthosilicates ($2MgO\text{-}SiO_2$ and $2FeO\text{-}SiO_2$). The olivine composition is about 53 weight percent fayalite ($2FeO\text{-}SiO_2$).

The liquid phase covers the olivine, and forms a wustite dendritic structure on solidification. The interdendritic phase has an olivine composition of 76 weight percent fayalite. The relative proportion of the dendrites and the interdendritic olivine phase was consistent within the whole melt region and was used to estimate the liquid phase composition of 7.5 weight percent MgO, 75.5 percent FeO, and 17 percent silica, shown in Figure 6-2.

Nafziger and Muan (63) investigated the equilibrium state of the solid phases present in the $MgO-FeO-SiO_2$ system at 1200°C and low oxygen potentials. Figure 6-3 shows the relationship between the composition of olivine and the composition of magnesiowustite in equilibrium at 1200°C. The activities of fayalite in olivine, and wustite in magnesiowustite change little with temperature (63, 64) in the temperature ranges of interest here, so the figure also closely represents the compositional relationships expected at 1300°C. Shown in the figure is the point determined from probe analyses of the olivine and the blocky magnesiowustite taken near the interface between the two phases. The magnesiowustite and olivine are not in equilibrium.

Figure 6-3 can also be used to determine if the liquid is at equilibrium with the olivine by comparing the composition of magnesiowustite that would be in equilibrium with the liquid and gas to the equilibrium composition of the olivine given in the figure. The activity of wustite in the liquid in equilibrium with the gas is determined by the equilibrium for the reaction

$$Fe_{0.947}O \text{ (wu.)} + CO \text{ (g)} = 0.947 \text{ Fe } (\gamma) + CO_2 \text{ (g)} . \quad (6-2)$$

The standard Gibbs free energy for reaction 6-2 is 15,713 Joules at 1300°C (from Table 4-1). The average CO_2/CO ratio of the gas in equilibrium with the melt is 0.2843, and the activity of wustite in magnesiowustite in equilibrium with the gas is calculated to be 0.945. (The gas equilibrium results will be presented in the next section.) Figure 6-4 shows how the activity of wustite in magnesiowustite varies with composition (64). Using the figure, the magnesiowustite in equilibrium with

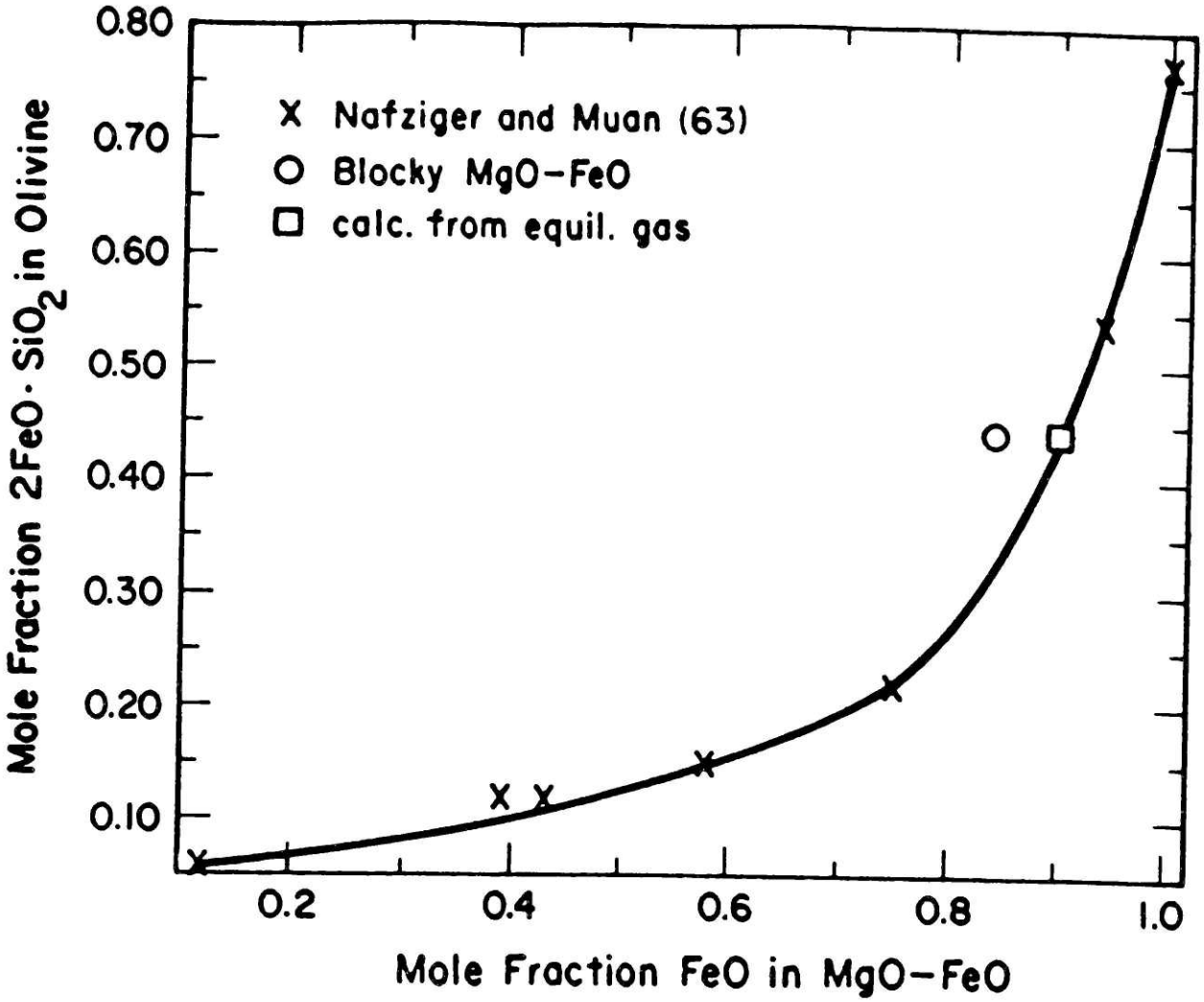

Figure 6-3. Compositional relationship of olivine and magnesiowustite solid-solutions at equilibrium at 1200°C. (63)

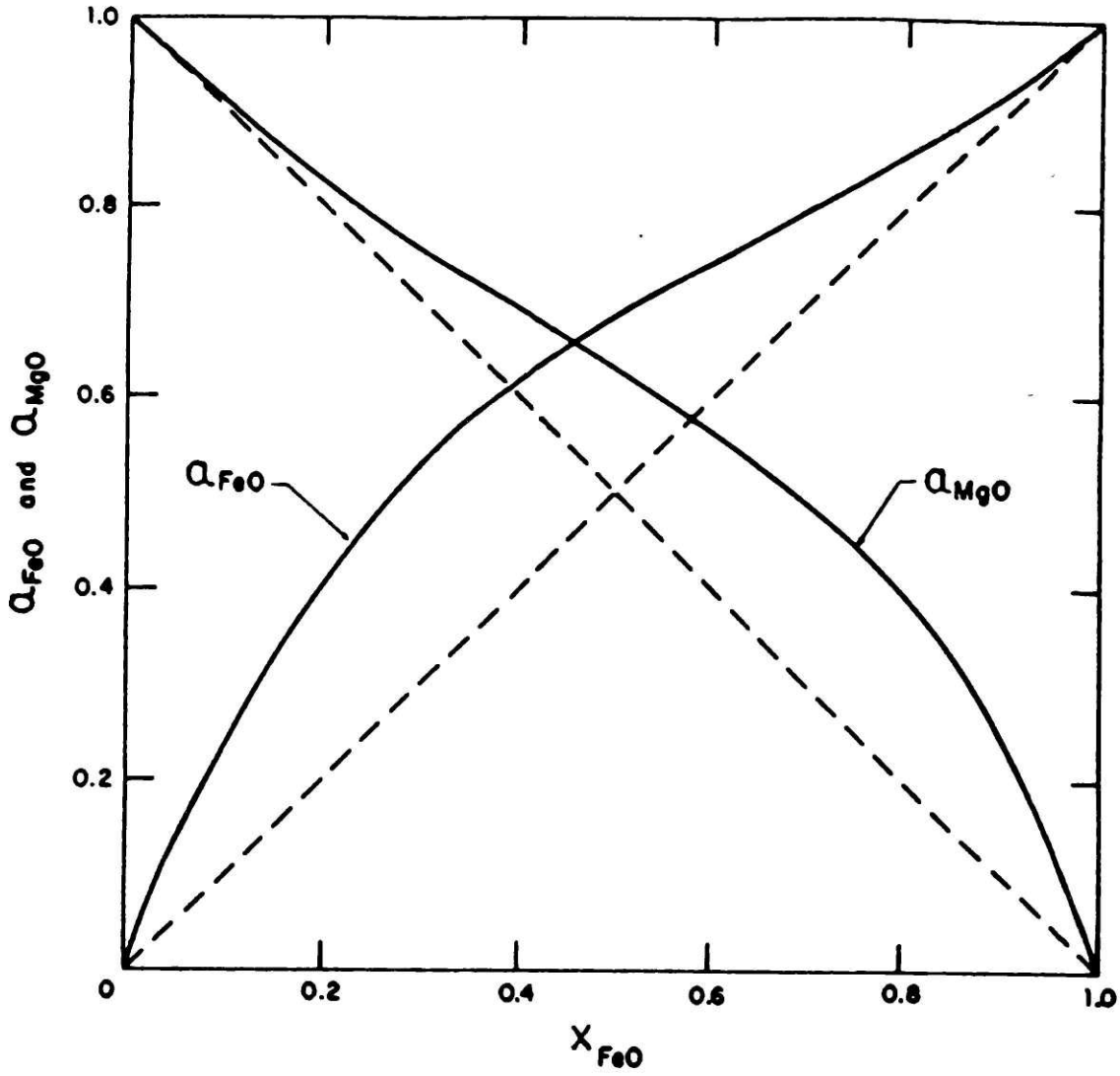

Figure 6-4. The activity-composition relationship of magnesiowustite at 1100-1300°C. (64)

the liquid and gas has a composition of X_{FeO}=0.900. The point corresponding to this composition and the measured composition of the olivine is shown in Figure 6-3. The melt is in equilibrium with the olivine.

There is a large wustite concentration gradient between the magnesiowustite in the crucible and the blocky magnesiowustite formed from the melt (73 vs. 88 percent FeO, respectively). There is a minor phase present between the crucible and the blocky magnesiowustite that appears to be olivine. No probe analyses were taken of this phase. There is also a smaller FeO concentration gradient across the blocky magnesiowustite (88 and 91 percent FeO at the crucible and olivine interfaces respectively). The concentration gradients indicate that corrosion of the crucible is controlled by diffusion of magnesium or ferrous ions across the minor separating phase, and diffusion through the blocky magnesiowustite. The relative proportions of the phases changed very little for times up to 30 hours at temperature, indicating that the corrosion of the crucible is very slow. The minor separating phase and the blocky magnesiowustite formed a protective layer on the crucible surface that inhibited the corrosion of the crucible. The indirect corrosion of refractories, in which solid-state interfacial compounds are formed, is known to proceed at much slower rates than direct corrosion (65).

The above analysis has implications to the study of the reduction kinetics in this system. The amount of liquid phase is not known,

so the activity of iron oxide as a function of weight change can not be determined accurately. Also the distribution of the components of the system among the phases in the system changes as the liquid composition changes and the solid phases adjust accordingly. However, the activity of iron oxide in the melt is known at the start of the reduction and changes only slightly after reducing for a short time, so the early reduction rates can be used to analyze the reduction kinetics of the melts.

6.2.2 Experimental Results

Figure 6-5 shows a typical strip chart recording of the sample weight change as a function of time. The scatter in the data is caused by the convective movement of the gases in the vertical tube furnace, or the occasional touching of the wire against the furnace structure. The scatter is at best about ± 0.1 mg or $\pm$ 1 percent of the strip chart range. Figure 6-6 shows the resulting reduction curve, and Figure 6-7 shows the calculated reduction rate curve using various time lengths in the "moving parabolic regression curve" program.

Reduction rate curves, similar to those shown in Figure 6-7, are useful for evaluating the reduction behavior of the melt. Short smoothing time intervals magnify the noise in the curve and tend to decrease the resolution of the plot. Increasing the smoothing time interval length improves the utility of the results, and has a similar effect as drawing the best fit curve through the points. Increasing the smoothing time interval further has no

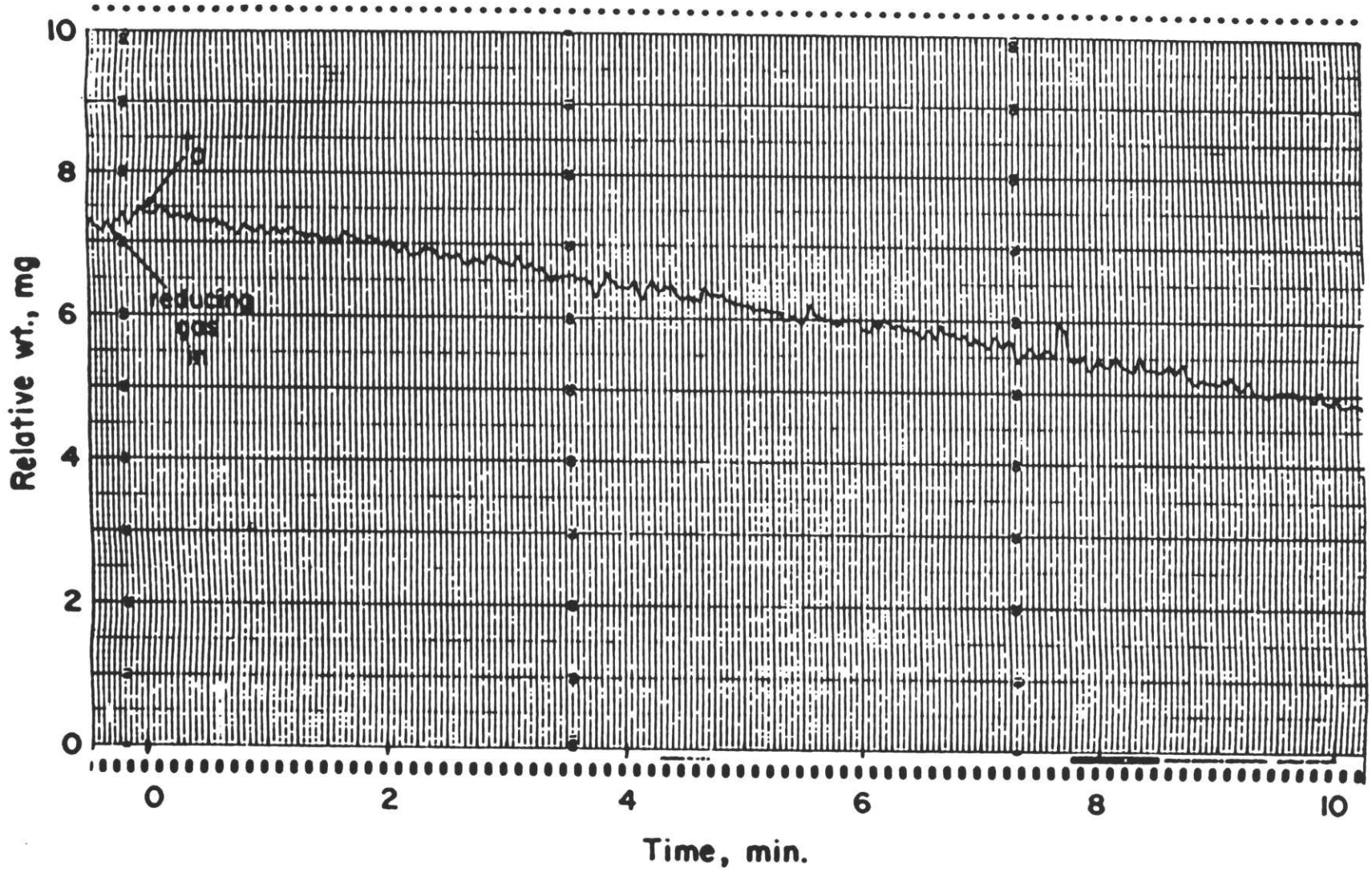

Figure 6-5. Strip chart recording at the beginning of a reduction test. Test 15

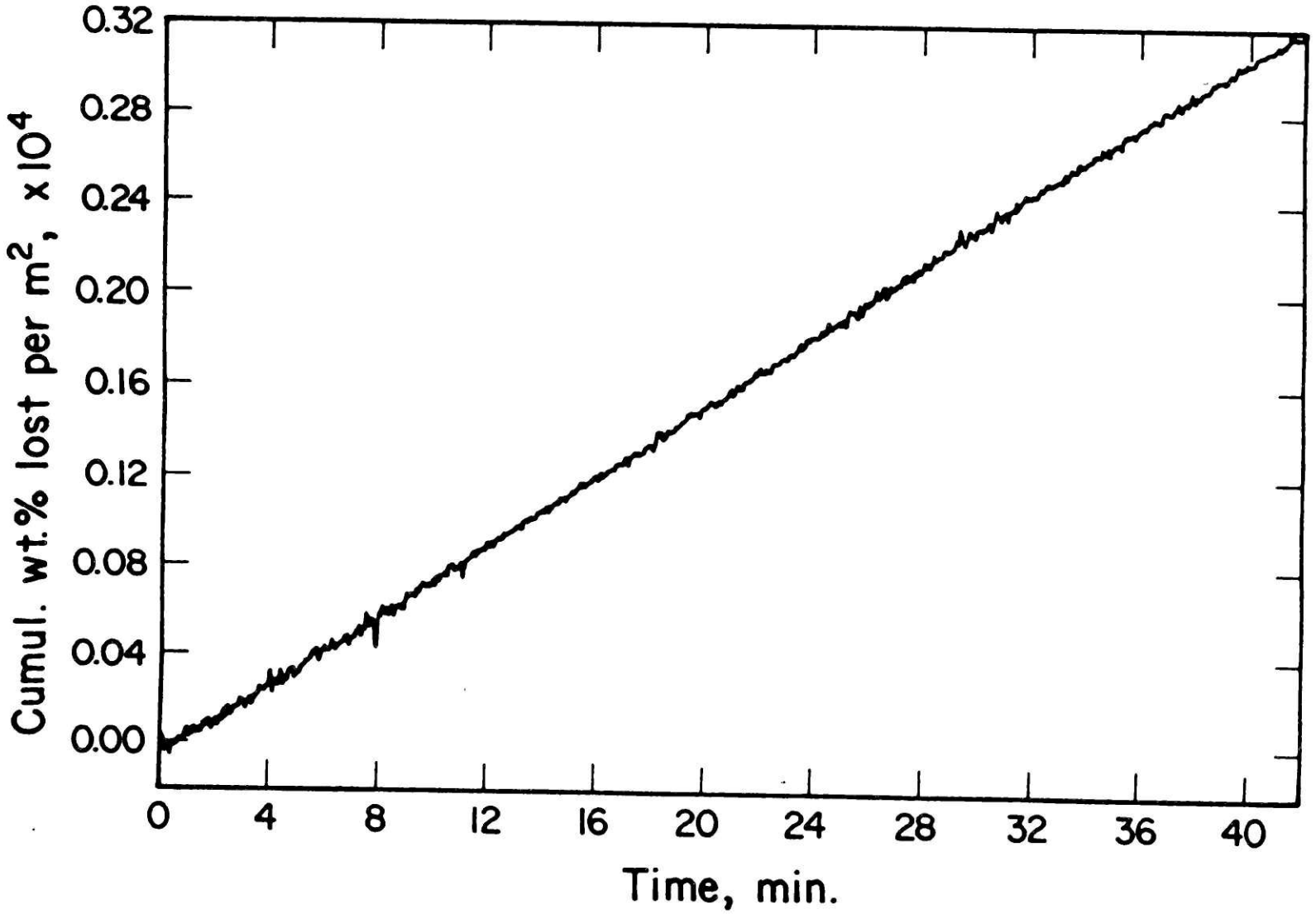

Figure 6-6. Reduction curve for test 6.

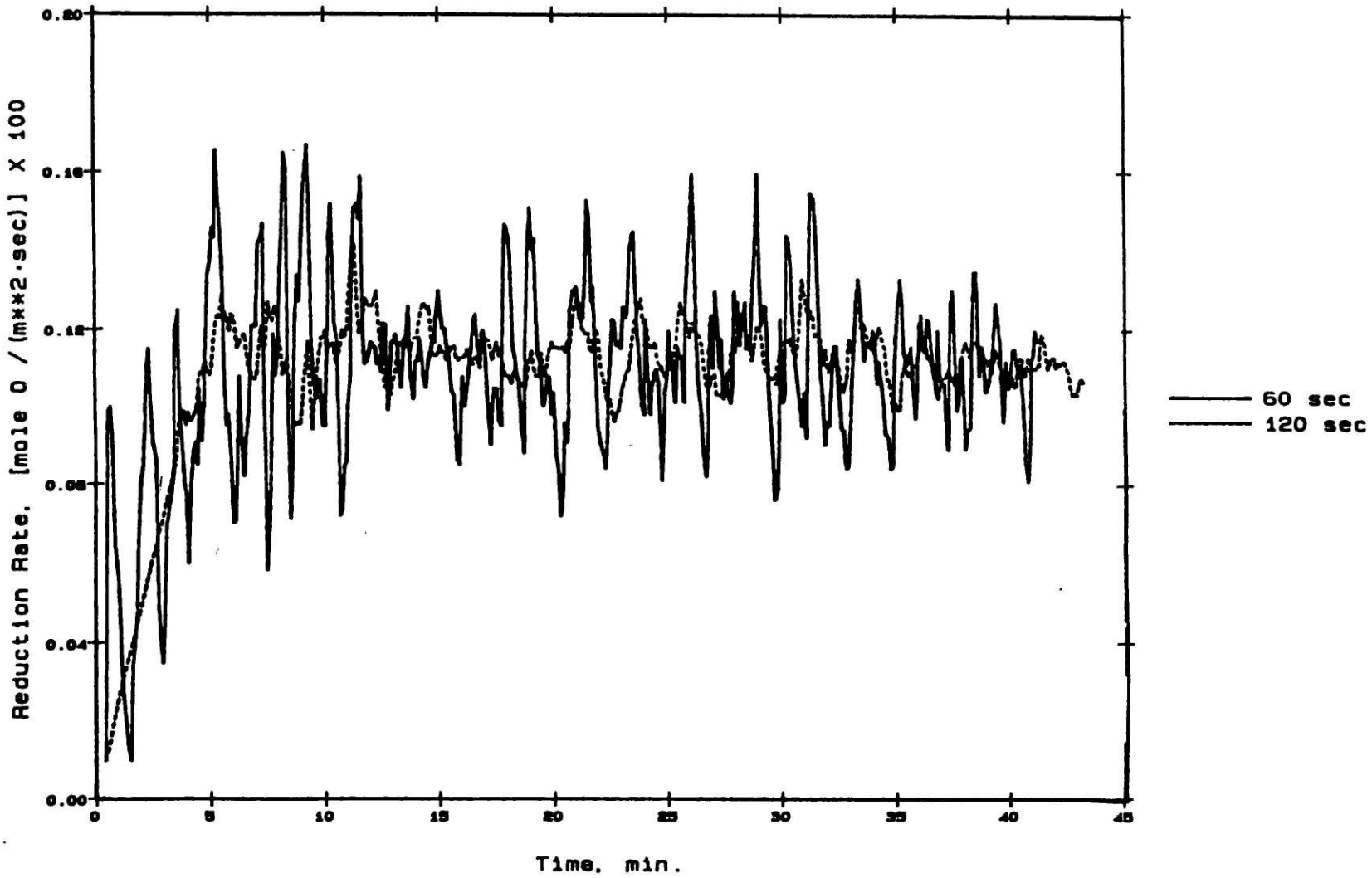

Figure 6-7. Effect of "smoothing time interval" in data analysis program on the apparent reduction rate. Test 15

significant benefit. A 120 second smoothing time interval is usually best for evaluating most of the tests.

Figure 6-8 shows the reduction rate curves for all of the successful tests using magnesia crucibles. Table 6-1 shows the pertinent experimental data for the tests. Tests 5 through 9 were evaluated manually by reading the relative sample weights off the strip chart and calculating the reduction rates similarly to the method used for tests employing the data acquisition computer.

The shapes of the reduction curves are significant. The samples reduced under the four lowest driving forces had increasing reduction rates with time up to about 5 minutes, after which the rate became essentially constant with time. This behavior indicates that nucleation and growth of the product iron grains is controlling the early reduction rates. To within the resolution offered by the experimental method, the early rates measured in these tests increase proportional to time.

The results fit the model for growth of iron grains when nucleation is fast and the reaction rate is dependent on the amount of gas-liquid-metal interface available (equation 3-20). In the model, nucleation of iron occurs quickly at a fixed number of sites. Electrons produced by the oxidation of carbon monoxide at the gas-liquid-metal line of contact are conducted through the iron grains to the reduction site at the metal-liquid interface. The reaction rate is proportional to the amount of iron-gas-

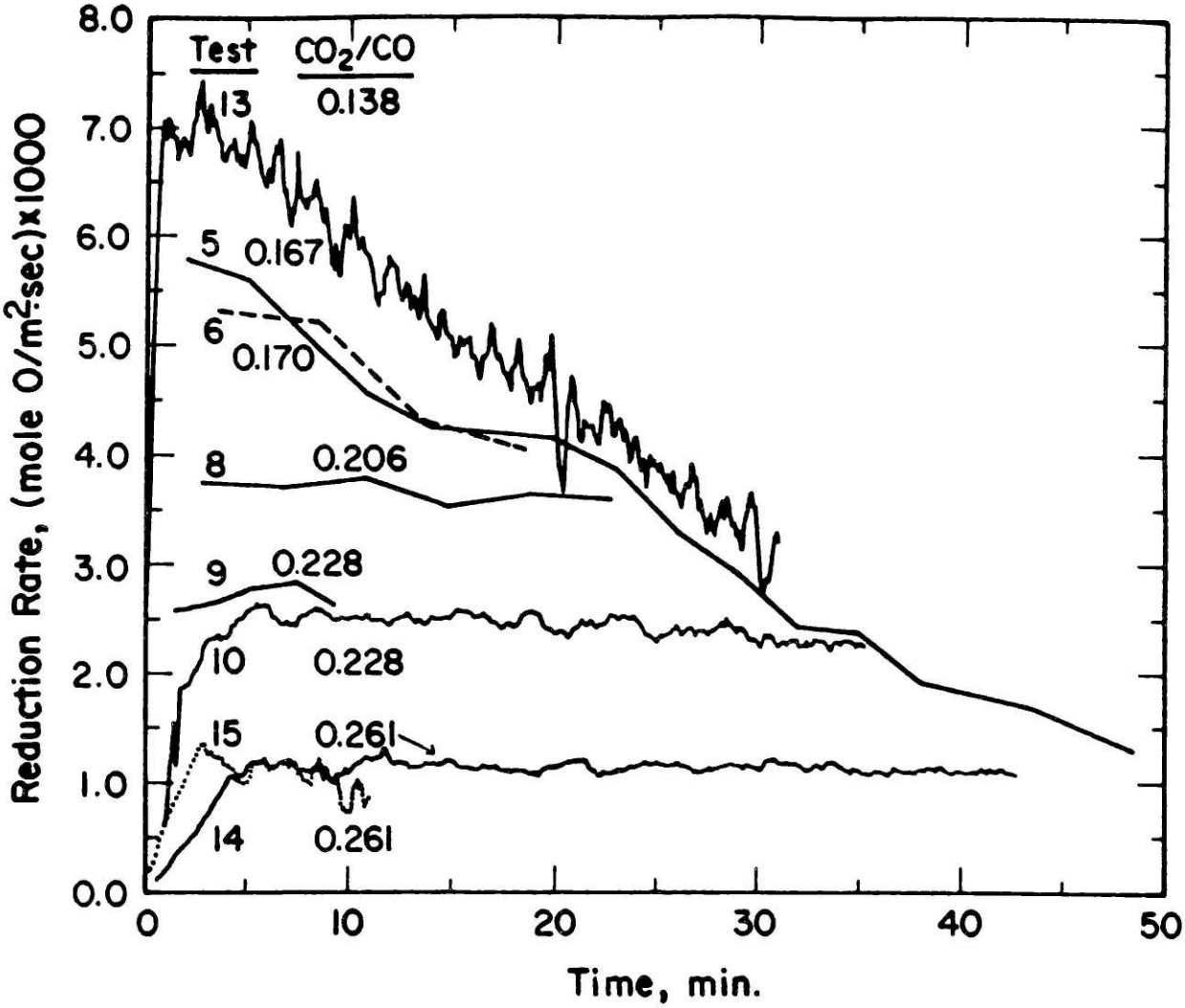

Figure 6-8. Effect of reducing gas composition on reduction rate curves. MgO crucibles. 1300°C

TABLE 6-1. Summary of Experimental Results and Conditions Using MgO Crucibles

Run	Sample wt, mg start	end	Surface Area, cm^2	Equil. CO_2/CO	Reduction CO_2/CO	Driving Force, atm[1]	Rate[2]	k_a[3]
5	1545	1503	2.52	0.284	0.167	0.101	5.7	5.67
6	1542	1504	2.46	0.295	0.170	0.0977	5.3	5.42
8	1614	1591	2.41	0.294	0.206	0.0649	3.8	5.85
9	1540	1532	2.77	0.284	0.228	0.0458	2.7	5.89
10	1508	1487	2.39	0.284	0.228	0.0458	2.5	5.45
13	1540	1499	2.82	0.294	0.138	0.129	6.8	5.29
14	1508	1503	2.58	0.285	0.261	0.0185	1.2	6.49
15	1408	1397	2.54	0.284	0.261	0.0185	1.1	5.95
avg.			2.56	0.2843				5.75
σ			0.16	0.0005				0.39

[1] driving force = $P_{CO}\, a_0 - P_{CO_2}$; calculated using $a_0 = 0.2843$;

[2] units for reduction rate are: [moles O /(m^2.sec)] X 1000

[3] k_a is the rate constant for the rate expression: $r = k_a[P_{CO}a_0 - P_{CO_2}]$; units for k_a are: [mole O /(m^2.sec.atm)] X 100

liquid interface available, or the total perimeter of the portion of the grain exposed to gas. If the growth rate is constant, the perimeters increase proportional to time, thus the reduction rate increases proportional to time.

Under high reduction driving forces, the iron grains grow too quickly to detect growth kinetics. However, the rates decrease rapidly after maintaining a maximum rate for a few minutes. At this stage the product iron phase displaces the gas-slag interface, causing a decrease in the reaction surface area. Reference is made to Figure 6-1, in which the iron phase produced under a gas of relatively low oxygen potential (CO_2/CO=0.170) is shown for test 6. Figure 6-9 shows the morphology of the iron produced under a gas of much higher oxygen potential (CO_2/CO=0.228) in test 10. Similar amounts of iron were produced in the tests (0.13 g and 0.073 g for tests 6 and 10, respectively). Under high reaction driving forces, the iron grains grow quickly and form a coherent iron layer. Under low reaction driving forces, the iron grains grow slowly and do not sinter together, and they sink beneath the gas-liquid interface, maintaining the original gas-slag surface area.

To correlate the results from tests conducted using high reaction driving forces to those using low reaction driving forces, it is necessary to look at the maximum reduction rates for the tests done under high driving forces. Under low driving forces, the reaction rates change little with time because the activity of

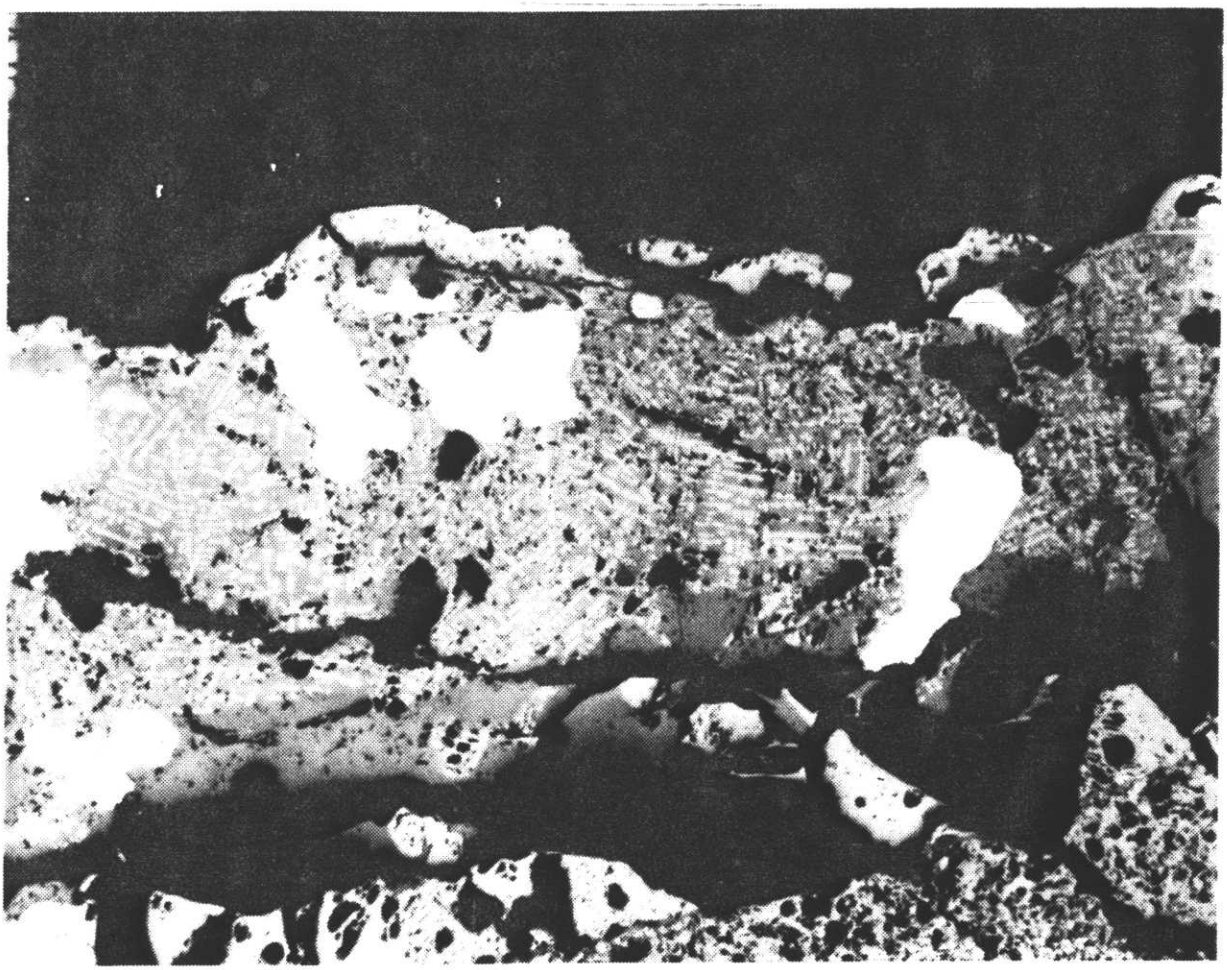

Figure 6-9. Morphology of iron produced under a low reduction driving force. Compare with Figure 6-1, which is morphology produced under high driving force. Test 10. 69X

oxygen in the melt remains essentially constant during the experiment. Figure 6-10 shows the maximum reaction rates plotted as a function of the reduction driving force using the chemisorption reaction model:

$$R = k_a [P_{CO} a_O - P_{CO_2}] . \qquad (6-3)$$

The data fit the model well. The average value for the reaction rate constant, k_a, is

$$k_a = 5.75 \times 10^{-2} \text{ mole O } /(m^2.\text{sec.atm}) . \qquad (6-4)$$

Figure 6-11 shows how the data fit the liquid-phase diffusion control model. The average slope, k, is

$$k = \rho D / M \delta , \qquad (6-5)$$

and has a value of 1.55×10^{-2} mole O $/(m^2.\text{sec})$. In equation (6-5), ρ is the density of the melt, 4000 kg/m^3, D is the inter-diffusivity of iron and oxygen ions (8, 20), 2.14×10^{-8} m^2/sec, M is the molecular weight of FeO, 0.07185 kg/mole, and δ is the effective diffusion boundary layer thickness in the melt. The calculated value of the effective diffusion boundary layer thickness is 77 mm, but the depth of the melt is only 2.5 mm at the center of the crucible. It is unlikely that liquid phase diffusion control is limiting the reaction.

The activity of silica in the melt is needed to estimate the fraction of open reaction sites available on the surface of the melt. The activity of silica in the olivine and hence the melt can be determined using the equilibrium for the reaction

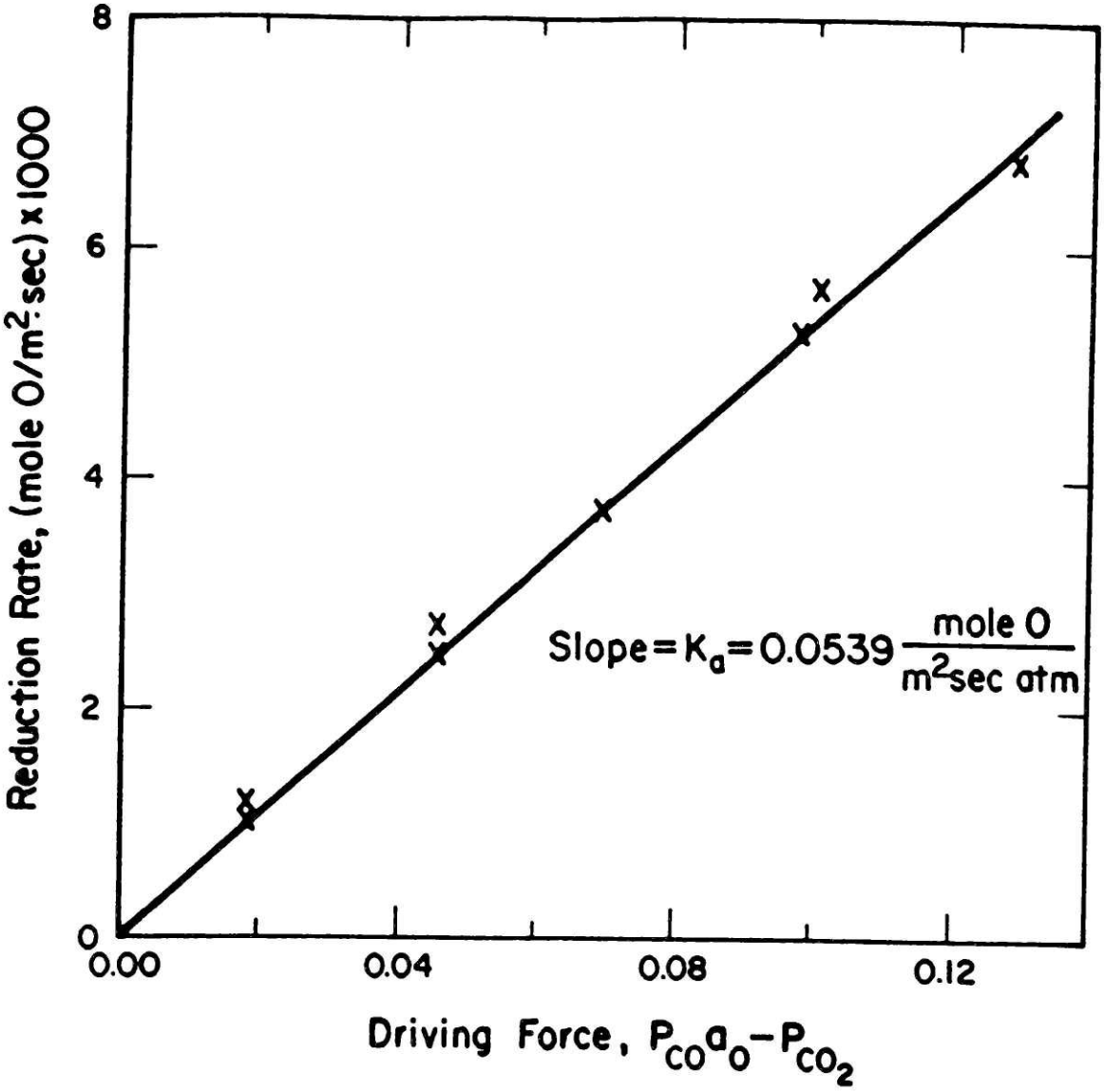

Figure 6-10. Comparison of the rates to the chemisorption model, equation (6-3).

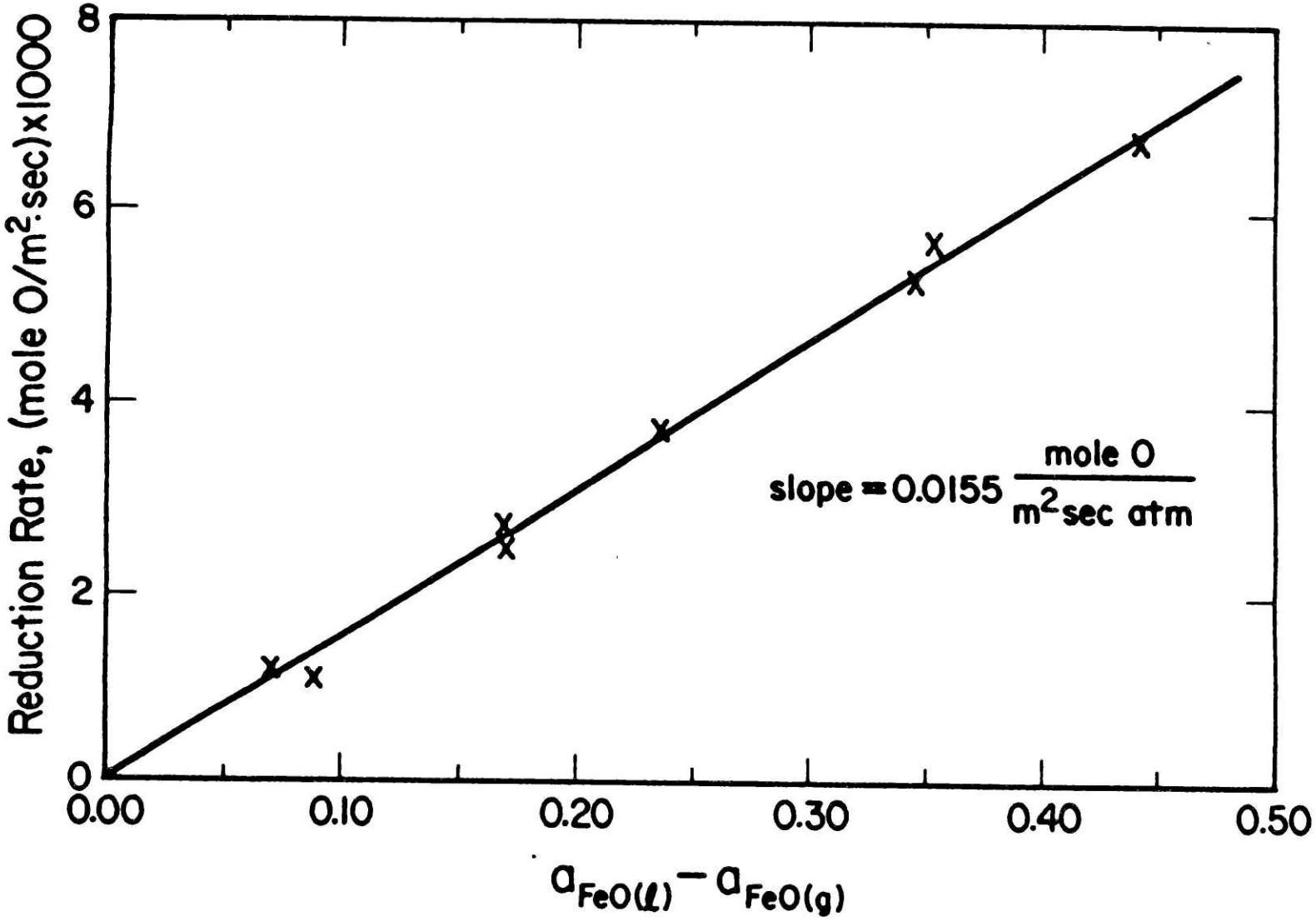

Figure 6-11. Comparison of the Experimental Results to the liquid-phase diffusion control model: $R = k [a_{FeO(l)} - a_{FeO(g)}]$. k given by equation (6-5)

$2\ Fe_{0.947}O\ (s) + 0.106\ Fe\ (\gamma) + SiO_2\ (s) = 2\ FeO\text{-}SiO_2\ (s)$. (6-6)

The standard Gibbs free energy for reaction 5 is -14,439 Joules at 1573 K from data provided by Barin and Knacke (66). The activity of fayalite in olivine is determined using the electron microprobe analysis of the olivine phase and the activity-composition relationship (63) shown in Figure 6-12. The activity of wustite in the melt was calculated as 0.945 in the previous section. The calculated activity of silica in the melt is 0.187.

6.3 Development of Iron Crucibles

An attempt was made to continue the test program using samples of higher silica contents contained in magnesia crucibles. The 25 percent silica mixture was heated to 1300°C in a magnesia crucible, and the melt crept up and over the the crucible wall. The surface tension of iron-silicate melts decreases with increasing silica content, thus increasing the wetting tendency of the higher silica content melts.

Several attempts were made to contain the melt in iron cups that were supported in magnesia or alumina crucibles. Figure 6-13 shows a cross-section of one such arrangement for a 12.8 percent silica melt and a magnesia crucible. The melt wet the iron cup and reacted with the magnesia support crucible. The reaction phase is visible in the region between the iron cup and the magnesia crucible. Figure 6-14 shows a magnification of the left rim of the iron cup in Figure 6-13.

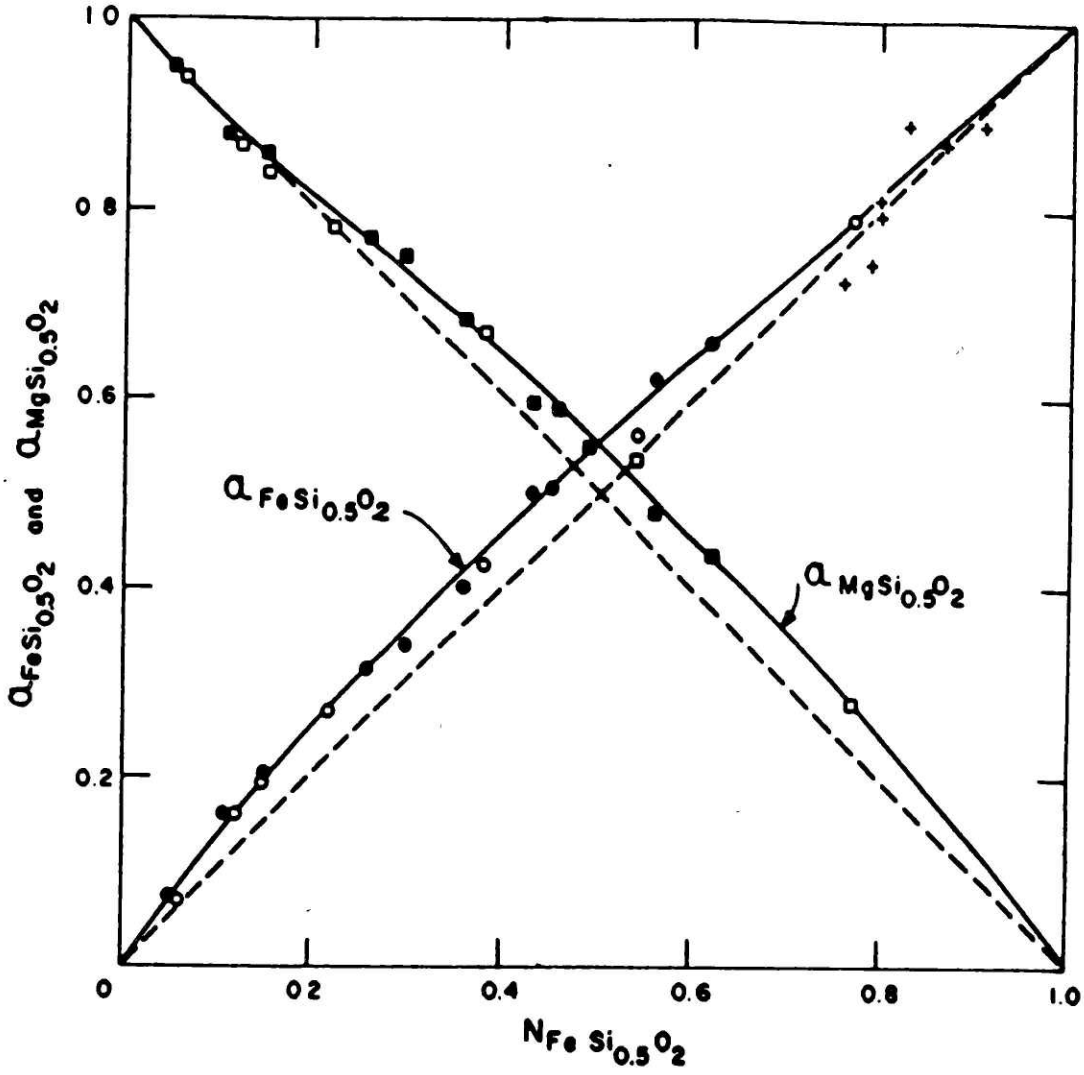

Figure 6-12. Activity-composition relationship of olivine at 1200°C. Points refer to different experimental techniques and correlations with other equilibria. from Nafziger and Muan (63)

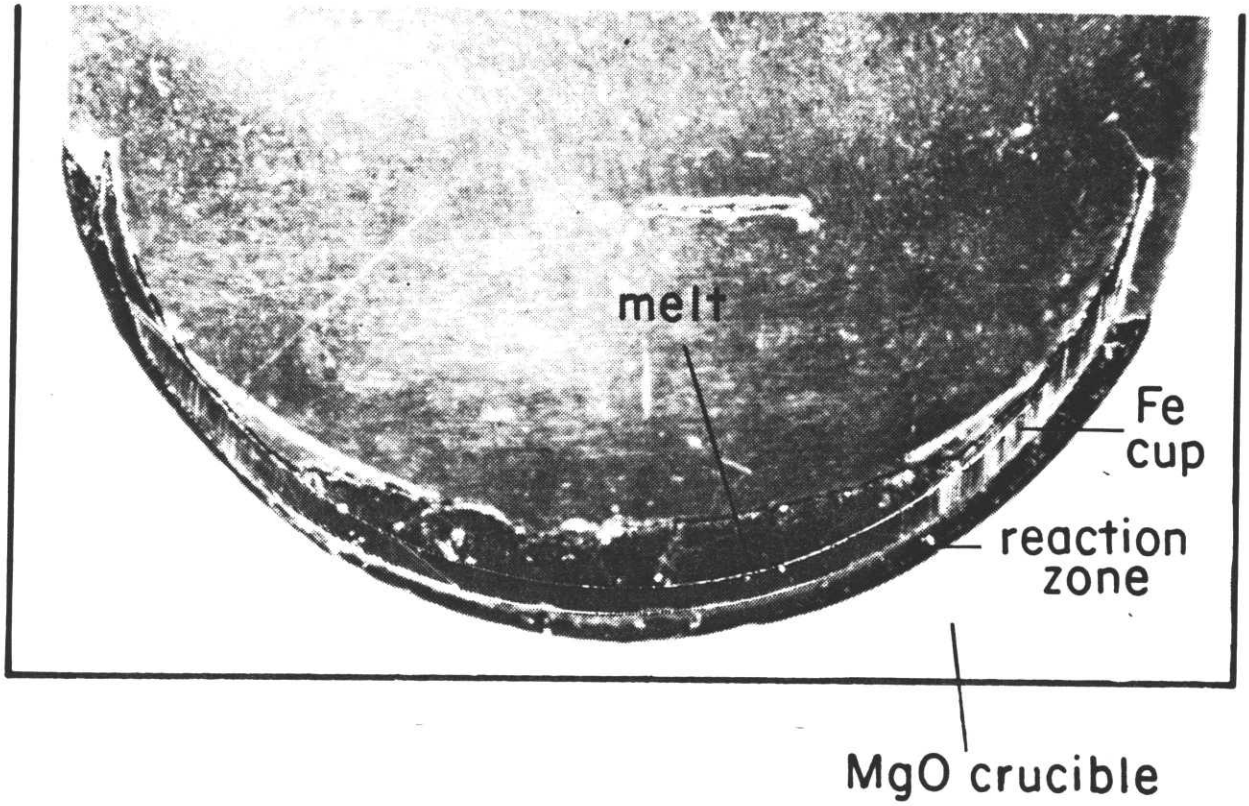

Figure 6-13. Melt contained in iron cup that is supported inside an MgO crucible. 8.5X

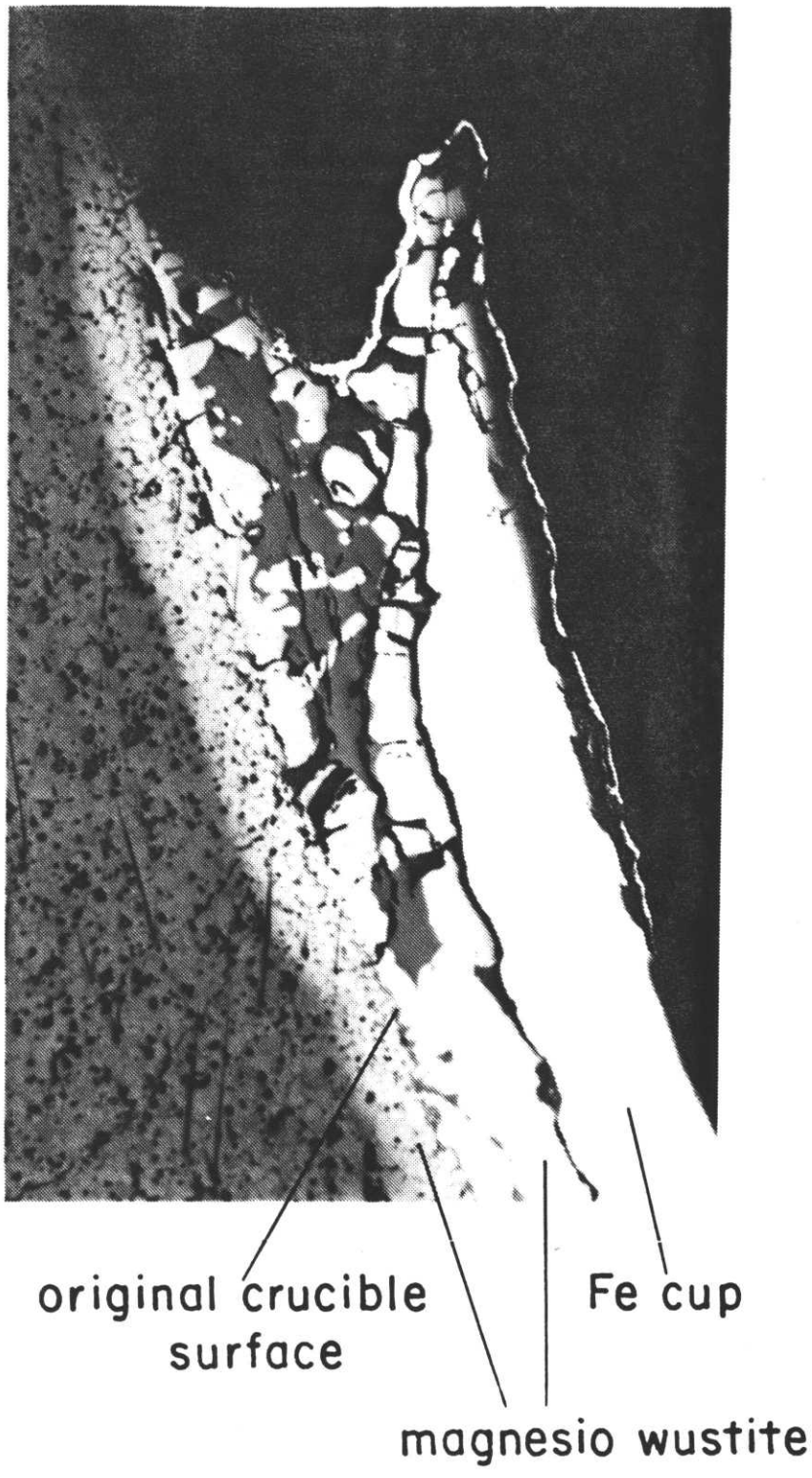

Figure 6-14. Magnification of the left side rim of the iron cup shown in Figure 6-13. 69X

The reaction zone of the melt with the crucible appears to contain magnesiowustite and olivine. This arrangement is unsatisfactory because this reaction zone reduces to form iron under reducing gases, evident in Figure 6-14, introducing significant error to the experimental results.

A series of tests were run with the iron cup suspended by wires attached to the cup in various ways. The liquid bonded any point of iron-iron contact, and filled any crevice or scratch on the inside or outside of the iron cup. In all of the trial tests, the slag formed a pool in the bottom of the cup, allowing simple gas-liquid surface areas to be measured. However, if the sample was left at temperature for more than about 3 hours, a slag pool began to form on the underside of the cup. If the sample was held at temperature for much longer times (10 hours) the slag would drip from the pool on the underside of the cup. Slag was not observed on vertical or near vertical smooth iron surfaces, probably because it was too thin.

To minimize the problems associated with the wetting characteristics of the slag, it became apparent that the attachment wires would have to be spot welded to the outside of the cups in such a way that the iron-iron contact regions would be minimized. Also, the cups would have to be free of scratches and other defects that tend to collect slag.

6.4 Results Using Iron Crucibles and Iron-Silicate Melts

6.4.1 Macroscopic Evaluation

Figure 6-15 is a macroscopic photograph of a cross-section of the iron crucible containing a 12 percent silica melt. Similar photographs were used to measure the dimensions needed to calculate the gas-liquid surface area. The slag formed a pool in the iron crucibles in all tests using pure iron-silicate and calcium-iron-silicate melts. If the slag was held at temperature for more than approximately three hours, the melt crept over the crucible lip and formed a pool on the underside of the cup. However, within the period of a standard test, all the slag remained in the cup.

The tendency of the melt to wet the iron crucible was most apparent for the melts with lower silica contents because the viscosity of the slags increases with silica content. Figure 6-16 is a scanning electron microscope (SEM) photograph of the iron surface on the inside of a crucible containing a 12 percent silica melt that was reduced in a gas of $CO_2/CO=0.166$ (32.5 percent silica at equilibrium) and slowly cooled under argon. The scale-like regions are extraneous slag that wet the inside iron surface. Most of the iron surface is covered by the reduced extraneous slag. Figure 6-17 is an SEM micrograph of the extraneous slag containing fayalite dendrites and rounded iron grains characteristic of a solidified iron-saturated melt with more than about 24 percent silica. For comparison, Figure 6-18 is an SEM micrograph of a slag droplet containing 12 percent silica on the iron surface from a test in which no reducing gases were used.

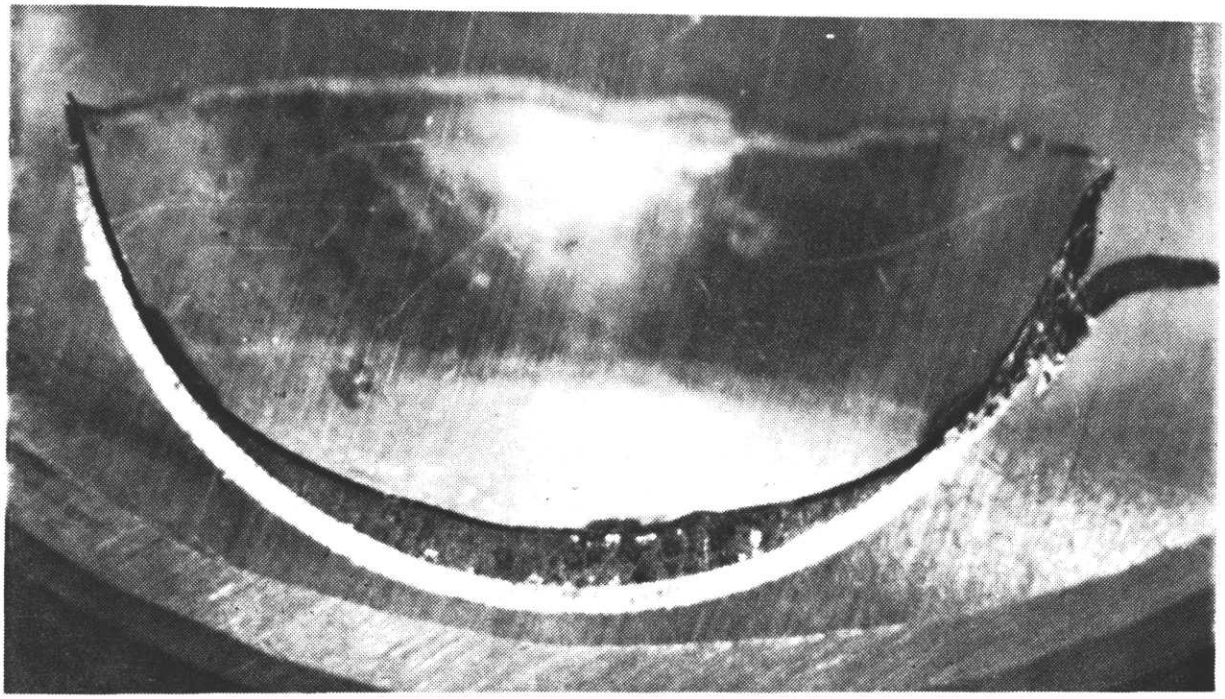

Figure 6-15. Cross-section of slag in iron crucible. Epoxy mounted. Test 72; 12 percent SiO_2; 8.6X

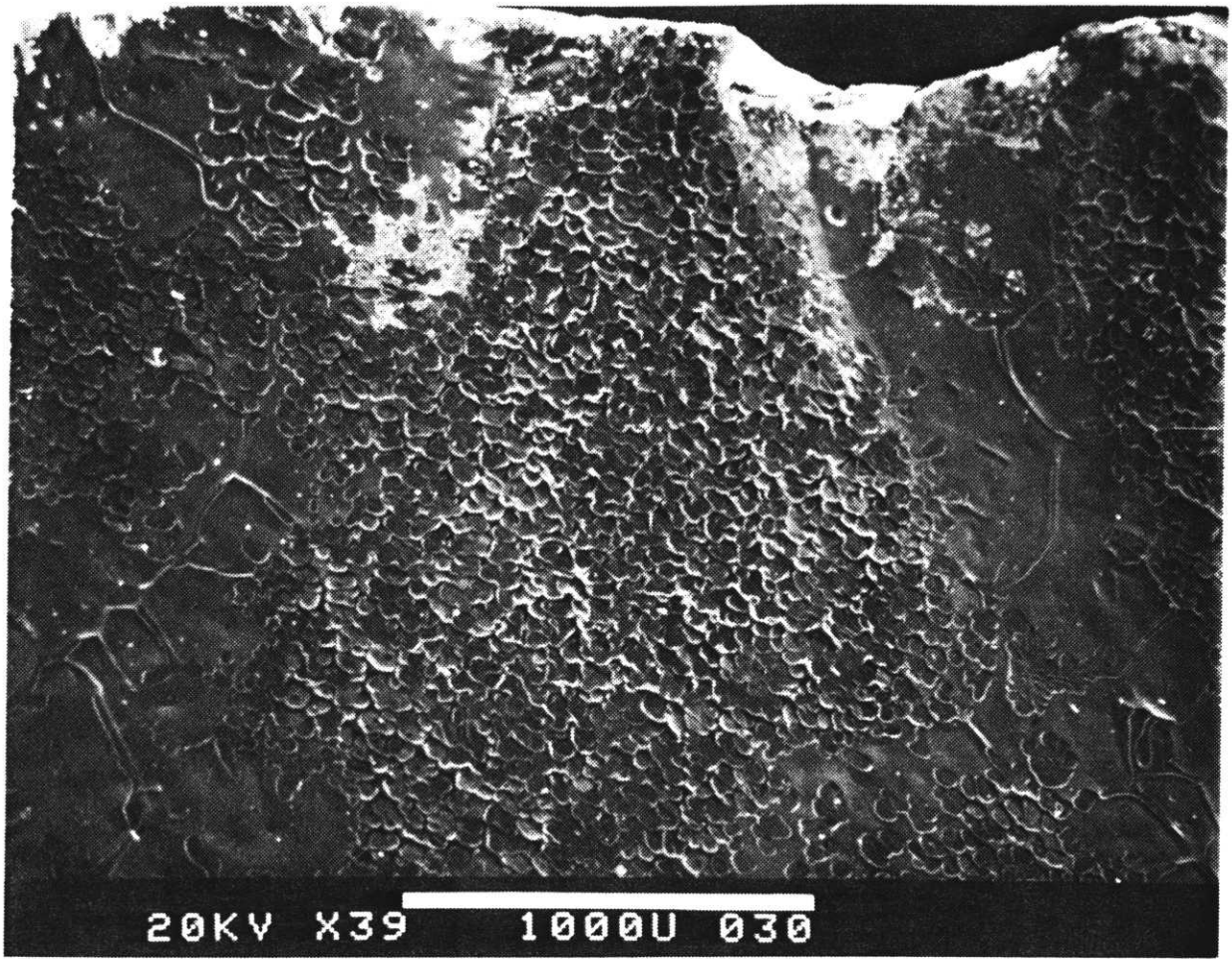

Figure 6-16. SEM photograph of the iron surface on the inside of a crucible after reduction, showing the nature of the extraneous slag. Test 55; 54.6X

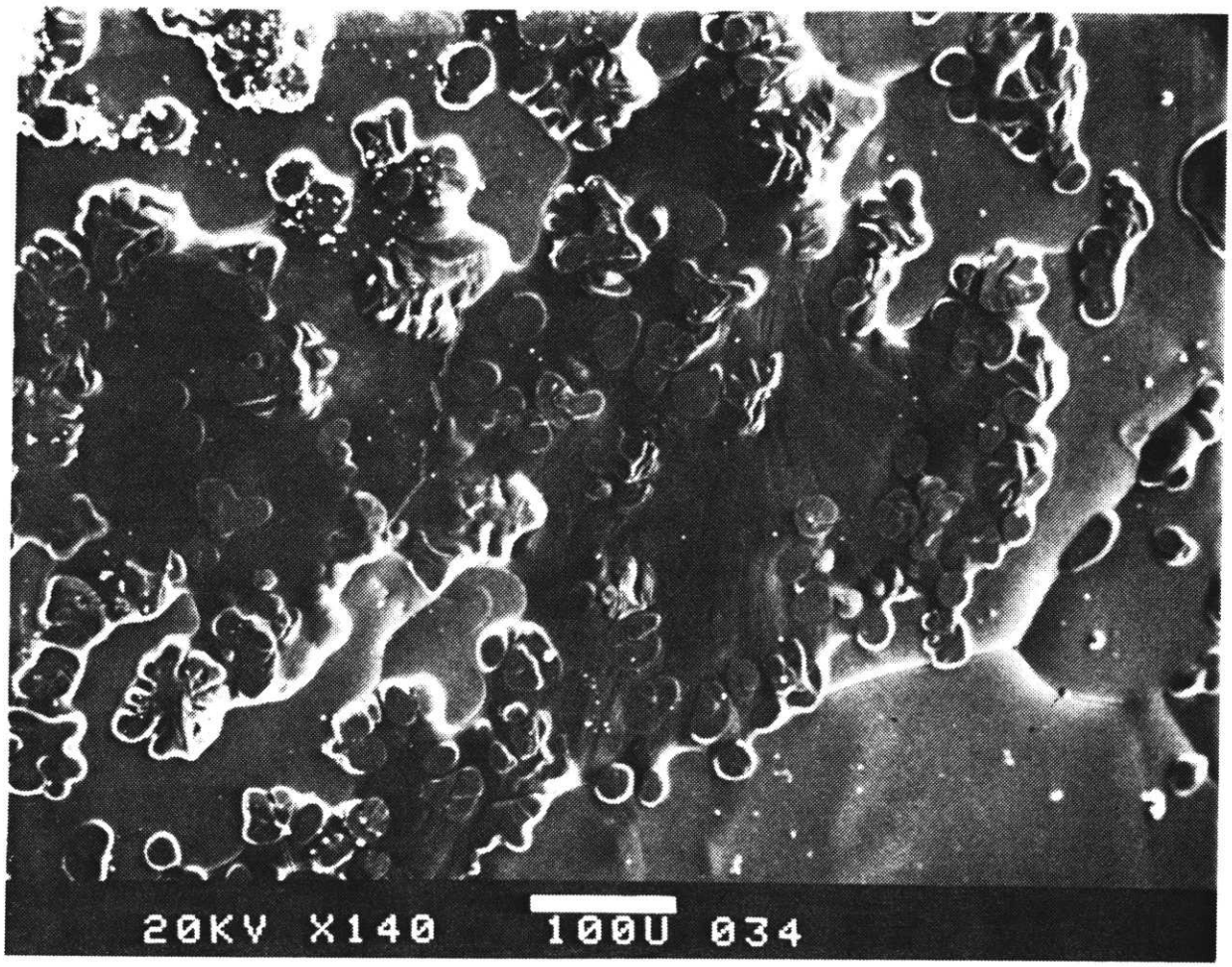

Figure 6-17. SEM photograph of extraneous slag on iron surface after reduction. Clover-shaped grain of fayalite is in lower left corner. Test 55; 198X

Figure 6-18. SEM photograph of unreduced extraneous slag on surface of crucible. Test 51; 12 percent SiO_2; Ar atm. 223X

The rounded droplet contains no fayalite, but contains many wustite grains that are characteristic of a solidified melt of relatively low silica content. The surface energy of iron-silicate melts decreases with increasing silica content, so the reduced extraneous slag shown in Figure 6-17 wets the iron more than the unreacted slag shown in Figure 6-18. The comparison of Figure 6-17 to Figure 6-18 shows that the extraneous slag approaches equilibrium with the gas and remains isolated from the main body of slag during the reduction.

6.4.2 Microscopic Evaluation

In all the tests using iron crucibles, the product iron began forming at the crucible-melt interface or on undissolved excess iron from the batch mixture. Figures 6-19 and 6-20 are micrographs showing the iron grains in a 12 percent silica melt and a 25 percent silica melt, respectively. The iron growth is localized, resulting in relatively few large grains that grow upward to the gas-slag interface. Figure 6-21 is a micrograph showing the dendritic iron grains that formed from a 12 percent silica slag reduced under a high reaction driving force.

Most of the reduction tests were run for only a short time because the iron that grew near the edge of the melt replaced the gas-slag interface. Figure 6-22 is a micrograph that shows iron growth at the crucible-melt-gas interface in a 12 percent silica melt. The iron growth shown in the figure replaced approximately 10 percent of the gas-slag interface of the main pool of melt.

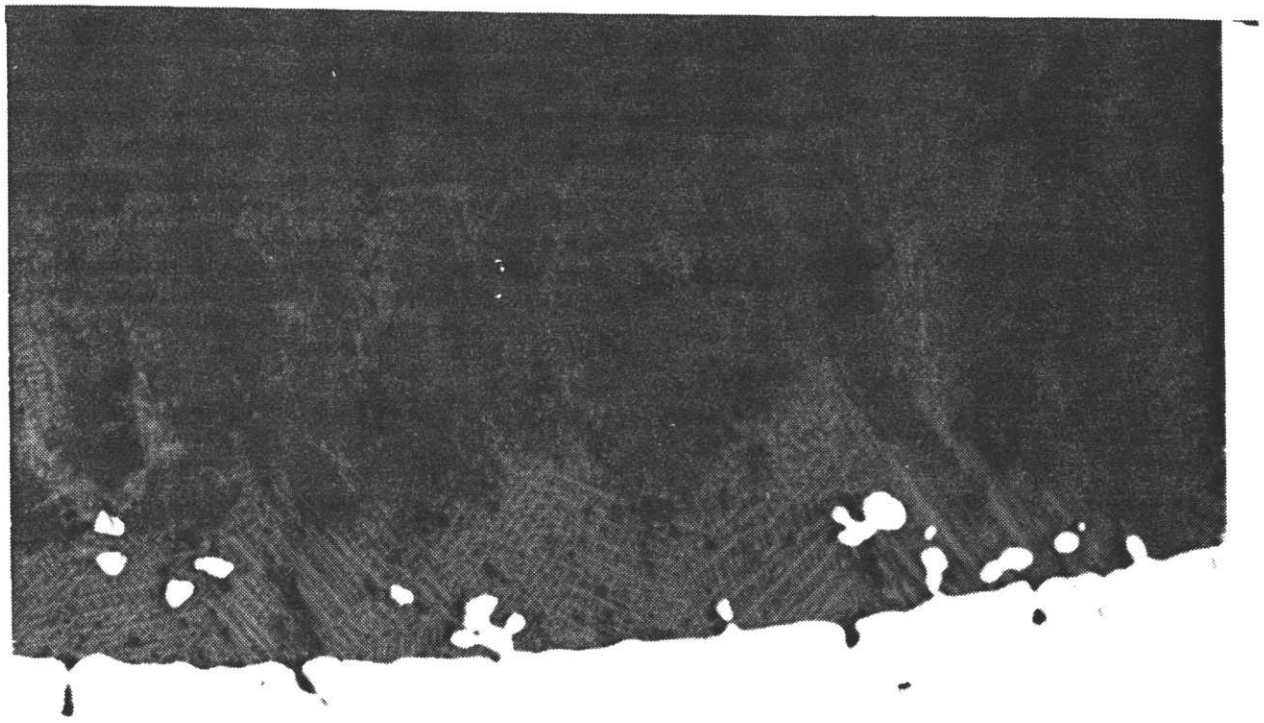

Figure 6-19. Micrograph showing iron produced from reduction grows from iron crucible. Test 50. 70X

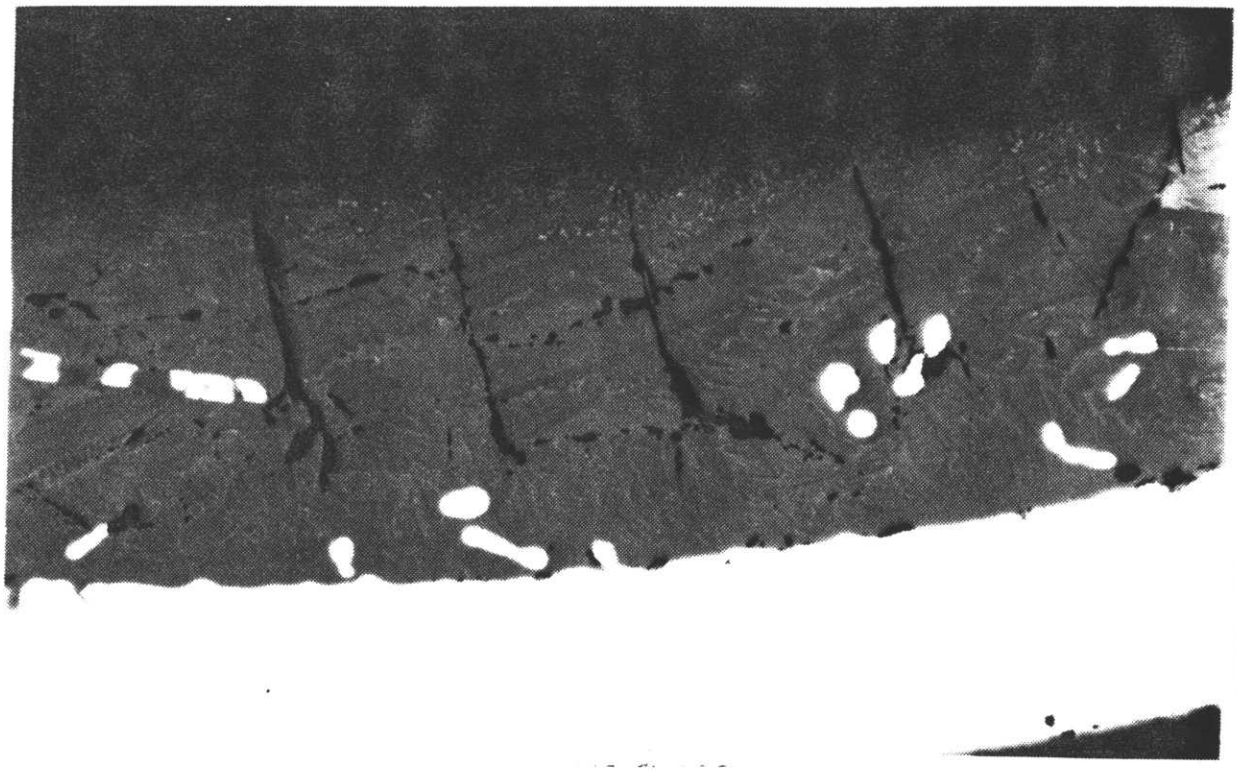

Figure 6-20. Micrograph showing iron produced by reduction grows from crucible. 25 percent SiO_2; Test 56 70X.

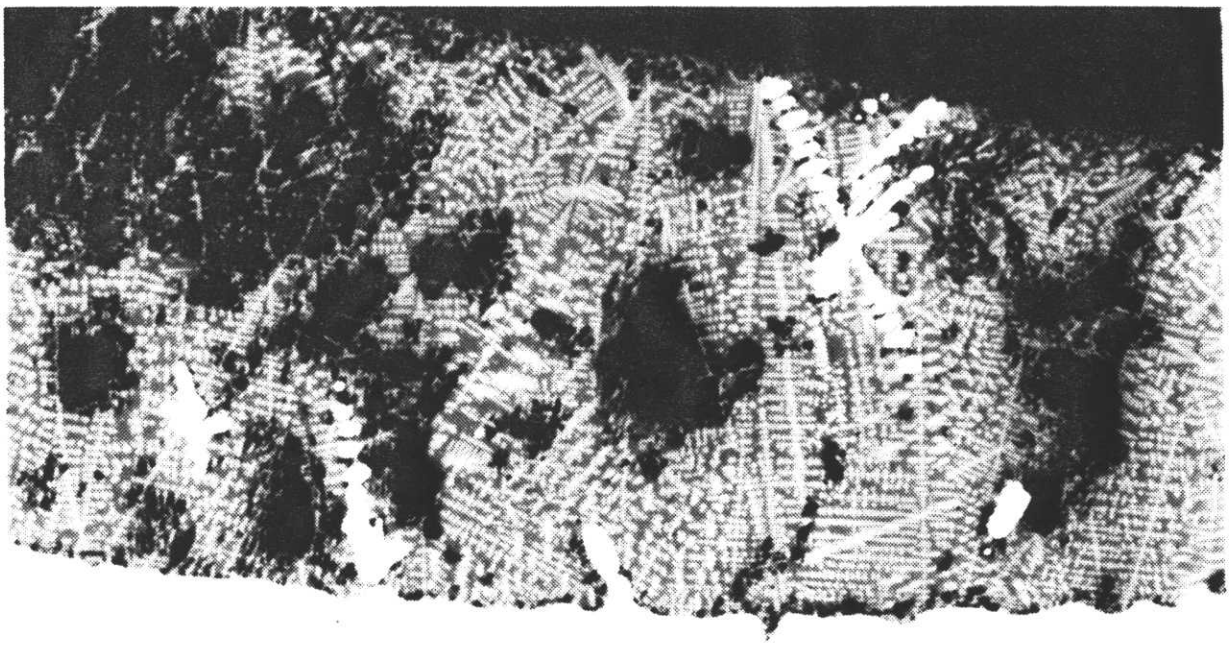

Figure 6-21. Micrograph showing the dendritic structure of iron formed under high reduction potentials; Test 48; 12 percent silica; 70X

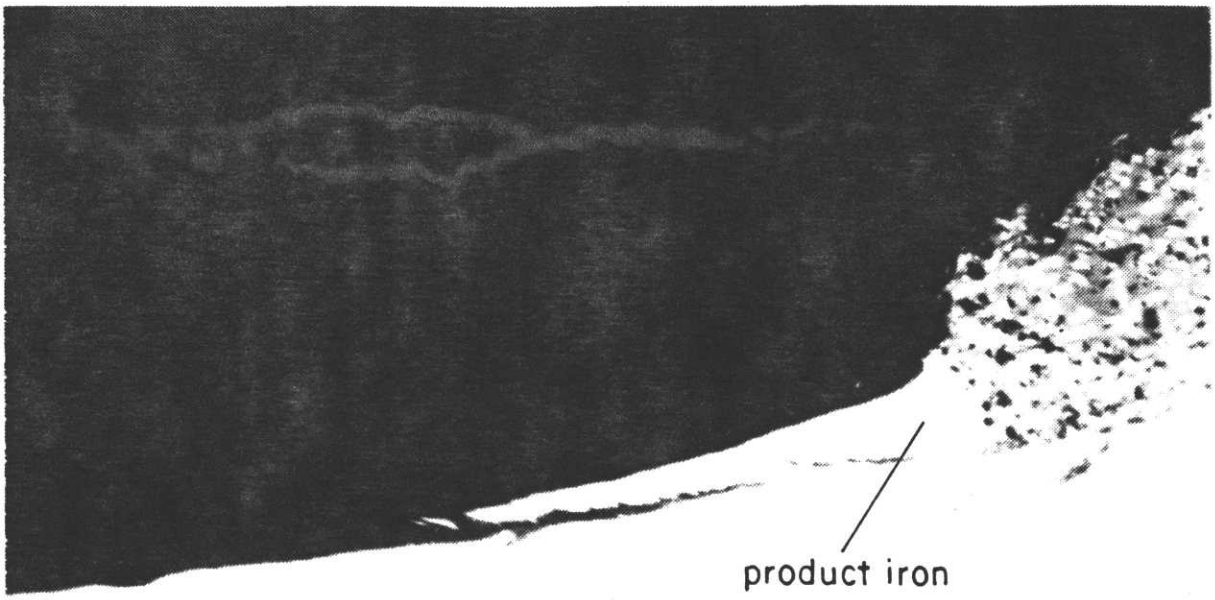

Figure 6-22. Micrograph showing iron produced at the gas-slag-crucible interface. Test 45; 12 percent SiO_2; CO_2/CO = 0.200; 280X

The sample lost 25 milligrams after a 30 minute exposure to a gas of CO_2/CO=0.200. Most tests were stopped after about 10 milligrams were lost on reduction.

6.4.3 Experimental Results

Table 6-2 is a summary of the experimental parameters and results for the successful tests using iron-silicate melts and iron crucibles. Figures 6-23 through 6-27 are the experimental reduction rate curves for 12, 12.8, 18, 25, and 30 percent silica melts respectively.

The dashed lines in the figures are calculated reduction rates that were extrapolated backwards from the end of the test to the starting time. The lines allow the comparison between the observed decrease in reaction rate and the decrease expected from the changing melt composition on reduction. The calculation is based on the decrease in both the thermodynamic driving force and reaction rate constant of the melt as the reaction proceeds, assuming the chemisorption model:

$$R = k_a [P_{CO} a_O - P_{CO_2}] . \qquad (6-6)$$

The oxygen activities of the melt as function of time were determined for each test using the cumulative weight lost as a function of time. The reduction rate and driving force at the end of each test were used to calculate the reaction rate constant, k_a, of the final melt. Figure 6-28 shows how the reaction rate constants for the final melts vary with the final silica contents

Table 6-2. Summary of Experimental Results and Conditions Using Iron-Silicate Melts and Iron Crucibles

Run	Sample wt, mg start	Sample wt, mg end	Surface Area, cm^2	Equil. CO_2/CO	Reduction CO_2/CO	Driving Force, atm [1]	Rate [2]	k_a [3]
12 Percent Silica								
48	398	391	1.622	0.301	0.143	0.138	10.0	7.23
49	298	292	1.460	0.301	0.200	0.0846	5.89	6.96
50	341	336	1.555	0.300	0.260	0.0323	2.40	7.43
55	398	390	1.625	0.300	0.166	0.116	7.82	6.75
71	432	426	1.646	0.302	0.223	0.0639	4.35	6.81
72*	264	256	1.364	0.301	0.162	0.0862	6.57	7.50
82	373	362	1.440	0.302	0.146	0.136	10.4	7.66
avg.				0.3010				7.191
σ				0.00082				0.358
12.8 Percent Silica								
41	247	232	1.478	0.299	0.167	0.113	7.64	6.78
43	248	235	1.451	0.298	0.167	0.113	7.93	7.04
avg.				0.2985				6.910
σ				0.0010				0.180
18 Percent Silica								
57	205	202	1.291	0.275	0.180	0.0810	4.16	5.16
59	129	126	0.925	0.275	0.149	0.110	5.49	4.98
87	216	211	1.172	0.275	0.192	0.0703	3.71	5.28
avg.				0.2750				5.140
σ								0.151
25 Percent Silica								
54	721	718	2.103	0.227	0.152	0.0688	1.85	2.84
53	392	387	1.582	0.227	0.144	0.0722	2.30	3.19
56	201	198	1.072	0.227	0.144	0.0725	2.36	3.26
60	151	149	1.178	0.227	0.113	0.102	2.96	2.91
avg				0.2270				3.050
σ								0.206
30 Percent Silica								
58	205	204	1.871	0.186	0.103	0.0758	1.42	1.87
61	121	119	1.756	0.186	0.0648	0.1141	1.70	1.49
avg				0.186				1.680
σ								0.269

1 driving force $=(P_{CO}\ a_0 - P_{CO_2})$; calculated using the avg. a_0 $(=CO_2/CO)$ at ea. SiO_2 level;

2 units for reduction rate are: [moles O /(m^2.sec)] X 1000

3 K_a is the rate constant for the rate expression: $R = k_a[P_{CO}a_0 - P_{CO_2}]$; units for k_a are: [mole O /(m^2.sec.atm)] X 100

* reducing gas in test 72 contained 28.6 percent Ar

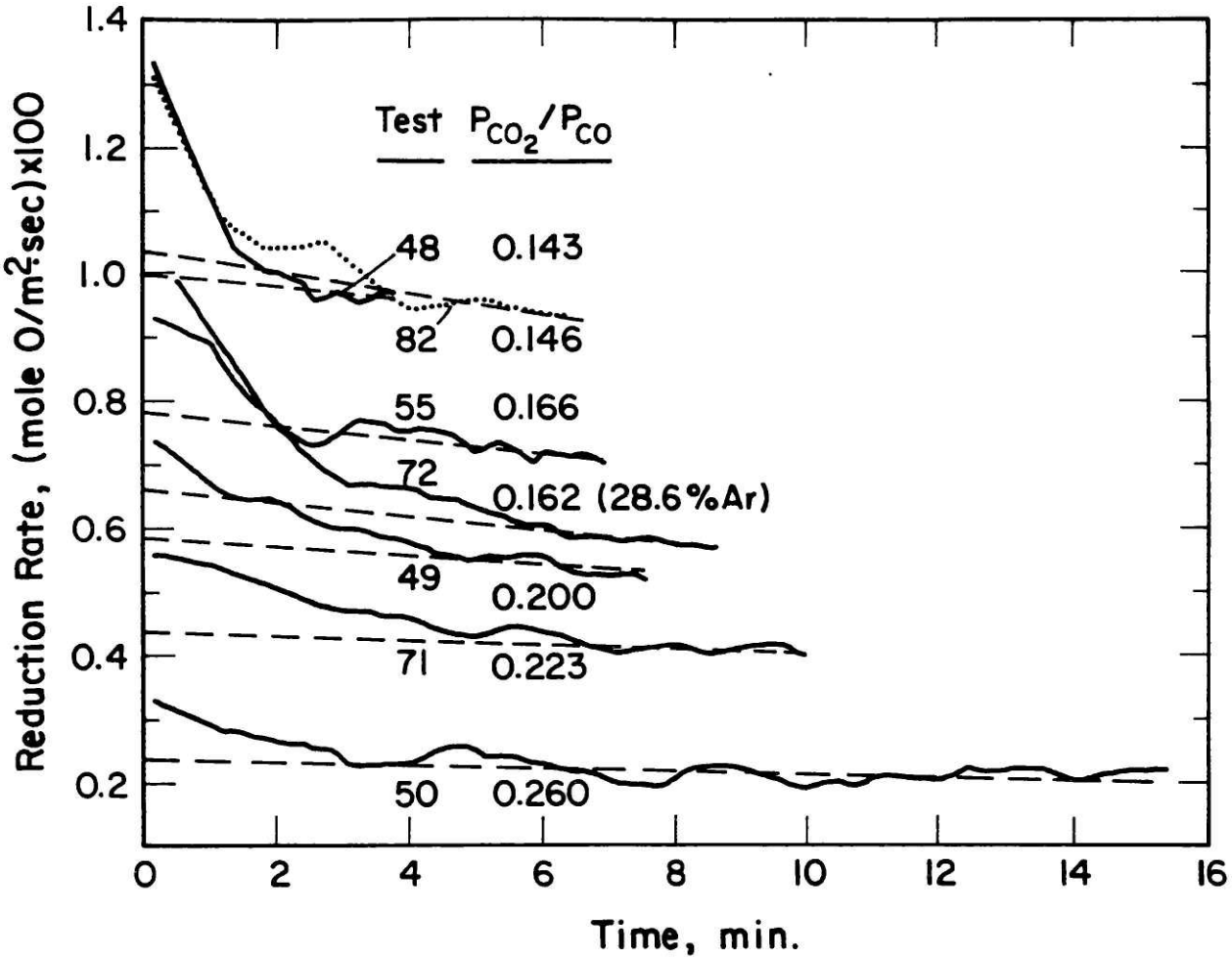

Figure 6-23. Reduction rate curves for the 12 percent silica melts reduced in iron crucibles.

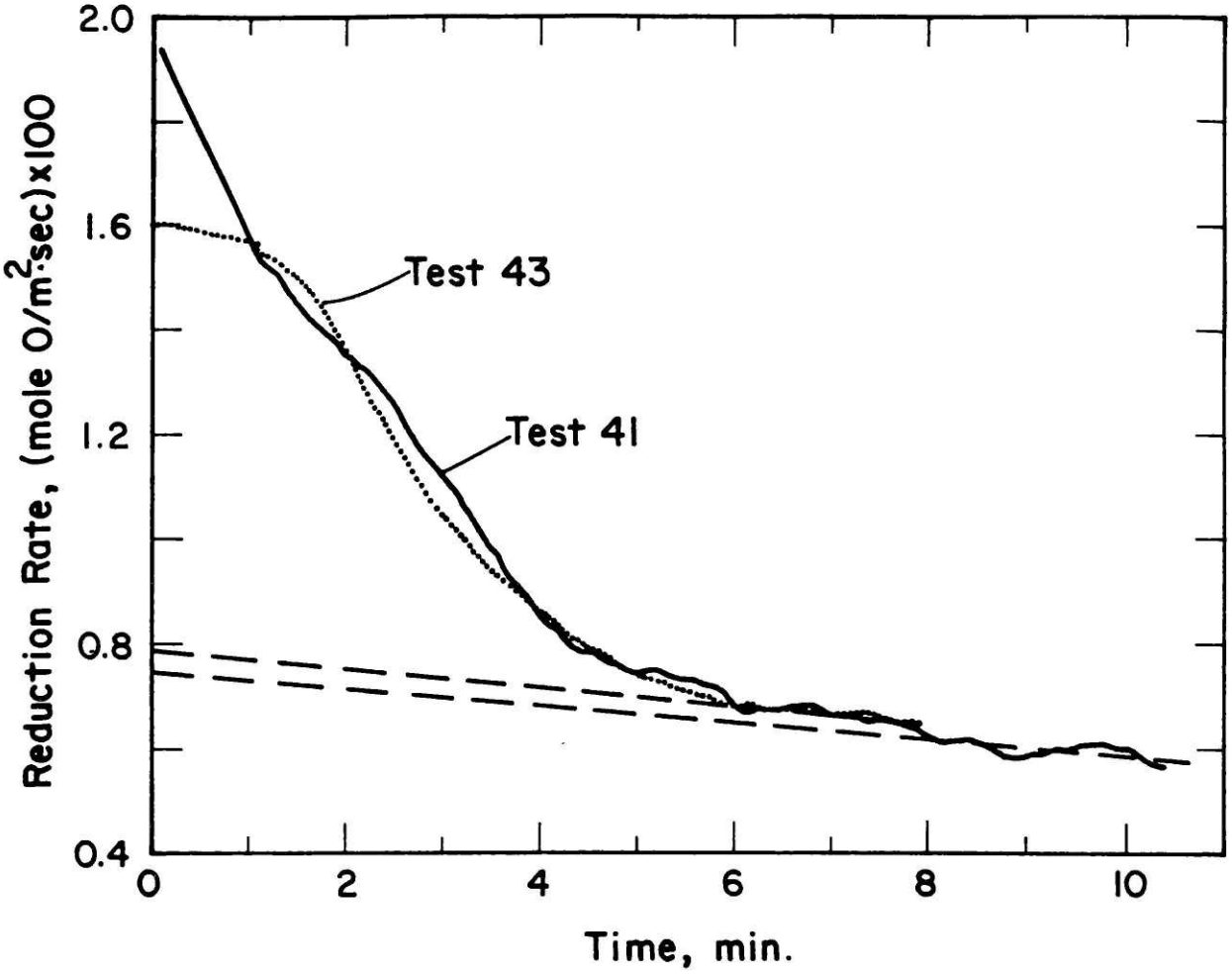

Figure 6-24. Reduction rate curves for 12.8 percent SiO_2 melts reduced in iron crucibles. 1300°C

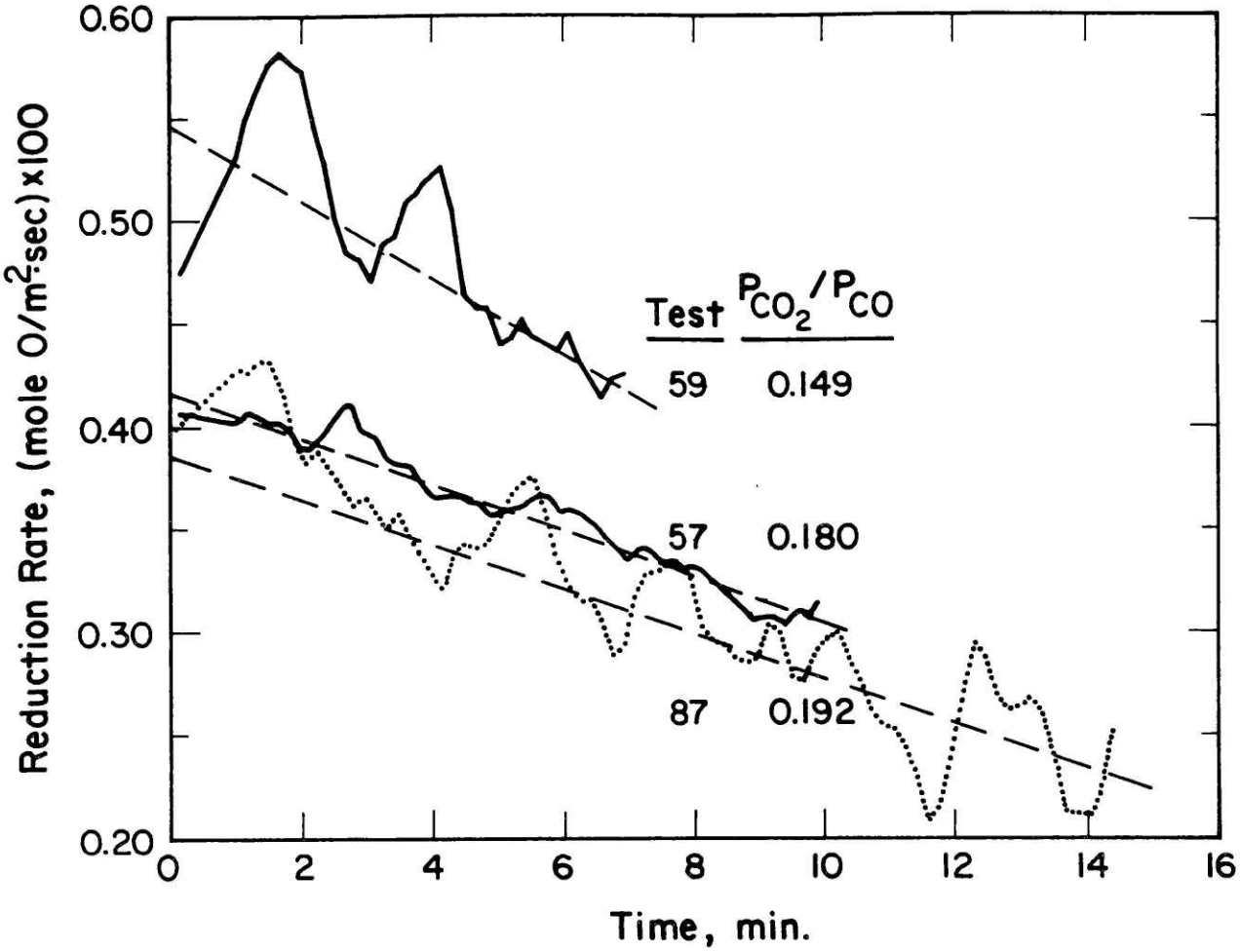

Figure 6-25. Reduction rate curves for 18 percent SiO_2 melts reduced in iron crucibles. 1300°C

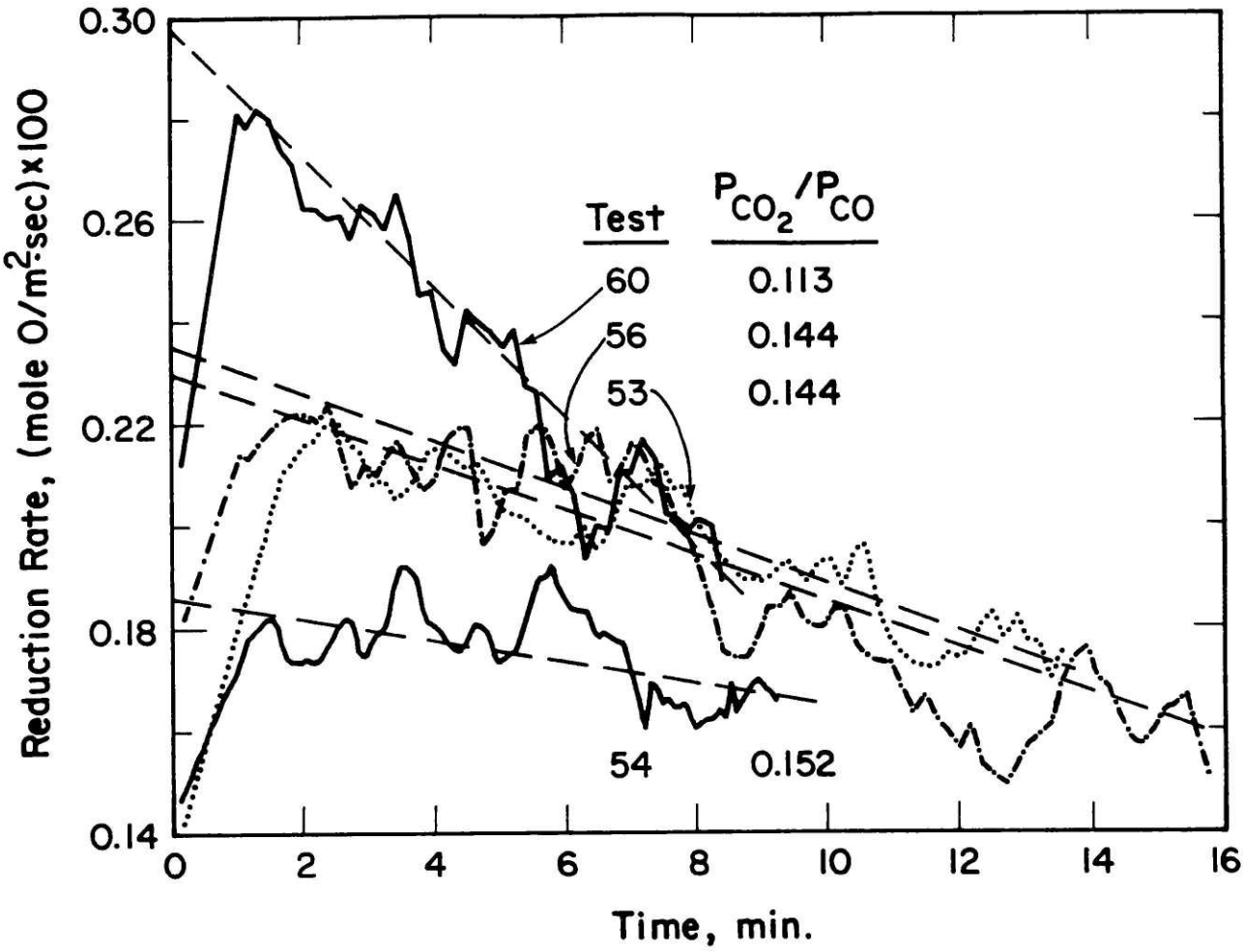

Figure 6-26. Reduction rate curves for 25 percent SiO_2 melts reduced in iron crucibles. 1300°C

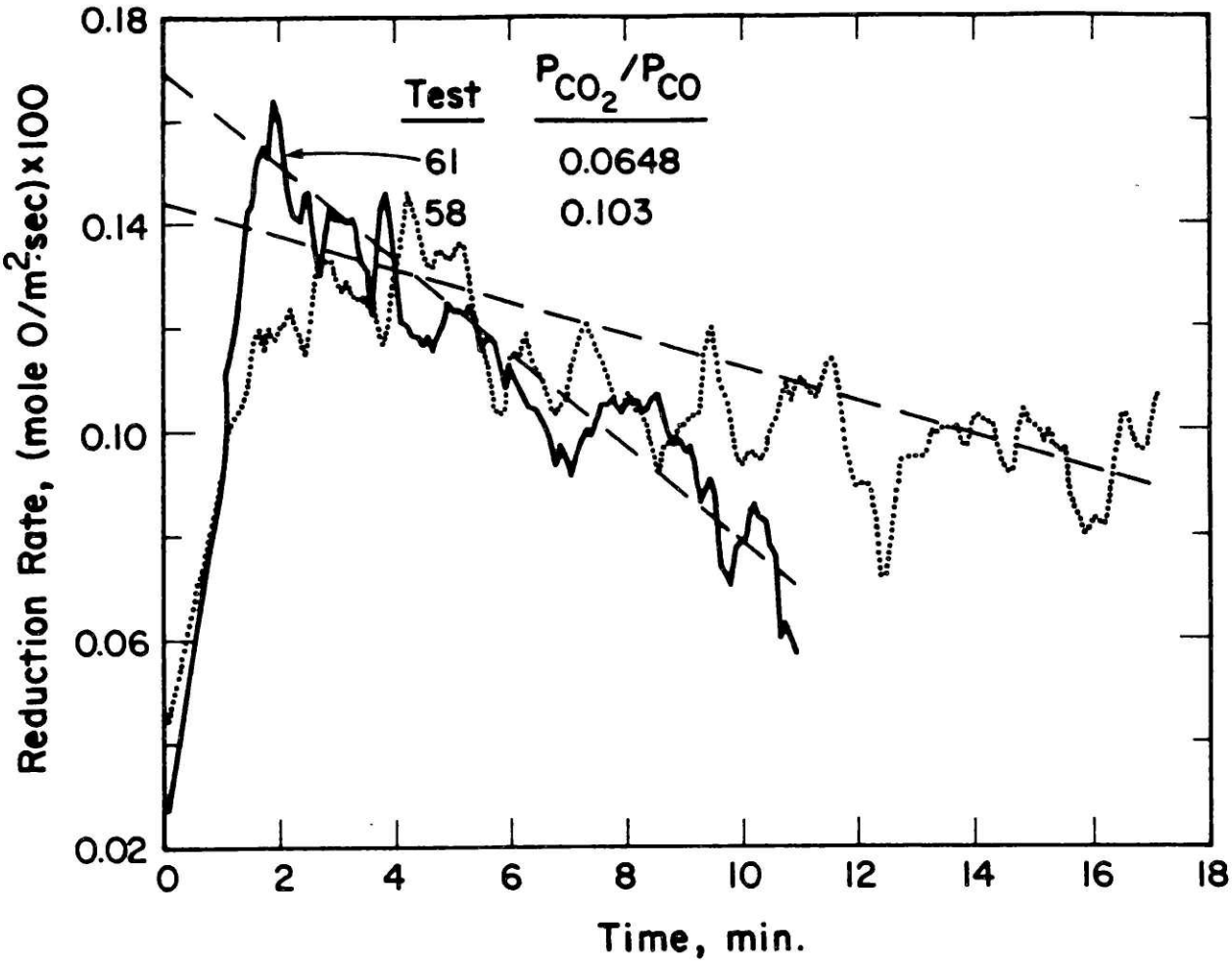

Figure 6-27. Reduction rate curves for 30 percent SiO_2 melts reduced in iron crucibles. 1300°C

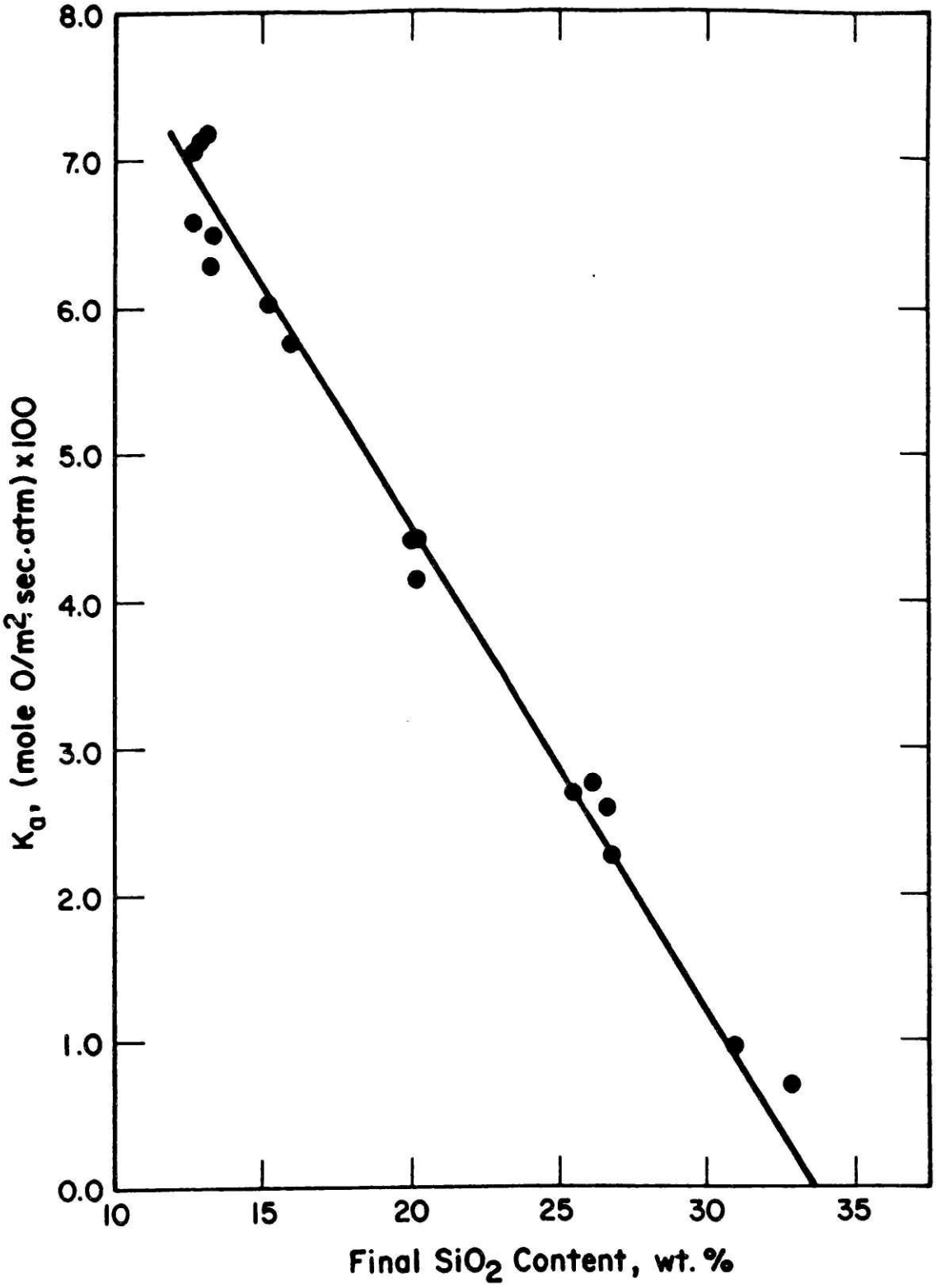

Figure 6-28. Relationship between the chemisorption rate constant k_a calculated from final reduction rates and SiO_2 content of melts at end of test.

of the melt. The reaction rate constant at time was determined using Figure 6-28 and the calculated silica contents of the melt as a function of time. The calculated reduction rates, shown in Figures 6-23 through 6-27, were then determined using equation (6-6) and the instantaneous reaction rate constants and thermodynamic driving forces.

Except in the early stages of the reaction, the calculated rates correlate well with the actual reaction rates. The early apparent reaction rates are greater than the calculated rates for the 12 and 12.8 percent silica melts because the apparent rates are based on the surface area of the main pool of slag. The effective reaction surface area is larger due to the extraneous slag that wet the iron on the inside of the crucible. However, the results indicate that after only a few minutes, the extraneous slag has no detectible effect on reduction rates.

The amount of extraneous slag present on the inside of the crucible is correlated in Figure 6-29 to the amount of iron surface inside the cup that is not covered by the main body of slag. The figure shows the relationship between the surface area of the main body of slag, expressed as a fraction of the total area in the crucible exposed to gas (slag plus iron), and the calculated initial rate, expressed as a ratio of the apparent initial rate for 12 and 12.8 percent silica melts. If the whole inside surface of the crucible is covered with slag, the points will fall on the 1:1 solid line shown in the figure. The iron sheets used to make the crucibles in the 12.8 percent silica

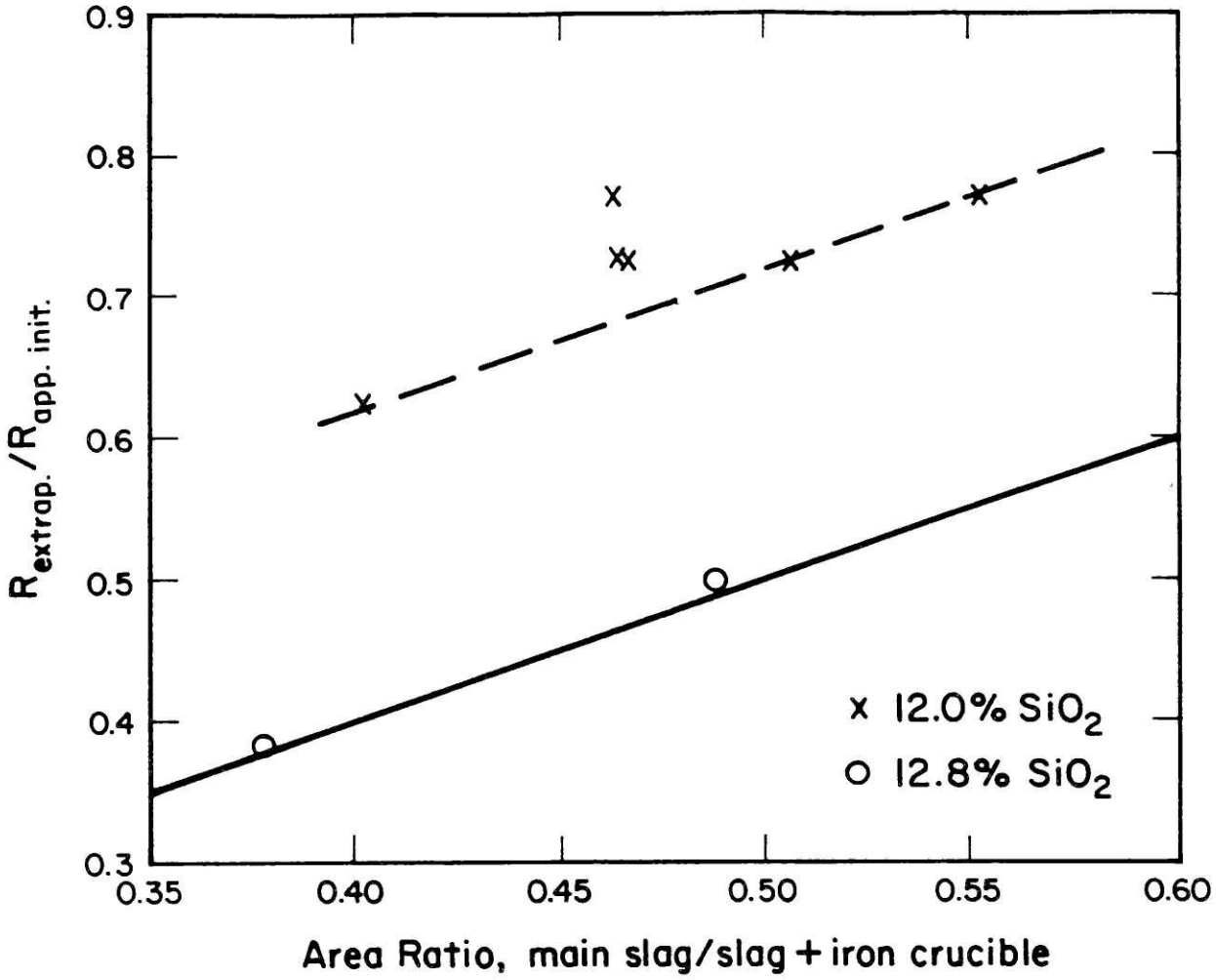

Figure 6-29. Relationship between apparent initial reduction rates and the amount of open iron surface on the inside of the crucible.

tests were dipped in hydrochloric acid to remove oxide and not polished before drawing to form the crucible. The iron surface was rough, and the slag spread completely over the inside of the crucible. In all of the remaining tests, the iron was polished before drawing into crucibles. Figure 6-29 shows that the extraneous slag in the 12 percent silica tests increases as the inside iron surface area increases. Only about 60 percent of the exposed iron in the inside of the cup is covered with slag at the start of the reduction.

The amount of extraneous slag that spread over the iron surface is calculated from the area between the actual and the calculated reduction rate curves in Figures 6-23 and 6-24. Typically, about 3 to 5 milligrams of slag spread over an area of iron of about 0.5 to 0.7 cm^2 on the inside of the crucible. The time needed to decrease the reduction rate of the extraneous slag to about 5 percent of the reduction rate of the main body of slag correlates well with the time at which the calculated and actual rates coincide. As the reaction proceeds, the observed rates and calculated rates match well, indicating that the reduction of the extraneous slag does not substantially contribute to the observed reaction rate during the later times of the tests.

At the higher silica contents, the early reduction rates are much lower than the calculated rates, indicating that the early reaction is not controlled by a chemisorption reaction step at the gas-liquid interface. The microscopic examination showed that the iron grain growth is localized on the iron crucible, so grain

growth may be controlling the early reactions. The early rates for these melts do not fit the models for nucleation and growth presented in Chapter 3.

Figure 6-30 shows how the extrapolated initial reduction rates are dependent on the thermodynamic driving force and silica contents of the melts, assuming that a chemisorption step controls the reaction. The slope of the lines is the average reaction rate constant from Table 6-2 for each of the melts.

Liquid-phase diffusion can be eliminated as a possible rate controlling step. Figure 6-31 shows how the extrapolated initial reduction rates are dependent on the thermodynamic driving force and silica contents of the melts assuming that diffusion in the liquid controls the reaction. Shown in the figure is the reaction rate obtained in test 72, in which the reducing gas contained 28.6 percent argon. If liquid phase diffusion was controlling the reaction, the rate for test 72 would be similar to the rates obtained for other 12 percent silica melts using gases of similar oxygen potential but containing no argon. Liquid phase diffusion is not controlling the reduction of the 12 percent silica melts.

The liquid phase diffusion control model is

$$R = (\rho\ D\ /\ K_e\ M\ \delta)\ [\ a_O\ (liq.) - a_O\ (gas)\ ] \qquad (6\text{-}7)$$

where ρ is the density of the melt, D is the interdiffusivity of iron and oxygen, K_e is the equilibrium constant for the reduction reaction, M is the molecular weight of FeO, and δ is the effective diffusion boundary layer thickness. The calculated boundary

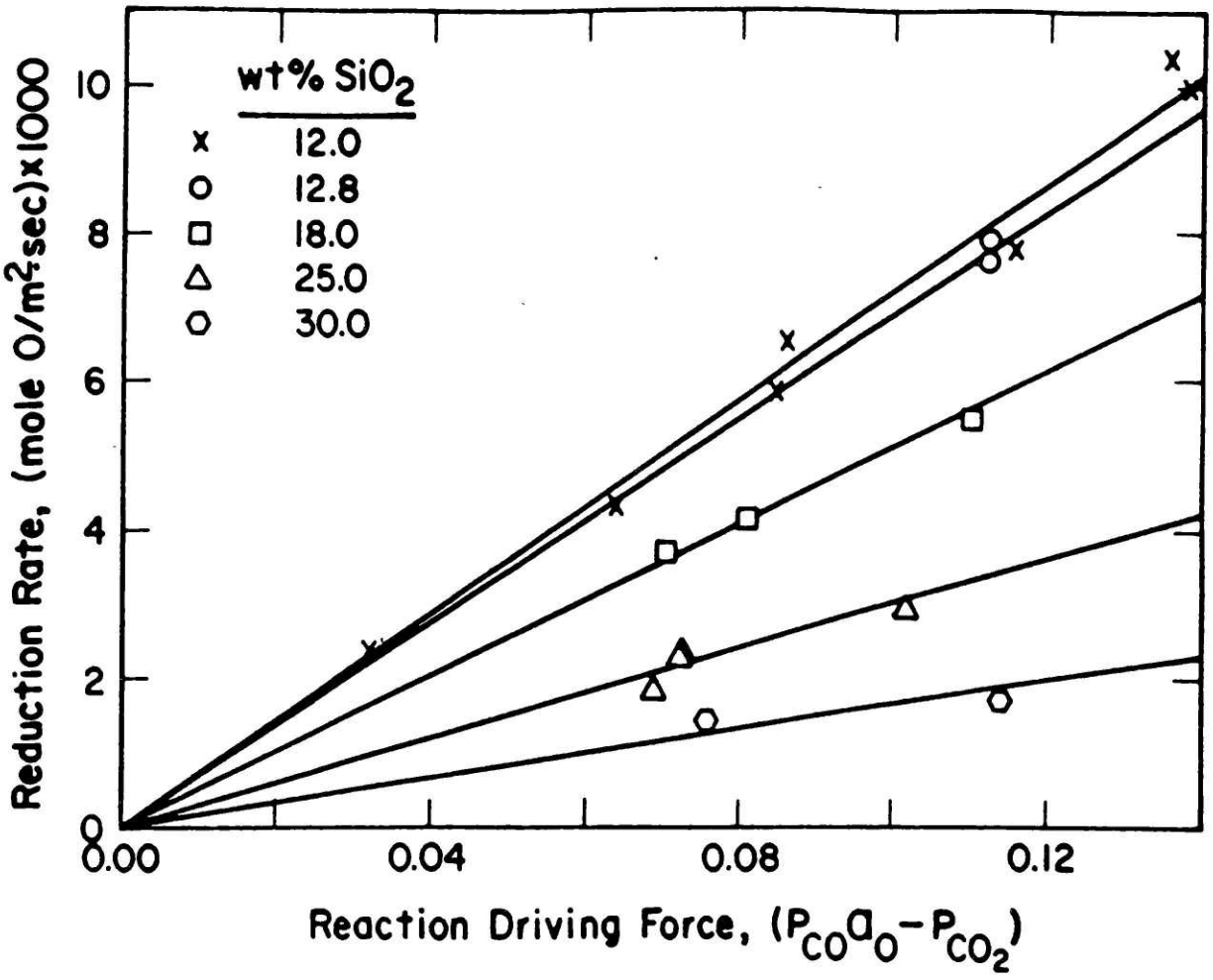

Figure 6-30. Reduction rate as a function of reaction driving force for different melts using the chemisorption model, equation (6-3).

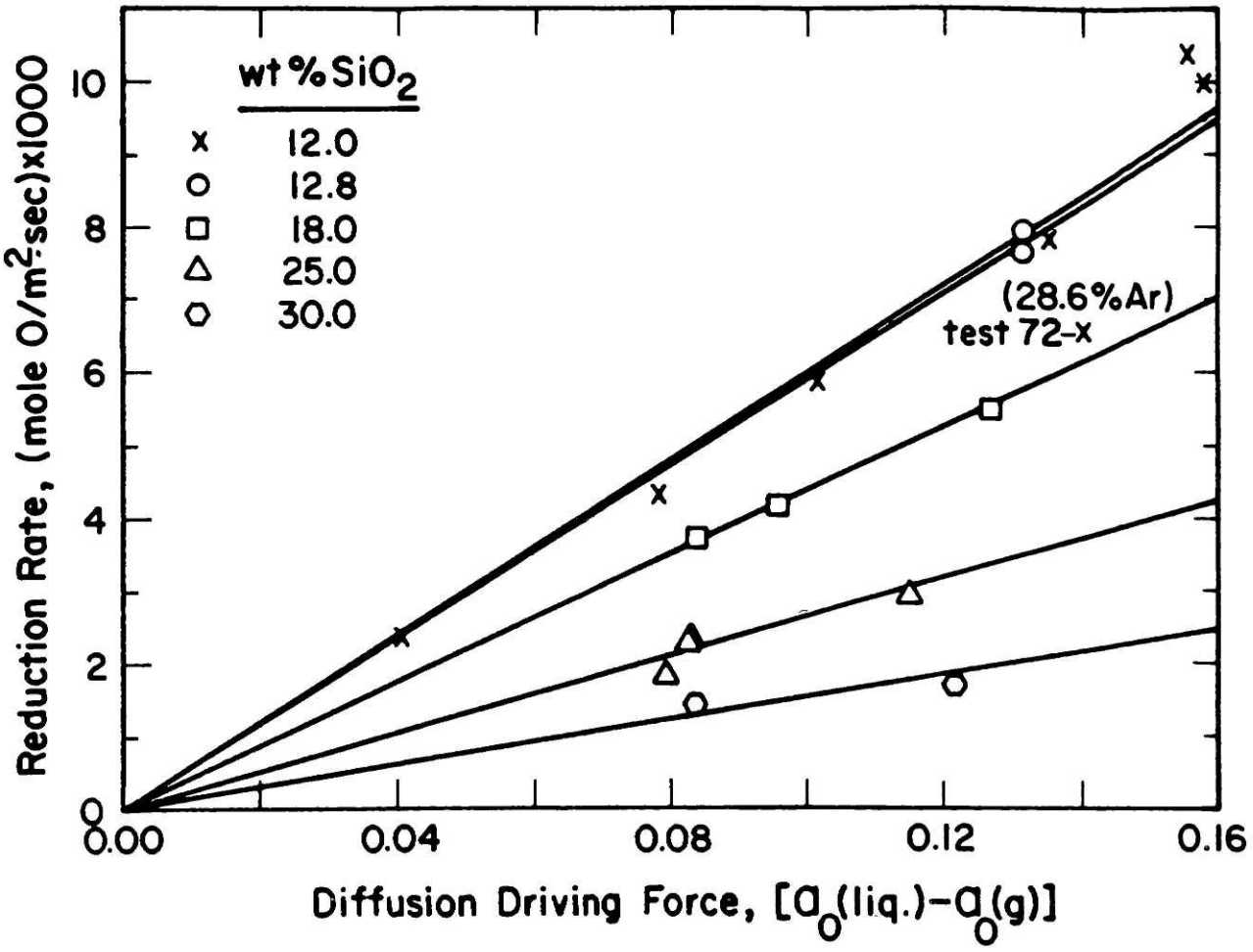

Figure 6-31. Reduction rate as a function of reaction driving force for different melts using the liquid-phase diffusion model, equation (6-7).

layer thickness for the 30 percent silica melts is 226 millimeters, using the interdiffusivity value of 2.15 X 10^{-8} m^2/sec determined by Mori and Suzuki (20) and Agrawal and Gaskell (19), a melt density of 3.93 Mg/m^3 determined by Gaskell and Ward (67), and 0.3314 for the equilibrium constant at 1300°C. Clearly, diffusion control is not limiting the reaction.

6.4.4 Tests Using Melts with P_2O_5 and CaO Additions

6.4.4.1 P_2O_5 Additions -- Some tests were conducted using the 12 and 25 percent silica mixtures with 1 to 3 mole percent P_2O_5 additions. Phosphates or phosphides are known to segregate strongly to interfaces in molten iron oxide and silicate systems (68, 69). Small phosphorous additions to the melt should decrease the observed reduction rates, if the reaction is controlled by a chemisorption step. Also, the effect of phosphorous on reactions involving the slag interface is of industrial interest because phosphorous is present in many commercial slags. The phosphorous was added to the base slag mixtures as calcined $2Fe_2O_3$-$(P_2O_5)_3$.

The tests on 12 percent silica melts containing 1 to 3 mole percent P_2O_5 were unsuccessful in providing quantitative results. The melt wet the iron crucibles so severely that reproducible results could not be obtained. Figure 6-32 shows a photograph of the cross-section of a crucible after a typical test containing a 12 percent silica melt with 2 mole percent P_2O_5. Although the lip of the iron cup was curled inward in an attempt to keep the melt in the cup, the slag migrated out of the cup and collected at the bottom of the crucible.

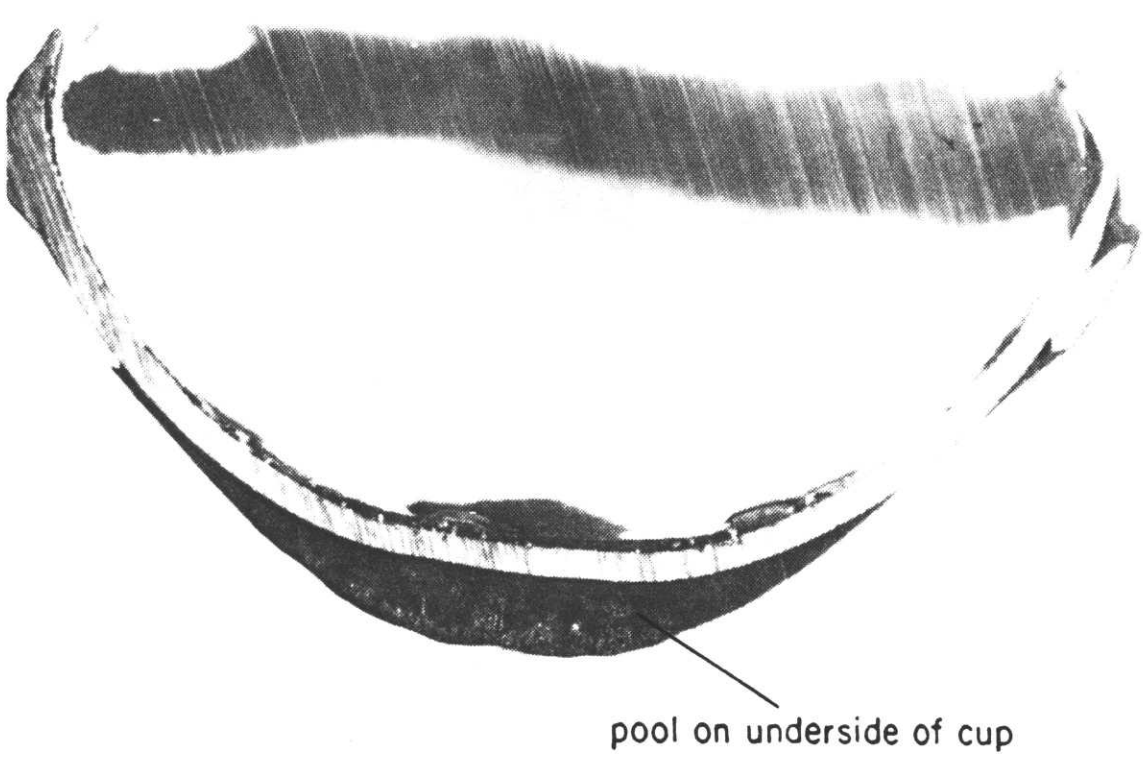

Figure 6-32. Cross-section of crucible and 12 percent SiO_2 melt with 2 mole percent P_2O_5 addition. Melt crept out of crucible and formed pool on underside of cup. 9.1X

Results using the 25 percent silica melts were only successful if the P_2O_5 additions were no greater than about 1 mole percent. Figure 6-33 shows the reduction curves obtained for the 25 percent silica melts containing 1 mole percent P_2O_5. The reduction behavior as indicated by shape of the curves is very similar to that obtained for melts containing 12 and 12.8 percent silica with no additions. The extraneous slag that spreads on the inside of the crucible eventually approaches equilibrium with the gas, and does not appreciably affect the reduction rates at later times.

In other tests in which the 25 percent silica melts with phosphorous additions were reduced at lower reduction potentials, the extraneous slag did not approach equilibrium with the gas during the time of the test. The extrapolated rates (dashed lines on the reduction rate curves) did not correlate with the actual rates that were observed in these tests. Either the extraneous slag was too voluminous to react to equilibrium within the time of the test, or the melt spread too quickly from the main body of slag, creating a constant supply of extraneous slag. The later explanation is supported by the fact that when the 25 percent silica melt with phosphorous additions is reduced under high reaction driving forces, the extraneous slag approaches equilibrium with the gas after only about 1.3 mg are lost from the sample (after about 10 minutes). Under low driving forces, the extraneous slag of the same melt does not equilibrate with the gas, even after 5 mg have been lost by reduction of the sample. The variability in the initial volume of the extraneous

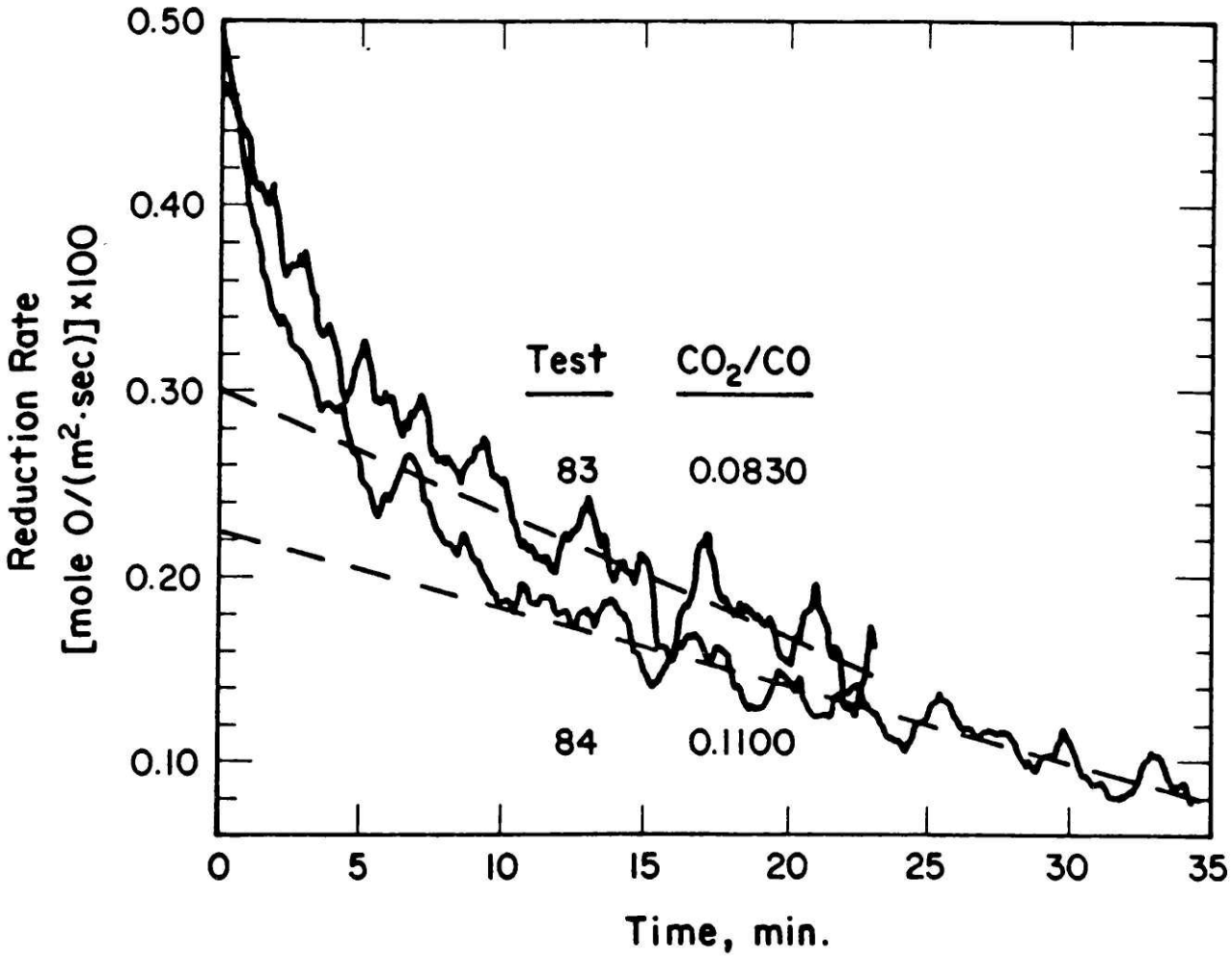

Figure 6-33. Reduction rate curves for 25 percent SiO_2 melts with 1 mole percent P_2O_5 additions. Dashed line: extrapolations from final rates based on calculated decrease in reaction driving force;

slag does not account for this discrepancy. Apparently, under low driving forces the extraneous slag is replenished from the main slag body faster than it can brought to equilibrium with the gas.

6.4.4.2 CaO Additions -- Calcia additions to iron-silicate melts decrease the activity of silica in the melt (48, 70), thereby decreasing the number of surface reaction sites occupied by silica. If the reduction is controlled by a chemisorption step, the observed reduction rates at constant silica levels should increase with calcia additions to the melt.

Dehydrated lime was added to new slag mixtures to make slags containing 22 and 35 weight percent silica with CaO/SiO_2 ratios of 0.311. Bodsworth's results (48) on the activity of FeO(l) in calcium-iron-silicate melts at iron saturation were used to determine the activity of silica in the melts by Gibbs-Duhem integration, using silica saturation as the reference silica activity. Higher CaO/SiO_2 ratios were not used because the activity of FeO(l) at silica saturation and higher CaO/SiO_2 ratios is not accurately known at 1300°C. Figure 6-34 shows the composition-activity relationships obtained for calcium-iron-silicates with CaO/SiO_2=0.311 at 1300°C.

Figure 6-35 shows the reduction rate curves obtained for the tests on each of the melts. The extrapolated rates shown in the figure were calculated as before, but the effect of composition on the reaction rate constant (k_a in equation 6-6) was determined

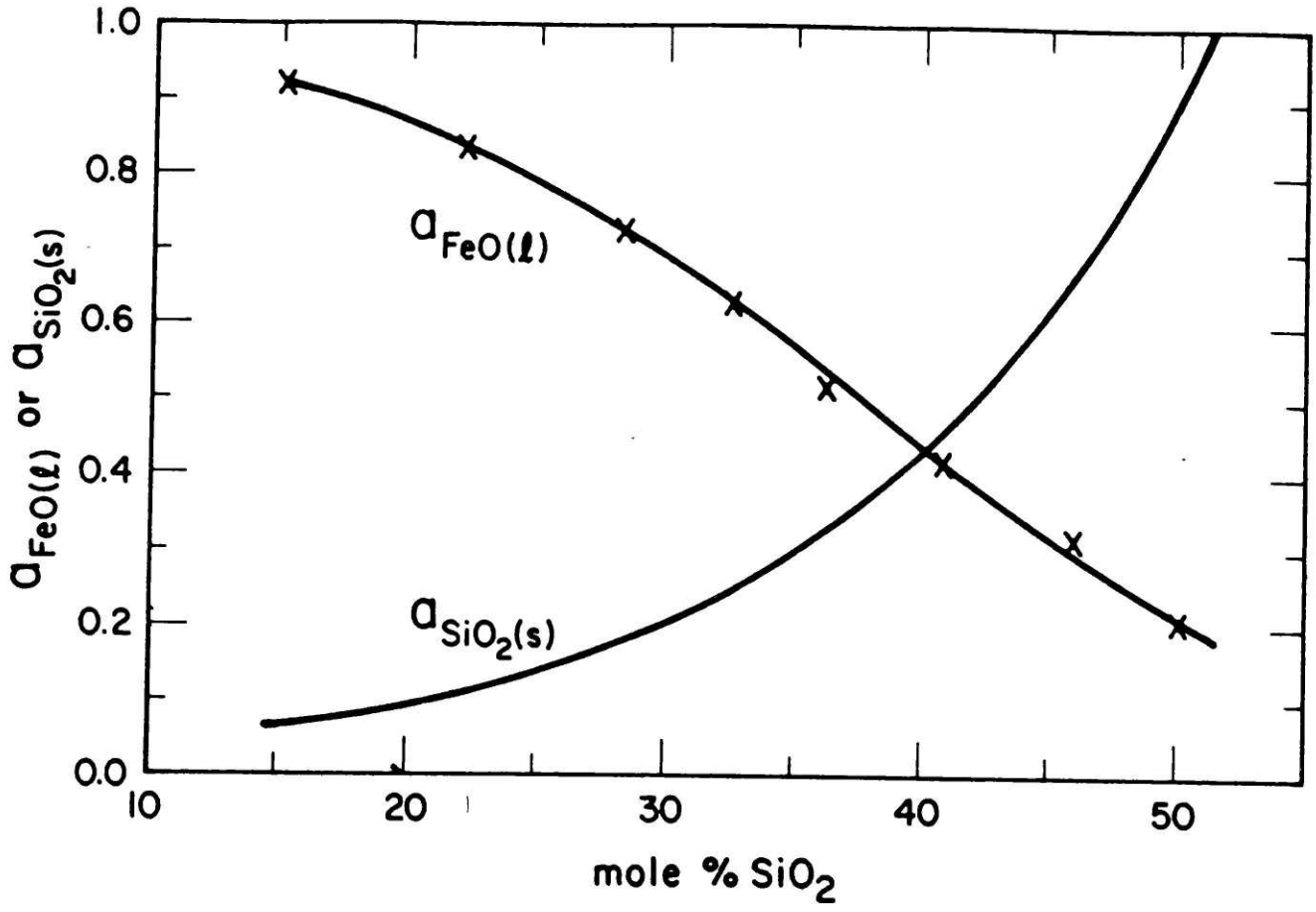

Figure 6-34. Activity-composition relation for CaO-FeO-SiO_2 melts at Fe saturation at 1300°C. CaO/SiO_2 = 0.333 , mole basis;

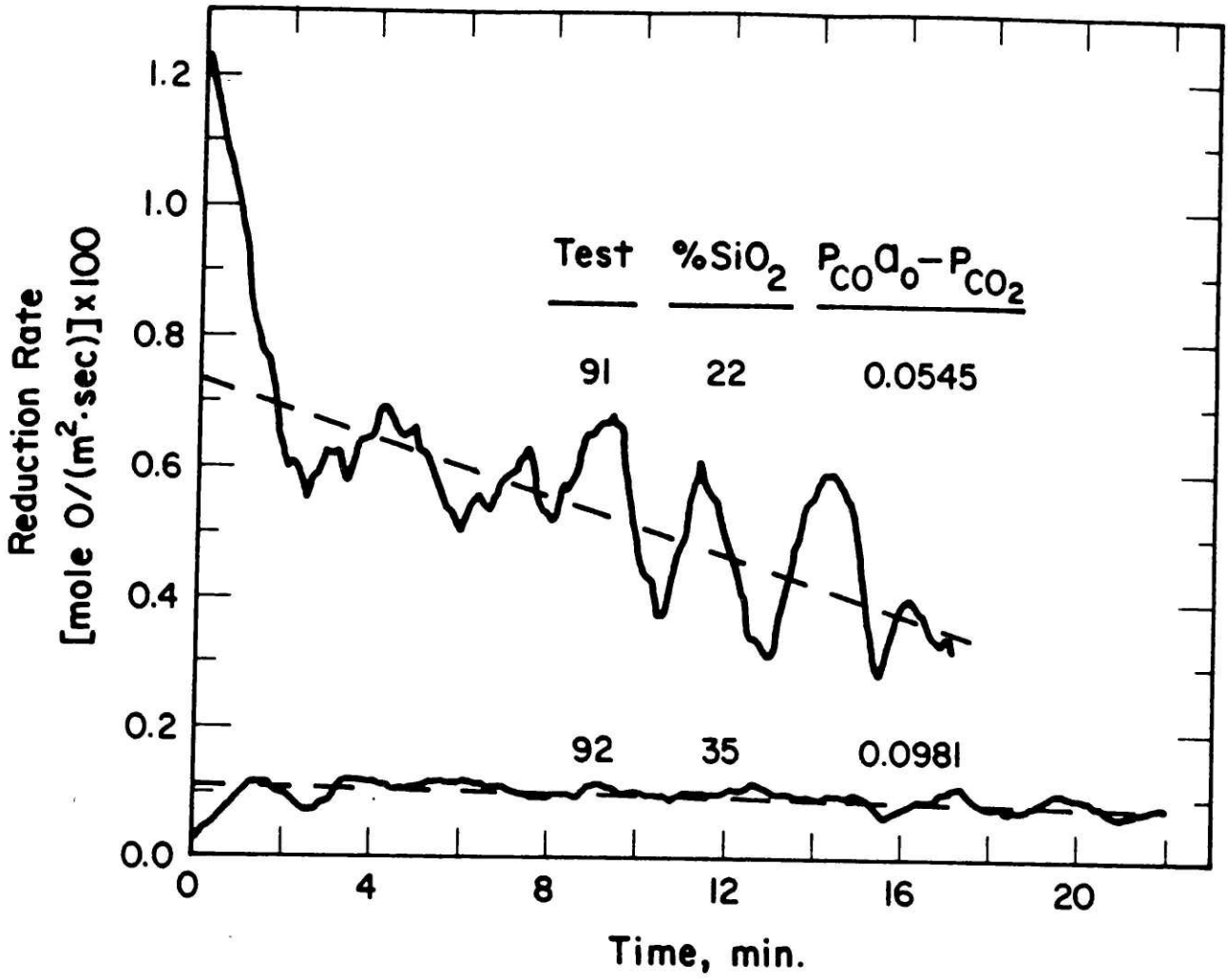

Figure 6-35. Reduction rate curves for melts with CaO/SiO_2 = 0.311; Dashed line: extrapolations from ending rates based on calc. decr. in reaction driving force;

from a plot of k_a versus the activity of silica (versus the percent silica used previously) of the final melts. The calculated extrapolated rates correlate well with the observed reaction rates after a few minutes into the test.

Table 6-3 summarizes the experimental parameters and results obtained with melts containing P_2O_5 and CaO additions. A 1 mole percent phosphorous addition to the 25 percent silica melt decreases the reaction rate constant 28 percent, from 0.0305 to 0.022 mole O /(m^2.sec). The reaction rate constant for an iron-silicate melt containing 22 percent silica is estimated at 0.038 mole O /(m^2.sec), and increases 96 percent to 0.0744 when 6.84 percent calcia replaces iron oxide. At the 35 percent silica level, an iron-silicate melt should have a reaction rate constant of about 0.013 mole /(m^2.sec). This compares with a reaction rate constant of 0.022 mole O /(m^2.sec) for a melt with the same silica content but containing 10.89 percent calcia.

6.5 Error Analysis

If dependent variable z is calculated from measured values x and y, and the errors in x and y, s_x and s_y, are independent, the error in z, s_z, is given by Baird (71) as

$$s_z = [\ (\partial z/\partial x)^2\ (s_x)^2 + (\partial z/\partial y)^2\ (s_y)^2\ ]^{1/2} . \qquad (6\text{-}8)$$

If z is a function of more variables, the equation is extended by adding similar terms. Unless noted, the errors used in the analysis are the estimate of the standard deviation of the

Table 6-3. Summary of Experimental Results and Conditions Using Iron-Silicate Melts Containing Phosphorous and Calcium Oxides

Run	Sample wt, mg start	Sample wt, mg end	Surface Area, cm^2	Equil. CO_2/CO	Reduction CO_2/CO	Driving Force, atm[1]	Rate[2]	k_a[3]
1 Mole Percent P_2O_5 and 25 Percent Silica								
83	241	235	1.334	0.226	0.0830	0.1323	3.00	2.27
84	196	188	1.340	0.226	0.110	0.1054	2.25	2.13
avg				0.226				2.20
CaO/SiO_2 = 0.311 (wt.% basis); 22 Percent Silica								
91	230	221	1.050	0.265	0.152	0.0981	7.3	7.44
CaO/SiO_2 = 0.311 (wt.% basis); 35 Percent Silica								
92	341	338	1.244	0.160	0.100	0.0545	1.2	2.20

1 driving force = $P_{CO}\ a_O - P_{CO_2}$; calculated using the avg. a_O ($=CO_2/CO$) for the melts

2 units for reduction rate are: [moles O /(m^2.sec)] X 1000

3 K_a is the rate constant for the rate expression: $R = k_a[P_{CO}a_O - P_{CO_2}]$; units for k_a are: [mole O/(m^2.sec.atm)]X100

population of measured values, s_x:

$$s_x = [\ \Sigma(x - x_{avg})^2 / n-1\ ]^{1/2} \quad , \qquad (6\text{-}9)$$

where, the x is each of the n independent readings, and x_{avg} is the average x value. If the standard deviation of the population of x is not known, but the range of probable values of x can be estimated, such as when values are extracted from a plotted relationship, Baird recommends that the estimated range of x be multiplied by 2/3 to obtain a value for the estimated standard deviation of x.

Table 6-4 summarizes the functions used to calculate the reaction driving force, reaction surface area, reaction rate, reaction rate constant, and the fraction of open surface reaction sites. Also shown in the table are approximate measurements and respective errors used to calculate reaction surface areas and the partial pressures of the gaseous species.

Table 6-5 shows the results of the error analysis. The values in the table will be used to compare the experimental results to the reaction-mechanism models in the next section, and are based on initial melt compositions and maximum reduction rates for tests 5 through 15 (MgO crucibles), and the calculated final melt compositions and reaction rates for all other tests.

The errors in the reaction driving forces are calculated from the errors in the partial pressures of the gas species and the errors in the calculated oxygen activities of the final melts. The

Table 6-4 Functions Used to Determine Calculated Values from Measured Values

I. Reaction Surface Area

a. $A = 2\pi rh = \pi p^2$

variables defined in Figure 5-1

$s_r = 0.11$ mm $r = 10$ mm
$s_h = 0.065$ mm $h = 2.5$ mm
$s_p = 0.024$ mm $p = 7.0$ mm

II. Reaction Driving Force

a. $P(CO) = Q(CO)P(t)/Q(CO_2)+Q(CO)$
b. $P(CO_2) = Q(CO_2)P(t)/Q(CO_2)+Q(CO)$

P(i)= partial pressures
P(t)= barometric pressure
Q(t)= flowrates determined from manometer calibrations

$s_{Q(CO)} = 1.5$ Nml/min
$Q(CO) \approx 230$ Nml/min
$sQ(CO_2) = 0.8$ Nml/min
$Q(CO_2) \approx 23$ to 60 Nml/min
$s_{P(t)} = 0.0013$ atm

c. $a_0 = P(CO_2)/P(CO)$ at equil.

d. $d.f. = P(CO)a_0 - P(CO_2)$

III. Reaction Rate

a. $R = R'/A$

R = final reduction rate
R' = absolute rate determined using the moving parabolic regression algorithm

IV. Reaction Rate Constant

a. $k_a = R / d.f.$

V. Fraction of Open Sites

a. $\theta_v = 1 /(1 + K_0 a(0) + K_{SiO_2} a_{SiO_2})$

$K_0 = 4$ $(s = 2.4)$
$K_{SiO_2} = 93$ $(s = 9)$

Table 6-5. Experimental Errors, Calculated Values, and Determined Errors in Calculated Values

Test	$s_{P(CO)}$ X1000 atm	$s_{P(CO_2)}$ X1000 atm	s_{a_O}	a_O	$s_{d.f.}$ atm	d.f. atm	Area cm^2	s_A cm^2	$s_{R'/A}$* X1000	s_R X1000	R X1000	sk_a X100	k_a X100	SiO_2 wt%	s_{SiO2} wt%	$s_{a_{SiO_2}}$	a_{SiO_2}	s_{θ_v} X100	θ_v X100
5	2.68	2.68	0.0005	0.2843	0.0030	0.101	2.56	0.16	0.14	0.19	5.7	0.25	5.67	17.0	0.8	0.071	0.19	1.8	5.1
6	2.67	2.67	0.0005	0.2843	0.0030	0.0977	2.56	0.16	0.14	0.18	5.3	0.25	5.42	17.0	0.8	0.071	0.19	1.8	5.1
8	2.56	2.56	0.0005	0.2843	0.0028	0.0649	2.56	0.16	0.07	0.11	3.8	0.31	5.85	17.0	0.8	0.071	0.19	1.8	5.1
9	2.51	2.51	0.0005	0.2843	0.0028	0.0458	2.56	0.16	0.14	0.15	2.7	0.49	5.89	17.0	0.8	0.071	0.19	1.8	5.1
10	2.51	2.51	0.0005	0.2843	0.0028	0.0458	2.56	0.16	0.07	0.09	2.52	0.38	5.45	17.0	0.8	0.071	0.19	1.8	5.1
13	2.77	2.77	0.0005	0.2843	0.0030	0.129	2.56	0.16	0.07	0.16	6.8	0.18	5.29	17.0	0.8	0.071	0.19	1.8	5.1
14	2.63	2.63	0.0005	0.2843	0.0029	0.0185	2.56	0.16	0.07	0.07	1.23	1.1	6.5	17.0	0.8	0.071	0.19	1.8	5.1
15	2.56	2.56	0.0005	0.2843	0.0028	0.0185	2.56	0.16	0.07	0.07	1.14	1.0	6.0	17.0	0.8	0.071	0.19	1.8	5.1
41	2.68	2.68	0.0033	0.284	0.0040	0.1003	1.478	0.034	0.07	0.15	5.8	0.28	5.79	15.95	0.15	0.0072	0.180	0.77	5.30
43	2.68	2.68	0.0032	0.289	0.0039	0.1045	1.451	0.036	0.07	0.18	6.5	0.29	6.27	15.20	0.14	0.0068	0.171	0.85	5.54
48	2.76	2.76	0.0031	0.298	0.0040	0.1356	1.622	0.036	0.05	0.22	9.6	0.29	7.08	12.85	0.11	0.0058	0.146	1.1	6.3
49	2.58	2.58	0.0031	0.296	0.0038	0.0800	1.460	0.036	0.05	0.14	5.3	0.36	6.68	13.31	0.11	0.0058	0.151	1.1	6.2
50	2.44	2.44	0.0031	0.299	0.0036	0.0310	1.555	0.035	0.05	0.07	2.00	0.78	6.45	12.70	0.11	0.0056	0.141	1.2	6.5
53	2.75	2.75	0.0047	0.218	0.0050	0.0647	1.582	0.037	0.03	0.05	1.60	0.21	2.47	26.15	0.11	0.020	0.400	0.18	2.56
54	2.73	2.73	0.0047	0.223	0.0049	0.0616	2.103	0.036	0.03	0.04	1.66	0.23	2.69	25.50	0.10	0.019	0.380	0.20	2.69
55	2.68	2.68	0.0031	0.297	0.0039	0.1123	1.625	0.035	0.05	0.16	7.1	0.27	6.30	13.20	0.11	0.0058	0.150	1.1	6.2
56	2.75	2.75	0.0046	0.214	0.0050	0.0612	1.072	0.037	0.03	0.07	1.72	0.26	2.81	26.58	0.13	0.021	0.415	0.17	2.47
57	2.64	2.64	0.0040	0.263	0.0043	0.0703	1.291	0.035	0.03	0.09	3.02	0.30	4.30	19.98	0.12	0.011	0.244	0.43	4.04
58	2.91	2.91	0.0045	0.179	0.0051	0.0689	1.871	0.035	0.04	0.04	0.90	0.12	1.31	30.92	0.12	0.030	0.608	0.10	1.72
59	2.74	2.74	0.0040	0.262	0.0044	0.0983	0.925	0.037	0.03	0.17	4.18	0.26	4.25	20.20	0.14	0.011	0.248	0.42	3.98
60	2.87	2.87	0.0046	0.214	0.0052	0.0907	1.178	0.033	0.03	0.06	1.87	0.14	2.06	26.76	0.14	0.022	0.421	0.17	2.44
61	3.09	3.09	0.0045	0.165	0.0054	0.0941	1.756	0.031	0.04	0.04	0.71	0.07	0.75	32.70	0.14	0.031	0.697	0.08	1.50
71	2.52	2.52	0.0031	0.299	0.0037	0.0621	1.646	0.035	0.05	0.10	4.06	0.42	6.54	12.60	0.11	0.0059	0.145	1.2	6.4
72	2.69	2.69	0.0032	0.295	0.0040	0.0817	1.364	0.034	0.04	0.15	5.69	0.39	6.96	13.61	0.12	0.0060	0.155	1.0	6.0
92	2.75	2.75	0.0031	0.297	0.0040	0.1318	1.440	0.035	0.05	0.23	9.28	0.28	7.04	13.18	0.12	0.0058	0.150	1.1	6.2
93	3.00	3.00	0.0047	0.202	0.0053	0.1099	1.334	0.036	0.05	0.07	1.45	0.09	1.32	28.05	0.14	0.021	0.470	0.18	2.20
94	2.88	2.88	0.0046	0.187	0.0051	0.0694	1.340	0.033	0.03	0.03	0.80	0.08	1.15	29.91	0.15	0.022	0.561	0.15	1.85
37	2.60	2.60	0.0039	0.262	0.0043	0.0587	1.172	0.035	0.05	0.08	2.31	0.32	3.94	20.20	0.12	0.011	0.248	0.42	3.98
91	2.73	2.73	0.0040	0.230	0.0045	0.0681	1.050	0.036	0.28	0.30	4.5	0.34	5.14	26.85	0.13	0.010	0.200	1.4	4.9
92	2.92	2.92	0.0052	0.149	0.0047	0.0445	1.244	0.038	0.05	0.06	0.83	0.13	1.87	36.25	0.12	0.026	0.410	0.28	2.52

Notes: Units for R (rate) = mole O /(m^2.sec)
Units for rate constants, k_a = mole O /(m^2.sec.atm)
* R'/A is the best estimate of error in the final reduction rates determined from reduction rate curves

errors in the partial pressures of the gaseous species were determined by applying equation 6-8 to equations II.a. and II.b. in Table 6-4. The errors in flowrates shown in Table 6-4 represent the standard errors of the estimates of the regression equations relating manometer height differences to gas flowrates.

The error in the oxygen activity of the melts tested in MgO crucibles is the standard deviation of the measured CO_2/CO ratios in equilibrium with the melt, determined prior to reduction in each test. For the other tests, the calculations of error in the oxygen activities of the final melts are based on the initial sample weights and silica contents, weight lost during reduction, composition-activity curves for the melts, and the equilibrium constant for the overall reaction. The estimated errors in the starting sample weights and the cumulative weights lost during the reactions are 0.7 and 0.1 mg respectively. The errors in the initial silica contents of the melts are estimated at 0.07 weight percent. To determine the errors in the activities of FeO(l) in the final melts, the estimated errors in the calculated final melt silica contents ($\%SiO_2 \pm s$) were projected onto the activity-composition curves. The errors in the activities of FeO(l) were then estimated, considering the estimated errors in the curves. The errors in the activities of FeO(l) in the melts increase from 0.006 at 13 percent silica, to 0.013 at 31 percent silica. The increase is related to the decreasing slope of the activity curve with silica level. The error in the equilibrium constant for the overall reaction was calculated assuming an

error of 85 J in the Gibbs free energy of reaction of 14450 J, and an error of 2K at the temperature of 1573 K. The equilibrium constant has a value of 0.3314 with an estimated error of 0.0027.

The errors in the final reduction rates are determined from the errors in the reduction curves and the errors in the reaction surface areas. The surface area of the melts in the tests using MgO crucibles is assumed to be independent of melt volume because the crucibles had vertical walls. The error in the surface area for these melts is 0.16 cm^2, and is the standard deviation of the measured surface areas of the nine tests. The errors in reaction surface areas for the other tests were determined by applying equation 6-8 to equation I.a., using the estimates of the measurement errors shown in Table 6-4. Approximate values for the measurements are shown in Table 6-4, but the actual measured values were used in the calculations.

The errors in the reduction rate curves near the end of the test, $s_{R'/A}$, were estimated from the scatter in the curves, and the fit of the extrapolated rates (dashed lines on the reduction curves), and are shown in Table 6-5. The variable R′ is the apparent weight lost per unit time, calculated from the raw reduction data. Applying equation (6-8) to equation III.a. in Table 6-4, the errors in the final reduction rates are calculated from

$$s_R = [(s_{R'/A})^2 + (R/A)^2 s_A^2]^{1/2} . \qquad (6\text{-}10)$$

The errors in the reaction rate constants were determined from the errors in the reaction driving forces and final reduction rates. The errors in the rate constants attributable to temperature were estimated using an activation energy of reaction of 174 kJ/mole provided by El-Rahaiby, et. al. (22), who studied the rates of isotopic exchange reactions on unsaturated melts in the $FeO-Fe_2O_3-SiO_2$ system.

The errors in the fraction of open reaction sites are determined by applying equation (6-8) to equation V.a. in Table 6-4. The errors in the adsorption coefficients, K_O and K_{SiO2}, are the standard deviations of the values calculated using the Gibbs-Langmuir adsorption isotherm. The errors in the activities of SiO_2 in the final melts are calculated from the ratios of X_O/X_{SiO2} in the melts, and ln aFeO(l) at each silica level and at silica saturation. These variables are used in Gibbs-Duhem integrations to calculate the silica activities.

6.6 Discussion of Results

6.6.1 Determination of the Rate Limiting Step

The calculated rate constants for the final melt compositions are compared to the derived rate constants for each of the proposed reaction steps shown in Table 3-2 to determine which of the steps is controlling the overall reaction. The rate constants, k_a, are based on the general chemisorption rate expression:

$$R = k_a [P_{CO} a_O - P_{CO_2}] . \qquad (6-11)$$

Depending on the reaction step that is controlling the overall reaction, the rate constant may be a function of the oxygen activity of the melt (a_O), the concentration of ferrous iron in the melt ($C_{[Fe^{2+}]}$, moles/cm^3), and/or the partial pressure of CO in the reducing gas. All of the derived rate constants are a function of the fraction of vacant reaction sites on the surface of the melt, θ_v, except step II.h. in Table 3-2:

$$3\ [Fe^{2+}] = 2\ [Fe^{3+}] + Fe(\gamma)\ . \qquad (6\text{-}12)$$

The fraction of vacant reaction sites are calculated using

$$\theta_v = 1\ /\ (\ 1 + K_O a_O + K_{SiO_2} a_{SiO_2}\ ) \qquad (6\text{-}13)$$

or

$$\theta_v = 1\ /\ (\ 1 + K_{SiO_2} a_{SiO_2}\ )\ . \qquad (6\text{-}14)$$

If the only adsorbed species in the the rate controlling step being evaluated is oxygen, equation (6-14) is used because the only surface sites not available for adsorption in this case are occupied by silica. The adsorption coefficients, K_i, in the equations are estimated in Chapter 4 to be 4 and 93 for oxygen and silica, respectively.

To compare the observed rates to the rate expressions for the various models, the experimental rate constants are multiplied or divided by the appropriate independent variables (a_O, $C_{[Fe^{2+}]}$, or P_{CO}) and plotted on the ordinate, and the corresponding fraction of vacant reaction sites raised to the first or second power are plotted on the abscissa. The slope of the line through the experimental points should be constant, and is equal to a function of the forward rate constant for the rate controlling

step and the equilibrium constants for the preceding and subsequent steps in the reaction mechanism.

An example of the procedure is made by assuming that step II.b. of Table 3-2 is controlling the overall reaction:

$$CO\ (ads.) + O^{2-}\ (ads.) = CO_2^{2-}\ (ads.) + v \quad . \quad (6\text{-}15)$$

The derived rate constant for the step is

$$k_a = \beta\ (\theta_v)^2 / (C_{[Fe^{2+}]}) \quad . \quad (6\text{-}16)$$

If step II.b. is rate limiting, a plot of $k_a(C_{[Fe^{2+}]})$ versus $(\theta_v)^2$ for the melts will pass through the origin and have a constant slope equal to β.

The results of Nagasaka, Iguchi, and Ban-ya (6), and El-Rahaiby, Sasaki, Gaskell, and Belton (22) are included in the comparisons because the studies are closely related and complementary to this study. Nagasaka, et. al. reduced iron-silicate melts held in iron crucibles under 10% CO and argon at 1270 to 1400°C. El-Rahaiby, et. al. used an isotopic exchange technique to study the rate of dissociation of CO_2 on the surface of unsaturated ($a_O = 1$) iron-silicate melts that were at equilibrium with the gas at temperatures from 1250 to 1400°C. If the rate expression contains $C_{[Fe^{2+}]}$, the concentration of ferrous iron in the bulk, the results on melts not saturated with iron will have a rate expression with $(Fe^{3+}/Fe^{2+})^2$ substituted for $C_{[Fe^{2+}]}$ for the same rate controlling reaction. (The term $C_{[Fe^{2+}]}$ is actually $C_{[Fe^{2+}]}/a_{Fe}$ in the rate expression derivations.) So, for such

models the results of El-Rahaiby, et. al. can not be compared directly to the others. Temperature adjustments to the rate results of Nagasaka, et. al. and El-Rahaiby, et. al. were made using the activation energies of reaction reported in the respective studies. The activity of silica in the unsaturated melts are determined from Figure 4-15, which shows the oxygen isobars and iso-activity lines of FeO(l) and SiO_2(s) across the liquidus region at 1300°C in the system $FeO-Fe_2O_3-SiO_2$. El-Rahaiby, et. al. described their melts using only oxygen activities and silica contents, so the compositions of the unsaturated melts were also estimated using Figure 4-15.

The densities of the liquids are needed to calculate the concentrations of ferrous iron in the melts. The densities used are those of Gaskell and Ward (67), and Kawai and Mori, et. al. (58) for iron-saturated melts at temperatures up to 1430°C. The densities of the unsaturated melts are estimated assuming that the change in density of iron-silicates with oxygen additions is proportional to the change in density of pure liquid iron oxide with oxygen additions. The assumption is reasonable because structure-related properties of liquid iron oxide and iron silicates are very similar. For example, the thermal expansion coefficients for liquid iron oxide determined by Mori and Suzuki (72) are in close agreement with those of liquid iron-silicates (58). Also, the interdiffusivity of FeO in liquid iron oxides is close to that in iron-silicates (19, 20). The specific relationship used to estimate the density of the unsaturated melts is:

$$\rho_{r1} = \rho_{r2} \times (\rho_{FeO(l),\, r1} / \rho_{FeO(l),\, r2}) , \qquad (6\text{-}17)$$

where ρ_{r1} is the density of the unsaturated silicate, ρ_{r2} is the density of the silicate at iron saturation, and $\rho_{FeO(l),\ r}$ is the density of liquid iron oxide at r1 and r2, in which

$$r = Fe^{3+} / \text{total Fe} . \qquad (6\text{-}18)$$

Table 6-6 and 6-7 show the values used to evaluate the models. Other values are shown in Table 6-5.

Figures 6-36 through 6-39 show comparisons of experimental results to the adsorption reaction models, I.a. through I.d. of Table 3-2, respectively. In Figure 6-36, the results of Nagasaka, et. al. (6) indicate that adsorption of CO may be the rate limiting reaction step. But the results of El-Rahaiby, et. al. (22) using the isotopic exchange technique on relatively oxidizing melts, show a much different relationship than the results on melts at iron saturation. The possibility that CO adsorption is controlling the reaction on iron saturated melts but not on unsaturated melts is unlikely. Also, the results on iron-saturated melts reduced in CO_2-CO show that the step is not controlling the reaction because the straight line through the experimental points does not pass through the origin. If this step is controlling the reaction, the adsorption of CO, and thus the reaction, would proceed only if more than about 1 percent of the reaction sites were available for adsorption. This behavior is also not likely, so the possibility that CO adsorption is controlling the reaction is dismissed.

Table 6-6 Values Used to Evaluate the Chemisorption Models

Test	Density g/cm^3	wt. % Fe_2O_3	$C_{[Fe^{2+}]}$ $moles/cm^3$
5-15	4.20	4.75	0.0457
41	4.28	4.90	0.0471
43	4.29	5.22	0.0475
48	4.37	6.29	0.0492
49	4.35	6.07	0.0488
50	4.37	6.36	0.0492
53	4.06	1.70	0.0408
54	4.05	1.84	0.0410
55	4.35	6.12	0.0488
56	4.05	1.61	0.0405
57	4.19	3.39	0.0447
58	3.95	0.93	0.0375
59	4.18	3.31	0.0445
60	4.05	1.59	0.0404
61	3.95	0.90	0.0365
71	4.39	6.41	0.0495
72	4.35	5.93	0.0487
82	4.36	6.13	0.0490
83	4.03	1.25	0.0397
84	4.00	0.93	0.0385
87	4.18	3.31	0.0445
91	3.85	1.00	0.0342
92	3.71	0.40	0.0269

Table 6-7 Values from the Studies of Nagasaka, et.al.(6), Sasaki, et.al.(21), and El-Rahaiby, et. al.(22) Used to Evaluate the Chemisorption Models

wt. % SiO_2	a_O	a_{SiO_2}	k_a*	wt. % Fe_2O_3	density g/cm^3	$C_{[Fe^{2+}]_3}$ mole/cm^3	$\left(\frac{Fe^{3+}}{Fe^{2+}}\right)^2$
Nagasaka, et. al., 1300°C							
16.7	0.282	0.190	6.8	4.60	4.26	0.0467	
22.3	0.247	0.295	5.1	2.67	4.13	0.0431	
26.1	0.219	0.400	3.8	1.72	4.06	0.0408	
28.9	0.195	0.510	3.4	1.20	4.02	0.0391	
31.6	0.211	0.640	2.8	0.86	3.98	0.0374	
Nagasaka, et. al., 1400°C							
4.2	0.256	0.053	35.6	7.64	4.39	0.0539	
7.9	0.250	0.098	28.5	6.18	4.26	0.0509	
16.7	0.228	0.189	17.3	3.36	4.00	0.0445	
22.4	0.200	0.296	9.8	2.03	3.86	0.0406	
26.2	0.179	0.396	9.0	1.35	3.78	0.0381	
29.0	0.161	0.495	8.9	0.96	3.70	0.0361	
31.7	0.142	0.614	7.6	0.68	3.63	0.0321	
El-Rahaiby, et. al., 1300°C, unsat. Fe-silicates							
11.5	1.0	0.160	3.9	13.5	4.01		0.0273
20.0	1.0	0.280	2.8	9.6	3.83		0.0161
30.0	1.0	0.640	1.8	5.6	3.69		0.0061
36.0	1.0	0.900	1.6	3.3	3.67		0.0022
38.7	0.85	1.000	1.3	2.4	3.67		0.0011
Sasaki, et.al. , 1420°C, FeO (1)							
	3.85		2.1	36.6	3.84		0.118
	2.01		5.8	29.8	3.90		0.0690
	1.72		6.9	27.9	4.01		0.0588
	1.70		6.3	27.9	4.01		0.0588
	1.22		8.3	24.0	4.10		0.0408
	1.01		10.2	22.0	4.14		0.0331
	1.00		9.6	22.0	4.15		0.0329
	0.94		13.2	21.8	4.17		0.0322
	0.85		13.5	21.7	4.18		0.0319
	0.68		14.1	17.7	4.28		0.0200
	0.51		21.4	14.9	4.38		0.0135
	0.46		25.1	13.6	4.41		0.0110
	0.42		27.5	12.9	4.47		0.0098
	0.38		30.9	11.7	4.48		0.0080
El-Rahaiby, et. al., 1420°C, CaO-FeO-SiO_2 (equimolar)							
32.0	12.0	0.192	1.4	13.7	2.82		0.360
32.0	10.0	0.184	1.6	13.2	2.82		0.313
32.0	8.0	0.181	1.9	12.6	2.83		0.270
32.0	6.0	0.178	2.4	12.0	2.84		0.238
32.0	4.0	0.175	3.2	10.9	2.88		0.162
32.0	2.0	0.168	5.4	9.1	2.92		0.0900
32.0	0.5	0.160	14.8	6.0	3.11		0.0346

* Units for k_a are [mole O /(m^2.sec.atm)] X 100

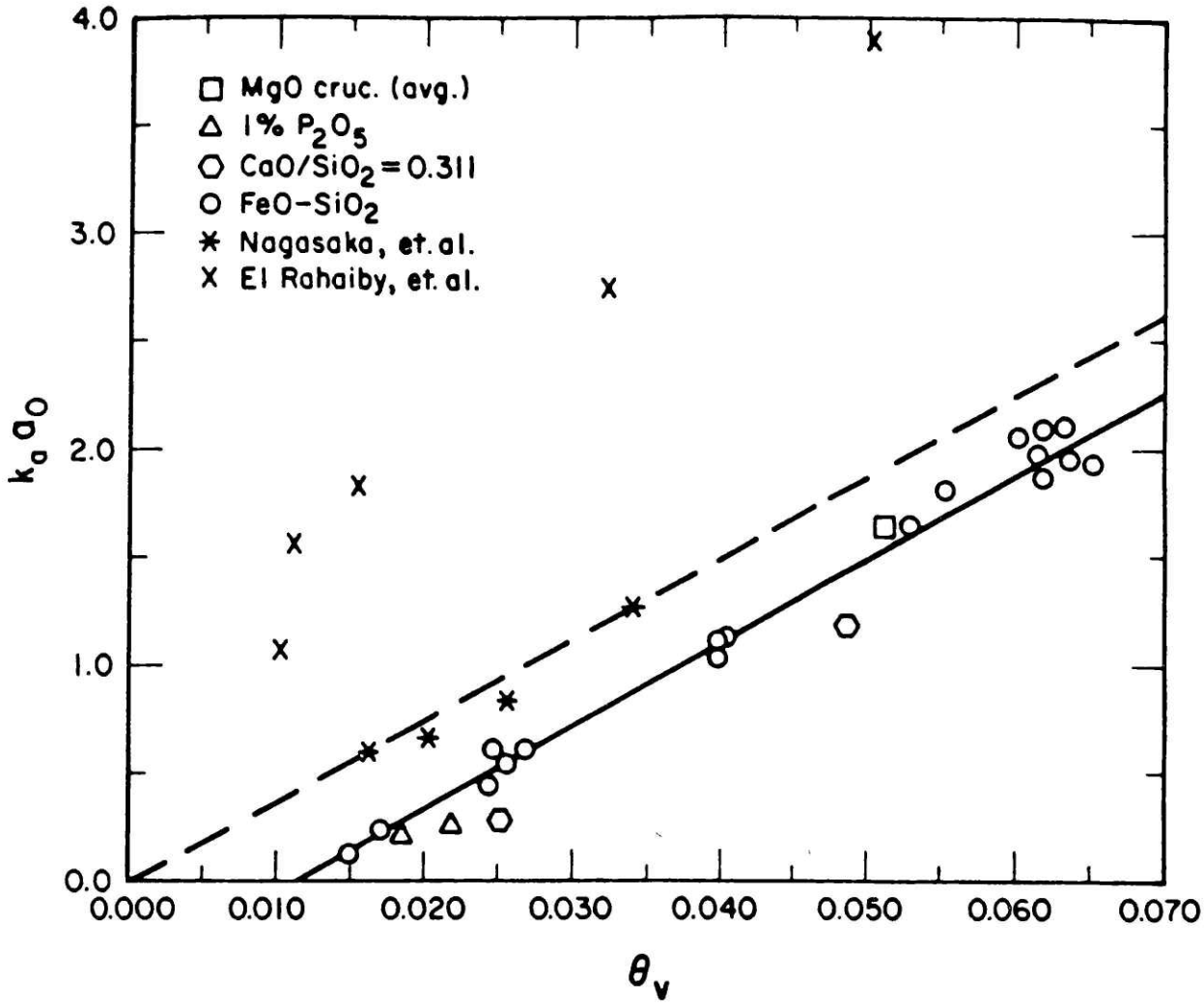

Figure 6-36. Comparison of Experimental Results to Model I.a. in Table 3-2. ordinate: [mole O /(m^2.sec.atm)] X 100; abscissa: equation (6-14)

CO (g) + v = CO (ads);

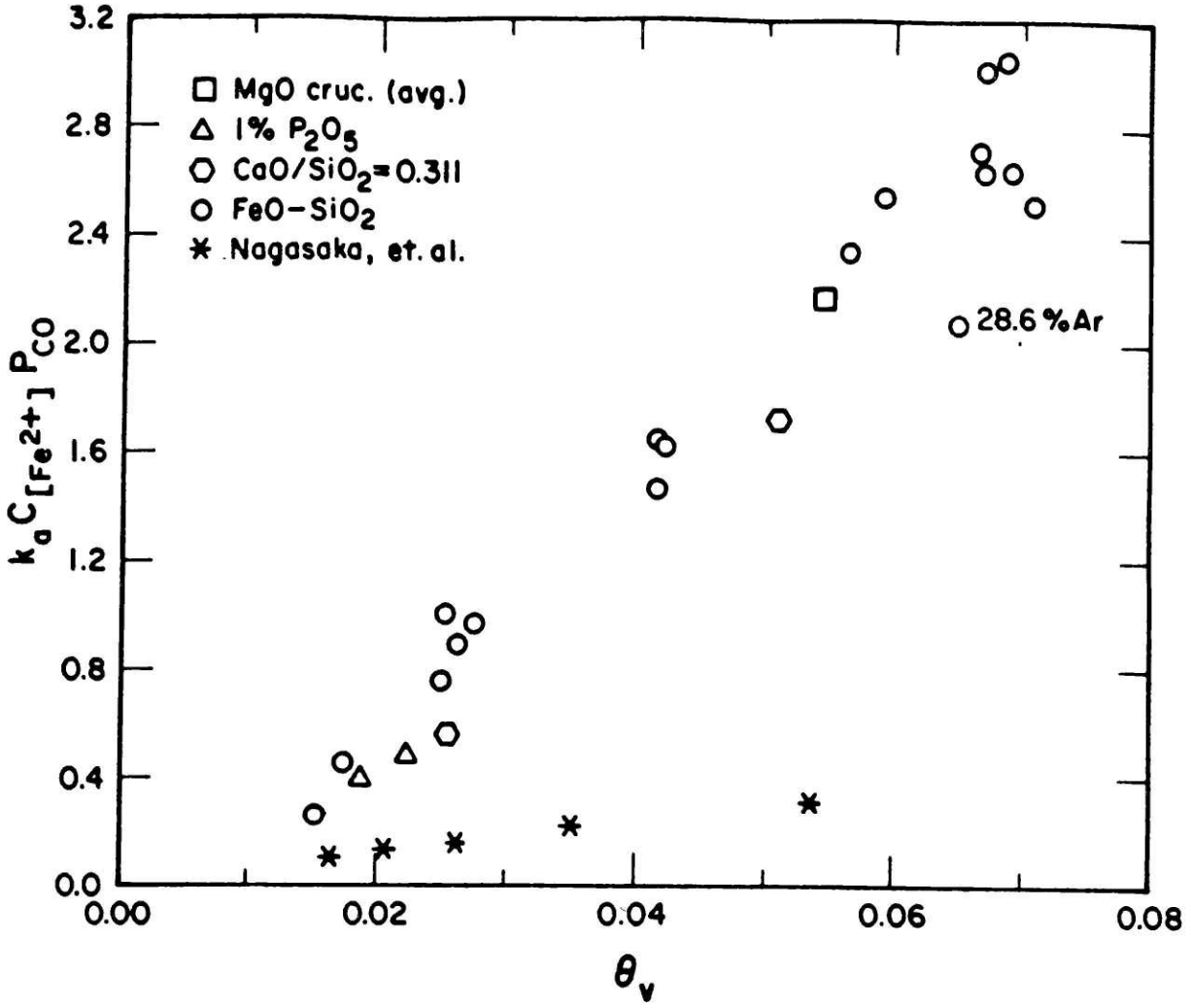

Figure 6-37. Comparison of Experimental Results to Model I.b_3 in Table 3-2. ordinate: [mole FeO /(m^5.sec)] X 10^{-3}; abscissa: equation (6-14);

$[O^{2-}] + v = O^{2-}$ (ads)

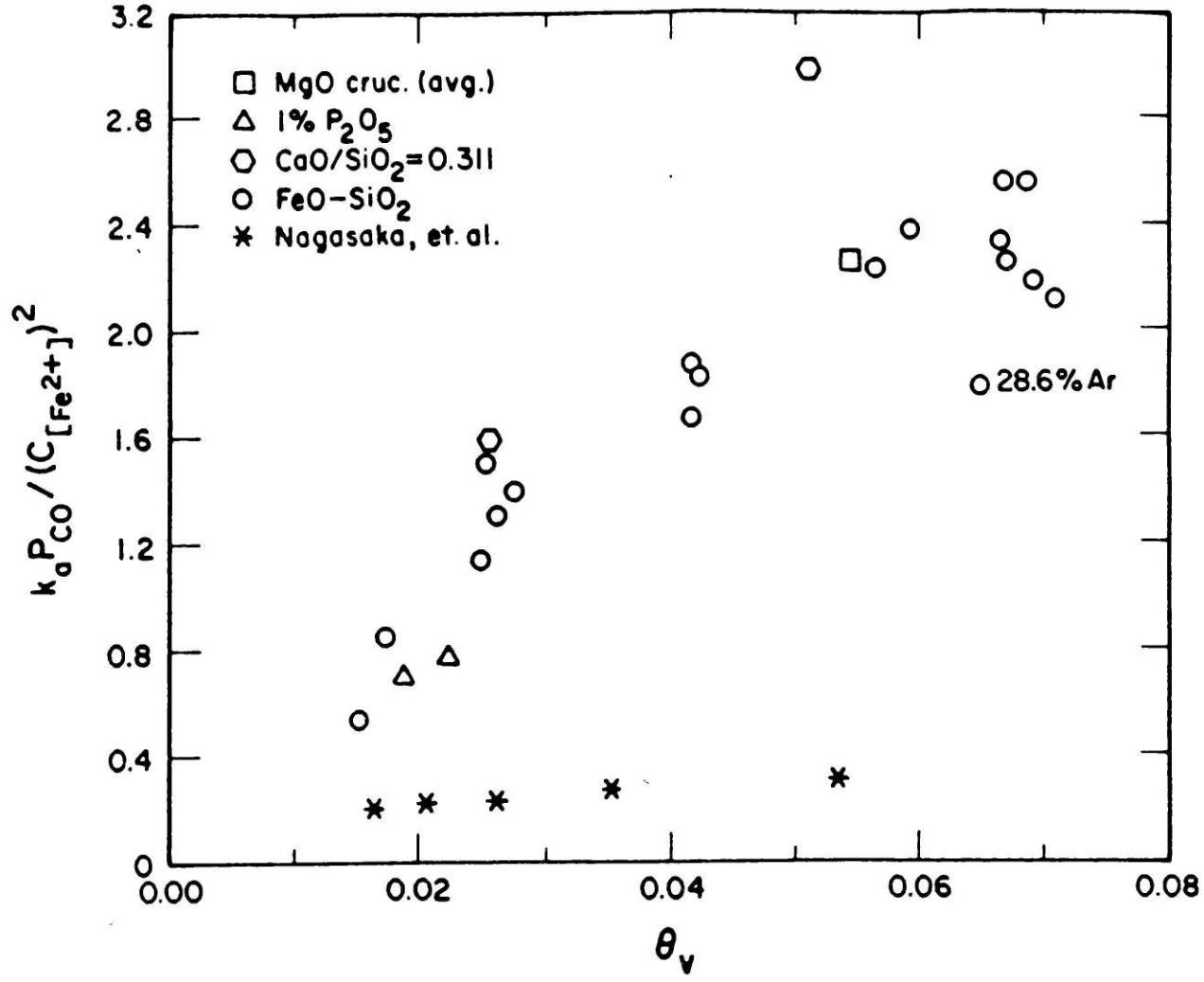

Figure 6-38. Comparison of Experimental Results to Model I.c. in Table 3-2. ordinate: [mole O.m^{4} /(mole Fe^{2+}.sec)] X 10^{-3}; abscissa: equation (6-14);

$$2[Fe^{3+}] + [O^{2-}] + v = 2[Fe^{2+}] + O\ (ads)$$

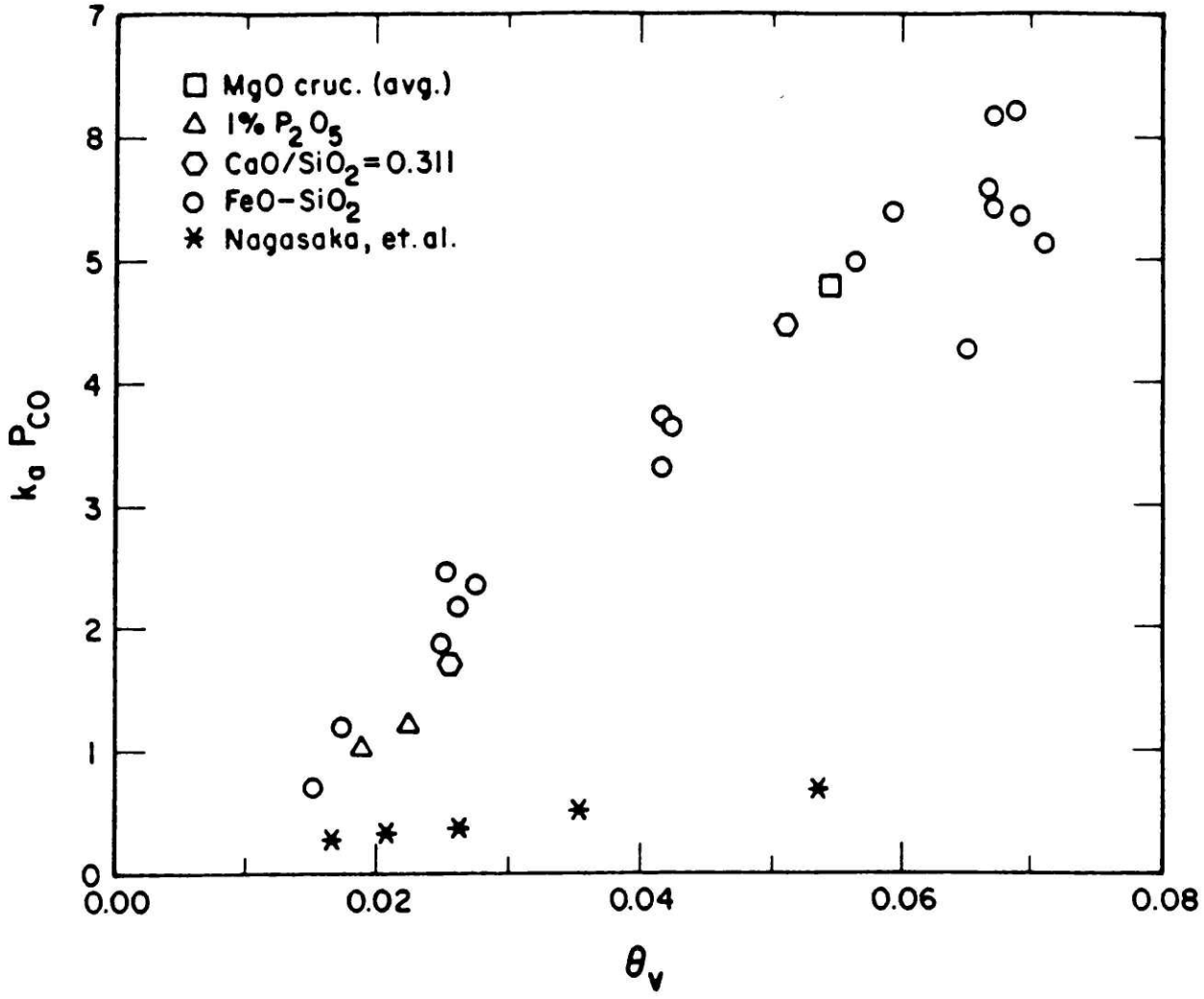

Figure 6-39. Comparison of Experimental Results to Model I.d. in Table 3-2. ordinate: [mole O /(m^2.sec)] X 100; abscissa: equation (6-14);

$$[Fe^{2+}] + [O^{2-}] + v = Fe\ (\gamma) + O\ (ads)$$

The rate constants for the other adsorption reactions, compared to the data in Figures 6-37 to 6-39, are dependent on the partial pressures of CO in the gas. The results for test 72, in which 28.6 percent argon was used in the reducing gas, and the results of Nagasaka, et. al., using 10 percent CO and argon, have different slopes than similar melts reduced under CO_2-CO gas mixtures. Steps I.b. through I.d. are not controlling the reaction.

Figures 6-40 to 6-45 show the comparisons of the experimental results to the rate models of the remaining reaction steps in Table 3-2. Steps II.b. and II.c. (Figures 6-40 and 6-41), reaction of adsorbed CO with adsorbed ionic or atomic oxygen to produce adsorbed ionic or molecular CO_2, respectively, plus a vacant reaction site are not controlling the reduction of the melts because the rates are not second order with respect to the fraction of vacant reaction sites. Step II.g. (Figure 6-42), the charge transfer between adsorbed CO_2^{2-} and ferric iron in the melt, does not control the reduction as shown by the poor fit of the data to the model.

Step II.h. (Figure 6-43), the charge transfer between ferrous and ferric ions to form iron, reaction 6-12, is not controlling the reduction of iron-silicates because the slope of the relationships are dependent on the partial pressures of CO in the gas, as shown by comparing the results of test 72 and Nagasaka, et. al. to the results on melts of similar compositions reduced using

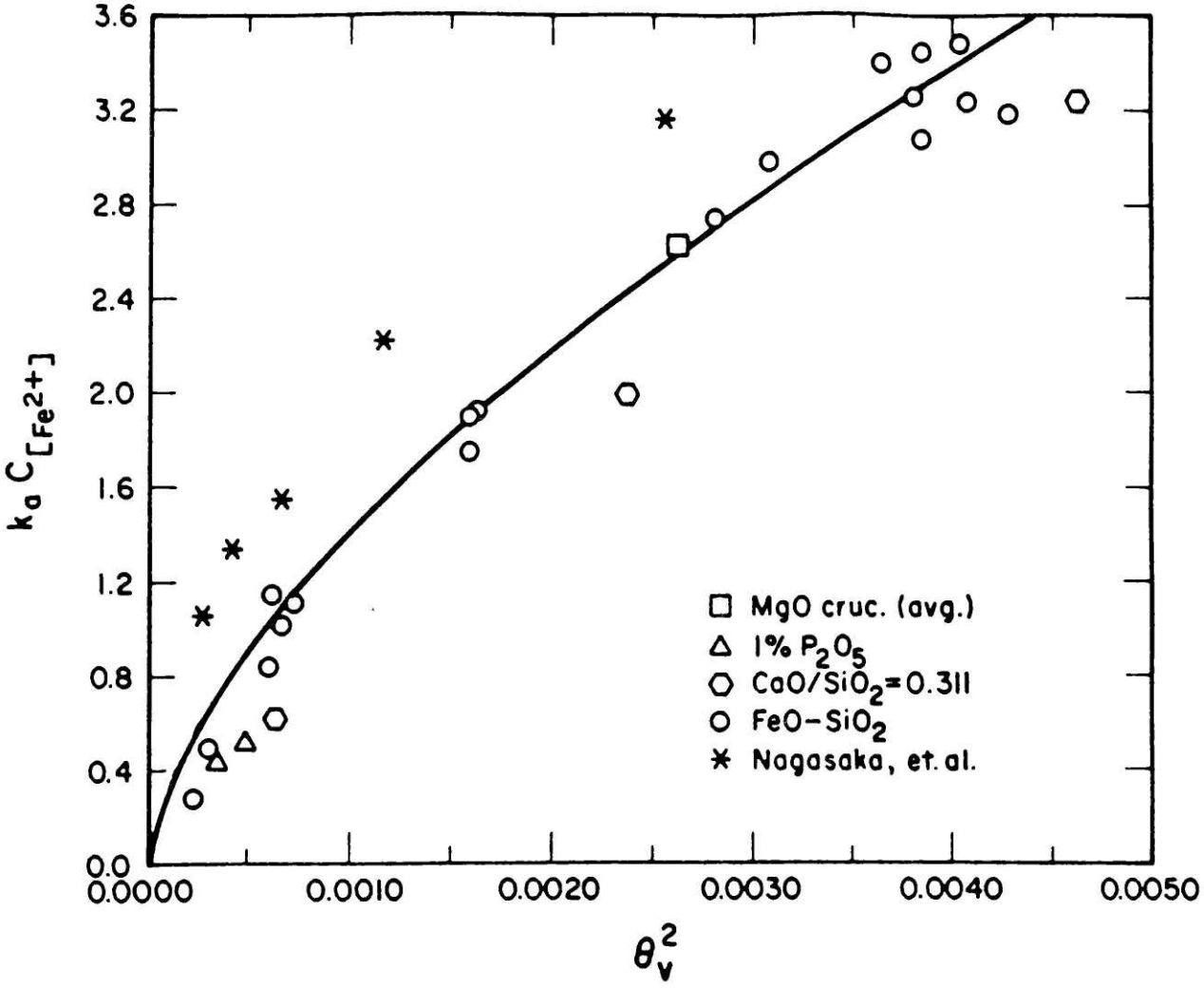

Figure 6-40. Comparison of Experimental Results to Model II.b. in Table 3-2. ordinate: [mole FeO /(m^3.sec)] X 10^{-3}; abscissa: equation (6-13) used for θ_v;

CO (ads) + O^{2-} (ads) = CO_2^{2-} (ads) + v

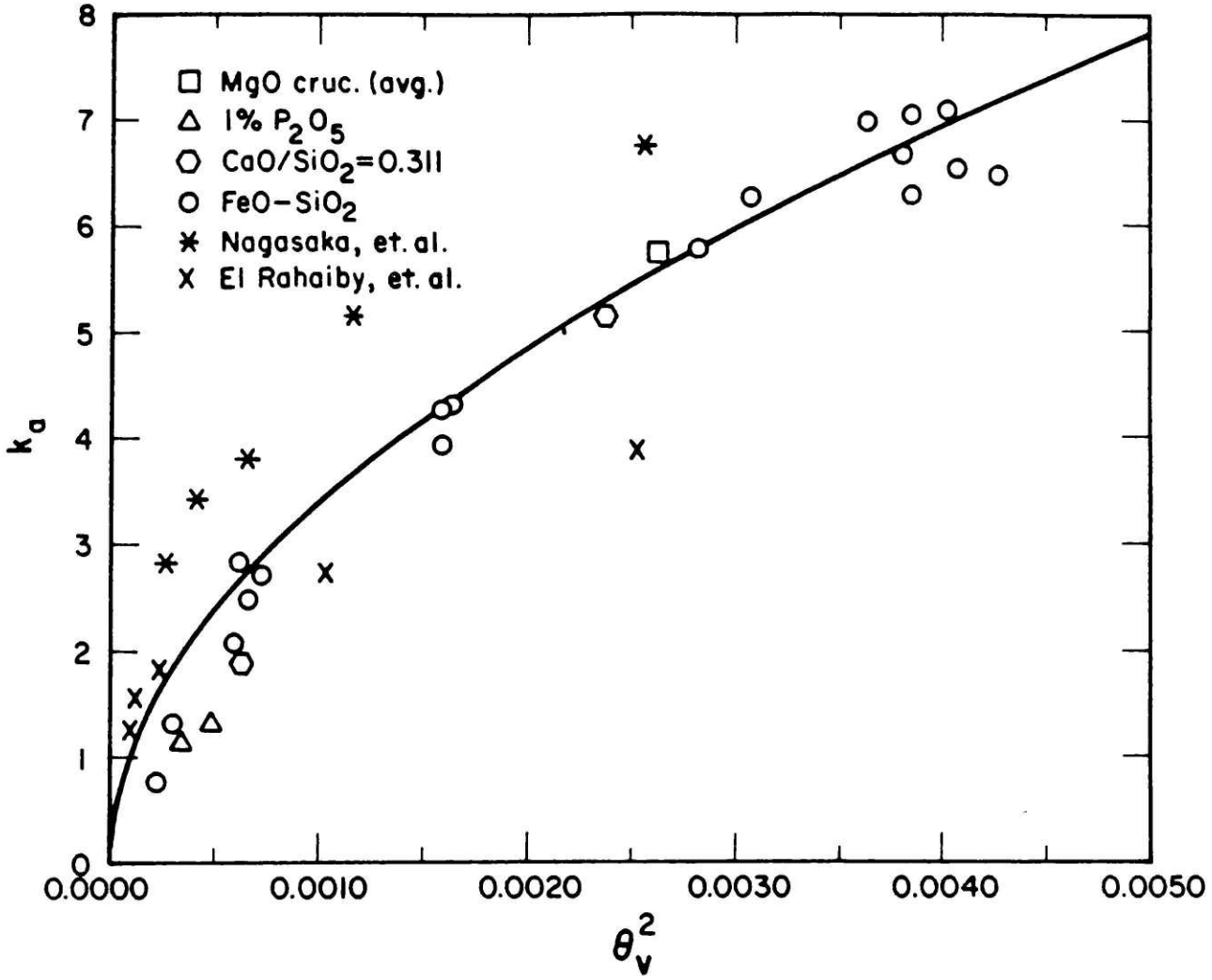

Figure 6-41. Comparison of Experimental Results to Model II.c. in Table 3-2. ordinate: [mole O /(m^2.sec.atm)] X 100; abscissa: equation (6-13) used for θ_v;

CO (ads) + O (ads) = CO_2 (ads) + v

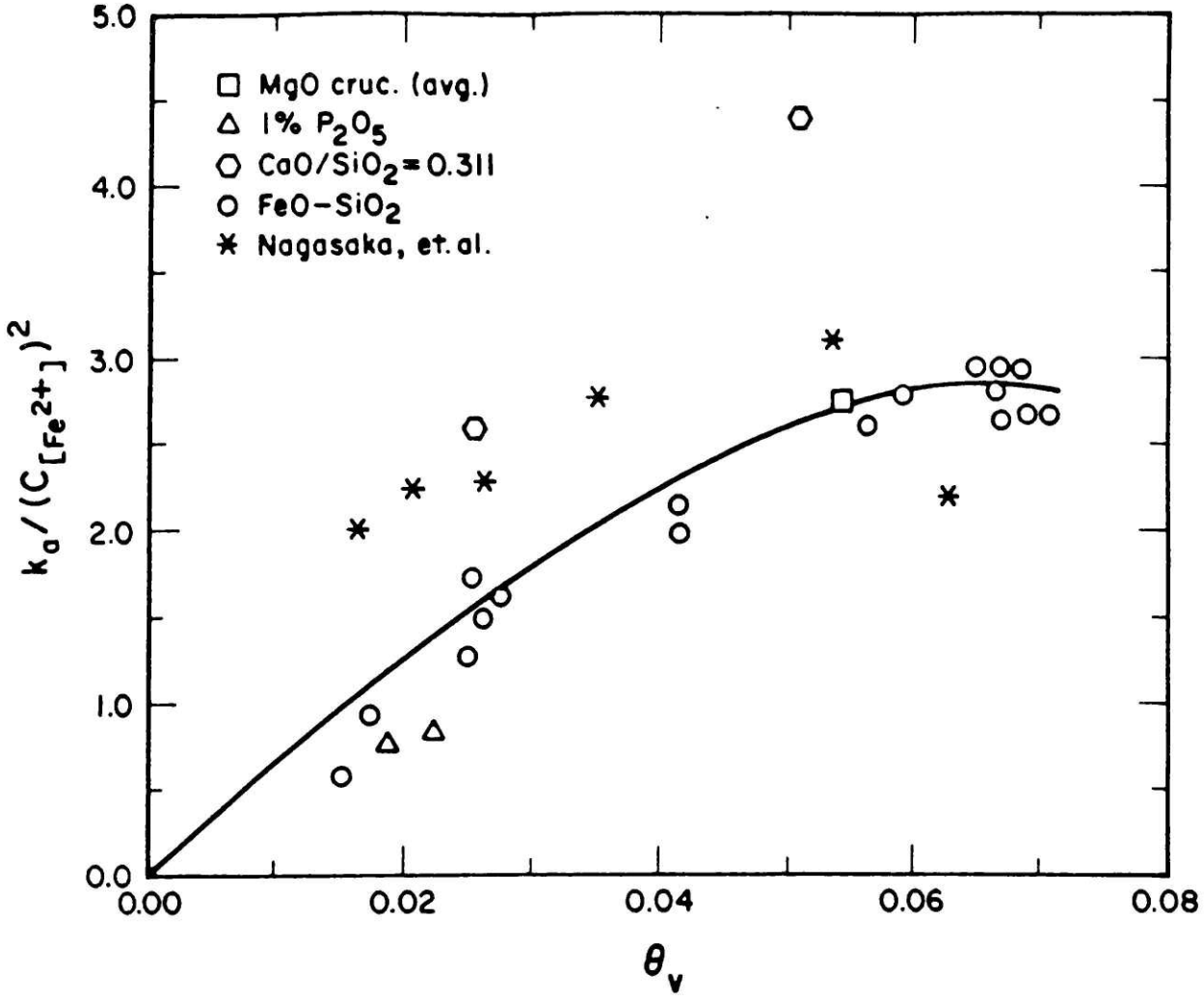

Figure 6-42. Comparison of Experimental Results to Model II.g. in Table 3-2. ordinate: [(mole $O.m^4$)/($(Fe^{2+})^2$.sec. atm)] X 10^{11}; abscissa: equation (6-14);

$$CO_2^{2-}\ (ads) + 2[Fe^{3+}] = CO_2\ (ads) + 2[Fe^{2+}]$$

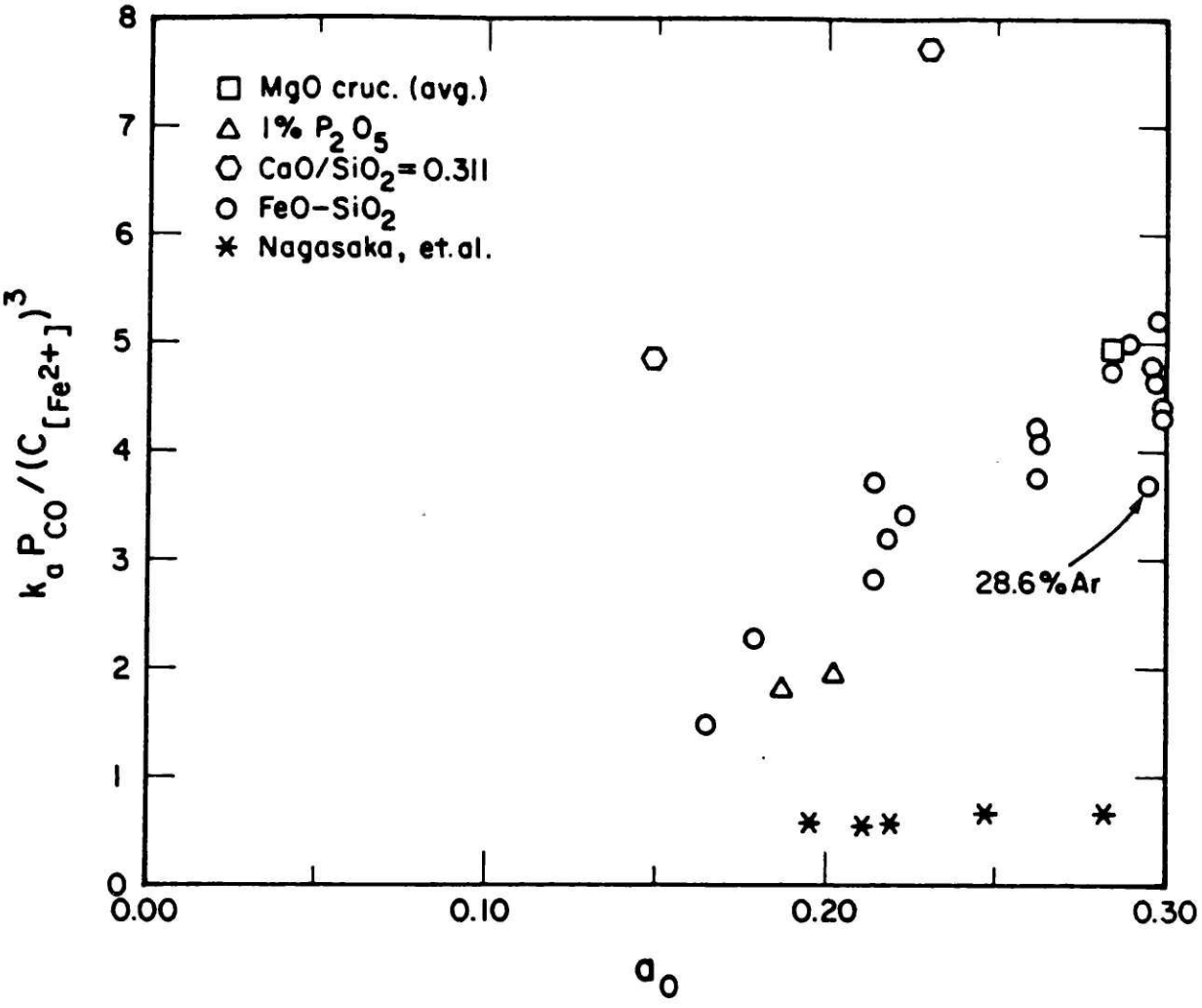

Figure 6-43. Comparison of Experimental Results to Model II.h. in Table 3-2. ordinate: $[(\text{mole O.m}^{7})/((Fe^{2+})^{3}.\text{sec})] \times 10^{16}$;

$3[Fe^{2+}] = 2[Fe^{3+}] + Fe\ (\gamma)$

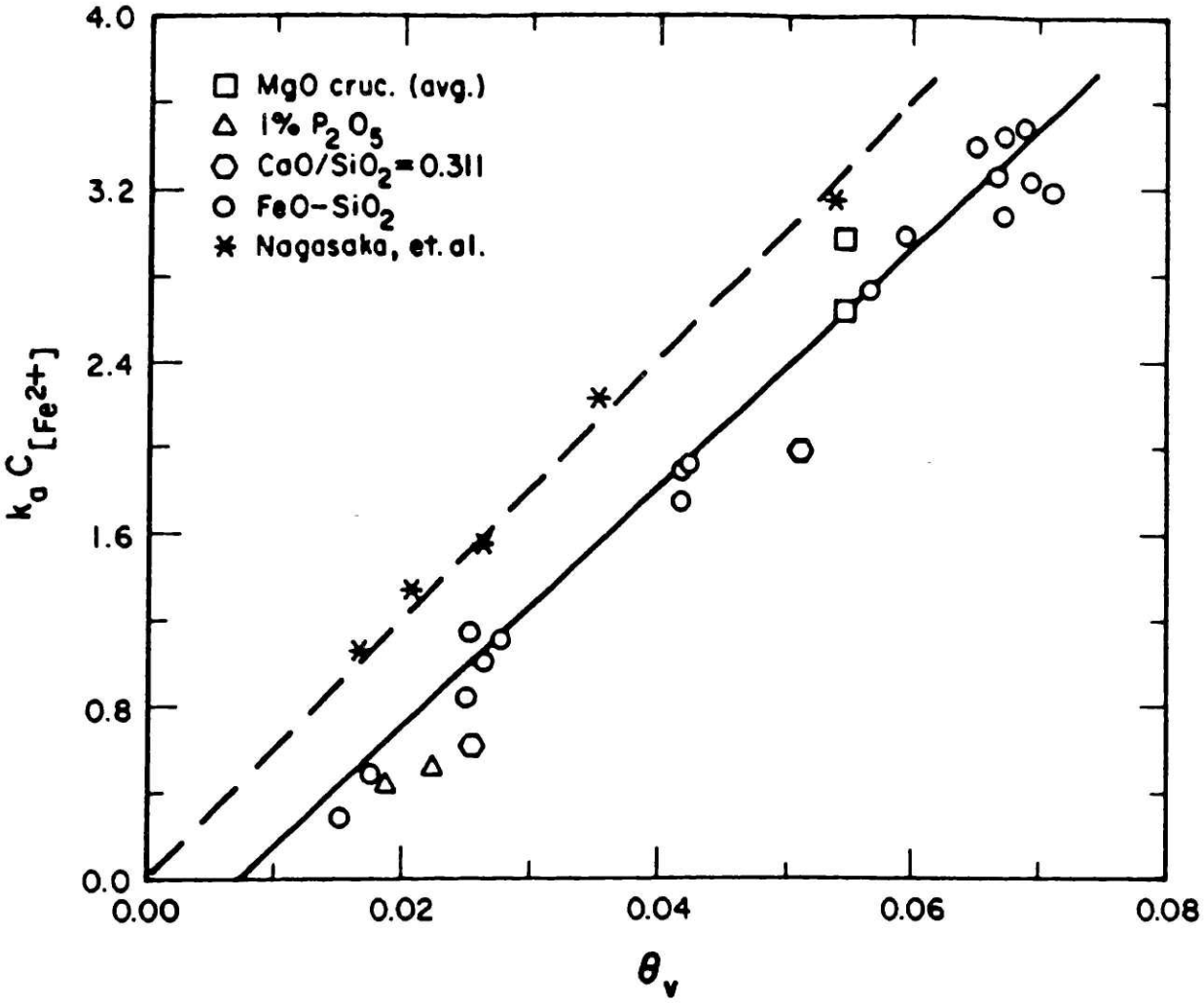

Figure 6-44. Comparison of Experimental Results to Model II.a. in Table 3-2. ordinate: [mole FeO /(m^5.sec.atm)] X 10^{-4}; abscissa: equation (6-14);

$$CO\ (g) + O^{2-}\ (ads) = CO_2^{2-}\ (ads)$$

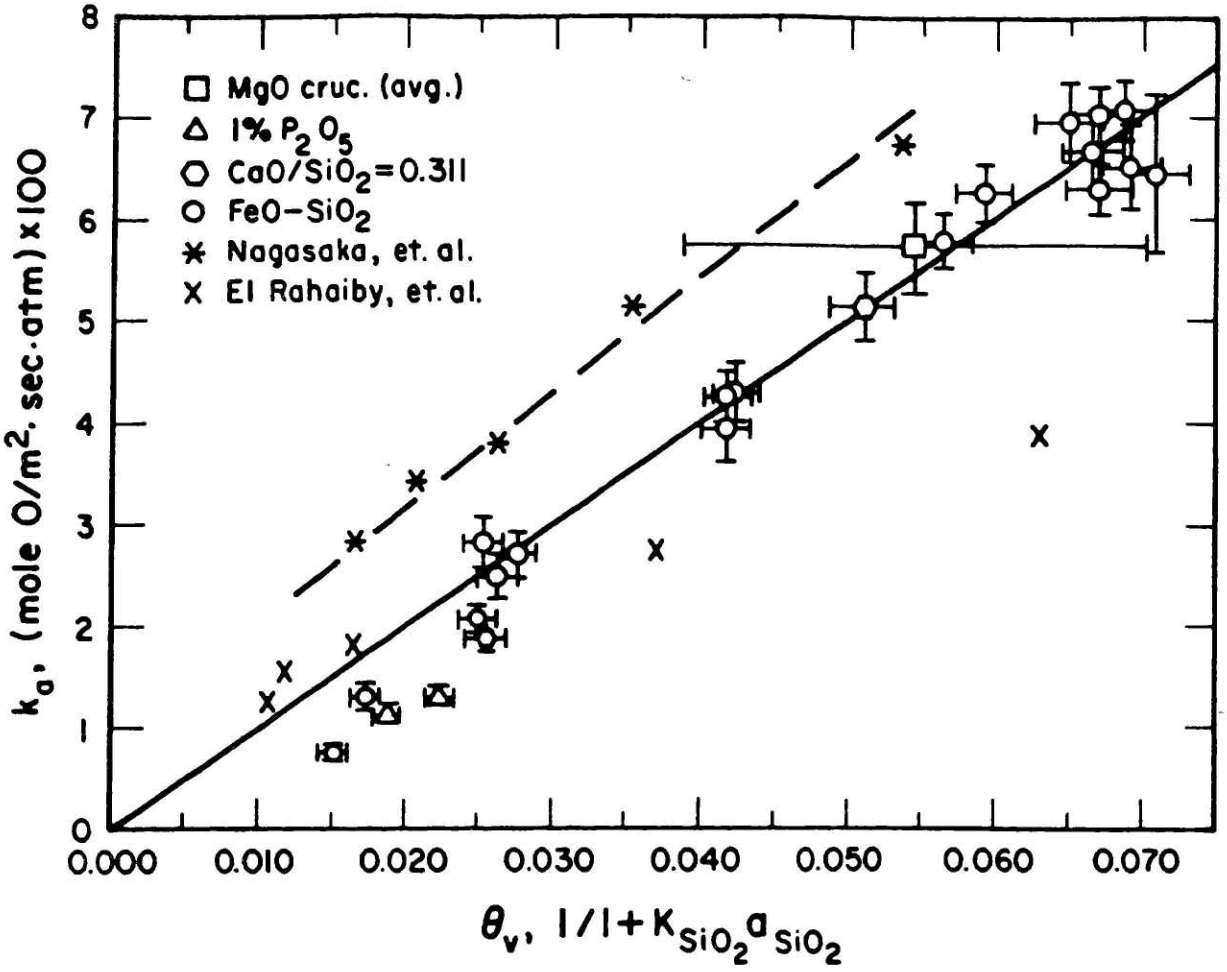

Figure 6-45. Comparison of Experimental Results to Models II.d., e., f. and III. in Table 3-2:

II.d. $CO\ (ads) + O\ (ads) = CO_2\ (g) + v$

II.e. $CO_2^{2-}\ (ads) + [Fe^{2+}] = CO_2\ (ads) + Fe\ (\gamma)$

II.f. $CO_2^{2-}\ (ads) + [Fe^{2+}] = CO_2\ (g) + Fe\ (\gamma) +$

III. $CO_2\ (ads) = CO_2\ (g) + v$

CO_2-CO gas mixtures. However, the results on melts containing CaO fit the model, indicating that the step may be controlling the reaction of these melts. Prange, Heusler, and Schwerdtfeger (73) studied kinetics of the reaction

$$Fe(\delta) = Fe^{2+} + 2e^- \qquad (6\text{-}19)$$

in $CaF_2(l)$ containing only about 0.0036 to 0.054 percent FeO using the single and double pulse galvanostatic technique at 1450°C with iron electrodes. The exchange current densities were very large, increasing from 2 to 10 amps/cm^2 with increasing FeO content. Reaction 6-12 can proceed no faster than the rates observed by Prange, et. al. for reaction 6-19, so the observed rates would be on the order of 0.5 mole O / m^2 sec for melts at 1450°C and containing very small levels of FeO. This is about 100 times faster than the observed rates at 1300°C. At the 70 percent FeO level, the reduction rates would be several orders of magnitude greater than the observed rates if reaction 6-12 controlled the reduction. It is unlikely that reaction 6-12 is the rate limiting step.

Figure 6-44 shows the comparison of the experimental results to the rate model derived for step II.a., the reaction of gaseous CO with adsorbed ionic oxygen to form adsorbed CO_2^{2-}. The results of Nagasaka, et. al. fit the model, but the results on all the melts reacted under CO_2-CO show a poor fit because the line through the points does not intersect the origin.

Steps II.d., II.e, II.f., and III have the same derived rate expressions, and Figure 6-45 shows the comparison of the

experimental results to this model. Shown in the figure are the estimated errors (standard deviations) of each test, determined in the previous section. The results on all the iron-saturated melts reduced under CO_2-CO, and the results from the isotopic exchange reaction on unsaturated melts at the three highest silica levels (30, 36, and 39 percent silica at saturation) fit the model well. Because of the good fit of the experimental results to the model for several different melt compositions, and the relatively poor fit of the results to the other models, one of the steps described by this model is probably controlling the overall reaction. The results of El-Rahaiby, et. al. at the two lowest silica levels (10 and 20 weight percent silica), and the results of Nagasaka, et. al. do not fit the model. Reasonable explanations for these discrepancies follow.

El-Rahaiby's, et. al. results did not compare satisfactorily with any of the models shown in Table 3-2. Their results at the lower silica levels are suspect. The 10 percent silica melts used by El-Rahaiby, et. al. precipitate wustite at temperatures up to about 1320°C, so the melts tested at lower temperatures contain more than the reported 10 percent silica. El-Rahaiby conducted three tests using the 10 percent silica melt at temperatures as low as 1260°C, at which temperature the crucible would contain about 38 weight percent solid wustite. Although the analyses used in the above comparisons were adjusted for the wustite precipita-

tion, the reliability of the data generated for this melt is questionable.

Of perhaps more significance, the melts were in contact with zirconia containment tubes. Although it was reported that the tubes were not noticeably attacked by the slag, iron-saturated silicate melts can dissolve from about 10 to 14 percent zirconia at temperatures from 1300 to 1400°C (74). Also, wustite is soluble in solid zirconia to about the 8 mole percent level. The lower silica melts used by El-Rahaiby, et. al. are expected to lose iron oxide to the containment tube, increasing the true silica contents of the melts. The net effect would be to improve the correlation of the results of El-Rahaiby, et. al. on low silica melts with the other experimental results. The effect of dissolved zirconia on chemisorption reaction kinetics is not known.

The rate constants reported by Nagasaka, et. al. are based on initial observed reduction rates. As shown in the preceding sections, the presence of extraneous slag on the surface of the iron crucible increases the apparent initial reduction rates for the 12 percent silica melts tested in polished iron cups. A test was run to determine if the same effect is present when reducing melts with higher silica contents in unpolished cups. Figure 6-46 shows the results obtained when reducing a 25 percent silica sample with a gas of $CO_2/CO=0.144$. The shape of the reduction rate curve indicates that extraneous slag is present on the

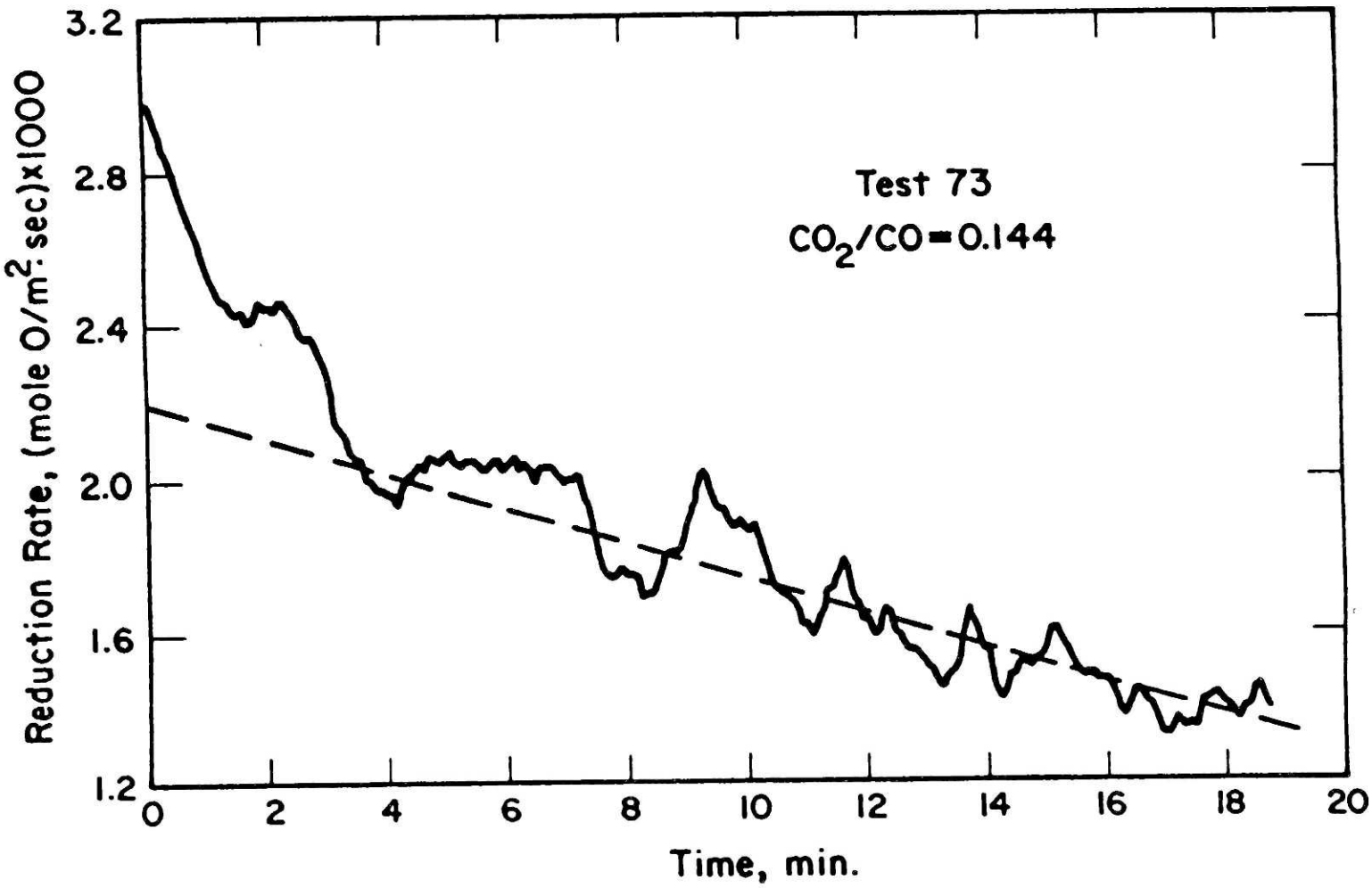

Figure 6-46. Reduction rate curve obtained by reducing the 25 %SiO_2 melt in an unpolished crucible. Test 73. CO_2/CO = 0.144

surface of the unpolished cup. Consequently, the initial reduction rate is about 36 percent higher than the extrapolated reduction rate in this particular test. It is likely that extraneous slag was present on the surface of the crucibles used by Nagasaka, et. al., resulting in higher apparent reduction rates relative the the results using polished cups.

To test the models at other temperatures, the results of Nagasaka, et. al. on iron-silicate melts reduced at 1400°C were compared to the derived rate models. The silica and oxygen activities of the melts are determined using the activity-composition relationships shown in Figure 4-9 for iron-saturated melts at 1400°C. The values used in the model comparisons are shown in Table 6-7. The adsorption coefficients for oxygen and silica in the melts are 3.7 and 64 respectively, determined using the Gibbs-Langmuir adsorption isotherm on Kidd and Gaskell's (37) surface energy data.

The results of Nagasaka, et. al. compare well with the model for steps II.d., II.e., II.f., and III. of Table 3-2, shown in Figure 6-47. However, the point corresponding to the lowest silica level, 4.2 percent silica, shows poor correlation and has a much lower rate constant than is predicted by the model. Liquid-phase diffusion control may be affecting the reaction rate of this melt. The melts in Nagasaka's study were about 1.5 mm deep in the crucible. The reduction rates calculated assuming liquid-phase diffusion control with this configuration are comparable to the observed rate after about 3.5 minutes of reduction. If several

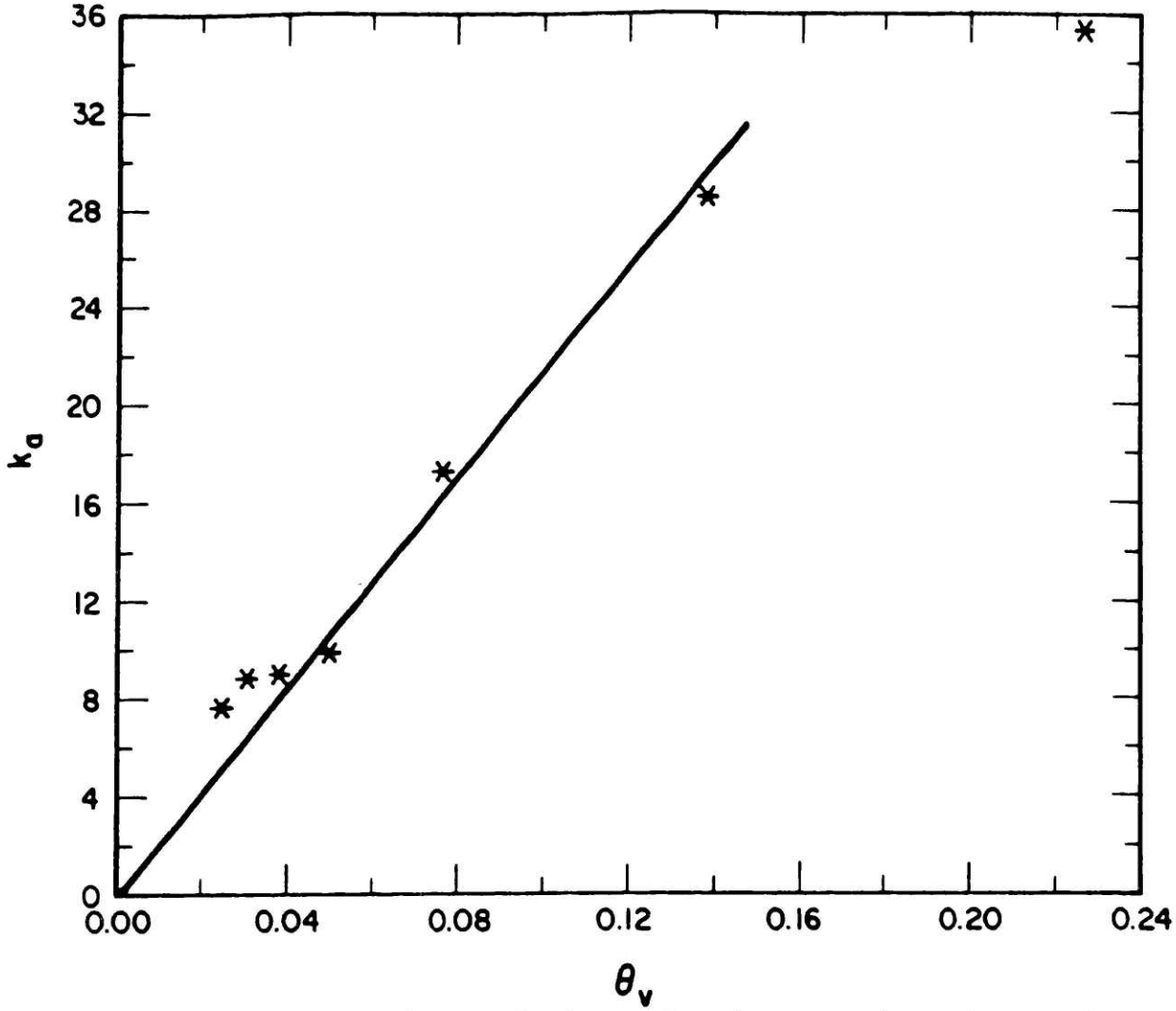

Figure 6-47. Comparison of the reduction results obtained by Nagasaka, et.al. at 1400°C using Fe sat. FeO-SiO_2 melts, to the derived rate expression for steps II.d., e., f., and III. of Table 3-2. abscissa: equation (6-14); ordinate: [mole O /(m^2.sec.atm)] X 100

II.d. $CO\ (ads) + O\ (ads) = CO_2\ (g) + v$

II.e. $CO_2^{2-}\ (ads) + [Fe^{2+}] = CO_2\ (ads) + Fe\ (\gamma)$

II.f. $CO_2^{2-}\ (ads) + [Fe^{2+}] = CO_2\ (g) + Fe\ (\gamma) + v$

III. $CO_2\ (ads) = CO_2\ (g) + v$

minutes of reduction are needed to estimate the initial reduction rate, the rate reported by Nagasaka, et. al. for this melt compares well with liquid-phase diffusion rate estimates.

The line through the experimental points at 1400°C in Figure 6-47 intersects with the origin, although at 1300°C, Figure 6-45, it did not. At 1400°C, the reduction rates are about 2 times faster than at 1300°C. If extraneous slag on the crucible is present in the same amounts at both temperatures, it will approach equilibrium with the gas in about half the time at 1400°C relative to 1300°C. If Nagasaka, et. al. determined the initial reduction rates using the first few minutes of reduction, it is likely the extraneous slag would not influence the rate determinations as much at the higher temperature.

The data of Sasaki, et.al. on the rate of the exchange reaction on liquid FeO is also analyzed using the rate models. The fraction of vacant reaction sites is calculated using the Langmuir adsorption equation for oxygen

$$\theta_v = 1 / (1 + K_O a_O) \quad . \qquad (6\text{-}20)$$

The other values used in the model comparisons are shown in Table 6-7. The experimental results on liquid iron oxides compare well with only the model for reaction step II.c. The relationship is shown in Figure 6-48.

A final comparison of experimental results to the chemisorption rate models can be made using the data of El-Rahaiby, et. al. on

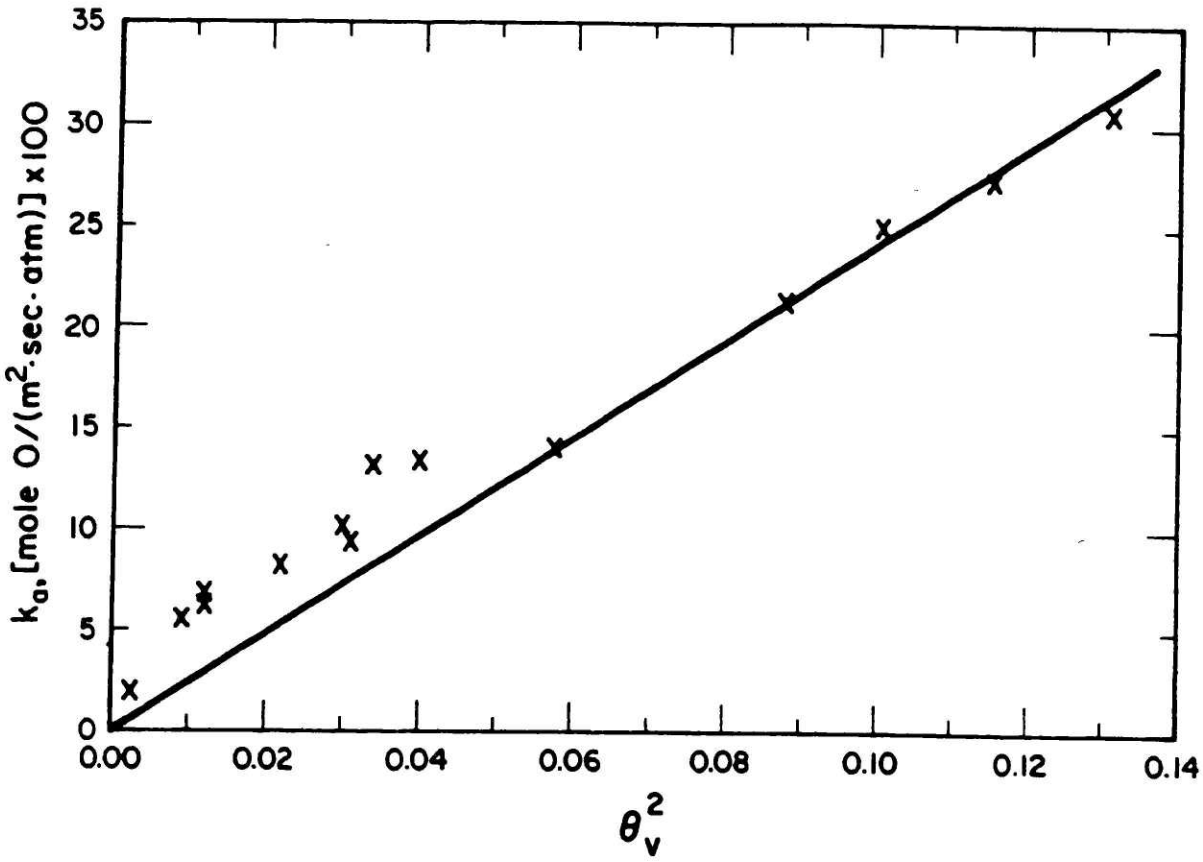

Figure 6-48. Comparison of the results obtained by Sasaki, et.al. (21) using the isotopic exchange technique on pure FeO(l), to model II.c. of Table 3-2; 1420°C; abscissa: equation (6-20);

CO (ads) + O (ads) = CO_2 (ads) + v

equimolar $CaO-FeO-SiO_2$ melts at 1420°C. The thermodynamic properties and composition of the melt were evaluated using the results of Timucin and Morris (75), who studied the system $CaO-FeO-Fe_2O_3-SiO_2$ at 1450 and 1550°C over the range of oxygen partial pressures from 1 to 10^{-11}. The densities were adjusted as before using the data of Kawai, et. al. (58) and Mori and Suzuki (72). The values used in the model comparisons are shown in Table 6-7. The experimental rate constants for these melts show a second order dependence on the fraction of vacant reaction sites. The only model that compares well with the experimental results is model II.c., the reaction between adsorbed CO and adsorbed atomic oxygen to form adsorbed CO_2. The results are shown in Figure 6-49.

6.6.2 Discussion of the Chemisorption Model Comparisons

The experimental results compare well with the rate model that describes the reactions

$$CO\ (g) + O\ (ads) = CO_2\ (ads) \qquad (6\text{-}21)$$

$$CO_2^{2-}\ (ads) + 2[Fe^{2+}] = CO_2\ (ads) + Fe\ (\gamma) \qquad (6\text{-}22)$$

$$CO_2^{2-}\ (ads) + 2[Fe^{2+}] = CO_2\ (v) + Fe\ (\gamma) + v \qquad (6\text{-}23)$$

$$CO_2\ (ads) = CO_2\ (ads) + v\ . \qquad (6\text{-}24)$$

Reactions (6-22) and (6-23) do not fit with the observations that the iron grows remotely from the gas-liquid interface. Reaction (6-24) is not rate limiting because CO_2 is only very weakly adsorbed on metallic and oxide surfaces. The probable rate limiting step for the reduction is reaction (6-21).

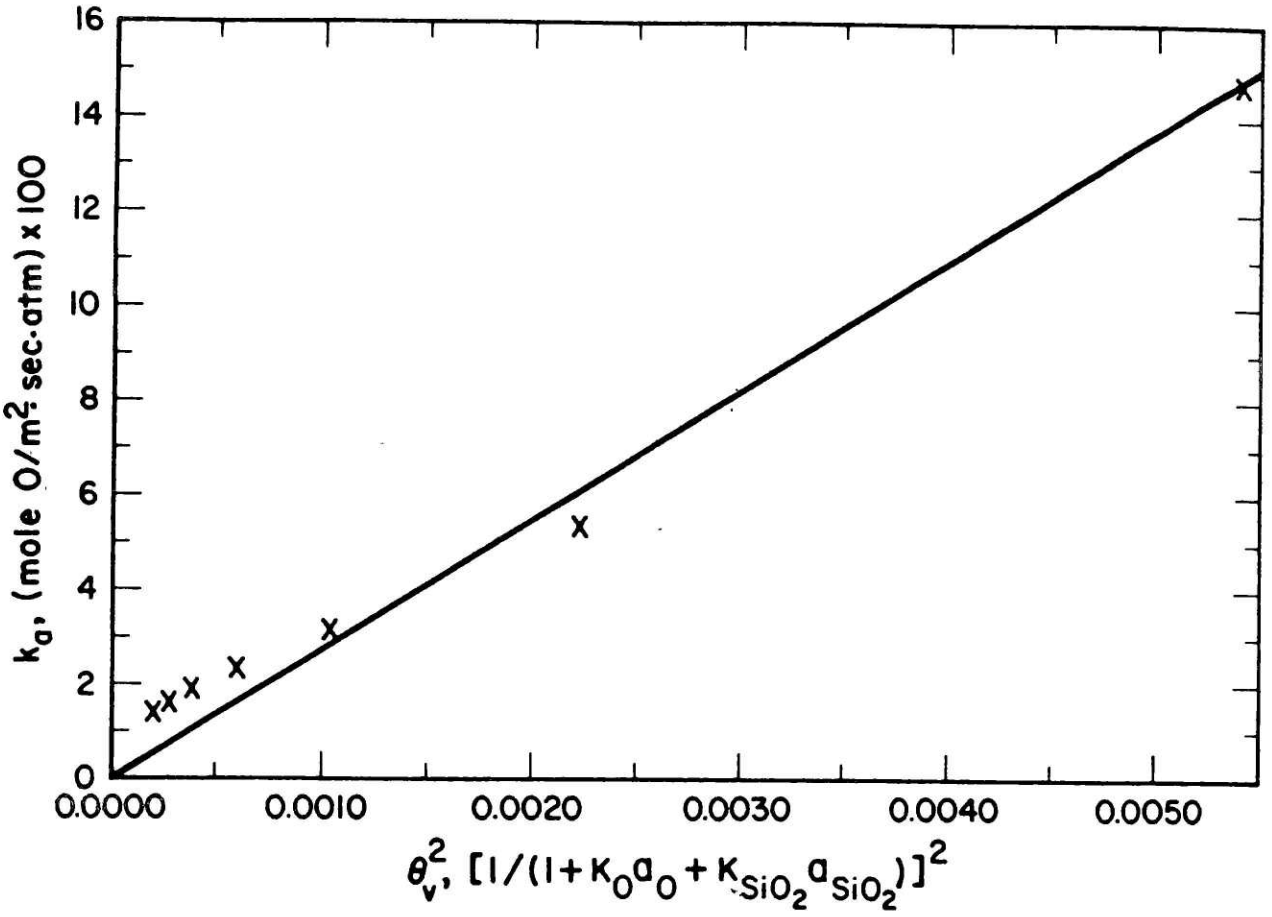

Figure 6-49. Comparison of the results obtained by El-Rahaiby, et.al. using the isotopic exchange technique on equimolar CaO-FeO-SiO_2 melts, to model II.c. of Table 3-2; 1420°C

CO (ads) + O (ads) = CO_2 (ads) + v

The rate limiting step in the isotopic exchange reaction on FeO(l) and equimolar CaO-FeO-SiO_2 melts at 1420°C, is similar to reaction (6-21) above, but involves adsorbed CO. For the FeO(l), the model appears to fit better at the higher concentrations of vacant sites (lower oxygen activities). The fraction of vacant reaction sites at which the model fits well is on the order of 0.30, relative to about 0.07 for the silicate melts. In Figure 6-48, the model does not fit well for FeO(l) at fractions of vacant sites less than about 0.20, indicating that this may be the level of vacancies on the surface needed for CO to adsorb significantly. It is difficult to draw conclusions from the data, but it is not unreasonable to expect much more CO to be adsorbed on a relatively "clean" surface of liquid oxide, than on a surface with much more adsorbed oxygen. Catalyzed oxidation of CO is greatly inhibited by high concentrations of adsorbed oxygen on the surface of many catalysts (23).

The effect of CaO additions on reaction rates of other melts can not be analyzed further using the models because of limited experimental or thermodynamic data. But, generally, the reaction rates are much faster for melts containing CaO, than those without. In catalytic reactions, the rates of oxidation of CO are much faster if the CO is adsorbed on the catalyst surface, than if CO reacts from the gaseous state. Presumably, the same would hold true for melts. It is likely that CaO additions dramatically enhance the adsorption of CO. The effect is probably related to the ability of calcia to form stable carbonates. Carbon monoxide

forms a carbonyl-type bond on metals, in which two metal atoms bond to the carbon atom. It is not unreasonable to assume that two oxygen atoms near the surface may also bond with the carbon to form a carbonate bond, which may be stabilized by the presence of calcium ions. The results on the melts with CaO/SiO_2 = 0.311 showed good correlation with the model that fit the silicates, indicating more than about 10 weight percent calcia is needed in the melt to affect the CO adsorption. Davies, et. al. (1) observed slower reduction kinetics with low levels of CaO in the melt than with melts free of CaO.

The two rate expressions that compared well with the experimental results involve only atomic species, but models involving charged species show poor correlation with the experimental results. Figure 6-50 shows the later correlation for the isotopic exchange reactions on the equimolar $CaO-FeO-SiO_2$ melts to step II.b. of Table 3-2. Oxygen adsorbed on solid iron has an effective hard sphere radius about 1/3 less than the ionic radius in the wustite lattice (28), indicating that oxygen lost electrons in the adsorption step on iron. The same phenomenon may occur on molten oxides.

6.6.3 Probable reaction mechanisms

The results of the correlations of experimental data to the derived rate expressions, and the observations on the location of the iron growth, indicate that the reduction of iron-silicate melts occurs by the following mechanism:

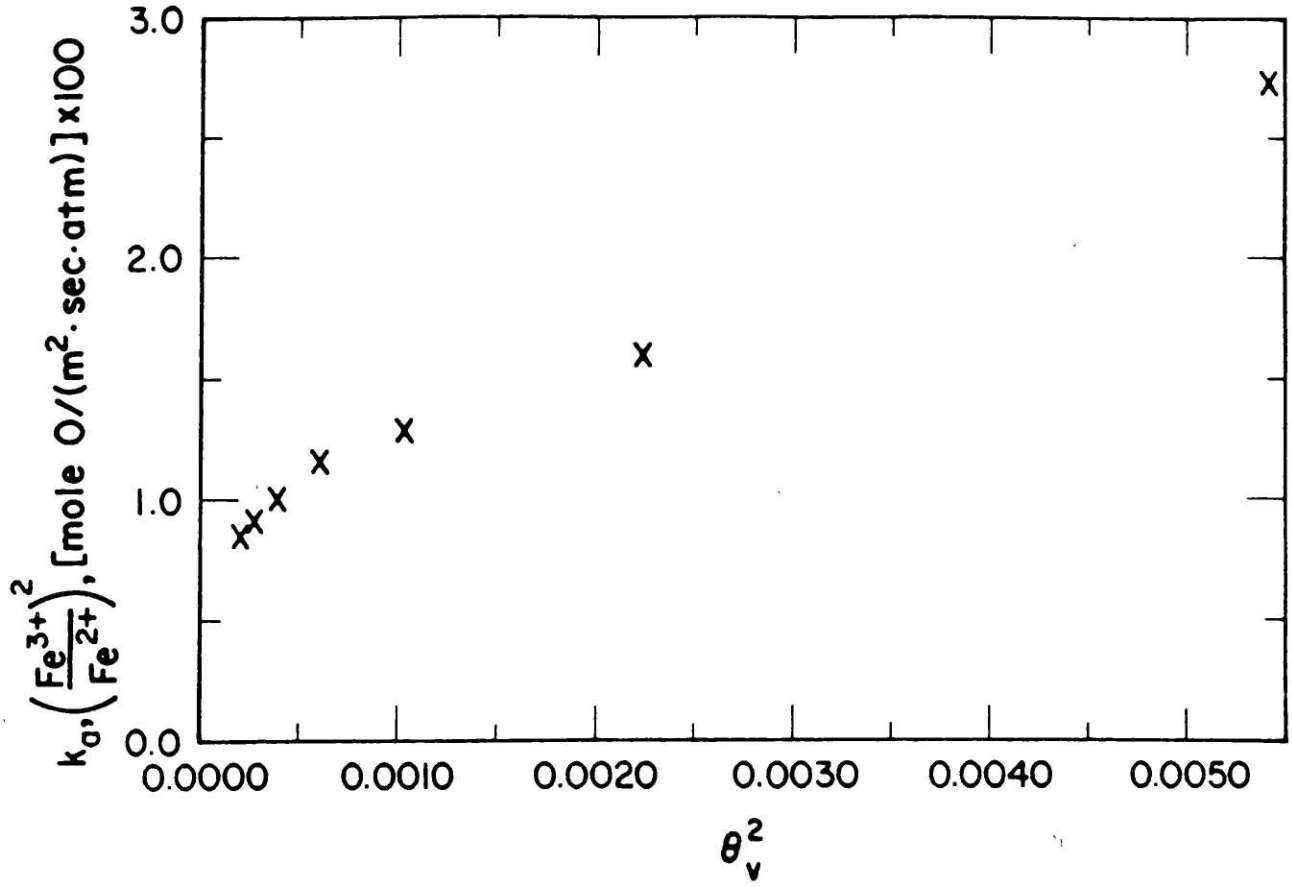

Figure 6-50. Correlation of the results on the isotopic exchange reaction on equimolar CaO-FeO-SiO_2 melts, with step II.b. of Table 3-2. 1420°C

$$CO\ (ads) + O^{2-}\ (ads) = CO_2^{2-}\ (ads) + v$$

a) coupled adsorption of oxygen from the bulk to the surface with the reduction of ferric iron to ferrous iron

$$\left.\begin{array}{l} [O^{2-}] + v = O\ (ads) + 2e^- \\ 2[Fe^{3+}] + 2e^- = 2[Fe2+] \end{array}\right)$$

$$2[Fe^{3+}] + [O2-] + v = 2[Fe^{2+}] + O\ (ads)$$

b) reaction of gaseous CO with adsorbed oxygen

$$CO\ (g) + O\ (ads) = CO_2\ (g)$$

c) formation of metallic and ferric iron from ferrous iron at the most feasible site

$$3[Fe^{2+}] = 2[Fe^{3+}] + Fe\ (\gamma) \quad .$$

The reaction on liquid iron oxide and melts with calcium would involve the additional step of the adsorption of CO. The rate controlling step in the mechanism is the oxidation of CO by the adsorbed oxygen, step b. The rate expression for the reaction on iron saturated liquid iron silicates is:

$$R = \beta\ \theta_v\ [\ P_{CO}\ a_O - P_{CO_2}\ ] \quad , \qquad (6\text{-}25)$$

where θ_v is defined by equation (6-14), and

$$\beta = 1.0\ (\pm\ 0.07)\ \text{mole O}\ /(m^2.\text{sec.atm})\quad (1300°C) \qquad (6\text{-}26)$$
$$= 2.2\ (\pm\ 0.05)\ \text{mole O}\ /(m^2.\text{sec.atm})\quad (1400°C)\ .$$

The activation energy of β is 172 kJ / mole.

On unsaturated liquid iron oxide and equimolar $CaO\text{-}FeO\text{-}SiO_2$ melts, the rate expression is:

$$R = \beta\ ([Fe^{2+}]/Fe^{3+}])^2\ \theta_v^{\,2}\ [\ P_{CO}\ a_O - P_{CO_2}\ ]\ , \qquad (6\text{-}27)$$

where θ_v is determined using equation (6-13), and

$$\beta = 27\ (\pm\ 5)\ \text{mole O}\ /(m^2.\text{sec.atm}) \qquad (6\text{-}28)$$
$$= 2.4\ (\pm\ 0.15)\ \text{mole O}\ /(m^2.\text{sec.atm})\ ,$$

for equimolar $CaO\text{-}FeO\text{-}SiO_2$(l) and FeO(l), respectively, at 1420°C. The rate constant β is an order of magnitude greater for $CaO\text{-}FeO\text{-}SiO_2$ than it is for FeO(l), indicating that the adsorption of CO on the $CaO\text{-}FeO\text{-}SiO_2$(l) may be much more significant than the adsorption on FeO(l).

6.6.4 Significance of the results

The results explain why calcia additions improve the reduction rates of melts. The change in reaction mechanism with calcia additions induces a catalytic effect on the surface, enabling faster reaction of the CO with the adsorbed oxygen. There may be other compounds that perform the same function, such as the alkaline earth oxides, which form relatively stable carbonates.

The results on the experiments with P_2O_5 additions caused the opposite effect. The "poisoning" effect of 1 mole percent P_2O_5

addition, caused by the occupation of surface reaction sites by phosphorous, reduced the the reduction rate by 28 percent. Also of interest is the dramatic change in wetting behavior of the melt with small phosphorous additions. The same effect would be present inside an iron-ore agglomerate during reduction, wherein the phosphorous would help the melt wet the solid oxide, blocking off the gas-solid reaction.

It is shown that the oxygen is adsorbed as atoms and not ions, indicating that the adsorption of oxygen on molten silicates and oxides may be very similar to the adsorption of oxygen on metals. Also, the reduction mechanisms are different for adsorbed atoms than for adsorbed ions. The rate expressions of the steps involving the later are dependent on the ratio of electron donors to electron acceptors in the melt, while those of the former are not. Adding species to the melt which shift this ratio will not affect the reaction rates unless the mechanism is changed, as is the case with CaO additions.

Chapter 7
CONCLUSIONS AND RECOMMENDATIONS

7.1 Conclusions

The kinetics of reduction of iron from silicate melts held in iron and MgO crucibles at 1300°C by $CO-CO_2$ gas mixtures have been investigated using a thermogravimetric technique. The experimental results are compared to derived rate expressions for several proposed rate-limiting steps to determine which step is controlling the overall reduction process. The experimental results obtained by other investigators are also compared to the derived rate expressions to determine the rate-limiting step for the reduction of other melts by carbon monoxide.

The rate-limiting step for the reduction of iron-saturated iron-silicate melts at 1300 and 1400°C by carbon monoxide is

$$CO\ (g) + O\ (ads) = CO_2\ (g) + v\ , \qquad (7\text{-}1)$$

for which the rate expression is

$$R = \beta\ \theta_v\ (\ P_{CO}a_O - P_{CO_2}\ )\ , \qquad (7\text{-}2)$$

where β is the reduced reaction rate constant, θ_v is the fraction of vacant reaction sites on the melt surface, and a_O is the CO_2/CO ratio in the gas in equilibrium with the melt. The values of β are 1 ± 0.07 and 2.2 ± 0.05 mole O / (m^2.sec.atm) at 1300 and 1400°C, respectively. The fraction of vacant reaction sites on the melt surface, θ_v, is calculated from

$$\theta_v = \frac{1}{1 + K_{SiO_2} a_{SiO_2}}\ . \qquad (7\text{-}3)$$

The adsorption coefficient K for silica is determined using surface energy data and the Gibbs-Langmuir adsorption isotherm, and has values of 93 at 1300°C and 64 at 1400°C.

The rate-limiting step for the reduction of liquid iron oxide and equimolar $CaO-FeO-SiO_2$(l) by CO at 1420°C, determined using data on the rates of the isotopic exchange reaction on the melts from Belton, et.al. (21,22), is

$$CO\ (ads) + O\ (ads) = CO_2\ (ads) + v \quad , \qquad (7\text{-}4)$$

for which the rate expression is

$$R = \beta\ \theta_v^{\,2}\ (\ P_{CO}a_O - P_{CO_2}\ ) \quad . \qquad (7\text{-}5)$$

The values of β are 2.4 ± 0.15 and 27 ± 5 mole O / (m^2.sec.atm) for the iron oxide and equimolar $CaO-FeO-SiO_2$ melts, respectively. The fraction of vacant reaction sites on the melt surface is calculated using

$$\theta_v = \frac{1}{1 + K_O a_O + K_{SiO_2} a_{SiO_2}} \quad . \qquad (7\text{-}6)$$

The adsorption coefficient K for oxygen is 3.7 at 1420°C.

Carbon monoxide is significantly adsorbed on the surface of the pure iron oxide and the equimolar $CaO-FeO-SiO_2$ melts, but not on the surface of the liquid iron silicate. In the case of the iron oxide, the relatively high fraction of vacant sites (35 percent relative to about 7 percent for the other melts) is conducive to the adsorption of the carbon monoxide. The calcium ions in the equimolar $CaO-FeO-SiO_2$(l) may stabilize the adsorbed CO by the formation of a carbonate-type bonds with the oxygen ions in the bulk phase but near the surface of the melt.

It is found that the oxygen is adsorbed on the surface of the melts in the atomic rather than the ionic (O^{2-}) form. The rate expressions for steps involving ionic oxygen contain a term for the concentration of ferrous iron in the melt, while the rate expressions for steps involving adsorbed oxygen atoms do not (equations 7-2 and 7-5), enabling the differentiation.

7.2 Recommendations for Future Work

A specific recommendation is made to investigate the affect strong carbonate formers have on interfacial reaction rates. If the tendency to produce carbonates enhances the adsorption of CO, then the strong carbonate formers should also enhance reduction or oxidation rates in CO_2-CO gas mixtures. Some possible additives include the potassium and sodium oxides, barium oxides, and lithium oxides.

If the propensity to form a carbonate bond on the surface causes CO to be more strongly adsorbed, then it is conceivable that strong sulfate formers may help catalyze sulfur oxidation, or improve the transfer of sulfur across interfaces. The kinetic investigations could extend into other systems as well.

A general recommendation is made to conduct surface energy studies on more systems, and to use the surface energy data to analyze interfacial reaction kinetics. The surface energy and kinetic studies need not be limited to gaseous interfaces. Interfaces play very dominant roles in high-temperature process, and information on these interfaces can now come only from surface energy and kinetic studies.

Appendix A

EXAMPLE DERIVATION OF A CHEMISORPTION RATE EXPRESSION

The overall reaction of interest is

$$FeO\ (l) + CO\ (g) = Fe\ (\gamma) + CO_2\ (g) \quad . \qquad (A\text{-}1)$$

A probable chemisorption reaction mechanism for the reaction is:

a) adsorption of CO on a vacant site, v, on the melt surface

$$CO\ (g) + v = CO\ (ads)$$

b) adsorption of O^{2-} on the melt surface

$$[O^{2-}] + v = O^{2-}\ (ads)$$

c) reaction of the adsorbed species to form an activated CO_2^{2-} complex

$$CO\ (ads) + O^{2-}\ (ads) = CO_2^{2-}\ (ads) + v$$

d) charge transfer from the ferrous iron to the complex

$$[Fe^{2+}] + CO_2^{2-}\ (ads) = Fe\ (\gamma) + CO_2\ (ads)$$

e) desorption of the adsorbed CO_2

$$CO_2\ (ads) = CO_2\ (g) + v \quad .$$

A summation of steps (a) through (e) results in a form of the overall reaction

$$[Fe^{2+}] + [O^{2-}] + CO(g) = Fe(\gamma) + CO_2 \quad . \qquad (A\text{-}2)$$

The square brackets refer to species in the melt, "ads" refers to species adsorbed on the surface, and v is a vacant surface reaction site. If step (c) is assumed to be the rate controlling step, the first order observed rate expression would be

$$R = [\ k_f\ a_{CO(ads)}\ a_{O^{2-}(ads)}\ ] - [\ k_b\ a_{CO_2^{2-}(ads)}\ a_v\ ] \qquad (A\text{-}3)$$

where R is the observed reaction rate per unit gas-melt interfacial area, k_f and k_b are the first order rate constants for the forward and reverse reactions respectively, and a_i are the

activities of species i. The thermodynamic activities of the adsorbed species are not directly measurable. But, assuming that the preceding and subsequent reaction steps to step (c) are virtually at equilibrium, the unknown activities can be expressed by known activities using the equilibrium constants, K_j, for each of the steps j in the proposed reaction mechanism:

$$a_{CO(ads.)} = K_a \, P_{CO} \, a_v \qquad (A-4)$$

$$a_{O^{2-}(ads.)} = K_b \, a_{[O^{2-}]} \, a_v \qquad (A-5)$$

$$CO_2^{2-}(ads.) = \frac{a_{CO\ (ads.)} \, a_{Fe(\gamma)}}{K_d \, a_{[Fe+2]}} \qquad (A-6)$$

$$a_{CO_2}(ads.) = \frac{P_{CO_2} \, a_v}{K_e} \quad . \qquad (A-7)$$

Also, the rate constants k_f and k_b are related to the equilibrium constant for reaction step (c) by

$$k_b = \frac{k_f}{K_c} \quad . \qquad (A-8)$$

The overall equilibrium constant, K_o can be expressed as the product of all the equilibrium constants of the reaction steps,

$$K_o = K_a K_b K_c K_d K_e \ . \qquad (A-9)$$

Substitution of equations (A-4) through (A-8) into equation (A-3) gives

$$R = k_f \, K_a \, K_b \, (a_v)^2 \left(P_{CO} \, a_{[O^{2-}]} - \frac{P_{CO_2}}{a_{[Fe2+]} \, K_o} \right) . \qquad (A-10)$$

Further simplification can be done by inserting the equilibrium

expression for $a_{[O^{2-}]}$ for the overall reaction (A-2),

$$a_{[O^{2-}]} = \left(\frac{P_{CO_2}}{K_o \; a_{[Fe^{+2}]} \; P_{CO}} \right) \quad , \qquad \text{(A-11)}$$

into equation (A-10), and using equation (A-9) to give

$$R = \left(\frac{k_f}{K_c \; K_d \; K_e} \right) \left(\frac{(a_v)^2}{a_{[Fe^{+2}]}} \right) \left(P_{CO} \; a_{,t} - P_{CO_2} \right) \qquad \text{(A-12)}$$

in which $a_{O,t}$ is the oxygen activity of the melt as a function of time. Assuming Henrian behavior of the vacant reaction sites and the ferrous ions in the melt,

$$R = \beta \frac{(\theta_v)^2}{C_{[Fe^{+2}]}} \left(P_{CO} \; a_{O,t} - P_{CO_2} \right) \quad , \qquad \text{(A-13)}$$

where β is a constant incorporating the reaction rate constant, the equilibrium constants, and the activity coefficients of the open reaction sites and the ferrous iron in the melt; θ_v is the fraction of vacant reaction sites; and $C_{[Fe^{+2}]}$ is the concentration of ferrous ions in the melt. All of the quantities in equation (A-13) can be determined. If reaction step (c) is controlling the overall reaction, equation (A-13) should describe the observed reaction rate.

Appendix B

PREDICTION OF SHAPE OF IRON GRAINS FORMED ON MELT SURFACE BY GASEOUS REDUCTION

For cylindrical-shaped iron grains growing into a melt with the axis perpendicular to the melt surface, the aspect ratio of the grain, y, is given as

$$y = d/x \ , \qquad \text{(B-1)}$$

where d is the diameter of the cylindrical grain and x is the axial length. The aspect ratio is calculated by expressing the total interfacial surface energy of the iron-gas and iron-liquid surfaces in terms of y. The resulting surface energy expression is differentiated with respect to y to find the value of y associated with the minimum total surface energy of the grain. The result of the calculation is

$$y = \left(\frac{2\,\gamma_{Fe-l}}{\gamma_{Fe-g} - \gamma_{l-g} + \gamma_{Fe-l}} \right) , \qquad \text{(B-2)}$$

where γ_{A-B} is the interfacial surface energy for a unit area of interface between phases A and B, and Fe, l, and g are the iron, liquid, and gas phases, respectively. Using the estimated interfacial surface energies given in section 3.4,

$$y = 0.91 \ , \qquad \text{(B-3)}$$

and the increase in total interfacial surface energy for the growth of a one milliliter grain of product iron is 4688 mJ/m^2. If a hemispherical-shaped iron grain is, the total interfacial surface energy increase is about 3177 $ergs/cm^2$ for the growth of a one milliliter grain.

The results of these calculations indicate that the growth of hemispherical iron grains are favored over the growth of cylindrical grains. For cylindrical grains to be favored, the surface energy of the iron-liquid interface would have to be about 300 ergs/cm^2, or 40 percent less than the liquid-gas surface energy. The interfacial energy between a metal and a slag usually lies between the separate values for the metal and the slag measured against gas (76). Formation and growth of cylindrical grains is unlikely.

Appendix C

SUMMARY OF THE METHOD USED TO DETERMINE THE FRACTION OF VACANT REACTION SITES ON THE MELT SURFACE

The Langmuir adsorption model assumes that there are vacant and occupied reaction sites on the melt surface such that for a binary system,

$$\theta_b + \theta_v = 1 \qquad \text{(C-1)}$$

and

$$\theta_i = \Gamma_i / \Gamma^\circ \qquad \text{(C-2)}$$

where θ_b and θ_v are the fraction of the total reaction sites, Γ°, occupied by solute b or that are vacant, respectively, and Γ_i is the number of sites occupied by species i. The adsorption reaction for solute b is

$$[b] + v = b\ (ads) \quad , \qquad \text{(C-3)}$$

where the brackets refer to the species in the bulk, v is a vacant site, and "ads" refers to an adsorbed species. The equilibrium of reaction C-3 is

$$K_b = \theta_b \ / \ (\theta_v\ a_b) \quad , \qquad \text{(C-4)}$$

where K_b is the adsorption coefficient, and ideal behavior of the reaction sites is assumed. Combination of equations (C-1) and (C-4) gives

$$\theta_v = 1 \ / \ (1 + K_b\ a_b) \quad . \qquad \text{(C-5)}$$

The Gibbs adsorption isotherm for species b is

$$d\sigma = -\ R\ T\ \Gamma_b\ d\ (\ln\ a_b) \quad , \qquad \text{(C-6)}$$

where σ is the surface energy of a melt with activity of species b of a_b. The Gibbs-Langmuir adsorption isotherm is

$$\sigma^{\circ}-\sigma = R\ T\ \Gamma_b^{\circ}\ \ln\ (\ 1 + K_b\ a_b\ )\ , \qquad (C\text{-}7)$$

and is derived by combination of equations (C-2), and (C-4) through (C-6), and integrating between σ°, a_b=0, and σ and a_b. In equation (C-7), σ° is the surface energy of the pure melt and Γ_b° is the surface saturation coverage of species b.

In this study, surface energy and activity data are used to determine the surface saturation coverage Γ_i° of silica or oxygen by applying equation (C-6). Equation (C-7) is solved for K_i, which is used in equation (C-5) to calculate the fraction of vacant reaction sites.

REFERENCES

1) M.W.Davies, G.S.F.Hazeldean, P.N.Smith, Physical Chemistry of Process Metallurgy, The Richardson Conference, July 1973, London, ed. by J.H.E.Jeffes and R.J.Tait, Inst. of Mining and Met., London, 95-107.

2) E.W.Mulholland, G.S.F.Hazeldean, M.W.Davies, J. Iron and Steel Inst., Sept. 1973, 632-639.

3) P. Grieveson, Physical Chemistry in Metallurgy, The Darken Conference, U. S. Steel, 8/76, pp. 83-88.

4) K. Upadhya, I. D. Sommerville, Trans. I. I. M. , vol. 33, 1980, pp. 58-65.

5) G. R. Belton, Met. Trans. B, 10B, March 1979, 118-120.

6) T. Nagasaka, Y. Iguchi, S. Ban-ya, Proceedings of the Int. Iron and Steel Society, Washington, D. C., ISS-AIME, 1986, pp. 482-484; ISIJ, vol. 24, 1984, p. B-288; see also Tetsu-to- Hagane, vol. 70, no. 2, 2/84, pp. A21-A24, and Tetsu-to-Hagane, vol 69, no. 12, 9/83, p. S761.

7) H. A. Fine, D. Meyer, D. Janke, H. J. Engell, Ironmaking Steelmaking, vol. 12, 1985, pp. 157-162.

8) H.Katayama, S.Taguchi, N.Tsuchiya, Tetsu-to-Hagane, 68, 1982, 2279-2286.

9) F. Tsukihashi, K. Kato, K. Otsuka, and T. Soma, Tetsu-to-Hagane, 68, 1982, pp. 750-758.

10) C.Borgianni, Ironmaking and Steelmaking, no. 2, 1978, 61-66.

11) M.P.Shalimov, V.N.Boronenkov, S.A.Lyamkin, Russian Metallurgy, 6, 1980, 31-34.

12) F.Fun, "Rates and Mechanisms of FeO Reduction from Slags", Met. Trans., 1, Sept. 1970, 2537-2541.

13) H.Krainer, H.P.Beer, H.Brandl, Techn. Mitt. Krupp. Forsch.-Ber., 24, 1966, 139-146.

14) E.T.Turkdogan, Physicochemical Properties of Molten Slags and Glasses, The Metals Society, London, 1983, p.46.

15) W.O.Philbrook, L.D.Kirkbride, J. Metals, 8, 1956,351-356.

16) S.K.Tarby, W.O.Philbrook, Trans. AIME, 239, 1967, 1005-17.

17) A.A.Plyshevskii, V.Ya.Belogurov, V.N.Mikhailets, Steel in the USSR, 12, Aug. 1982, 347-349.

18) ibid. ref. 14, pp. 44-45.

19) D. P. Agrawal, D. R. Gaskell, Met. Trans. B, 6B, June 1975, 263-267.

20) K. Mori, K. Suzuki, Trans. ISIJ, 9, 1969, 409-412.

21) Y. Sasaki, S. Hara, D. R. Gaskell, G. R. Belton, Met. Trans. B, vol 15B, 9/84, pp.563-571.

22) S. K. El-Rahaiby, Y. Sasaki, D. R. Gaskell, G. R. Belton, Met. Trans. B., vol 17B, 6/86, pp. 307-316.

23) T. Engel, in The Chemical Physics of Solid Surfaces and Heterogeneous Catalysis, ed. by D. A. King and D. P. Woodruff, vol. 4, Fundamental Studies of Hetergeneous Catalysis, 1982, Elsevier, pp. 72-93.

24) G. I. Golodets, J. R. H. Ross, Heterogeneous Catalytic Reactions Involving Molecular Oxygen, vol. 15 of Studies in Surface Science and Catalysis, Elsevier, 1983, p. 84.

25) ibid., p. 60.

26) J. W. May, Advances in Catalysis, vol. 21, Academic, 1970, pp. 151-277.

27) H. Viefhaus, H. J. Grabke, Surf. Sci., vol. 109, pp. 1-10.

28) K. O. Legg, F. P. Jona, D. W. Jepson, P. M. Marcus, J. Physics, C, Sol. State Phys., vol. 8, 1975, pp. 1492-95.

29) ibid. ref. 52, p. 79.

30) C. Wagner, in The physical Chemisrty of Steelmaking, J. F. Elliott, editor, M.I.T. Press, Cambridge, MA., 1958, pp.237-251.

31) C. Wagner, in Advances in Catalysis, vol. 20, D. D. Eley, H. Pines, P. B. Weisz, editors, Academic Press, 1970, pp.323-381.

32) V. V. Rao, O. Trass, Can. J. Chem. Eng., vol. 42, 1964, pp.95-99.

33) D. R. Sain, G. R. Belton, Met. Trans., vol. 7B, 1976, pp.235-243.

34) S. Taniguchi, A. Kikuchi, S. Maeda, Tetsu-to-Hagane, vol.62, no.2, 1976, pp.191-200.

35) L. E. Murr, Interfacial Phenomena in Metals and Alloys, Addison-Wesly, 1975, p. 183.

36) E. T. Turkdogan, Physiochemical Properties of Molten Slags and Glasses, The Metals Society, London, 1983, p. 172.

37) Kidd, and D. R. Gaskell, Met. Trans. B, 12/86, pp. 771-776.

38) P. J. Spencer, O. Kubacshewski, Calphad, vol. 2, no. 2, 1978, pp.147-167.

39) L.S. Darken, R. W. Gurry, J. Am. Chem. Soc. , vol.67 , 8/45, pp.1398-1412.

40) L. S. Darken, R. W. Gurry, J. Am. Chem. Soc. , vol.68 , 5/46, pp.798-816.

41) D. R. Stull, H. Prophet, JANAF Thermochemical Tables, NSRDS-NBS37. U. S. Dept. Commerce, Washington, D. C., 1971.

42) L. S. Darken , R. W. Gurry, Physical Chemistry of Metals, McGraw-Hill, 1953, p.397.

43) J. F. Marucco, P. Gerdanian, M. Dode, Compt. Rend., vol. 265, p.566 (1967)

44) M. W. Chase, Jr., J. L. Curnutt, et. al., JANAF Thermochemical Tables, 1982 Supplement, J. Physical and Chemical Reference Data, vol. 11, No. 3, p828, (1982).

45) A. Muan, Trans.-AIME, J. of Metals, pp.965-976, 9/55.

46) A. Muan, E. F. Orborn, Phase Equilibria Among Oxides in Steelmaking, Addison-Wesley, p.67, 1965.

47) R. Schuhmann, Jr., and P. J. Ensio, Trans-AIME, J. of Metals, pp.401-411, 5/51.

48) C. Bodsworth, J. Iron and Steel Inst. (London), pp13-24, 9/59.

49) S. Ban-ya, A. Chiba, A. Hikosaka, Tetsu-to-Hagane, vol. 66, no.10, pp.1484-1493, 1980.

50) E. J. Michal, R Schuhmann, Jr., Trans. AIME, J. of Metals, pp.723-728, 7/52.

51) S. Ban-ya, Y. Iguchi, H. Honda, and H. Ishizuka, Tetsu-to-Hagane, vol.71, no. 7, pp.846-852, 1985.

52) R. Schuhmann,Jr., Acta Met., vol. 3, pp219-226, 5/55.

53) N. Korakas, Inst. of Min. and Met., Transactions, vol 72, pp35-53, 1962.

54) R. Schuhmann, Jr., R. G. Powell, and E. J. Michal, Trans. AIME, J. of Metals, pp.1097-1104, 9/53.

55) G. R. Belton, Met. Trans. B, vol. 7B, pp.35-41, 3/76.

56) P. Kozakevitch, Rev. Met., vol. 47, no. 8, pp.505-516, 1949.

57) T. B. King, J. Soc. Glass Tech., vol. 35, pp.241-259, 1951.

58) Y. Kawai, K. Mori, H. Shiraishi, N. Yamada, Tetsu-to-Hagane, vol.62, pp.53-61, 1976.

59) T. B. King, The Physical Chemistry of Melts, Inst. of Mining and Metallurgy, London, pp.35-45, 1953.

60) K. Irie, S. Hara, D. R. Gaskell, K. Ogino, Osaka Univ., unpublished, 1985.

61) CRC Standard Mathematical Tables, W. H. Beyer, ed., 26th edition, CRC Press, p.128.

62) Phase diagrams for Ceramists, vol. 1, E. M. Levin, C. R. Robbins, H. F. McMurdie, editors, American Ceramic Society, 1964, figure 682.

63) R. H. Nafziger, A. Muan, American Mineralologist, vol. 52, 1967, pp. 1364-1385.

64) W. C. Hahn, Jr., A. Muan, Trans. T.M.S.-A.I.M.E., vol. 224, 6/62, pp. 416-420.

65) K. Sandhage, Ph.D. Thesis, M. I. T., 1986.

66) I. Barin, O. Knacke, Thermochemical Properties of Inorganic Substances, Springer Verlag, Berlin, 1976.

67) D. R. Gaskell, R. G. Ward, Trans.-AIME, 239, Feb. 1967, pp. 249-252.

68) C. F. Cooper, C. L. McCabe, Physical Chemistry of Process Metallurgy I, ed. by G. R. St. Pierre, A. I. M. E., Interstate N.Y., 1961, p. 117-132.

69) P. Kozakevitch, Liquids: Structure, Properties, Solid Interactions, ed. by T. J. Hughel, Elsevier, N.Y., 1965, pp.243-284.

70) M. Timucin, A. E. Morris, Met. Trans., 1, Nov. 1970, pp.3193-3201.

71) D. C. Baird, "The Propagation of Uncertainties", Chapter 3, An Introduction to Measurement Theory and Experimental Design, Prentice-Hall, 1962.

72) K. Mori, K. Suzuki, Trans. ISIJ, vol. 8, 1968, pp. 382-385.

73) R. Prange, K. Heusler, K. Schwerdtfeger, Met. Trans. B, vol. 15B, 6/84, pp. 281-288.

74) T. S. Jones, S. Kimura, A. Muan, J. Am. Ceram. Soc., vol. 50, pp. 141-148.

75) M. Timucin, A. E. Morris, Met. Trans, vol. 1, 11/70, pp. 3193-3201.

76) F. D. Richarson , Physical Chemistry of Melts in Metallurgy, Academic, 1974, p. 443.

BIOGRAPHY

The author was born and raised on the Mesabi Iron-Ore Range of Northern Minnesota, and graduated from Mt. Iron High School in 1973. He graduated from the University of Minnesota with a Bachelor of Science Mineral Engineering degree in 1978, and received the Masters of Science Mineral Engineering degree, mineral processing option, from the same school in 1979. The title of the thesis is "The Effect of Temperature and Dolomite Additions on the Microstructure of Iron-Ore Pellets". At the University of Minnesota, the author held officer positions in the student chapter of A.I.M.E., the I. T. Board, and the student senate.

After graduation, the author was employed by the U. S. Steel Corporation as a research engineer at the Minerals Beneficiation Research Laboratory in Coleraine, Minnesota (now disbanded). His main job responsibililties included the development of fluxed iron-ore pellets, and improving quality control in the Minntac mine and plant. He also served for three years as an A.I.S.I. steel fellow, promoting the causes of the domestic steel at local colleges and universities.

In February 1983, the author became the first U. S. Steel Industrial Research Fellow, and later became a candidate for the Doctor of Science degree in Metallurgy with a Management of Technology minor. At M.I.T., he was chairman of the Graduate Materials Committee.

The author is a member of The Metallurgical Society and Iron and Steel Society of A.I.M.E., the American Society of Metals, the American Ceramic Society, and the American Foundrymen's Society. He is currently employed by Corning Glass Works in the Ceramic Product Development Division, and is developing ceramic molten metal filters for application in steel foundries and steel mills.